Journal of Heat Transfer

RESEARCH PAPERS

TECHNICAL BRIEFS

ANNOUNCEMENTS AND SPECIAL NOTES

Effective Conductivity of a Composite in a Primitive Tetragonal Lattice of Highly Conducting Spheres in Resistive Thermal Contact With the Isolating Matrix

Cristina Filip
Department of Thermics,
Universitatea Politehnică,
Splaiul Independenţei 153,
Bucureşti/România

Bertrand Garnier[1]
e-mail: bertrand.garnier@univ-nantes.fr

Florin Danes

Laboratoire de Thermocinetique,
UMR CNRS 6607,
Ecole Polytechnique de l'Université de Nantes,
3 rue Christian, Pauc,
44300 Nantes, France
e-mail: florin.danes@neuf.fr

A state-of-the-art study and a physical and numerical 3D finite element study of anisotropic conduction through composites filled with isometric inclusions of different conductivity were performed by modeling the longitudinal conduction across a tetragonal lattice of spheres in imperfect contact with the surrounding matrix. In dimensionless variables, the effective conductivity E is expressible as a function of a geometrical parameter B, reflecting the relative thickness of the gap between spheres, the Kapitza resistance C of the contact inclusion/matrix, and the relative resistivity D of the filler. The computation of some 600 E values at some 25 levels of the factors B, C, and D allows one to find some features, such as the leading role of the factor whose value is the highest of three, the low effect of the interactions between factors, the imperfect equivalence of the effects of the three factors, the slow and linear E dependence on the second and third greatest factor, and finally, the asymptotically exact linear relationship between E and the logarithmated sum of factors, with a slope depending only slightly on the relative magnitudes of factors. [DOI: 10.1115/1.2768096]

Keywords: thermal conductivity, composite, thermal contact resistance, finite elements

1 Aim of the Present Work

A thermal model will be proposed here to describe the stationary 3D thermal conduction in two-phase composite materials made of a continuous polymer "matrix" uniformly filled with isometric inclusions, which do not touch one another at more than a point and are in imperfect thermal contact with the matrix. The main aim of the model is the investigation of the conditions that generate good conductive composite materials on polymer basis, i.e., composites with (effective) conductivities at least three times greater than the conductivity of the matrix. That implies a focus on a highly conductive filler (at least ten times more conductive than the polymer) and also on a filler amount near the maximal one allowed by the elaboration process of the composite, in view to reduce the role of the thermal resistance of the polymer layer between neighboring inclusions within the overall effective resistance of the composite medium. This implies that the minimal thickness of this layer is <10% of the inclusion size. An allowable and limited imprecision of the model—for example, no more than 5% maximal error compatible with its use under practical circumstances and with eventual measurements of the effective conductivity—requires that the model must be quantitative, deductive, predicting, without free parameters, deterministic, and in agreement with the partial differential equation of the heat transfer and with the true boundary conditions at the borders and at the interface inclusion/matrix.

2 State of the Art of Modeling the Conductivity of Filled Composites

2.1 Effects of the Structure of Filled Composite Materials.
Size of Inclusions. If the inclusions are in perfect thermal contact with the matrix, the inclusion size is no matter for the heat transfer, since the effective conductivity depends only on the ratios of lengths and not on the length itself. But if the thermal contact is imperfect, the effective conductivity of composite depends too on the inclusion size [1].

Shape of inclusions. The effective conductivity λ_{eff} is affected by the inclusion shape, but the extent of this effect and its very sign are not well understood.

Variability of the filler size. It has probably an important effect on the heat conduction, but this dependence is not yet quantified.

Uniformity. The composite geometry and, hence, its properties are supposedly uniform, i.e., independent of the location within a volume containing a lot of inclusions.

Dimensionality. One can distinguish the usual 3D composites, from the 2D composites (i.e., two-dimensional transversal sections through a normal composite)

Anisotropy. The anisotropy of composite vector properties as the conductivity is common because it can occur from the anisotropy of vector properties within any phase, from the anisotropic shape of the inclusions, or from the anisotropic location of inclusion in the composite body.

Regularity in the Location of Inclusions. One can differentiate random and ordered composites, whose inclusions (all in equal size) form a lattice. The industrial filled polymers are, in fact, random composites, but the models with a random structure are cumbersome. The quantitative description of the "randomness" is nowadays very ambiguous: the different ideas on the type of ran-

domness are unfortunately not yet in position to be confirmed or not, neither by the structure determination of real composites nor in every measurement. The geometric or thermal modeling of random composites is still at the very beginning.

Besides, Bao et al. [2] found in a 2D geometry that the effective λ_t is only slightly sensitive to various divergences from the regularity of inclusion's size, shape, or location, except for filler amounts very close ($<1\%$) to the percolation threshold.

2.2 Heat Transfer in Composites. The heat transfer in composites is mostly described under stationary conditions. Araki et al. [3] investigates the transient heat transfer in composites, but without specific conclusions. The sole quantified heat transfer feature is the effective (thermal) conductivity λ_{eff} or its relative value $E \equiv \lambda_{\text{eff}}/\lambda_m$, where λ_m is the (isotropic) conductivity of the matrix. Araki et al. [3] prefer the description through the space fields of the temperature and of the heat flux density. Zinchenko [4] describes the heat transfer using the total heat flux that crossed a small area between two neighboring inclusions.

For a long time, every effect of the phase interface on the effective conductivity in composites was wholly neglected, i.e., the thermal contact was supposed perfect. Lu [5] showed that the thus committed error is particularly important in composites with polymer matrix, even when any surface reaction is lacking, since the mixing stage by the industrial fabrication induces inevitable stresses in the polymer layers around each inclusion. These layers always present a gradual variation of all physical properties of the composite, according to Privalko and Novikov [6].

The real contact, however, is then always imperfect; hence, the effective conductivity is, in fact, lower than those computed for the perfect contact. Chen [7] elucidates the macroscopic features of the (usual imperfect) thermal contact through an analysis of the local continuity of the heat flux density ϑ and temperature gradient Π, at the interface—supposed infinitely thin—between two different media. The former is discontinuous only in the two tangential directions, whereas the later is discontinuous only in the normal direction. The Kapitza contact resistance r_c is defined as the temperature jump at the interface divided by the heat flux density, both considered in the normal direction.

The various alternative models of the contact imperfection [6,8–10] introduce two unknown parameters instead of a single such parameter as in the method of the Kapitza resistance, but the contact resistance between matrix and inclusion is yet barely predictable and its direct measurement [11] is at the very beginning. Therefore, the use of these more intricate concepts remains simply impossible to use in a quantitative manner.

2.3 Effect of the Contact Resistance on the Conductivity of Composites. In the first models, the contact resistance is neglected, or is accounted only for low filler amounts. The effective conductivity was computed there within the frame of approximate models, that do not respect the geometry of the system, the heat transfer differential equations or the boundary conditions.

Benveniste and Miloh [12] apply the average field model of Bruggeman. The self-consistent approximation leads to the formula of Benveniste [13]

$$E = \frac{(1 + 2\varphi) + 2(C + D)(1 - \varphi)}{1 - \varphi + (C + D)(2 + \varphi)} \quad (1)$$

where C is the relative thermal contact resistivity, D the relative thermal resistivity of the filler, and φ the filler amount (ratio between filler and total volume). The same formula is obtained simultaneously, using the old *multipoles method* of Rayleigh, 1892, by Hasselman and Johnson [14], who indicate that it can be corrected only in the limit $\varphi \to 0$. Chiew and Glandt [15] found that the error of the multipoles method increases not only with increasing φ but also with increasing filler conductivity, the formulas, such as Eq. (1), becoming inapplicable if $C + D < 0.15$.

The filler resistivity D has to be replaced, for an imperfect

contact, by $(C + D)$, as one can see already in the Eq. (1). Consequently, if C is high enough, i.e., $C > (1 - D)$, then the effective conductivity falls with increasing filler amount. This feature is captured in a semi-empirical formula proposed by Wang and Yi [16] for the effective conductivity.

Every et al. [1] broadened the average field model to higher filler contents of spherical inclusions, resulting in the semi-empirical implicit relationship,

$$(1 - C)\ln(1 - \varphi_c) = \left\{ \ln\left[\frac{DE + C - 1}{D + C - 1} \right] \right\} + \left(\frac{1 + 2D}{3} \right)\ln E \quad (2)$$

Davies and Brenner [17] treated the near-contact case with correct (applied at infinity) boundary conditions. The heat flux $q_{s \to p\infty}$ between a single sphere of radius r and a semi-infinite domain, both infinitely conductive thus isothermal (temperatures τ_s, respectively, τ_p) across a thin curved gap part of a half space of conductivity λ_p, is given (by $D \to 0$ and dimensionless gap thickness $B \ll C$) by

$$q_{s \to p\infty} = 2\lambda_p r |\tau_p - \tau_s| \ln(C^{-1}) \quad (3)$$

where C is linked to the contact resistances r_p of the plane and r_s of the sphere by

$$C \equiv (r_p + r_s)\lambda_p/r$$

Acceptable differential models of the composite with imperfect contact inclusion/matrix (respecting the true geometry of the system, the Fourier and Laplace equations, and the boundary conditions of the sphere surface) appear only later: a 2D model is proposed by Gonçalves and Kolodziej [8] in a quadratic primitive unit cell with circular inclusion, and a 3D model for the three cubic cells with spherical inclusions was proposed and solved by Cheng and Torquato [18].

Inasmuch as the practitioner does not have easy access to the contact resistance, his true concern is rather the sensitivity (still unknown yet) of the effective conductivity to the inclusion size r. Indeed, if the *intensive* contact resistance (r_c, expressed in square meters per degrees Kelvin per watt) does not vary as r changes, then—for a given filler amount—the effective conductivity E grows with increasing inclusion radius, $dE/dr > 0$ and coarse filler is preferable. But if the *relative* contact resistance ($C \equiv \lambda_p(r_c/r)$) does not vary as r changes, then E is not affected by the inclusion size, $dE/dr = 0$, and the best choice is that of a finer filler, since the composite pieces are more uniform, as shown by Danes et al. [19].

2.4 Approximate Computing of the Conductivity in Composites. Approximate methods do not use the true differential system of heat conduction; at least one of the three elements needed for a correct model (true geometry of phases, Laplace PDE, and correct boundary conditions) is lacking. Most of them ignore the existence of the imperfect thermal contact. The others are acceptable only within a limited area of parameters; for example, they lead typically to a too low conductivity for high filler content. The formulas are of several kinds, as follows:

- *Empirical* ones, which originate not in a model, but are induced either from the measurements or by fitting the numerical results of a model. These formulae contain sometimes free parameters, whose values are chosen precisely in order to better fit the data. The semi-empirical formulae originate only partly from the generalization of measurement values, since they combine such values with general or theoretical principles.
- *Ohm's law* models, which originate in electrokinetics and combine, in various arbitrary ways, different sets of series and parallel resistances, without link to the real location of the inclusions or to their size or form.
- Bruggeman's model of *average fields*—average heat flux density and average temperature gradient—also known as EMA (effective medium approximation), modifies gradually

the outer medium of a given inclusion by introducing all other inclusions.

- Hashin's *self-consistent* approach (also known as the model of the equivalent inclusion) replaces all the real spherical inclusions poured in the matrix by a single fictitious two-layer inclusion (from a filler core and a matrix outer shell) plunged in a homogeneous medium of uniform conductivity. This last conductivity is just the effective conductivity of the composite.

3 Differential Equations Model of Heat Transfer in Composites

3.1 The Differential System. In each point of the analyzed space, the differentially heat transfer models obey to Fourier's law $j = -\lambda \nabla \tau$ of proportionality between the vectors j of the heat flux density and $\nabla \tau$ of the temperature gradient, where λ is the local value of the thermal conductivity, i.e., in composites λ_f within each inclusion and λ_m within the matrix (i.e., outside of the spheres). Under stationary conditions, this leads to the Laplace partial differential equation: $\nabla^2 \tau = 0$, when the conductivities are invariable.

The effective conductivity λ_{eff} is defined as the limiting value, for an infinite distance L, of the ratio between the product (heat flux density j times the distance L of two parallel isotherm planes, 1 and 2) and the temperature difference of these two planes: $\lambda_{\text{eff}} \equiv \lim_{L \to \infty}(L|j_{a \to b}|)/|\tau_1 - \tau_2|$.

Thermal sources and sinks are absent in the composite models, except for Cruz [20]. The thermal contact between each inclusion and the matrix is of resisting nature, i.e., obeying for each point of the interface, the twin equations (boundary conditions of third kind) $j'_n = j''_n = (\tau'' - \tau')/r_c$, with the prime and double prime denoting the outer and inner sides of the sphere surface, τ and j_n being the temperature and the normal component of the heat flux density, on the sphere surface and r_c—the contact resistance.

3.2 Space Frames of the Heat Transfer. One can distinguish three manners to consider the heat transfer geometry in composites, as follows:

- Most heat transfer models use an elementary cell as a space frame. Its classical definition (implicit by [21]) uses identical and stackable cells, cell borders that do not intersect the sphere, and well-defined boundary conditions at cell borders. The standard boundary conditions on the cell's borders [22] are those of a normal slice across a flux tube: isothermal walls on the two cell's faces perpendicular to the main heat gradient (whose direction defines the effective conductivity), and adiabatic walls for all other faces. Other boundary conditions on the transversal faces were introduced: general first kind (the temperature changes with the location) for Cruz [20] or second kind (namely, constant heat flux) for Islam and Pramila [23].
- The most general heat transfer description in ordered composites [24] uses periodical relations to define geometry, thermal properties of matter, as well as boundary conditions both on cell borders and at the contact interfaces.
- In the work centered on the local description of heat transfer, the main feature is the total heat flux between two neighboring inclusions, instead of the effective conductivity.

3.3 Complete Global Solving. The first complete analytical solutions for the effective conductivity of 3D regular arrays of spheres in perfect contact with the matrix, first published by McPhedran and McKenzie [25] for 3D simple (primitive) cubic lattice *sc*, McKenzie et al. [26] for 3D body- and face-centered-cubic lattices (bcc and fcc) are later improved by Sangani and Acrivos [27]. The complete global solution for the 3D regular case with imperfect contact is provided by Cheng and Torquato [18]. By truncation to the value I of the integer i, the infinite linear algebraic system whose unknown variables are the coefficients $b_{n,m}$ (denoted B_n/E_0 by Cheng and Torquato [18]) becomes

$$K_n b_{2n-1,m} + \sum_{i=1}^{i=I} \sum_{j=0}^{j=2i-1} k_{n,m,i,j} \frac{2 - \delta_{j,0}}{2} b_{2i-1,j} = \delta_{n,1} \delta_{m,0} (\Delta T)^3 \sqrt{\frac{\varphi_{\max}}{\varphi}}$$

(4)

where m is a multiple of 4, $m < 2n$, $\delta_{i,j}$ is the Kronecker delta

$$\delta_{i,j} \equiv \begin{cases} 0, & if \quad j \neq i \\ 1, & if \quad j = i \end{cases},$$

$$K_n \equiv \frac{1 + \dfrac{1+n}{nM} + \dfrac{1+n}{H}}{M^{2 \cdot n + 1} \cdot \left(\dfrac{1}{M} - 1 + \dfrac{n}{H}\right)},$$

and $k_{n,m,i,j} \equiv h_{n,m,i,j} + h_{n,-m,i,j}$, with $h_{n,m,i,j}$ defined by $h_{n,m,i,j} = L_{2 \cdot (n+i-1)}^{j+m} \gamma_{2 \cdot n-1+m}^{2 \cdot i-1+j} \gamma_{2 \cdot n-1-m}^{2 \cdot i-1-j}$, L_c^d and γ being the Laplace function of degree (c,d), and γ_a^b the gamma function $\gamma_a^b \equiv \sqrt{(a+b)!/a! \cdot b!}$. After resolution of the system, one can obtain E by $E = 1 - 4\pi\mu b_{1,0}$, where μ is the number of spheres in an elementary cell. Numerical values of the coefficients $k_{n,m,i,j}$ of the $b_{n,m}$ for $n < 20$ are available from Cheng and Torquato [18] for the three cubic arrays.

3.4 Simplified Formulas From the Global Solution. More or less precise formulas for E as series can be obtained by a truncated development of the complete analytic solution. This approximation presents primarily E as a truncated sum of rational functions of the third root $\varphi^{1/3}$ of the relative filler content. The "series" method, although more straightforward to apply than the numerical thus cumbersome "complete" method, results in formulas not at all guaranteed; each work found important errors in the previous one.

Cheng and Torquato [18] therefore developed a version of the same kind of solution—truncated at the fifth order for the imperfect contact case and for the three cubic lattices: $E = 1 + 3\varphi/[(1/L_1) - \varphi - \Psi(\varphi)]$, with $L_k(C,D,k) \equiv 1 - [(2k-1)C - D]/\{1 + (2k/2k-1)[(2k-1)C+D]\}$ and $\xi \equiv \varphi^{1/3}$. For a *sc* lattice, $\Psi(M,H,\varphi) \equiv 1.30472\xi^{10}L_2 + 0.07232\xi^{14}L_3 - 0.52895\xi^{17}(L_2)^2 + 0.15256\xi^{18}L_4 - 0.30667\xi^{21}L_2L_3 + 0.01045\xi^{22}L_5 + \Re(\xi^{25})$. Probable sign errors before ξ^{17} and ξ^{21} must be pointed out. The formula is biased $\sim 5\%$ if $B < 0.05$ (for the cubic lattices: $6\varphi(1+B)^3 = \pi$).

Malyshev and Malyshev [28] funded in the same way, for perfect contact in a *sc* lattice: $\Psi(D,\varphi) \equiv a_{231}/b_{231} + c_{231}$, where $a_{231} = 1.3091L_2\xi^{10}(1 + 0.1173L_3\xi^{11})^2$, $b_{231} = 1 - 0.4054L_2\xi^7 - 6.6568L_2L_3\xi^{18}$, and $c_{231} = 0.0723L_3\xi^{14} + 0.15256L_4\xi^{18}$.

There is finally an empirical solution, claimed by Cheng and Torquato [18] as much more precise than the above series (bias $< 1\%$ for the two cases: $C = 3 \cap D = 0.1$ and $C = 0.5 \cap D = 10,000$ in a fcc lattice) is $E = [1 + 2\varphi L_1 - 2(1-\varphi)(L_1)^2 \zeta_2]/[1 - \varphi L_1 - 2(1-\varphi) \times (L_1)^2 \zeta_2]$, where ζ_2 is a *microstructure parameter* whose values are given by the table of $\zeta_2(\varphi)$ from McPhedran and Milton [29].

3.5 Local Solutions. If inclusions are almost touching, the adequate geometric variable is no more the filler amount φ, but the relative thickness B of the matrix layer between nearest spheres. In isotropic lattices, one can use $\varphi(1+B)^3 = \varphi_{\max}$, where the maximal filler amount $\varphi_{\max}$ depends only on the Bravais lattice, for example, $\varphi_{\max} = \pi/6 = 0.5236$ in the *sc*. The boundary conditions are either not defined or are accounted for at an infinite distance. One must introduce local models, which lead to the total heat flux θ_{II} between the two proximate spheres, flux linearly linked to the effective conductivity E: $\theta_{\text{II}} = c_1(E + C_2)$. The coeffi-

cients C_1 and C_2 depend, among others, on the geometry.

Batchelor and O'Brien [30] deduce the first and the second Batchelor's relationships, where B, C, and D are respectively the outer, contact, and inner reduced thermal resistances,

$$\max(C,D) \ll B \ll 1 \Rightarrow E = -K_{1a} - K_B \ln\left(1 - \frac{\varphi}{\varphi_{\max}}\right) \quad (5)$$

$$\max(B,C) \ll D \ll 1 \Rightarrow E = -K_{1b} - 2K_B \ln D \quad (6)$$

For the *sc* lattice, Batchelor and O'Brien [30] obtain $K_B = 0.5\pi \cong 1.57$. Sangani and Acrivos [27] found from the analytic complete method, that for the *sc* lattice: $K_{1a} = 0.69$ and $K_{1b} = 5.91$.

Zinchenko [4] founds, for the longitudinal heat flux $J_{q,\mathrm{cen}}$ between spheres along the symmetry axis of the two-spheres system with perfect thermal contact inclusions/matrix,

$$[C \ll \min(D,B)] \cap [\max(D,B)] \cap \ll 1 \Rightarrow J_{q,\mathrm{cen}} = K_{Z1}$$
$$- K_{Z2} \ln(BD^2), \quad \text{equivalent to} \quad [C$$
$$\ll \min(D,B)] \cap [\max(D,B)] \cap \ll 1 \Rightarrow E = k_{Z1} - K_{Z2}\ln(BD^2) \quad (7)$$

Davies and Brenner [17] obtain for the near-contact case with imperfect contact, $\max(D,C) \ll B \ll 1 \Rightarrow \theta_{s \to p\infty} = -2\lambda_p r |T_p - T_s| \ln B$, and $\max(B,D) \ll C \ll 1 \Rightarrow \theta_{s \to p\infty} = -2\lambda_p r |T_p - T_s| \ln C$. This is equivalent to

$$\max(D,C) \ll B \ll 1 \Rightarrow E = K_{D1} - 2 \ln B \quad (8)$$

$$\max(B,D) \ll C \ll 1 \Rightarrow E = K_{D2} - 2 \ln C \quad (9)$$

In the previous equations, K_{1a}, K_{1b}, K_B, K_{Z1}, K_{Z2}, k_{Z1}, K_{D1}, and K_{D2} do not depend on B, C, or D.

4 Main Features of the Adopted Model

4.1 General Assumptions and Dimensionless Variables. In order to alleviate the modeling and subsequent computations, but without too much loss of precision or of generality, the following assumptions have to be made:

- Neglect the internal heat sources, as well as the radiating and the convective heat transfer modes.
- The conductivity of each material does not depend on time, position, direction, and temperature.
- The thermal contact between inclusion and matrix can be described by means of a single characteristic: the thermal contact resistance, also known as the Kapitza resistance.
- All inclusions are spherical, of equal size, and have in each point of their interfaces the same contact resistance.
- The single dependent feature searched for is the effective conductivity of the composite.
- The considered spheres make up a lattice, i.e., they are regularly scattered within the physical 3D space.

In view of dropping the number of the handled variables and parameters, each physical quantity is to be reduced to its dimensionless counterpart. This results in the following general relationship:

$$E = E(C,D,\Gamma) \quad (10)$$

where one can distinguish the following:

- A single dependent variable—the reduced thermal effective conductivity E, defined as the ratio between the conductivity of the composite and the one of the polymer matrix
- Two thermal factors (i.e., independent variables), as follows:

  - reduced inclusion resistivity D, defined as the ratio between the conductivities of the polymeric material of the inclusions and the metallic material of the matrix

- reduced contact resistivity C—the thermal contact resistance divided by the radius of the sphere radius and multiplied by the matrix conductivity

- A set Γ of 0 to 6 simplexes (geometrical dimensionless factors), which can be either angles, ratios between two appropriate lengths, or φ—the relative volume amount of the inclusions. All temperature effects on E, via the geometry Γ of the composite (thermal dilatation of the constituent materials), as well as via the temperature dependences of the conductivities of materials or of the contact resistance, are neglected.

4.2 Describing the Regular Geometries. For keeping the number of independent variables as low as possible, the choice of the assumed geometry is of great importance. The best choice is that of a single geometrical simplex, since there are already two other factors (C and D, resistivities of the interface and of the filler conductivity).

There are only 14 ways to fully fulfill the 3D space with regularly scattered points or with spheres, namely, the 14 Bravais lattices, each being characterized by its crystallographic unit cell—a solid defined by three pairs of opposite parallel faces. A Bravais lattice is uniquely defined as follows:

- its symmetry features
- the shifting type, accounting for the differently shifted array copies intercalated between the triple set of points (or of sphere centers) in the simple lattice

4.3 Assuming a Differential Heat Transfer Model

4.3.1 Heat Transfer in Ordered Arrays of Spheres. One can solve the correct stationary heat transfer differential equations for each of the 14 Bravais lattices, by applying periodical boundary conditions. Until now, the only available solutions $E = E(C, D, \varphi)$ are those of Cheng and Torquato [18] for the three cubic Bravais lattices (primitive P, body centered I, and face centered F). Here, the relative filler amount φ is the ratio between the volume of all spheres in a unit cell (1, 2, and 4 for the P-, I-, and F-shifting versions, respectively) and the whole cell volume. Furthermore, two unit cells (P-hexagonal and P-orthorhombic) were treated only for the perfect contact.

The numerical solving of the heat transfer partial differential equation (PDE) requires special symmetry conditions, which are not fulfilled in all Bravais lattices. Indeed, the existence of a classical (thermal) elementary cell—whose borders do not intersect the inclusions, as imposed by the actual finite element packages—requires that there are three mirror planes and they do not cross the spheres. Only three Bravais lattices can be also treated by finite element (FE): the primitive lattices of the cubic, tetragonal, and orthorhombic crystal systems.

Besides, the number N_G of simplex (geometrical factors) in the relationship (10) can be 1 only for the cubic lattices and for the hexagonal compact one (i.e., with $c/a = \sqrt{2/3}, b/a = 1$). For the other three cases, namely, those of the hexagonal (noncompact), rhombohedral, and tetragonal lattices, N_G can be reduced to 1 by introducing a supplementary restriction between the length of the unit cell of one hand and the sphere radius on the other hand.

4.3.2 Assumed Geometry. In light of the previous analysis, the following heat transfer model was adopted here, in sight of a subsequent use for a thermally dedicated 3D finite element computational package: the elongated primitive (without extra points) tetragonal lattice, whose parameters are: (i) all three angles measure 90 deg and (ii) two of the three cell sides are equal. The thermal elementary cell will be the same as the crystallographic cell, but shifted with a half step in all three space directions; the sole sphere, which appears thus in the elementary cell, is centered at the cell symmetry center.

An elongated form of the cell will be adopted, i.e., with side

lengths $a=c<b$, and not a flattened one (where $b<a=c$). The main reduced effective conductivities E_x, E_y, and E_z, along the directions whose side lengths are a, $c(=a)$ and respectively, b, are thus ordered $E_z<E_x=E_y$, feature common in the industrial thermoplastic plates, as noted by Garnier et al. [11] or Danes et al. [19]. In such an elongated cell, the longitudinal conductivity E_z of the composite is the single one, among the principal effective conductivities, to be very sensitive to the filler amount in the most interesting case—that of the near percolating conditions, when the polymer layer between the highly conductive spheres is much thinner than the inclusion size. Therefore, in the following, the computation of the "transversal" principal conductivity in the plane by (i.e., E_x) is neglected and E_z will be designated simply as "effective conductivity" quoted E.

The cell faces with Dirichlet boundary conditions are, for the computation of the effective conductivity in the longitudinal direction, the two square faces of the elementary cell. Moreover, the cell symmetry leads to adiabatic boundary conditions for all four rectangular (elongated) cell faces.

As supplementary geometrical requirement in order to have only one simplex, the equality between sphere diameter $2r$ and transversal length $2a$ of the cell (i.e., the side of the two square faces of the elementary cell) is imposed, $r=a$. The sphere is consequently tangent to all four rectangular (elongated) faces of the cell.

As geometric simplex, one will choose here B, defined as the relative minimal distance between two spheres in the longitudinal direction Oz, i.e. the ratio between this distance ($2b-2r$) and the sphere diameter $2r$. Therefore, the explored dependence (10) becomes

$$E = E(B,C,D) \qquad (11)$$

As $r=a$ according to the previous point, the definition $B \equiv b/a -1$ follows. The filler amount φ is correlated (tetragonal cell) to B by $\varphi = sphere\ volume/cell\ volume = \pi/6(1+B)$.

5 Solving the Problem

5.1 Elementary Cells and Dimensionless Variables. The tetragonal unit cell is composed of a sphere of radius a centered in a parallelipipedic cavity of dimensions $2a \times 2a \times 2b$ (Fig. 1(a)) with upper and lower faces isothermal at temperatures, respectively, τ_1 and τ_2, the four lateral faces being adiabatic. Accounting for the symmetries, only one-sixteenth of the original cell need to be meshed (Fig. 1(b)). The frontal faces of this elementary cell are also isothermal, but now at temperatures τ_1 and $0.5(\tau_1+\tau_2)$, whereas the three lateral faces are anew adiabatic.

Let σ and τ be the filler and matrix temperatures, respectively, λ_f and λ_m the thermal conductivities of the filler and the matrix, r_c the thermal contact resistivity, and λ_{eff} the effective longitudinal conductivity. The adimensionnal variables and parameters are defined as follows:

- $X=x/a$; $Y=y/a$ for the two lateral dimensions and $Z=z/a$ for the longitudinal one
- $S=(2\sigma-\tau_1-\tau_2)/(\tau_1-\tau_2)$; $T=(2\tau-\tau_1-\tau_2)/(\tau_1-\tau_2)$ for the unknown inner and outer temperature fields
- $B=(b-a)/a$ and $D=\lambda_m/\lambda_f$, for the conductive resistances B of the matrix gap (between neighbor spheres) and D of the filler sphere
- $C=r_c\lambda_m/a$ and $E=\lambda_{eff}/\lambda_m$, for the contact resistance and the effective longitudinal conductivity

5.2 Model Equations. The temperatures are governed by the Laplace equations $\nabla^2 S=0$, $\nabla^2 T=0$. At the inclusion boundary Ω, defined by $X^2+Y^2+Z^2=1$, there is a continuity of the normal part (symbol $\perp$) of the heat flux vectors, but a temperature lag between the two interface values $\mathbf{T}_\Omega$ and S_Ω
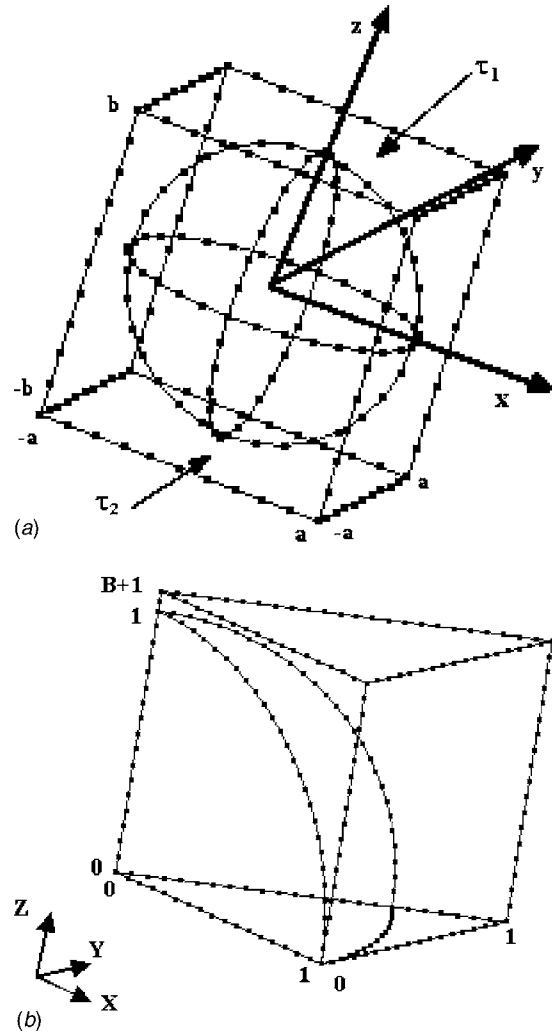
Fig. 1 (a) Crystallographic unit cell and (b) FE-computed elementary cell

$$\nabla S_{\perp\Omega} = D \cdot \nabla T_{\perp\Omega} = C(T_\Omega - S_\Omega) \qquad (12)$$

here $\nabla S_{\perp\Omega}$ and $\nabla T_{\perp\Omega}$ are the rates of variation at the sphere surface of the inner and outer temperatures, along the normal direction.

The boundary conditions at the borders of the elementary cell are of Neumann type except at the upper and lower faces, where constant temperature is prescribed

$$S(X,Y,0) = T(X,Y,0) = 0 \quad \text{and} \quad S(X,Y,B+1) = T(X,Y,B+1) = 1 \qquad (13)$$

The dimensionless heat flux Q crossing the elementary cell (Fig. 2) is calculated by integrating the heat flux in the z direction over the upper face of the elementary cell

$$Q = \int_0^1 \left(\int_0^X \left. \frac{\partial T}{\partial Z} \right|_{Z=0} dY \right) dX \qquad (14)$$

Then, the effective conductivity E is deduced from $E = 2Q(1+B)$.

5.3 Modeling Strategy. The solving methods can be either analytic (at least at the beginning of the computation, as finally all became numeric) or purely numeric. None of these are exact; the analytical one approximates the solution, whereas the purely numerical method approximates the derivatives within the PDE.

Our choice was a purely numerical FE tool—Comsol v3.2 [31].
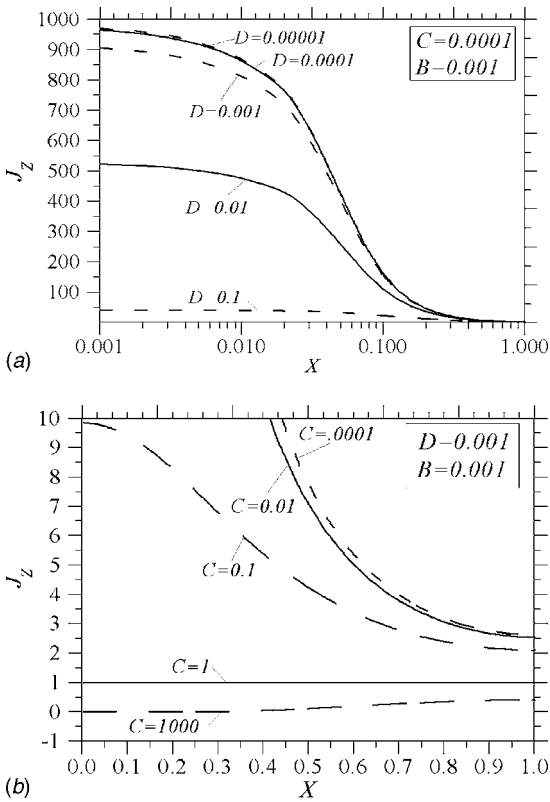
Fig. 2 (*a*) Effect of the inner thermal resistance *D* on the longitudinal heat flux density, along the line from ($X=0$, $Y=0$, $Z=1.001$) to ($X=1$, $Y=0$, $Z=1.001$) and (*b*) effect of the thermal contact resistance *C* on the longitudinal heat flux density, along the line from ($X=0$, $Y=0$, $Z=1.001$) to ($X=1$, $Y=0$, $Z=1.001$)

All the computations were performed using the 3D stationary heat transfer module with conduction option. This code, designed for solving multiphysics partial differential equations in an interactive environment, allows the direct application of the thermal contact resistance scheme, i.e., a temperature drop at the filler/matrix interface proportional to the normal heat flux.

The filler and matrix regions were meshed using the automatic mesh generator of the finite element code. No refinement of the mesh around small geometrical features, such as boundary or interface, was considered. The finite elements are quadratic and of Lagrange type, which provides high precision. The number of tetrahedra taken into account during the solving of the finite element problem do not depend on the physical properties (i.e., C and D) but only on the geometrical parameter B. This number changes from 48,000 to 58,000 as B decreases from 0.075 to 0. The number of freedom's degrees is about 1.5 times greater.

The convergence of solution depends also on C and D. The computation time ranges from 60 s to 120 s, with a PC Pentium 4 with a processor frequency of 3.06 GHz and RAM of 512 Mo.

Additional runs were performed with extremal values of B, C, and D using three to four times more finite elements (i.e., degrees of freedom between 285,000 and 300,000), requiring higher computation time (300–700 s). The obtained effective thermal conductivities do not change more than 0.1%.

5.4 Distribution of the Longitudinal Heat Flux Density. After solving the heat equation using finite elements, one can compute the reduced longitudinal heat flux density J_Z (X,Y,B,C,D) on the upper face, defined as

$$J_Z = \frac{2a}{\lambda_m(\tau_1 - \tau_2)} j_z \qquad (15)$$

where $j_z = \lambda_m (\partial \tau / \partial z)|_{z=b}$ is the dimensional heat flux density, $a = 0.002$ m, $\lambda_m = 0.2$ W/(K m) and $\tau_1 - \tau_2 = 1$ K. Equation (15) allows one to compute J_Z by $J_Z = \lim_{Z \to B+1} \partial T / \partial Z$.

Figure 2(*a*) illustrates the following:

- For very close particles, low filler resistivity and low contact conductance, the longitudinal heat flow is mainly located within the region where the matrix layer becomes very thin (in the *Z* direction), i.e., for $X < 0.1$, where the gap thickness is $< B + 0.005$.
- As the filler resistance D increases, the heat flow becomes more uniformly distributed.
- As the thermal contact resistance C increases, the heat flow distribution becomes also more uniform (Fig. 2(*b*)).

For values of $C > 1$, the heat flux distribution becomes different: higher heat fluxes are obtained at the periphery of the transversal planes (i.e., for X and/or Y close to 1).

6 Results

6.1 Response, Factors, and Their Ranges of Variation. Response. The studied dependent variable (or the variable of interest), called in the following response from a regression perspective, is here the reduced effective longitudinal conductivity E of a tetragonal array of spheres with resistive surface and imbedded in a matrix of different thermal conductivity, as described in Sec. 4.

Factors. The studied independent variables (or the parameters of interest), intentionally modified in a given controlled manner, are called in the following factors. The following are three factors, the reduced (dimensionless) versions of the three partial thermal resistances:

- B—the reduced outer resistance of the matrix layer between nearest spheres
- C—the reduced contact resistance, located at the sphere interface between the two materials
- D—the reduced inner resistance

All other independent variables (precision of computing, choice of the meshing, etc.) are neglected as their effects were checked to be much smaller than the one of B, C, and D factors.

Ranges of Variation in the FE Study. A number of 585 reduced effective longitudinal conductivity E of a tetragonal array of spheres with resistive surface and imbedded in a matrix of different thermal conductivity, as described in the Sec. 4, was computed by the 3D finite element method exposed in Sec. 5, as a function $E(B,C,D)$ of the three quoted partial thermal resistances: $B = x \times 10^{-4}$ with $x \in [0, 10, 25, 50, 75, 100, 150, 200, 250, 375, 500, 625, 750]$, $C = 10^x$ with $x \in [-5, -4, -3, -2, -1, 0, 1, 2, 3,]$, and $D = 10^x$ with $x \in [-5, -4, -3, -2, -1]$.

A fifth of this data rounded to the fourth decimal digit is presented in Table 1. This is a two-entry table of FE-computed E values, for each of the 117 combinations of B and C at constant $D (= 10^{-3})$.

The obtained effective conductivities lie in the range [0.34, 17], covering, therefore, most of the eligible E range; the lower limit of E for the adopted geometry is 0.33. On another side, the local model shows that the upper limit of E (reached at $B=C=D=0$) is logarithmically infinite, but the condition B, C, and D, simultaneously null, are not realistic, since the minimal physically possible value for known materials is $D = 10^{-6}$, where the corresponding maximum E (obtained at $B=C=0$) is < 20.

6.2 Sign of Effects of Factors B, C, and D on Effective Conductivity. The simplest effects—those of the single factors—are characterized by the first-degree derivatives of the response

Table 1 Effective conductivity *E* as function of layer resistance *B*, for different contact resistances *C* and with a constant inner resistance *D*=0.001

$B\downarrow C\rightarrow$	0.00001	0.0001	0.001	0.01	0.1	1	10	100	1000
0	14.3983	12.9747	9.8898	6.4961	3.1523	0.9995	0.4258	0.3522	0.3446
0.001	9.8933	9.7683	8.9070	6.3613	3.1421	0.9995	0.4260	0.3524	0.3448
0.0025	8.5894	8.5375	8.0968	6.1786	3.1271	0.9995	0.4263	0.3526	0.3450
0.005	7.5946	7.5676	7.3209	5.9239	3.1026	0.9995	0.4268	0.3531	0.3455
0.0075	7.0059	6.9876	6.8160	5.7087	3.0790	0.9995	0.4273	0.3536	0.3459
0.01	6.5937	6.5798	6.4476	5.5249	3.0559	0.9995	0.4279	0.3540	0.3464
0.015	6.0159	6.0065	5.9156	5.2204	3.0118	0.9995	0.4289	0.3550	0.3473
0.02	5.6101	5.6030	5.5337	4.9749	2.9699	0.9995	0.4299	0.3559	0.3482
0.025	5.2997	5.2940	5.2387	4.7706	2.9303	0.9995	0.4310	0.3568	0.3492
0.0375	4.7504	4.7465	4.7085	4.3748	2.8398	0.9995	0.4336	0.3591	0.3514
0.05	4.3743	4.3713	4.3424	4.0825	2.7592	0.9995	0.4361	0.3615	0.3537
0.0625	4.0916	4.0893	4.0659	3.8527	2.6869	0.9995	0.4387	0.3638	0.3560
0.075	3.8669	3.8649	3.8454	3.6645	2.6215	0.9995	0.4413	0.3661	0.3583

with regard to the factor variables. A decrease of the contact resistance *C* or of the inner resistance *D* leads always to a raise of the effective conductivity,

$$\left(\frac{\partial E}{\partial C}\right)_{B,D} < 0; \quad \left(\frac{\partial E}{\partial D}\right)_{B,C} < 0 \qquad (16)$$

The first effect is illustrated by the data in Table 2 and the second on Fig. 3. The sign for the effect of the (matrix) layer resistance is on the contrary, depending on the range of the effective conductivity. As illustrated by the results from Table 2, at given *C* and *D* each increase of *B* brings *E* closer to 1 (i.e., leads to a rise of *E* if *E*<1 and to a decrease of *E*), if *E*>1,

$$\left(\frac{\partial E}{\partial B}\right)_{C,D} (E-1) < 0$$

The same feature can be approximately expressed, with *C* or *D* as arguments (instead of E), by

$$\left(\frac{\partial E}{\partial B}\right)_{C,D} (C+D-1) > 0 \qquad (17)$$

i.e., *E* rises when *B* drops if $C+D<1$, and *E* sinks when *B* drops if $C+D<1$. Moreover,

$$C+D=1 \Rightarrow E \cong 1 \ \forall B \qquad (18)$$

Table 2 Validation through already-published computation results

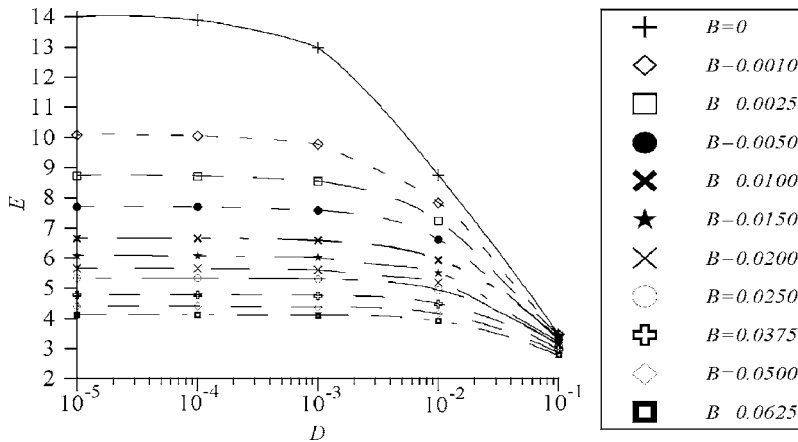| No.	Parameters			Computed Entity	Literature source				This work	Discrepancy
	B	*C*	*D*		Author	Computation	Representation	Value		
1	0	0	0	$\partial E/\partial \ln B$	[30]	Analytic local	Numerical	−1.571	−1.560	0.8
2	0.005	0	0	E	[24]	Analytic global	Graphical	7.6	7.8	2.7
3	0	0	0	$\partial E/\partial \ln D$	[25]	Analytic global	Graphical	−2.9	−2.8	3.4
4	0	0	0.1	E	[27]	Analytic global	Numerical	3.47	3.473	0.1
5	0	0	70000	E	[27]	Analytic global	Graphical	0.344	0.344	0
6	0.7	0	0	E	[32]	Finite elements	Numerical	0.48	0.47	2.1
7	0	0.5	0.00001	E	[18]	Analytic global	Numerical	1.4478	1.44820	0.04
8	0	0.5	0.1	E	[18]	Analytic global	Numerical	1.3135	1.31363	0.01
9	0	2	0.00001	E	[18]	Analytic global	Numerical	0.7174	0.71077	0.05
10	0	3	0.1	E	[18]	Analytic global	Numerical	0.5910	0.59183	0.13

Fig. 3 Effective conductivity *E* as function of the inner resistance *D*, for different layer resistances *B*, for a constant contact resistance *C*=0.001
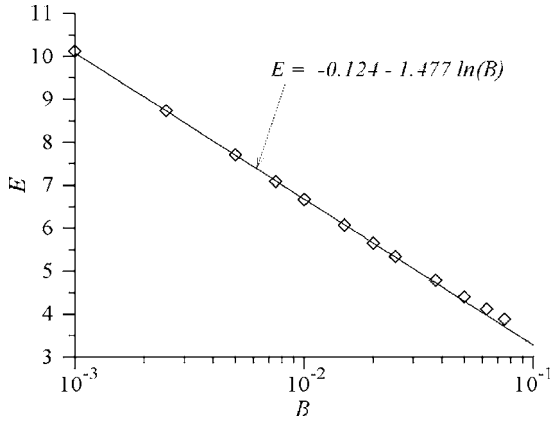
Fig. 4 Effective conductivity E as function of the matrix layer resistance B, by constant and much smaller contact and inner resistances, C and D

The pure and interaction second-degree effects are advantageously defined by the second derivatives of E with respect to the different factors and, respectively, to the combinations of two different factors. We found that for $M+R<1$, all second-order effects are positive

$$\text{Inf}\left\{\left(\frac{\partial^2 E}{\partial B^2}\right)_{C,D}, \left(\frac{\partial^2 E}{\partial C^2}\right)_{D,B}, \left(\frac{\partial^2 E}{\partial D^2}\right)_{B,C}, \left(\frac{\partial^2 E}{\partial B \, \partial C}\right)_D, \left(\frac{\partial^2 E}{\partial C \, \partial D}\right)_B, \right.$$
$$\left. \left(\frac{\partial^2 E}{\partial D \, \partial B}\right)_C\right\} \gtrsim 0 \qquad (19)$$

but by $M+R>1$ only the second-degree effects not containing B are positive, whereas the remainder became negative.

6.3 Effect Magnitudes. The observed features are as follows:

- The greatest partial resistance turns out to be too the most influential, i.e., for X,Y,Z as factors

$$Z = \sup\{X,Y,Z\} < 1 \Rightarrow \left|\left(\frac{\partial E}{\partial Z}\right)_{X,Y}\right|$$
$$= \sup\left\{\left|\left(\frac{\partial E}{\partial Z}\right)_{X,Y}\right|, \quad \left|\left(\frac{\partial E}{\partial X}\right)_{Y,Z}\right| \left|\left(\frac{\partial E}{\partial Y}\right)_{Z,X}\right|\right\} \quad (20)$$

If D is, for example, the greatest of the three factors, then the D effect is more important than those of C or B, i.e., $D > \sup\{B,C\} \Rightarrow |(\partial E / \partial D)_{B,C}|$
$> \sup\{|(\partial E / \partial C)_{D,B}|, |(\partial E / \partial B)_{C,D}|\}$

- If the greatest factor—say Z—is much greater than the other ones (but much less than 1), then the response E is well approximated with a linear function of the logarithmed Z

$$X + Y \ll Z \ll 1 \Rightarrow E \cong K_1 - K_2 \log Z \qquad (21)$$

where K_1 and K_2 are positive and fast independent of the three factors.

The condition $\alpha \gg \beta$ can tentatively be translated by $\alpha > 10\beta$. Thus, for example,

$$10 \sup\{C,D\} < B < 0.1 \Rightarrow E \cong K_{1B} - K_{2B} \ln(B)$$

as illustrated in Fig. 4.

- If the smallest factor—say X—is much smaller (<0.01) than the others (and too $\ll 1$), then the response E is well approximated with a linear function of X:

$$X \ll \inf\{Y,Z,1\} \Rightarrow E \cong K_3 - K_4 X$$

where K_3 and K_4 are positive functions of the greater factors (Y and Z).

(a)

(b)
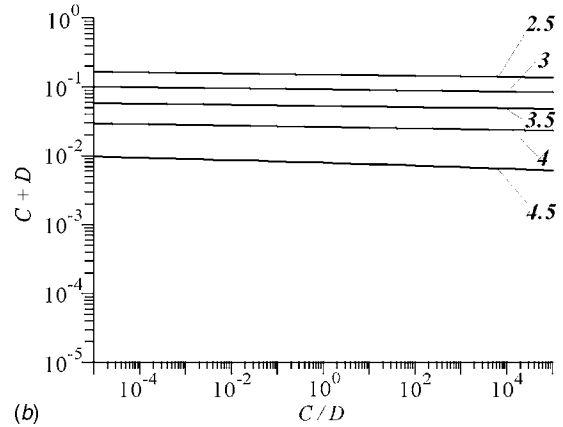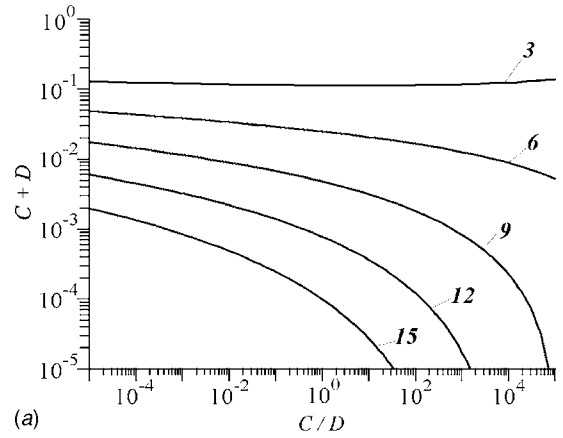
Fig. 5 (a) Dependence of the effective conductivity E on contact C and inner D resistances, at constant low $B(B=0)$ and (b) Dependence of the effective conductivity E on contact C and inner D resistances, at constant high $B(B=0.0625)$

The condition $\alpha \gg \beta$ can also be translated here by $\alpha > 10\beta$.

6.4 Substitutability of D by C. As already quoted in Sec. 2, Benveniste [13], Hasselman and Johnson [14], and recently, Wang and Yi [16] pointed out, that the factor C is substitutable by D in the dependence $E(B,C,D)$, i.e.,

$$C_1 + D_1 = C_2 + D_2 \Rightarrow E(B,C_1,D_1) = E(B,C_2,D_2)$$

this feature not being captured in the analytical treatments for a simple cubic lattice of McPhedran and McKenzie [25], Sangani and Acrivos [27], or Cheng and Torquato [18]. In order to verify, in a tetragonal lattice, the substitutability of C and D by a given value of E, the approximate dependence of E at constant B as function of the sum $C+D$ and of the ratio C/D is shown in Fig. 5, namely at low B (Fig. 5(a), where $B=0$) and at high B (Fig. 5(b), for $B=0.0625$). One can observe the following:

- Substitutability represents an asymptotic feature, valid only when B or $C+D$ are high enough, i.e., when the computed E is rather low; for $E<4$, the dependence E versus (C/D) is slow for a constant sum $C+D$ and a constant B.
- At high effective conductivity, the effect of a resistance decrease on the E increase is more pronounced for C than for D, especially for high (C/D) ratios.

6.5 Quantitative Comparison of the Effects of Factors. At equal values of factors, their effect on E is not quite equal, as our more accurate study (0.01% error of E, realized by a Lagrange-multipliers technique) shows. The extra 141 points with values
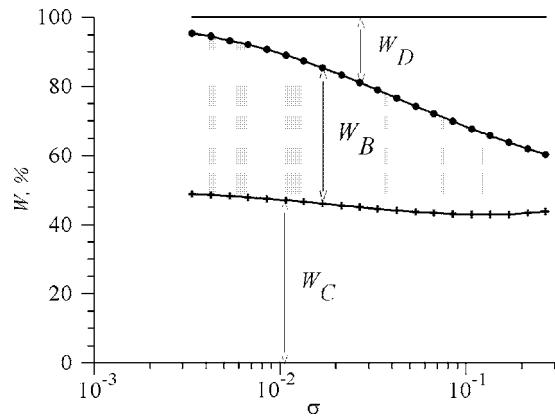
Fig. 6 Weights of pure factors *B*, *C*, and *D* within the total variation of the effective longitudinal conductivity *E*, at nearby equal values of the three factors

inserted between 0.001 and 0.1 values of each factor and with B, C, and D either identical or differing by 1.25 or 1.28, were grouped into 21 factorial experiment plans 2^3.

The weights of each effect in the global variability of E are the sum of the squared contrasts of the respective effect and are to be attributed to the point in the center of the experiment plan. It turns out, that the mixed effects represent only 0.1–0.2% of the total variability of E. The pure effects of single factors are not equal and change with the sum of factors, as illustrated by Fig. 6, which gives the relative effective longitudinal conductivity E as function of the sum σ of the dimensionless resistances, sum defined by

$$\sigma = B + C + D \qquad (22)$$

One can conclude from Fig. 6 that, at least for a factor sum σ between 0.003 and 0.3, the weight of B decreases with increasing σ, the weight of D increases as σ grows, and the weight of C presents a (flat) minimum for $\sigma \cong 0.15$. In the whole investigated range, W_C is the greatest of the three weights. The second greatest is W_B for $\sigma < 0.071$ and W_D for $\sigma > 0.071$.

The quasi-equality of W_C and W_D at great thermal resistances (44% and, respectively, 40%, at $\sigma = 0.3$) makes it likely that the Benveniste [13] finding of the C/D substitutability in the cubic array is also of value in the tetrahedric one, but only asymptotically for increasing B.

Moreover, the dependence E versus $\ln \sigma$ turns out to be linear; for B, C, D nearby equal, and σ between 0.003 and 0.03, one can compute by finite elements,

$$E = -0.63 - 1.64 \ln \sigma \qquad (23)$$

6.6 Validation of Numerical Results. The only known experimental validation is that of Lu and Kou [32], for four points within a narrow range of parameters: $B \in \{0, 0.3, 0.6, \text{ and } 0.9\}$, $C = 0$, $D = 30,000$, resulting in a measured E of 0.6–0.65, represented only graphically with $<5\%$ error of representation and other 5% error coming from heat losses. The discrepancies between these E values and those of our work do not exceed 7%. The validation of our results through the previously published computed ones is summarized in Table 2.

The validation of our results through the previously published ones is summarized in Table 2. One can infer that the discrepancy is within 0.1% for E and within 1% for the slopes of E versus the logarithm of factors. When the literature contained only graphics of the results, the agreements were within 3%.

7 Conclusive Discussion

The previous models of the conduction properties for composite materials are not quite satisfactory; the available solutions, even if they are physically right, are either geometrically limited (isolated couple of spheres), physically limited (isotropic conductivity, as in the cubic lattices), cumbersome, or limited to low filler amounts and to relatively low effective conductivities. Nevertheless, it turns out that most significant features of the effective thermal conductivity in composites with isometric inclusions—the anisotropy and the quasi-percolating dependence of the filler amount, among others—can be advantageously simulated by a finite element computing of the conduction in a tetragonal array of spheres, whose inner conductivity differs from that of the surrounding matrix and which manifest an imperfect contact between inclusions and matrix.

As shown in Sec. 2, the good choice of variables is the dimensionless effective longitudinal conductivity E as depending variable and the three following terms of the total dimensionless thermal resistivity along the line joining the centers of two neighboring spheres, as factors: external resistivity B of the matrix layer between spheres, contact resistivity C at the interface inclusion/matrix, and internal resistivity D between the spherical inclusions.

A judicious choice of the computing parameters, as the 16 times reduction of the elementary cell through use of symmetries, the introduction of extra points in the gap between spheres, and the use of extremalization techniques based on Lagrange multipliers, allows a good precision of results—estimated at 0.01% random error for E, by using the 3D-conduction module of the finite element program Comsol v.3.2.

The computed E values show at first that, by $C + D > 1$, the composite is less conductive ($E < 1$) than the bare matrix, and second, that practically interesting results (i.e., presenting $E > 3$) can be obtained only if the sum σ of the three named characteristic resistivities becomes <0.1.

Providing that $E > 1$, the effect of each factor in E (B, C, D) turns out to be negative as expected, whereas the second-order pure or mixed effects are positive and of lesser importance. If one of the three factors is much greater than the others, then its effect becomes predominant. Then, in the total variability of E, the dependence of the main factor, let us call it Z, is logarithmic (i.e., of the form $E = -m - n \ln Z$, where m and n are linear positive functions of the two other factors).

A transformation of the set of independent variables $\{B, C, D\}$ into $\{\beta, \gamma, \sigma\}$, where $\beta = B / \sigma$, $\gamma = C / \sigma$, and $\sigma = B + C + D$ can be advantageous for an easier estimation of E as in order to compare our own FE results to the literature predictions.

A suitable form seems to be a generalization of the relationship (23) to

$$E = -M - N \ln \sigma \qquad (24)$$

with M and N—two positive and slowly varying, i.e., fast constant—functions of β and γ. The given equation is asymptotically exact in the limit of evanescent total resistivity, i.e., for $E \rightarrow \infty$.

The limiting slope $\Pi(\beta, \gamma)$ defined by $\Pi = \lim N_{\sigma \rightarrow 0}$ is, according to the present study,

$$\Pi\left(\frac{1}{3}, \frac{1}{3}\right) = 1.64; \quad \Pi(0,0) = 1.92; \quad \Pi(0,1)$$

$$= 1.48; \quad \text{and} \quad \Pi(1,0) = 1.40$$

As a comparison, the other sources lead to $\Pi(1,0) = 1.57$ ($=\pi / 2$) for Batchelor and O'Brien [30] and to $\Pi(1,0) = \Pi(0,1) = 2$ for Davis and Brenner [17], whereas Zinchenko [4] found that $\Pi(0,0) / \Pi(1,0) = 2$.

Nomenclature

a, b, c = half length of cell sides (m)

a, b = half width and height of a tetragonal cell (m)

B = dimensionless outer (gap between spheres) resistance $b/a - 1$

C = dimensionless contact (sphere surface) resistance, $r_c \cdot \lambda_m / a$

D = dimensionless inner (within the sphere) resistance, λ_f / λ_m

E = dimensionless effective conductivity, $\lambda_{\text{eff}} / \lambda_m$

j = longitudinal (z-axis) heat flux density (W/m^2)

J = dimensionless heat flux density $a \cdot j / [\lambda_m \cdot (\tau_1 - \tau_2)]$ on the upper face

q = longitudinal (z-axis) heat flux (W)

Q = dimensionless heat flux

r = sphere radius (m)

r_c = contact resistance (m^2 K/W)

S = dimensionless filler (inner) temperature, $[2 \cdot \sigma / (\tau_1 - \tau_2)] - 1$

T = dimensionless matrix (outer) temperature, $[2 \cdot \tau / (\tau_1 - \tau_2)] - 1$

W_B, W_C, W_D = weight of factors B, C, D in the total variability of E

x, y, z = space directions

X, Y, Z = dimensionless x, y and z (divided by a)

X, Y, Z = smallest, median and greatest factors $\{B, C, D\}$

Greek Letters

α, β, γ = the three cell angles

β, γ = weight of B and C in the sum σ

Γ = set of geometrical parameters

∇ = gradient operator (m^{-1})

∇^2 = nabla operator (Laplacian) (m^{-2})

φ = filler (volume) amount

φ_{max} = maximal filler (volume) amount

λ, λ_t = generic conductivity (W/(m K))

λ_{eff} = effective conductivity (W/(m K))

λ_f, λ_m = filler and matrix conductivities, (W/(m K))

Π = limiting slope E versus ($lg\sigma$) at $\sigma \to 0$

σ = filler temperature (K); global dimensionless resistance along the polar axis, $B + C + D$

τ = generic or matrix temperature (K)

τ_1 = temperature at the upper cell face

τ_2 = temperature at the lower cell face

References

[1] Every, A., Tsou, Y., Hasselman, D., and Raj, R., 1992, "The Effect of Particle Size on the Thermal Conductivity of ZnS/Diamond Composites," Acta Metall. Mater., **40**, pp. 123–129.

[2] Bao, K., Lu, H., and Grimvall, G., 1993, "Transversal Thermal Conductivity in Fiber-Composite With Non-Ideal Geometries," Int. J. Heat Mass Transfer, **36**, pp. 4033–4038.

[3] Araki, N., Tang, D. W., Makino, A., Hashimoto, M., and Sano, T., 1998, "Transient Characteristics of Thermal Conduction in Dispersed Composites," Int. J. Thermophys., **19**, pp. 1239–1251.

[4] Zinchenko, A., 1998, "Effective (Thermal) Conductivity of Loaded Granular Materials by Numerical Simulations," Philos. Trans. R. Soc. London, Ser. A, **356**, pp. 2953–2998.

[5] Lu, S., 1998, "Effective Conductivities of Aligned Spheroid Dispersion Estimated by an Equivalent Inclusion Model," J. Appl. Phys., **84**, pp. 2647–2655.

[6] Privalko, V., and Novikov, V., 1995, "Modeling of Thermal Conductivity in Heterogeneous Polymers," *Thermal and Electrical Conductivity of Polymer Materials*, Y. Godovsky, and V. Privalko, eds., Adv. Polymer Sci., Vol. 119, Springer-Verlag, Berlin, pp. 31–77.

[7] Chen, T., 1993, "Interfacial Discontinuities in Thermal Conduction," Int. J. Eng. Sci., **31**, pp. 425–434.

[8] Gonçalves, L., and Kolodziej, J., 1993, "Modeling the Effective Thermal Conductivity of Composites With Imperfect Contact Matrix/Fiber," Int. Commun. Heat Mass Transfer, **20**, pp. 111–121.

[9] Ramani, K., and Vaidyanathan, A., 1995, "Finite Element Analysis of Effective Thermal Conductivity of Filled Polymeric Composites," J. Compos. Mater., **29**, pp. 1725–1740.

[10] Zou, M., Yu, B., and Zhang, D., 2002, "An Analytical Solution for Transverse Thermal Conductivity of Unidirectional Fibre Composites With Thermal Barrier," J. Phys. D, **35**, pp. 1867–1874.

[11] Garnier, B., Dupuis, T., Gilles, J., Bardon, J., and Danes, F., 2002, "Thermal Contact Resistance Between Matrix and Particle in Composite Materials, Measured by a Thermal Microscopic Method Using a Semi-Intrinsic Thermocouple," *Proc. of 12th Int. Heat Transfer Conf., Grenoble*, Vol. 4, J. Taine, eds., Elsevier, New York, pp. 9–14.

[12] Benveniste, Y., and Miloh, T., 1986, "Effective Thermal Conductivity of Composites With Imperfect Thermal Contact at Constituent Interfaces," Int. J. Eng. Sci., **24**, pp. 1537–1532.

[13] Benveniste, Y., 1987, "Effective Thermal Conductivity of Composites With a Thermal Contact Resistance Between Constituents: Non-Dilute Case," J. Appl. Phys., **61**, pp. 2840–2843.

[14] Hasselman, D., and Johnson, L., 1987, "Effective Conductivity of Composites With Interfacial Thermal Resistance," J. Compos. Mater., **21**, pp. 508–515.

[15] Chiew, Y., and Glandt, E., 1987, "Effective Conductivity of Dispersions: Effect of Resistance at the Surfaces of Particles," Chem. Eng. Sci., **42**, pp. 2677–2685.

[16] Wang, J., and Yi, X., 2004, "Effect of Interfacial Thermal Barrier Resistance and Particle Shape on the [Effective] Thermal Conductivity of AlN/Polyimide Composites," Compos. Sci. Technol., **64**, pp. 1623–1628.

[17] Davis, A., and Brenner, H., 1997, "Use of Boundary Conditions of the 3rd Kind to Model Heat Conduction Between Two Proximate Rough Surfaces Separated by an Insulator," Int. J. Heat Mass Transfer, **40**, pp. 1459–1465.

[18] Cheng, H., and Torquato, S., 1997, "Effective Conductivity of Periodic Arrays of Spheres With Interfacial Resistance," Proc. R. Soc. London, Ser. A, **453**, pp. 145–161.

[19] Danes, F., Garnier, B., Dupuis, T., Lerendu, P., and Nguyen, T., 2005, "Non-Uniformity of the Filler Concentration and of the Transverse Thermal and Electrical Conductivities of Filled Polymer Plates," Compos. Sci. Technol., **65**, pp. 945–951.

[20] Cruz, M., 1998, "Effective Conductivity Computation in 3-D Ordered Composites With a Thermally Conducting Disperse Phase," *Proc. of 11th Int. Heat Transfer Conf., Kiongju, Korea*, Taylor and Francis, New York, Vol. 7, pp. 9–14.

[21] Botterill, J., Salway, A., and Teoman, Y., 1989, "Effective Thermal Conductivity of Granular Beds by High Temperatures, 2: Models and Prediction," Int. J. Heat Mass Transfer, **32**, pp. 595–609.

[22] Springer, G., and Tsai, S., 1967, "Thermal Conductivities of [Containing Fibres Oriented] Unidirectional Materials," J. Compos. Mater., **1**, pp. 166–173.

[23] Islam, M., and Pramila, A., 1999, "Thermal Conductivity of Fiber Reinforced Composites by [2D] Finite Elements Method," J. Compos. Mater., **33**, pp. 1699–1715.

[24] McKenzie, D., and McPhedran, R., 1977, "Exact Modeling of Cubic Lattice Permittivity and Conductivity," Nature (London), **265**, pp. 128–129.

[25] McPhedran, R., and McKenzie, D., 1978, "Thermal Conductivity of Lattices of Spheres. 1: The Simple Cubic Lattice," Proc. R. Soc. London, Ser. A, **359**, pp. 45–63.

[26] McKenzie, D., McPhedran, R., and Derrick, G., 1978, "Thermal Conductivity of Lattices of Spheres. 2: The Body Centered and Face Centered Cubic Lattices," Proc. R. Soc. London, Ser. A, **362**, pp. 211–232.

[27] Sangani, A., and Acrivos, A., 1982, "Effective Conductivity of a Periodical Array of Spheres," Proc. R. Soc. London, Ser. A, **386**, pp. 263–275.

[28] Malyshev, V., and Malyshev, P., 1987, "Estimation of the Dielectric Permittivity of a Periodic Array of Solid Bodies," Doklady Akad. Nauk Ukrain. SSR, Ser. AN, **12**, pp. 48–53.

[29] McPhedran, R., and Milton, G., 1981, "Bounds and Exact Theories for the Transport Properties of Inhomogeneous Media," Appl. Phys. A: Solids Surf., **26**, pp. 207–220.

[30] Batchelor, G., and O'Brien, R., 1977, "Thermal or Electrical Conduction Through a Granular Material," Proc. R. Soc. London, Ser. A, **355**, pp. 313–323.

[31] Comsol 2005, *COMSOL Multiphysics*, User's Guide v3.2, http://www.comsol.com/

[32] Lu, K., and Kou, S., 1993, "The Effective Thermal Conductivity of Porous Material With Spherical Inclusions in Tetragonal or Simple Cubic Array," Int. Commun. Heat Mass Transfer, **20**, pp. 489–500.

A Theoretical Study on Convective Condensation of Water Vapor From Humid Air in Turbulent Flow in a Vertical Duct

V. Dharma Rao[1]
Department of Chemical Engineering,
College of Engineering, Andhra University,
Visakhapatnam-53003, India
e-mail: v.dharmarao@yahoo.com

V. Murali Krishna
Department of Mechanical Engineering,
G.V.P. College of Engineering,
Visakhapatnam-530041, India
e-mail: mk_vemula@rediffmail.com

K. V. Sharma
Department of Mechanical Engineering, JNTU,
Kukatpally, Hyderabad-500072, India
e-mail: kvsharmajntu@yahoo.com

P. K. Sarma
Director, R&D
GITAM, Rishikonda,
Visakhapatnam-530045, India
e-mail: sarmapk@yahoo.com

The problem of condensation of water vapor from humid air flowing in a duct in turbulent flow is formulated theoretically. Vapor condensing at the dew-point temperature of the vapor-air mixture diffuses to the wall of the duct through an air film. The flow of the condensate is laminar. The condensing vapor releases both convection and latent heats to the wall of the duct. Thus, it is treated as a combined heat and mass transfer problem. The mass, momentum, and energy balance equations for the vapor-air mixture flowing in the duct and the diffusion equation for the vapor species are considered. T_i, the temperature at gas-to-liquid interface, at which condensation takes place, is estimated with the help of the heat balance and mass balance equations at interface. The local and average values of the condensation Nusselt number, condensate Reynolds number, gas-liquid interface temperature, and pressure drop are estimated from the numerical results for different values of the system parameters, such as relative humidity and temperature of air at inlet, gas phase Reynolds number, and total pressure at inlet. The gas phase convection Nusselt and Sherwood numbers are also computed. A comparison of the present work with experimental data, for the case of in-tube condensation of vapor from humid air, shows satisfactory agreement. [DOI: 10.1115/1.2767678]

Keywords: humid air, in-tube convective condensation, turbulent flow in a duct, two-phase flow

1 Introduction

The condensation of water vapor from humid air flowing through duct is often met in air cleaning and conditioning systems, humidity control systems, atmospheric condensers, power plant cooling, refrigerating engineering, and also heat exchangers with narrow channels. If the temperature of duct surface is lower than the dew-point temperature of air, then water vapor contained in the air undergoes condensation on the duct surface and flows down in the form of a film. The total wall heat flux during condensation of water vapor includes the component due to convection spent on cooling the vapor-gas mixture in the boundary layer and the latent heat spent on vapor condensation. Hence, the process of water vapor condensation from humid air is governed by the convection through the vapor boundary layer and the diffusion of vapor to the surface followed by its condensation. Thus, the heat and mass transfer processes are interrelated during the condensation of humid air, presenting a complex phenomenon, which needs a combined solution of mass, momentum, and energy balances, and the diffusion equation. If the surface of the duct is below the freezing temperature of water, the condensate on the surface freezes and forms frost. However, possibility for formation of frost is precluded in the present analysis.

The problem often encountered in conventional film condensation is the decrease in condensation rates due to the presence of small amount of noncondensable gas. However, the problem in the present investigation relates to the case of vapor condensation containing high percentage of noncondensable gas, such as air. Early works in literature [1–3] show that heat and mass transfer during condensation of humid air can be evaluated using the em-

pirical correlations for flows without phase transition. Smol'skii et al. [4] and Novikov and Shcherbakov [5] performed experiments to investigate heat and mass transfer during condensation of water vapor from humid air in narrow channels. Smol'skii et al. [6] found experimentally that, during condensation of vapor from humid air, the hydraulic pressure losses are much higher than in a one-phase stream. Brdlik et al. [7] performed experiments to investigate heat and mass transfer during condensation of water vapor from humid air on a vertical surface under natural convection conditions. Recently, Desrayaud and Lauriat [8] used Reynolds analogy for numerical study of heat and mass transfer on a vertical parallel plate channel under natural convection conditions and established correlations for latent and sensible Nusselt numbers. Pele et al. [9] studied the effect of the flow rate of saturated humid air on the laminar filmwise condensation inside a vertical cooled pipe during turbulent forced convection. They found that the local condensate heat transfer coefficient decreases along the length of the pipe. According to Takarada et al. [10], the analogy between the heat and mass transfer is applicable at low concentrations of vapor. The problem of condensation of humid air is theoretically investigated in literature [11–14] by solving integral boundary layer equations for energy and diffusion and using analogy between heat and mass transfer processes.

Terekhov and Patrikeev [13] obtained experimental and numerical results for condensation of humid air in the channel at elevated pressures in forced convection. More recently, Volchkov et al. [14] obtained numerical solution of the system of differential energy, diffusion, and boundary layer flow equations for the laminar and turbulent flows of humid air with surface steam condensation. They observed that the heat released due to condensation of water vapor is practically independent of the particular flow regime and coincides with the relations obtained from energy and mass balance equations at the wall aided by the heat and mass transfer analogy. Terekhov and Patrikeev [13] and Volchkov et al. [14]

---

humid air

T_0 $\rho_{g,0}$ u_0 P_0

condensate film

g

T_w T_i T_i T_w

δ_l

$T_d > T_i > T_w$

T_d = dew point temperature
T_i = gas-to-liquid interface temperature
T_w = duct wall temperature
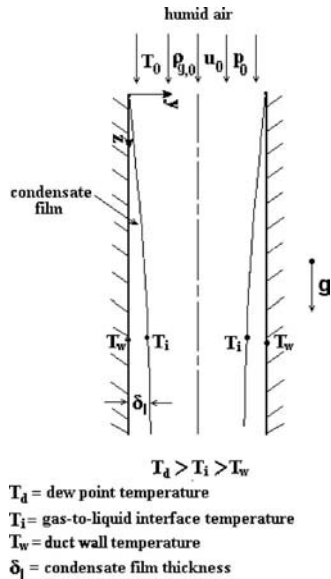δ_l = condensate film thickness

Fig. 1 Physical model and configuration

ignored the thermal resistance offered by the condensate film formed on the duct wall in view of very low condensation rates. Sarma et al. [15] tackled the problem of condensation of vapors on a vertical fin in the presence of noncondensable gas making use of the analogy between heat and mass transfer. Dharma Rao et al. [16] theoretically investigated the effect of the presence of a noncondensable gas, such as air on condensation rate for external condensation for the cases of stagnant as well as flowing vapor. Another slightly related problem of evaporation and condensation of vapor from humid air in laminar flow in a vertical channel was tackled by Hammou et al. [17]. Lambrechts et al. [18] conducted an experimental investigation into the heat transfer characteristics during in-tube condensation of horizontal smooth, microfin, and herringbone tubes. Briggs and Sabaratnam [19] reported experimental data for condensation of steam with and without the presence of air on three rows of integral-fin tubes situated in a bank of plain tubes covering a wide range of vapor velocities and air concentrations. Hence, in view of its importance, the problem of condensation of vapor from air in turbulent flow through a vertical duct is tackled theoretically. The condensate film on the wall of the duct is assumed to be a thin film in laminar flow. The condensation rates are obtained by a conjugate analysis of the problem of forced convection of the humid air in the duct with Nusselt's analysis of condensation for the condensate film. The analogies between momentum, heat, and mass transfer are used in the numerical solution of the integral boundary layer equations of momentum, energy, and diffusion for the humid air.

2 Physical Model and Formulation

The physical model is shown in Fig. 1. Humid air enters at the top of a vertical duct of width W at Reynolds number $Re_{g,0}$, temperature T_0, and relative humidity $R_{H,0}$, where T_0 is above the dew-point temperature T_d. The flow of air is turbulent. The breadth of the duct is assumed to be large in comparison to its width and the flow is assumed to be two dimensional as in a parallel plate channel. The incoming humid air contains two species, namely, the water vapor and air. The total pressure of the vapor and air mixture at inlet is P_0. Water vapor condenses if the vapor-air mixture is cooled below its dew-point temperature T_d. The dew-point temperature at any distance z in the duct corresponds to the partial pressure of the water vapor at the temperature T and total pressure P. The wall of the duct is maintained at a uniform temperature T_w, which is below the dew-point tempera-

ture. Thus, $T_w < T_d$ for $0 \leq z \leq L$. At the inlet, the partial pressure of water vapor $p_{v,0}$ can be obtained as $p_{v,0} = (R_{H,0})(p_{v,0}^*)$, where $p_{v,o}^*$ is the saturation vapor pressure of water at temperature T_0. The vapor pressure data for water are correlated in the form of an expression as shown below.

$$p_v^* = \exp\left(\frac{-5965.6}{T} + 18.79 - 0.0075T\right) \tag{1}$$

where T and p_v^* are temperature in Kelvin and saturation vapor pressure in bars, respectively. The density of water vapor ρ_v and density of air ρ_a, respectively, are given by

$$\rho_v = \frac{p_v}{R_v T} \quad \rho_a = \frac{(P - p_v)}{R_a T} \tag{2}$$

The density of the vapor-air mixture ρ_g is given by

$$\rho_g = \rho_v + \rho_a \tag{3}$$

where $R_v = 462 \times 10^{-5}$ bar m^3/kg water K and $R_a = 287 \times 10^{-5}$ bar m^3/kg air K. At the inlet (at $z=0$), P_0, T_0, and the partial pressure of water vapor $p_{v,0}$ are prescribed. The partial pressure of air species at inlet is equal to $(P_0$-$p_{v,0})$. The densities of the vapor and air are calculated using Eq. (2). The density of the vapor-air mixture at inlet $\rho_{g,0}$ is calculated using Eq. (3). Since air does not condense at the system conditions, its density ρ_a remains constant. Condensation takes place by diffusion of water vapor species toward the cold duct wall through the air film. The flow of the condensate downward along the wall of the duct is caused by gravity and also due to the flow of gas over the film. δ_l is the thickness of the condensate film and u_i the velocity at film free surface. The condensate film is assumed to be thin due to low rate of condensation. The problem of condensation of vapor from the flowing air-vapor mixture is governed by the following equations for the gas phase and the condensate film.

2.1 Equations for Gas Phase. The mass, momentum, and energy balance equations for the gas phase and the diffusion equation for the vapor species are written as follows. The density of the gas phase ρ_g is assumed to be a function of z alone.

Mass balance,

$$\frac{\partial u}{\partial z} + \frac{\partial v}{\partial y} + \frac{u}{\rho_g}\frac{d\rho_g}{dz} = 0 \tag{4}$$

Momentum balance,

$$u\frac{\partial u}{\partial z} + v\frac{\partial u}{\partial y} = u_{\max}\frac{du_{\max}}{dz} + \frac{\partial}{\partial y}\left[(\nu_g + \varepsilon_m)\frac{\partial u}{\partial y}\right] + g \tag{5}$$

It may be noted that the first term on right hand side (RHS) in Eq. (5) is written using the identity that

$$-\frac{1}{\rho_g}\frac{\partial p}{\partial z} = u_{\max}\frac{du_{\max}}{dz} \tag{6}$$

Since the gas flow in the duct is turbulent, the body force term in Eq. (5) is ignored.

Energy balance,

$$u\frac{\partial T}{\partial z} + v\frac{\partial T}{\partial y} = \frac{\partial}{\partial y}\left[(\alpha_g + \varepsilon_H)\frac{\partial T}{\partial y}\right] \tag{7}$$

Diffusion. The equation of diffusion for the vapor species is as follows:

$$u\frac{\partial \rho_v}{\partial z} + v\frac{\partial \rho_v}{\partial y} - \rho_v u\frac{1}{\rho_g}\frac{d\rho_g}{dz} = \frac{\partial}{\partial y}\left[(D_{va} + \rho_g\varepsilon_D)\frac{\partial \rho_v}{\partial y}\right] \tag{8}$$

2.2 Equations for Condensate Film. The flow of the condensate as a falling film is governed by the following momentum and energy balance equations.

$$\frac{\partial^2 u}{\partial y^2} + \frac{g(\rho_l - \rho_v)}{\mu_l} = 0 \qquad (9)$$

$$\frac{\partial^2 T}{\partial y^2} = 0 \qquad (10)$$

The advection terms are neglected in the energy balance equation following Nusselt.

2.3 Boundary Conditions. The boundary conditions for the gas phase ($\delta_l \leq y \leq W$) and condensate film ($0 \leq y \leq \delta_l$) are as follows. δ_l is the thickness of the condensate film.

At inlet, i.e., at $z=0$,

$$u = u_0 \quad v = 0 \quad T = T_0 \quad \rho_g = \rho_{g,0} \quad \rho_v = \rho_{v,,0} \quad \text{for } 0 \leq y \leq W \qquad (11)$$

For $z > 0$,

$$u = u_{max} \quad v = 0 \quad T = T_{max} \quad \rho_v = \rho_{v,max} \quad \text{at } y = W/2 \qquad (12)$$

$$u = u_i \quad T = T_i \quad \rho_v = \rho_{v,i} \quad \text{at } y = \delta_l \text{ and } y = (W - \delta_l) \qquad (13)$$

$$u = 0 \quad v = 0 \quad T = T_w = \text{const} \quad \text{at } y = 0 \text{ and } y = W \qquad (14)$$

The shear balance between the flowing gas stream and the condensate film at the gas-to-liquid interface is given by

$$\tau_{l,i} = \tau_{g,i} \quad \text{where } \tau_{l,i} = \left. \mu_l \frac{\partial u}{\partial y} \right|_{y=\delta_l, l} \quad \text{and} \quad \tau_{g,i} = \left. \mu_g \frac{\partial u}{\partial y} \right|_{y=\delta_l, g} \qquad (15)$$

2.4 Heat Balance at $y = \delta_l$. The heat transferred from the gas phase to the condensate film at $y = \delta_l$ comprises two components, namely, the sensible heat by convection and the latent heat released by the condensing vapor. The resulting equation is as follows:

$$q_{l,i} = q_{g,i} + \lambda_i \frac{d\dot{m}_l}{dz} \qquad (16)$$

where $q_{l,i}$ and $q_{g,i}$ are the condensation and convection heat fluxes, respectively. λ_i is the latent heat of condensation of vapor at T_i the temperature at the gas-to-liquid interface. The term $(d\dot{m}_l/dz)$ appearing in Eq. (16) is the rate of change of condensate mass flux over a length dz. The process of condensation is controlled by diffusion mass transfer. $(d\dot{m}_l/dz)$ is given by the following equation:

$$\frac{d\dot{m}_l}{dz} = \frac{j_{g,i}}{1 - (C_{v,i}/\bar{C}_i)} \qquad (17)$$

where $C_{v,i}/\bar{C}_i = \rho_{v,i} R_v T_i / 18P$. The subscript i refers to the gas-to-liquid interface and $j_{g,i}$ is the mass transfer flux at the gas-to-liquid interface ($y = \delta_l$).

2.5 Integral Equations

2.5.1 Gas Phase. The flow of air is developing up to certain distance from inlet. During the developing region, the thickness of the velocity boundary layer is δ_m. Thus, $u = u_{max}$ at $y = \delta_m$. Similarly, the boundary layer thicknesses for temperature and vapor density are δ_t and δ_c, respectively.

The above equations for the gas phase are tackled by using integral method of analysis. These equations are integrated partially with respect to y from $y = \delta_l$ to $y = W/2$. In the developing region, the upper limit of integration is the respective boundary layer thickness. Thus, the equations in integral form are obtained as follows.

Momentum balance in integral form,

$$\frac{d}{dz}\left[\int_{\delta_l}^{\delta_m} (u_{max} - u)u \, dy\right] + \frac{du_{max}}{dz}\left[\int_{\delta_l}^{\delta_m} (u_{max} - u) \, dy\right] + \left[\int_{\delta_l}^{\delta_m} (u_{max} - u)u \, dy\right] \frac{1}{\rho_g}\frac{d\rho_g}{dz} = \frac{\tau_{g,i}}{\rho_g} \qquad (18)$$

Energy balance in integral form,

$$\frac{d}{dz}\left[\int_{\delta_l}^{\delta_t} (T_{max} - T)u \, dy\right] + \left[\int_{\delta_l}^{\delta_t} (T_{max} - T)u \, dy\right] \frac{1}{\rho_g}\frac{d\rho_g}{dz} = \frac{q_{g,i}}{\rho_g C_{p,g}} \qquad (19)$$

Diffusion equation in integral form,

$$\frac{d}{dz}\left[\int_{\delta_l}^{\delta_c} u(\rho_{v,max} - \rho_v) \, dy\right] + \left[\int_{\delta_l}^{\delta_c} u \, dy\right] \frac{\rho_{v,max}}{\rho_g}\frac{d\rho_g}{dz} = j_{g,i} \qquad (20)$$

where $\tau_{g,i}$ and $q_{g,i}$ are the shear stress and heat flux at the interface, respectively.

Let

$$\delta = \int_{\delta_l}^{\delta_m} \left(1 - \frac{u}{u_{max}}\right) dy \qquad (21)$$

$$\delta_2 = \int_{\delta_l}^{\delta_m} \left(1 - \frac{u}{u_{max}}\right)\frac{u}{u_{max}} dy \qquad (22)$$

$$\delta_3 = \int_{\delta_l}^{\delta_t} \left(1 - \frac{T - T_i}{T_{max} - T_i}\right)\frac{u}{u_{max}} dy \qquad (23)$$

$$\delta_4 = \int_{\delta_l}^{\delta_c} \left(1 - \frac{\rho_v - \rho_{v,i}}{\rho_{v,max} - \rho_{v,i}}\right)\frac{u}{u_{max}} dy \qquad (24)$$

$$\delta_5 = \int_{\delta_l}^{\delta_c} \left(\frac{u}{u_{max}}\right) dy \qquad (25)$$

Equations (18)–(20) are simplified using the above definitions as shown below.

Momentum balance,

$$\frac{d}{dz}(u_{max}^2 \delta_2) + u_{max}^2 \delta_2 \frac{1}{\rho_g}\frac{d\rho_g}{dz} + u_{max}\delta\frac{du_{max}}{dz} = \frac{\tau_{g,i}}{\rho_g} \qquad (26)$$

Energy balance,

$$\frac{d}{dz}[u_{max}(T_{max} - T_i)\delta_3] + u_{max}(T_{max} - T_i)\delta_3 \frac{1}{\rho_g}\frac{d\rho_g}{dz} = \frac{q_{g,i}}{\rho_g C_{p,g}} \qquad (27)$$

Diffusion equation,

$$\frac{d}{dz}[u_{max}(\rho_{v,max} - \rho_{v,i})\delta_4] + u_{max}(\rho_{v,max} - \rho_{v,i})\delta_5 \frac{1}{\rho_g}\frac{d\rho_g}{dz} = j_{g,i} \qquad (28)$$

Let

$$H = \frac{\delta}{\delta_2} \qquad (29)$$

The above equations are written in the form as shown below.

$$\frac{d\delta_2}{dz} + \delta_2(2 + H)\frac{1}{u_{max}}\frac{du_{max}}{dz} + \delta_2 \frac{1}{\rho_g}\frac{d\rho_g}{dz} = \frac{\tau_{g,i}}{\rho_g u_{max}^2} \qquad (30)$$

$$\frac{d\delta_3}{dz} + \delta_3 \frac{1}{u_{\max}} \frac{du_{\max}}{dz} + \frac{\delta_3}{(T_{\max} - T_i)} \frac{dT_{\max}}{dz} + \delta_3 \frac{1}{\rho_g} \frac{d\rho_g}{dz}$$

$$= \frac{q_{g,i}}{u_{\max} \rho_g C_{p,g}(T_{\max} - T_i)} \qquad (31)$$

$$\frac{d\delta_4}{dz} + \delta_4 \frac{1}{u_{\max}} \frac{du_{\max}}{dz} + \delta_4 \frac{1}{(\rho_{v,\max} - \rho_{v,i})} \frac{d\rho_{v,\max}}{dz} + \delta_5 \frac{1}{\rho_g} \frac{d\rho_g}{dz}$$

$$= \frac{j_{g,i}}{u_{\max}(\rho_{v,\max} - \rho_{v,i})} \qquad (32)$$

where $\tau_{g,i}$ appearing on the RHS of Eq. (30) is the shear stress at the gas-to-condensate interface, i.e., at $y = \delta_l$. Since the condensation rate is expected to be of low order of magnitude, it is assumed that $\delta_l \ll W/2$. Since the condensate is a falling film of low Reynolds number (less than 25), the velocity at the interface would be very low. Hence, $u_i \ll u_{\max}$.

Schlichting [20] and Oosthuizen and Naylor [21] illustrated the numerical solution of the problem of turbulent flow of a constant density single-phase fluid in a duct making use of Eq. (30) without density gradient and the following set of equations.

$$\frac{dH}{dz} = -e^{5(H-1.4)} \left[\frac{1}{u_{\max}} \frac{du_{\max}}{dz} + \frac{0.0135(H-1.4)}{\delta_2} \left(\frac{u_{\max}\delta_2}{\nu_g} \right)^{-1/6} \right] \qquad (33)$$

$$\frac{1}{u_{\max}} \frac{du_{\max}}{dz} = \frac{2}{(W - 2H\delta_2)} \left[\delta_2 \frac{dH}{dz} + H \frac{d\delta_2}{dz} \right] \qquad (34)$$

$$\frac{\tau_{g,w}}{\rho_g u_{\max}^2} = \frac{f}{2} = \frac{0.123 \times 10^{-0.678H}}{(u_{\max}\delta_2/\nu_g)^{0.268}} \qquad (35)$$

where $\tau_{g,w}$ appearing in Eq. (35) is the shear stress at the duct wall. In view of low values of δ_l and u_i, it is assumed that the velocity gradients for the gas phase at $y = \delta_l$ and $y = 0$ can be assumed to be equal. Hence, Eq. (35) is modified as follows by replacing $\tau_{g,w}$ with $\tau_{g,i}$.

$$\frac{\tau_{g,i}}{\rho_g u_{\max}^2} = \frac{f}{2} = \frac{0.123 \times 10^{-0.678H}}{(u_{\max}\delta_2/\nu_g)^{0.268}} \qquad (35a)$$

Following Eq. (35a), $q_{g,i}$ and $j_{g,i}$ are defined as shown below using the analogies of momentum with heat and mass transfer, respectively.

$$\frac{q_{g,i}}{u_{\max}\rho_g C_{p,g}(T_{\max} - T_i)} = \frac{f}{2} \mathrm{Pr}_g^{-2/3} \qquad (36)$$

$$\frac{j_{g,i}}{u_{\max}(\rho_{v,\max} - \rho_{v,i})} = \frac{f}{2} \mathrm{Sc}_g^{-2/3} \qquad (37)$$

The variation of the gas density ρ_g due to condensation of vapor from the gas phase is taken into account in the continuity equation, viz., Eq. (4). As a result, the momentum and energy balance equations and the diffusion equation, viz., Eqs. (30)–(32) contain the density gradient term. Hence, it is felt that Eqs. (33)–(37), which contain ρ_g and ρ_v, include variable density effect into the constitutive equations for a weakly compressible fluid, viz., the vapor-air mixture. Equations (33)–(35) suggested by Schlichting [20] are for an incompressible fluid with constant properties flowing over an impermeable surface. However, it is observed in the problem investigated presently that the velocity of the condensate film is very low compared to that of the humid air due to low rate of condensation. Further, the vapor-air mixture contains the vapor in low concentration and hence the change in the average density and other properties of the mixture is low over the length of the condenser. In view of these facts, it is assumed that the use of Eqs. (33)–(35) is justified.

The viscosity, thermal conductivity, and specific heat of the vapor-air mixture as functions of those of the vapor and air are calculated making use of the following equations given by Fullarton and Schlunder [22].

$$\mu_g = \frac{(\sqrt{18}\mu_v Y_v + \sqrt{29}\mu_a Y_a)}{(\sqrt{18}Y_v + \sqrt{29}Y_a)} \qquad (38)$$

$$k_g = \frac{Y_v K_v}{(Y_v + Y_a A)} + \frac{Y_a K_a}{(Y_a + Y_v A)} \qquad (39)$$

where

$$A = \frac{1}{3.6}[0.8876(1 + \sqrt{K_v/K_a})]^2$$

$$C_{p,g} = Y_v C_{p,v} + Y_a C_{p,a} \qquad (40)$$

Equations (30), (33), and (34), with the aid of Eq. (35a), are to be solved numerically to obtain δ_2, H, and $u_{\max}$. The developing region for the velocity boundary layer ends when δ_m becomes equal to $W/2$. δ_m can be expressed as a function of δ_2 and H by the following procedure. The velocity profile is assumed as follows:

$$\frac{u - u_i}{u_{\max} - u_i} = \left(\frac{y - \delta_l}{\delta_m - \delta_l} \right)^{1/N} \qquad (41)$$

δ and δ_2 are obtained by evaluating the integrals in Eqs. (21) and (22) using Eq. (41).

$$\delta = \frac{1}{(N+1)} \delta_m \text{ and } \delta_2 = \frac{N}{(N+1)(N+2)} \delta_m \qquad (42)$$

$$H = \frac{\delta}{\delta_2} = \frac{(N+2)}{N} \qquad (43)$$

The inequalities that $u_i \ll u_{\max}$ and $\delta_l \ll \delta_m$ were used in obtaining Eqs. (42) and (43). From Eqs. (42) and (43), the exponent N is obtained in terms of H as follows:

$$N = \frac{2}{H - 1} \qquad (44)$$

Using the above equation, δ_m is expressed as a function of δ_2 and H as given below:

$$\delta_m = \frac{H(H+1)}{(H-1)} \delta_2 \qquad (45)$$

At each step size (Δz), the numerical values of δ_2 and H are substituted in the above expression. The developing region ends when $\delta_m = W/2$. The assumed temperature and vapor density profiles are

$$\frac{T - T_i}{T_{\max} - T_i} = \left(\frac{y - \delta_l}{\delta_t - \delta_l} \right)^{1/N} \qquad (46)$$

$$\frac{\rho_v - \rho_{v,i}}{\rho_{v,\max} - \rho_{v,i}} = \left(\frac{y - \delta_l}{\delta_c - \delta_l} \right)^{1/N} \qquad (47)$$

where δ_t and δ_c are the thermal and concentration (i.e., vapor density) boundary layer thicknesses, respectively. By a procedure similar to that used in the case of δ_m, δ_t and δ_c are expressed as a function of δ_3, δ_4, and H making use of Eqs. (23) and (24).

2.5.2 Condensate Film. The formulation and analysis for the condensate film is as follows. It is assumed that the condensate film is in laminar flow. Integration of the Eq. (9) using the Eqs. (13) and (14) gives the following expression for the velocity profile in the condensate film:

$$\frac{u}{u_i} = \frac{y}{\delta_l}\left[1 + F\left(1 - \frac{y}{\delta_l}\right)\right] \quad (48)$$

where

$$F = \frac{g(\rho_l - \rho_v)\delta_l^2}{2\mu_l u_i} \quad (49)$$

Condensate mass flux $\dot{m}_l$,

The condensation rate per unit breadth of the wall of the duct $\dot{m}_l$ can be obtained from the following equation:

$$\dot{m}_l = \rho_l \int_0^{\delta_l} u\, dy \quad (50)$$

The integral in the above equation is evaluated using Eq. (48), and the following equation is obtained for condensate mass flow rate for unit breadth of the film:

$$\dot{m}_l = \frac{\rho_l u_i \delta_l}{2}\left(1 + \frac{F}{3}\right) \quad (51)$$

Condensate film thickness δ_l. Using the velocity profile for the liquid film,

$$u_i = \frac{\delta_l}{\mu_l(1 - F)}\tau_{g,i} \quad (52)$$

From Eqs. (51) and (52), an equation for δ_l is obtained as shown below:

$$\delta_l = \left[\frac{2\nu_l \dot{m}_l}{\tau_{g,i}}\frac{(1 - F)}{(1 + F/3)}\right]^{1/2} \quad (53)$$

Interface temperature T_i. Integration of Eq. (10) subject to the boundary conditions given in Eqs. (13) and (14) yields the following temperature profile for the condensate film:

$$\frac{T - T_w}{T_i - T_w} = \frac{y}{\delta_l} \quad (54)$$

Making the use of temperature profile, the heat flux $q_{l,i}$ is given by

$$q_{l,i} = k_l \frac{T_i - T_w}{\delta_l} \quad (55)$$

Thus, from Eqs. (16) and (55), an expression for T_i is written as follows:

$$T_i = T_w + \frac{\delta_l}{k_l}\left[q_{g,i} + \lambda_i \frac{d\dot{m}_l}{dz}\right] \quad (56)$$

Equation (56) is in implicit form to estimate T_i, since the terms δ_l, $(d\dot{m}_l/dz)$, $q_{g,i}$ on the RHS are also function of T_i. Hence, Eq. (56) is to be solved for T_i with the help of Eqs. (17), (36), and (53) for $(d\dot{m}_l/dz)$, $q_{g,i}$, and δ_l, respectively.

2.6 Heat and Mass Transfer Coefficients. The gas phase convection heat transfer coefficient h_g is defined by the equation

$$q_{g,i} = h_g(T_{av} - T_w) \quad (57)$$

where T_{av} is the local mean temperature of the gas phase defined as follows:

$$T_{av} = T_{max} + \frac{1}{u_0 W}\int_{\delta_l}^{W} u(T - T_{max})dy \quad (58)$$

The condensation heat transfer coefficient (h_l) is defined as given below:

$$q_{l,i} = h_l(T_{av} - T_w) \quad (59)$$

The diffusion mass transfer coefficient (h_D) is defined by the equation

$$j_{g,i} = h_D \rho_{v,av} \quad (60)$$

where $\rho_{v,av}$ is the local mean density of the vapor in the gas phase defined as follows:

$$\rho_{v,av} = \rho_{v,max} + \frac{1}{u_0 W}\int_{\delta_l}^{W} u(\rho - \rho_{v,max})dy \quad (61)$$

2.7 Equations in Normalized Form for Gas Phase and Condensate Film. The following dimensionless variables and parameters are considered.

$$u^+ = u/u_0 \quad v^+ = v/u_0 \quad T^+ = (T - T_w)/(T_0 - T_w) \quad \rho_g^+ = \rho_g/\rho_{g,0} \quad \rho_v^+$$
$$= \rho_v/\rho_{v,0} \quad z^+ = z/W$$

$$y^+ = y/W \quad \delta_m^+ = \delta_m/W \quad \delta_c^+ = \delta_c/W \quad \delta_t^+ = \delta_t/W \quad \delta_2^+ = \delta_2/W \quad \delta_3^+$$
$$= \delta_3/W \quad \delta_4^+ = \delta_4/W$$

$$\delta_5^+ = \delta_5/W \quad k^+ = k_g/k_l \quad \delta_l^+ = \delta_l/W \quad \lambda_i^+ = \lambda_i/\lambda_0 \quad \mathrm{Re}_g$$
$$= u_0 W/\nu_g \quad \mathrm{Sc}_g = \nu_g/D_{va}$$

$$\mathrm{Re}_l = 4\dot{m}_l/\mu_l \quad \tau_g^+ = \tau_g/\rho_{g,0}u_0^2 \quad q_g^+ = q_g W/k_g(T_0 - T_w) \quad j_g^+$$
$$= j_g W/D_{va}\rho_{g,0} \quad (62)$$

Gas phase. Equations (30), (33), (34), (35a), (31), (36), (32), and (37) are written below in normalized form making use of the dimensionless variables and parameters defined above.

$$\frac{d\delta_2^+}{dz^+} + \delta_2^+(2 + H)\frac{1}{u_{max}^+}\frac{du_{max}^+}{dz^+} + \delta_2^+\frac{1}{\rho_g^+}\frac{d\rho_g^+}{dz^+} = \frac{\tau_{g,i}^+}{\rho_g^+(u_{max}^+)^2} \quad (63)$$

$$\frac{dH}{dz^+} = -e^{5(H-1.4)}\left[\frac{1}{u_{max}^+}\frac{du_{max}^+}{dz^+} + \frac{0.0135(H - 1.4)}{\delta_2^+}(u_{max}^+\delta_2^+\mathrm{Re}_g)^{-1/6}\right] \quad (64)$$

$$\frac{1}{u_{max}^+}\frac{du_{max}^+}{dz^+} = \frac{2}{(1 - 2H\delta_2^+)}\left[\delta_2^+\frac{dH}{dz^+} + H\frac{d\delta_2^+}{dz^+}\right] \quad (65)$$

where

$$\frac{\tau_{g,i}^+}{\rho_g^+(u_{max}^+)^2} = \frac{f}{2} = 0.123 \times 10^{-0.678H}(\mathrm{Re}_g u_{max}^+\delta_2^+)^{-0.268} \quad (66)$$

$$\frac{d\delta_3^+}{dz^+} + \delta_3^+\frac{1}{u_{max}^+}\frac{du_{max}^+}{dz^+} + \frac{\delta_3^+}{(T_{max}^+ - T_i^+)}\frac{dT_{max}^+}{dz^+} + \delta_3^+\frac{1}{\rho_g^+}\frac{d\rho_g^+}{dz^+}$$
$$= \frac{q_{g,i}^+}{\mathrm{Re}_g \mathrm{Pr}_g u_{max}^+(T_{max}^+ - T_i^+)} \quad (67)$$

where

$$\frac{q_{g,i}^+}{\mathrm{Re}_g \mathrm{Pr}_g u_{max}^+(T_{max}^+ - T_i^+)} = \frac{f}{2}\mathrm{Pr}_g^{-2/3} = \frac{\tau_{g,i}^+}{\rho_g^+(u_{max}^+)^2}\mathrm{Pr}_g^{-2/3} \quad (68)$$

$$\frac{d\delta_4^+}{dz^+} + \delta_4^+\frac{1}{u_{max}^+}\frac{du_{max}^+}{dz^+} + \delta_4^+\frac{1}{(\rho_{v,max}^+ - \rho_{v,i}^+)}\frac{d\rho_{v,max}^+}{dz^+} + \delta_5^+\frac{1}{\rho_g^+}\frac{d\rho_g^+}{dz^+}$$
$$= \frac{j_{g,i}^+}{\mathrm{Re}_g \mathrm{Sc}_g u_{max}^+(\rho_{v,max}^+ - \rho_{v,i}^+)} \quad (69)$$

where

$$\frac{j_{g,i}^+}{\mathrm{Re}_g \mathrm{Sc}_g u_{max}^+(\rho_{v,max}^+ - \rho_{v,i}^+)} = \frac{f}{2}\mathrm{Sc}_g^{-2/3} = \frac{\tau_{g,i}^+}{\rho_g^+(u_{max}^+)^2}\mathrm{Sc}_g^{-2/3} \quad (70)$$

where

$$\text{Re}_g = \text{Re}_{g,0} \frac{\rho_g^+}{\mu_g^+} \quad \text{Pr}_g = \text{Pr}_{g,0} \frac{u_g^+ C_{pg}^+}{k_g^+} \text{ and } \text{Sc}_g = \text{Sc}_{g,0} \frac{\mu_g^+}{\rho_g^+ D_{va}^+}$$

$$(71)$$

Condensate film. Equation (17) is written in normalized form as follows:

$$\frac{d\,\text{Re}_l}{dz^+} = \frac{4\mu^+}{\text{Sc}_g} \frac{j_{g,i}^+}{1 - (C_{v,i}/C_i)} \quad \text{where} \quad \frac{C_{v,i}}{C_i} = \left(\frac{p_{v,0}}{T_0}\right)\left(\frac{\beta T_i^+ + 1}{P}\right)\rho_{v,i}^+$$

$$(72)$$

where Re_l is the condensate Reynolds number. Equation (53) is written in normalized form to give the following equation for the dimensionless condensate film thickness δ_l^+.

$$\delta_l^+ = \frac{1}{\text{Re}_g}\left[\frac{\gamma\,\text{Re}_l}{2} \frac{(1-F)}{\tau_{g,i}^+ (1+F/3)}\right]^{1/2}$$

$$(73)$$

It is assumed that the factor F is by far less than 1. Hence,

$$\delta_l^+ = \frac{1}{\text{Re}_g}\left(\frac{\gamma\,\text{Re}_l}{2\,\tau_{g,i}^+}\right)^{1/2}$$

$$(74)$$

It is found while obtaining the numerical results that the maximum value of the parameter F is 0.06 at the exit of the duct for the system parameters considered in the analysis. Thus, the assumption that $F \ll 1$ is justified. The boundary conditions in normalized form are as follows:

At the inlet, i.e., at $z^+ = 0$,

$$u^+ = 1 \quad T^+ = 1 \quad \rho_g^+ = 1 \quad \rho_v^+ = 1 \quad \text{for } 0 \leqslant y^+ \leqslant 1 \quad (75)$$

For $z^+ > 0$,

$$u^+ = u_{\max}^+ \quad T^+ = T_{\max}^+ \quad \rho_v^+ = \rho_{v,\max}^+ \quad \text{at } y^+ = 0.5 \quad (76)$$

$$u^+ = u_i^+ \quad T^+ = T_i^+ \quad \rho_v^+ = \rho_{v,i}^+ \quad \text{at } y^+ = \delta_1^+ \text{ and } y^+ = (1 - \delta_1^+)$$

$$(77)$$

$$u^+ = 0 \quad T^+ = 0 \quad \text{at } y^+ = 0 \text{ and } y^+ = 1 \quad (78)$$

Dimensionless interface temperature T_i^+. Equation (56) is written in normalized form to give the equation for T_i^+, the dimensionless temperature at the gas-to-condensate interface, i.e., at $y^+ = \delta_l^+$.

$$T_i^+ = \delta_l^+\left[k^+ q_{g,i}^+ + \frac{\text{Pr}_1}{4S}\lambda_i^+ \frac{d\,\text{Re}_1}{dz^+}\right]$$

$$(79)$$

Nusselt and Sherwood numbers. The local convection and condensation Nusselt numbers ($\text{Nu}_{g,z}$ and $\text{Nu}_{l,z}$) and Sherwood number ($\text{Sh}_{g,z}$) are computed from the equations given below.

$$\text{Nu}_{g,z} = \frac{q_{g,i}^+}{T_{av}^+}$$

$$(80)$$

$$\text{Nu}_{l,z} = \frac{T_i^+}{\delta_l^+ T_{av}^+} = \frac{1}{T_{av}^+}\left[k^+ q_{g,i}^+ + \frac{\text{Pr}_l}{4S}\lambda_i^+ \frac{d\,\text{Re}_l}{dz^+}\right]$$

$$(81)$$

$$\text{Sh}_{g,z} = \frac{j_{g,i}^+}{\rho_{v,av}^+}$$

$$(82)$$

$$\delta_m^+ = \frac{H(H+1)}{(H-1)}\delta_2^+$$

$$(83)$$

$$\delta_t^+ = \delta_m^+\left(\frac{\delta_3^+}{\delta_2^+}\right)^{2/(H+1)}$$

$$(84)$$

$$\delta_c^+ = \delta_m^+\left(\frac{\delta_4^+}{\delta_2^+}\right)^{2/(H+1)}$$

$$(85)$$

The normalized thicknesses of the momentum, and thermal and concentration boundary layers (δ_m^+, δ_t^+, and δ_c^+) at any z are calculated using Eqs. (83)–(85), respectively. The value of each of these normalized variables tends to unity when the respective developing stage ends and remains constant at unity subsequently. The normalized average temperature (T_{av}^+) and vapor density ($\rho_{v,av}^+$) in the gas phase are computed using the following equations:

$$T_{av}^+ = T_{\max}^+ - u_{\max}^+(T_{\max}^+ - T_i^+)\delta_3^+$$

$$(86)$$

$$\rho_{v,av}^+ = \rho_{v,\max}^+ - u_{\max}^+(\rho_{v,\max}^+ - \rho_{v,i}^+)\delta_4^+$$

$$(87)$$

Both $T_{\max}^+$ and $\rho_{v,\max}^+$ appearing in Eqs. (86) and (87), respectively, are considered to be equal to unity. The average Nusselt number ($\text{Nu}_{g,av}$) and Sherwood number ($\text{Sh}_{g,av}$) of gas phase and the condensate Nusselt number ($\text{Nu}_{l,av}$) computed from their respective local values at each z^+. The average values are obtained as integrated average of local values using Simpson's rule.

$$\text{Nu}_{g,av} = \frac{1}{L}\int_0^L \text{Nu}_{g,z} dz$$

$$(88)$$

$$\text{Nu}_{l,av} = \frac{1}{L}\int_0^L \text{Nu}_{l,z} dz$$

$$(89)$$

$$\text{Sh}_{g,av} = \frac{1}{L}\int_0^L \text{Sh}_{g,z} dz$$

$$(90)$$

2.8 Pressure Drop. P, the pressure of air-water vapor mixture at any z, can be obtained from the following equation:

$$P = \frac{n_T R T_{av}}{V}$$

$$(91)$$

where $n_T = n_v + n_a$ is the total number of moles of air-water vapor mixture and R is the universal gas constant. The pressure gradient at any z is given by the following equation:

$$\frac{dP}{dz} = (R_v \rho_v + R_a \rho_a)\frac{dT_{av}}{dz} + R_v T_{av}\frac{d\rho_v}{dz}$$

$$(92)$$

For $z > 0$, the vapor density ρ_v decreases with z. T_{av} is the bulk temperature of the vapor-air mixture. The density of vapor ρ_v at the temperature T_{av} is calculated using Eq. (2). Equation (92) is written as follows:

$$\frac{1}{R_v \rho_{v,0}(T_0 - T_w)}\frac{dP}{dz^+} = \left(\rho_v^+ + \frac{R_a \rho_a}{R_v \rho_{v,0}}\right)\frac{dT_{av}^+}{dz^+} + \left(\frac{1}{\beta} + T_{av}^+\right)\frac{d\rho_{v,av}^+}{dz^+}$$

$$(93)$$

Total pressure drop over the length L,

$$\Delta P = P_0 - P_{z=L}$$

$$(94)$$

3 Method of Solution

The equations for the gas phase, viz., Eqs. (63)–(65) are numerically solved to obtain δ_2^+, H, and $u_{\max}^+$ in steps of Δz^+. The normalized shear stress at the interface $\tau_{g,i}^+$ is calculated using Eq. (66). The unknowns δ_3^+ and δ_4^+ are obtained by solving Eqs. (67) and (69). $q_{g,i}^+$ and $j_{g,i}^+$ appearing in these equations are evaluated with the aid of Eqs. (68) and (70). The values of variables prescribed at the inlet, i.e., at $z = 0$ are P_0, T_0, $R_{H,0}$, and

$\rho_{g,0}$. The system parameters are $\mathrm{Re}_{g,0}$, $\mathrm{Pr}_{g,0}$, $\mathrm{Pr}_{l,0}$, S_0, $\mathrm{Sc}_{g,0}$. At each value of z, the $\tau_{g,i}^+$, $q_{g,i}^+$, and $j_{g,i}^+$ are computed from Eqs. (66), (68), and (70), respectively.

At the inlet ($z^+=0$), $T=T_0$ and $\rho_v=\rho_{v,0}$. At each increment in the downstream distance, the normalized temperature and vapor density of the gas phase are calculated from Eqs. (86) and (87), respectively. Making use of the value of $\rho_{v,\mathrm{av}}$, the density of the vapor-air mixture ρ_g is calculated from Eq. (3). The density gradient, i.e., $(d\rho_g/dz)$ is computed from the values of ρ_g over an increment Δz. The pressure of the vapor-air mixture at any z is calculated as shown below.

$$p_v = R_v\rho_v T_{\mathrm{av}} \quad p_a = R_a\rho_a T_{\mathrm{av}} \quad P = p_v + p_a \qquad (95)$$

The dew-point temperature T_d is calculated corresponding to the partial pressure of water vapor p_v. The normalized interface temperature T_i^+ is calculated by a trial-and-error procedure from Eq. (79) with the aid of Eqs. (72) and (74). A trial value for T_i^+ is assumed, which is used to compute various terms present on RHS of Eq. (79). An approximate value for Re_l is also calculated by integration of Eq. (72) for a step size (Δz^+). Thus, the resulting value of RHS of Eq. (79) gives an improved value of T_i^+. The same is used again to compute RHS of Eq. (79). Thus, the process of successive approximates is repeated until the evaluated RHS coincides with the assumed T_i^+ within an accuracy of 0.01%. The increment in Re_l over step size Δz^+ is obtained from Eq. (72). Thus, proceeding with successive step sizes (Δz^+), the value of Re_l at each z^+ (measured from inlet $z=0$) is known; at any z^+, the $\mathrm{Nu}_{g,z}$, $\mathrm{Nu}_{l,z}$, and $\mathrm{Sh}_{g,z}$ are calculated from Eqs. (80)–(82), respectively. The local pressure is computed making use of Eq. (93). The average values for condensation and convection Nusselt numbers, temperature at gas-to-liquid interface, and Sherwood number are evaluated as integrated averages over the length of the duct. ΔP, the pressure drop over the length of the duct, is computed, which is equal to (P_0-P_L), where P_L is the pressure at $z=L$.

4 Results and Discussion

The present theoretical work is validated with the experimental data of Pele et al. [9], who conducted experiments inside a cooled vertical pipe to study the laminar film wise condensation of water vapor from saturated humid air in turbulent flow. The experimental setup of Pele et al. [9] consists of two coaxial vertical tubes of 1.5 m length. The inner diameter (d) is 0.0335 m and the diameters of the annular sections are 0.04 and 0.12 m. The saturated air flows through the inner tube and the cooling water flows in the annular space. Experimental Nusselt numbers ($h_l d/k_l$) of Pele et al. [9] for two different conditions are shown in Fig. 2. Numerical results are obtained for the same conditions of gas Reynolds number ($\mathrm{Re}_{g,0}$), gas inlet temperature (T_0), and wall temperature (T_w) as those of Pele et al. [9] for $d_e=0.0335$ m, where d_e is the equivalent diameter for the case of duct. The local condensation Nusselt numbers ($h_l d_e/k_l$) are computed using Eq. (81) along the length of the duct. The Nusselt numbers computed from the present theory show the orders of magnitude sufficiently close to the experimental data of Pele et al. [9].

Results are obtained to explore the effects of various system parameters, such as the relative humidity of the air entering the duct $R_{H,0}$, the gas phase Reynolds number at the duct inlet $\mathrm{Re}_{g,0}$, temperature of the air at duct inlet T_0, and the total pressure of the air in the duct at inlet P_0. The effects of these system parameters on local condensate Nusselt numbers ($\mathrm{Nu}_{l,z}$) are shown in Fig. 3. It can be observed from Curves 1 and 3 of Fig. 3 that an increase in $R_{H,0}$ results in an increase in the condensate Nusselt number, which can be attributed to the increase in the humidity (water vapor content in air) with an increase in $R_{H,0}$ when the total pressure remains constant. Curves 1 and 2 of Fig. 3 also show an increase in the value of $\mathrm{Nu}_{l,z}$ as $\mathrm{Re}_{g,0}$ increases. The vapor flow rate also increases as the flow rate of the air-water vapor in-
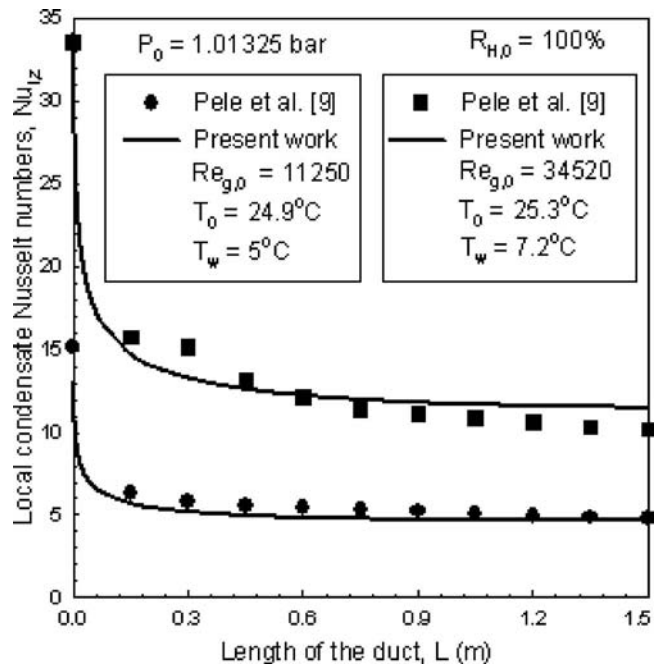

Fig. 2 Comparison of present work with experimental data

creases. Further, if T_0 increases, the saturation vapor pressure increases resulting in an increase in the humidity of water vapor in the gas phase. Hence, it can be found from Curves 3 and 5 that the $\mathrm{Nu}_{l,z}$ increases with increase in T_0. Curves 3 and 4 of Fig. 3 indicate an increase in the value of $\mathrm{Nu}_{l,z}$ as P_0 is decreased, which can be due to the decrease in the saturation and dew-point temperatures with a decrease in the system inlet pressure P_0. The gas phase convection Nusselt number $\mathrm{Nu}_{g,z}$ plays an important role in forced convection condensation process, which is considered presently. The local convection Nusselt number ($h_g W/k_l$) is shown plotted as a dashed line in Fig. 3 as a function of normalized downstream distance (z/L). At any (z/L), the difference between the condensate and convection Nusselt numbers corresponds to the latent heat flux due to condensation of vapor. The variation of gas phase Nusselt number ($\mathrm{Nu}_{g,z}$) with $R_{H,0}$, T_0, and P_0 is not significant. The $\mathrm{Nu}_{g,z}$ is a strong function of $\mathrm{Re}_{g,0}$. Curves 6 and 7 of Fig. 3 show that the gas phase Nusselt number ($h_g W/k_l$) in-
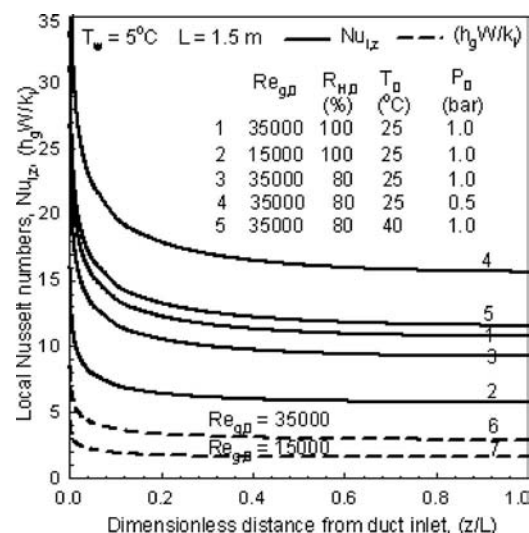

Fig. 3 Effect of $\mathrm{Re}_{g,0}$, T_0, $R_{H,0}$, and P_0 on $\mathrm{Nu}_{l,z}$ and ($h_g W/k_l$)
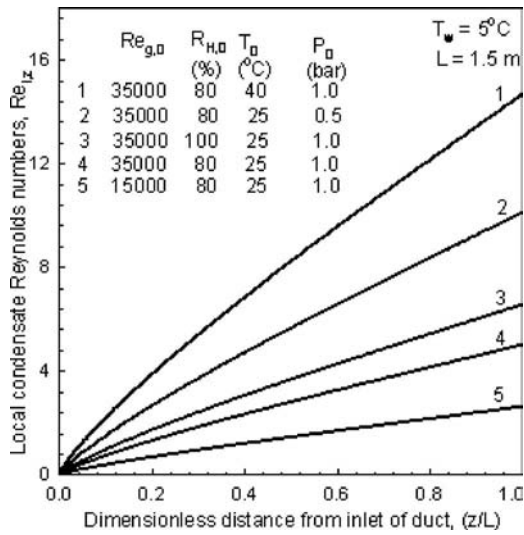
Fig. 4 Effect of various parameters on local condensate Reynolds number

Fig. 6 Effect of $Re_{g,0}$, T_0, and $R_{H,0}$ on local gas-vapor mixture pressure

creases with an increase in $Re_{g,0}$. Empirical expressions of Soliman et al., Traviss et al., and Shah to calculate heat transfer coefficients in convective in-tube condensation of pure vapor are presented by Carey [23]. These condensation heat transfer coefficients for pure vapor are found to be much higher than those obtained in the present case of condensation of water vapor from humid air.

The effects of the system parameters, which have been explained above can also be viewed from Fig. 4, in which the local condensate Reynolds number ($Re_{l,z}$) is shown plotted as a function of the downstream distance. $Re_{l,z}$ is found to increase either with an increase in $R_{H,0}$ (see Curves 3 and 4), or with an increase in $Re_{g,0}$ (see Curves 4 and 5), or with a decrease in P_0 (shown by Curves 2 and 4), or with an increase in T_0 (see Curves 1 and 4). Since the local condensate Reynolds number $Re_{l,z}$ is defined as $(4\dot{m}_l/\mu_l)$, the effect of temperature on μ_l the viscosity of the condensate is also found be considerable. The viscosity of the condensate is evaluated at a temperature of $(T_d+T_w)/2$.

An important outcome of the present work, namely, the effect of the system parameters on the gas-liquid interface temperature (T_i), is shown in Fig. 5. The T_i increases with downstream dis-
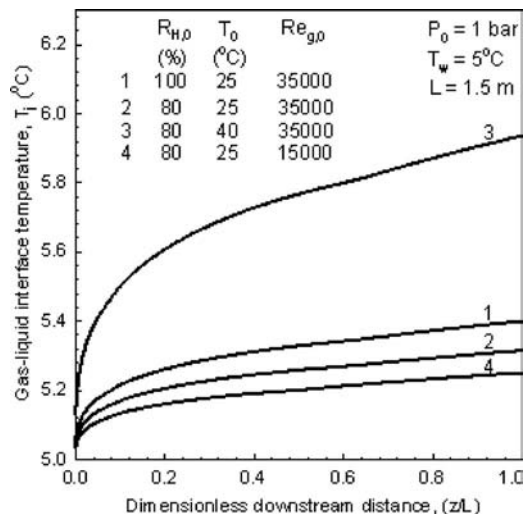
tance due to the heating of condensate film. The condensate film receives both convection and latent heats on the gas phase. Curves 1 and 2 show an increase in T_i with an increase in $R_{H,0}$, which is due to an increase in the latent heat released. Curves 2 and 3 show the variation of T_i with T_0. The T_i increases with T_0, due to an increase in condensation heat transfer to the condensate film. Curves 2 and 4 indicate that T_i increases with an increase in $Re_{g,0}$. The marginal increase in T_i with an increase in $Re_{g,0}$ indicates lower effect of the convection heat transfer in comparison with the latent heat.

The effect of system parameters $Re_{g,0}$, $R_{H,0}$, and T_0 on the local gas-vapor mixture pressure (P_z) is shown in Fig. 6. It can be observed from Fig. 6 that an increase in $R_{H,0}$ (see Curves 1 and 2) or a decrease in $Re_{g,0}$ (see Curves 1 and 3) results in an increase in pressure drop across the length of the duct. An increase in the value of $R_{H,0}$ means an increase in the partial pressure of water vapor in the water vapor-air mixture. Further, if T_0 increases, the saturation vapor pressure increases. Thus, Curves 1 and 4 show an increase in the pressure drop ΔP with an increase in T_0.

The variation of $Nu_{l,av}$, the average condensation Nusselt number, and $Re_{l,e}$, condensate Reynolds number at the exit (i.e., at $z=L$) with $R_{H,0}$ and T_0 are shown in Fig. 7. Numerical results are obtained for values of $R_{H,0}$ ranging from 50% to 100% and for two different values of T_0 ($T_0=25\,^\circ$C and $T_0=40\,^\circ$C). The $Nu_{l,av}$ lies between 7.7 and 11.9 (Curve 1) at $T_0=25\,^\circ$C and lies between 9.35 and 15.07 (Curve 2) at $T_0=40\,^\circ$C. The $Re_{l,e}$ varies from 2.85 to 6.59 for $T_0=25\,^\circ$C (Curve 3) and lies between 8.31 and 19.29 for $T_0=40\,^\circ$C (Curve 4). As discussed previously, the $Nu_{l,av}$ and $Re_{l,e}$ increase with an increase in $R_{H,0}$ and T_0.

The variation of $T_{i,av}$, the average gas-to-liquid interface temperature, and total pressure drop ΔP with $R_{H,0}$ and T_0 is shown in Fig. 8. Numerical results are obtained for values of $R_{H,0}$ ranging from 50% to 100% and for two different values of T_0 ($T_0=25\,^\circ$C and $T_0=40\,^\circ$C). The $T_{i,av}$ lies between 5.15 and 5.31$\,^\circ$C (curve 1) at $T_0=25\,^\circ$C and lies between 5.44 and 5.94$\,^\circ$C (curve 2) at $T_0=40\,^\circ$C. The $T_{i,av}$ increases with $R_{H,0}$ and T_0 due to increase in heat transfer to the condensate film with $R_{H,0}$ and T_0. The two-phase pressure drop is also important in in-tube condensation. Curves 3 and 4 of the same figure show the effect of $R_{H,0}$ and T_0 on the total pressure drop (ΔP). The ΔP increases with an in-

Fig. 5 Gas-liquid interface temperature (T_i); effect of different parameters

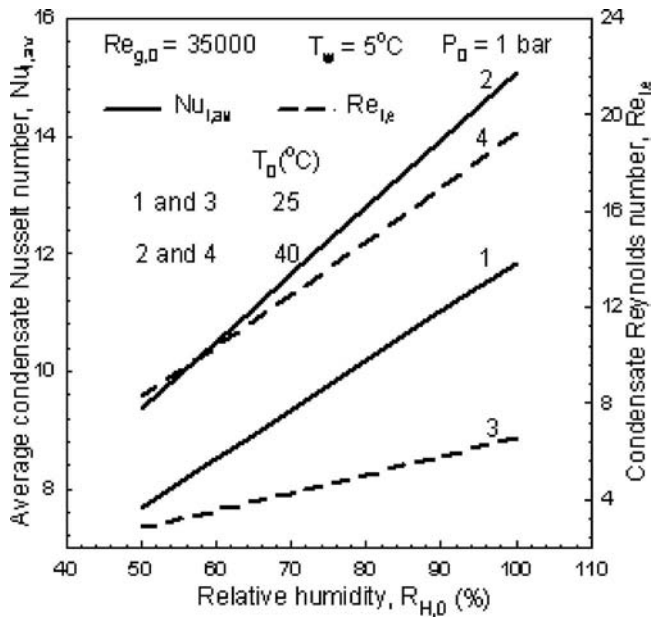**Fig. 7 Effect of $R_{H,0}$ on average condensate Nusselt and condensate Reynolds number**

crease in $R_{H,0}$ and T_0. It is observed that the frictional component of the pressure drop ΔP_{fr}, which is defined as $(4\rho_g u_0^2(f/2))$, is a considerably low fraction of the total pressure drop ΔP. ΔP_{fr} remains almost constant at different values of $R_{H,0}$ but varies slightly when T_0 is changed. The $\Delta P_{fr}=0.163$ kPa for $T_0=25\,^{\circ}$C and $\Delta P_{fr}=0.182$ kPa for $T_0=40\,^{\circ}$C.

Figure 9 shows the effect of $Re_{g,0}$ on $Nu_{l,av}$, $Re_{l,e}$, and average gas phase Sherwood number $(Sh_{g,av}xk^{+})$. The $Nu_{l,av}$ lies between 4 and 15 (see Curve 1). Curve 2 of Fig. 9 indicates that $Re_{l,e}$ varies from 1.9 to 7.6. The average gas phase Sherwood number is shown plotted as Curve 3 of Fig. 9. The Nusselt and Sherwood numbers are close enough to one other, since the Prandtl and Schmidt numbers are nearly the same for the water vapor-air mixture. The effect of $Re_{g,0}$ on $T_{i,av}$ and ΔP is shown in Fig. 10. The

Fig. 9 Variation of $Nu_{l,av}$, $(Sh_{g,av}xk^{+})$ and $(Re_{l,e})$ with $Re_{g,0}$

$T_{i,av}$ increases from $5.51\,^{\circ}$C to $5.85\,^{\circ}$C as $Re_{g,0}$ increases from 10^4 to 6×10^4 (curve 1) due to an increase in convection heating. Also as expected, the ΔP decreases with an increase in $Re_{g,0}$ (Curve 2). The frictional pressure drop ΔP_{fr} varies from 0.0197 kPa to 0.475 kPa as $Re_{g,0}$ increases from 10^4 to 6×10^4. Figure 11 shows the effect of P_0 on $Nu_{l,av}$ and $Re_{l,e}$. P_0 varies from 0.5 bar to 2.5 bars. The $Nu_{l,av}$ lies between 6 and 17 (curve 1), and $Re_{l,e}$ varies from 2 to 10 (curve 2).

5 Conclusions

A theoretical model is postulated for the case of in-tube flow condensation of water vapor from vapor-air mixture in a vertical duct. The numerical results of the present theoretical study agree satisfactorily with the experimental data available in literature. The salient parameters controlling the process are found to be T_0, $Re_{g,0}$, $R_{H,0}$, and P_0. The effect of the above system parameters on local and average condensation heat transfer coefficients and pressure drop are obtained from the numerical results. The present

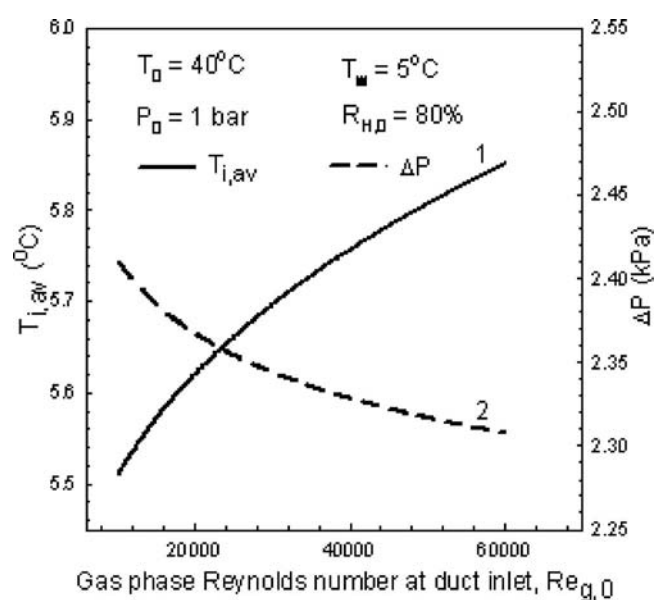**Fig. 8 Effect of $R_{H,0}$ on average gas-liquid interface temperature and total pressure drop**

Fig. 10 Effect of $Re_{g,0}$ on average interface temperature and total pressure drop
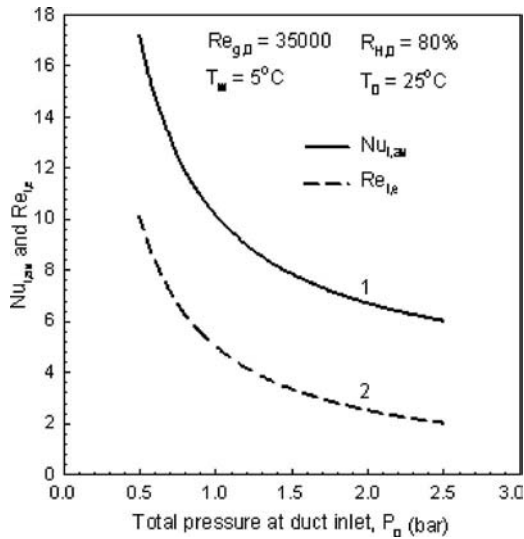
Fig. 11 Effect of P_0 on $Nu_{l,av}$ and $Re_{l,e}$

theoretical analysis may also be used for the case of flow in a horizontal duct. An example of water vapor-air mixture is considered in view of its wide practical utility. However, this theoretical model can be applied to any vapor-gas combination with suitable substitution of property equations.

Acknowledgment

Nomenclature

C_p = specific heat at constant pressure
$C_{p,g}^+$ = normalized gas specific heat at constant pressure $(C_{p,g}/C_{p,g,0})$
D_{va} = mass diffusion coefficient
D_{va}^+ = normalized mass diffusion coefficient $(D_{va}/D_{va,0})$
f = friction factor
F = factor, see Eq. (49)
g = gravitational acceleration
h_l = local condensation heat transfer coefficient
h_g = local convection heat transfer coefficient
h_D = local diffusion mass transfer coefficient
H = ratio of boundary layer thickness (δ/δ_2)
j = diffusion mass flux
j^+ = normalized diffusion mass flux $(jW/D_{va}\rho_{g,0})$
k = thermal conductivity
k^+ = gas-to-liquid thermal conductivity ratio (k_g/k_l)
k_g^+ = normalized gas thermal conductivity $(k_g/k_{g,0})$
L = length of the duct
$\dot{m}$ = condensate mass flux
n = number of moles
N = variable defined as $(2/(H-1))$
Nu_l = condensation Nusselt number (h_lW/k_l)
Nu_g = convection Nusselt number (h_gW/k_g)
P = total pressure
Pr = Prandtl number $(\mu C_p/k)$
p = partial pressure
$Re_{g,0}$ = gas phase Reynolds number at inlet $(\rho_{g,0}u_0W/\mu_{g,0})$

Re_l = condensate Reynolds number $(4\dot{m}_l/\mu_l)$
R_H = relative humidity (p_v/p_v^*)
R = gas constant
q = heat flux
q^+ = normalized heat flux $(qW/k_g(T_0-T_w))$
S = subcooled boiling $(C_{p,l}(T_0-T_w)/\lambda_0)$
Sc = Schmidt number (μ_g/ρ_gD_{va})
Sh = Sherwood number (h_DW/D_{va})
T = temperature of gas-vapor mixture
T^+ = normalized temperature $(T-T_w)/(T_0-T_w)$
u = component of air velocity in z direction
u^+ = normalized u velocity (u/u_0)
V = total volume of gas-vapor mixture
v = component of air velocity in y direction
v^+ = normalized v velocity (v/u_0)
W = width of the duct
Y_v = mole fraction of vapor (p_v/P)
Y_a = mole fraction of air $(1-Y_v)$
y^+ = normalized distance in y direction (y/W)
z = downstream distance
z^+ = normalized distance in z direction (z/W)

Greek Symbols

α = thermal diffusivity
β = temperature ratio parameter $(T_0-T_w)/T_w$
δ = boundary layer thickness
δ_l = thickness of the condensate film
δ^+ = normalized boundary layer thickness (δ/W)
ΔP = pressure drop of vapor-air mixture
ε = turbulent diffusivity
γ = viscosity ratio parameter $(\rho_{g,0}\mu_l^2/\rho_l\mu_g^2)$
λ = latent heat of condensation
λ^+ = normalized latent heat of condensation (λ/λ_0)
μ = dynamic viscosity
μ^+ = gas-to-liquid viscosity ratio (μ_g/μ_l)
μ_g^+ = normalized gas viscosity $(\mu_g/\mu_{g,0})$
ν = kinematic viscosity (μ/ρ)
ρ = density
ρ_g^+ = normalized gas density $(\rho_g/\rho_{g,0})$
ρ_v^+ = normalized vapor density $(\rho_v/\rho_{v,0})$
τ = shear stress
τ^+ = normalized shear stress $\tau_g/\rho_{g,0}u_0^2$

Subscripts

0 = inlet
a = air species
av = average
c = concentration
D = diffusion mass transfer
d = dew point
e = exit, i.e., at $z=L$
g = gas phase, i.e., air-water vapor mixture
H = heat transfer
i = gas-to-liquid interface
l = liquid (condensate)
m = momentum
max = center line
t = thermal
v = water vapor
w = wall

References

[1] Semein, V. M., 1956, "Humid Air Heat Transfer During Steam Condensation," Therm. Eng., **4**, pp. 11–15.
[2] Pchelkin, Yu. N., 1961, "Humid Air Heat and Mass Transfer," Therm. Eng., **6**, pp. 72–75.

[3] Baklastov, A. M., and Sergazin, Zh. F., 1965, "Heat and Mass Transfer During Steam Condensation From Humid Air," Izv, VUZov. Energetika, **2**, pp. 59–64.

[4] Smol'skii, B. M., Novikov, P. A., and Shcherbakov, L. A., 1971, "Heat and Mass Transfer During Condensation of Water Vapor From Moist Air in Narrow Channels," Inzh.-Fiz. Zh., **21**(1), pp. 71–74.

[5] Novikov, P. A., and Shcherbakov, L. A., 1972, "Heat and Mass Transfer During Droplet Condensation of Water Vapor From a Stream of Rarefied Humid Air in Narrow Rectangular Channels," Inzh.-Fiz. Zh., **23**(4), pp. 737–742.

[6] Smol'skii, B. M., Novikov, P. A., and Shcherbakov, L. A., 1973, "The Mechanism of Vapor Condensation From Humid Air in Narrow Channels and the Hydrodynamics of a Two-Phase Flow During Droplet Condensation," Inzh.-Fiz. Zh., **24**(2), pp. 240–244.

[7] Brdlik, P. M., Kozhinov, I. A., and Petrov, N. G., 1965, "Experimental Investigation of Heat and Mass Transfer During Condensation of Water Vapor From Humid Air on a Vertical Surface Under Natural Convection Conditions," Inzh.-Fiz. Zh., **8**(2), pp. 243–246.

[8] Desrayaud, G., and Lauriat, G., 2001, "Heat and Mass Transfer Analogy for Condensation of Humid Air in a Vertical Channel," Heat Mass Transfer, **37**, pp. 67–76.

[9] Pele, C., Baudoin, B., and Barrand, J. P., 1994, "Effect of Humid Air Flow Rate on the Film-Wise Condensation Inside a Vertical Cooled Pipe: Numerical and Experimental Study," Int. J. Heat Mass Transfer, **37**(13), pp. 1829–1837.

[10] Takarada, M., Ikeda, S., Izumi, M., Shimada, R., Sasaki, S., and Yamakawa, N., 1997, "Forced Convection Heat and Mass Transfer From Humid Air Under Condensation Conditions," *Proceedings of Exp. Heat Transfer, Fluid Mechanics and Thermodynamics*, Brussels, Vol., 2, pp. 1103–1116.

[11] Khose, A. N., and Patrikeev, V. N., 1986, "Gas Dynamics, and Heat and Mass Transfer During Condensation of Pressurized Humid Air in Narrow Channels," *Thermophysics and Gas Dynamics of Boiling and Condensation Processes*, RPI, Riga, Vol. 3, pp. 154–161.

[12] Terekhov, V. I., Terekhov, V. V., and Sharov, K. A., 1998, "Heat and Mass Transfer During Steam Condensation From Humid Air," Inzh.-Fiz. Zh., **71**(5), pp. 788–794.

[13] Terekhov, V. I., and Patrikeev, V. N., 1999, "Forced Convection Heat and Mass Transfer From Pressurized Humid Air in the Channel," Russ. J. Eng. Thermophys., **9**, pp. 1–18.

[14] Volchkov, E. P., Terekhov, V. V., and Terekhov, V. I., 2004, "A Numerical Study of Boundary-Layer Heat and Mass Transfer in a Forced Flow of Humid Air With Surface Steam Condensation," Int. J. Heat Mass Transfer, **47**, pp. 1473–1481.

[15] Sarma, P. K., Anjaneya Reddy, M., Bergles, A. E., and Sadik Kakac , 2001, "Condensation of Vapours on a Fin in the Presence of Non-Condensable Gas," Int. J. Heat Mass Transfer, **44**(17), pp. 3233–3240.

[16] Dharma Rao, V., Phanikumar, D., Sarma, P. K., and Sivannarayana, P., 2002, "Effect of the Presence of a Non-Condensable Gas on Condensation Rates During External Condensation," Proc. of Andhra Pradesh Akademi of Sciences, **6**(4), pp. 251–260.

[17] Hammou, Z. A., Benhamou, B., Galanis, N., and Orfi, J., 2004, "Laminar Mixed Convection of Humid Air in a Vertical Channel With Evaporation or Condensation at the Wall," Int. J. Therm. Sci., **43**, pp. 531–539.

[18] Lambrechts, A., Liebenberg, L., Bergles, A. E., Martin, G. L., and Meyer, J. P., 2006, "Heat Transfer Performance During Condensation Inside Horizontal Smooth, Micro-Fin and Herringbone Tubes," ASME J. Heat Transfer, **128**, pp. 691–700.

[19] Briggs, A., and Sabaratnam, S., 2005, "Condensation From Pure Steam and Steam-Air Mixtures on Integral-Fin Tubes in a Bank," ASME J. Heat Transfer, **127**, pp. 571–580.

[20] Schlichting, H., 1979, *Boundary Layer Theory*, 7th ed., McGraw-Hill, New York.

[21] Oosthuizen, P. H., and Naylor, D., 1999, *Introduction to Convective Heat Transfer Analysis*, McGraw-Hill, New York.

[22] Fullarton, D., and Schlunder, E. U., 1986, "Approximate Calculation of Heat Exchanger Area for Condensation of Gas-Vapor Mixtures," Int. Chem. Eng., **26**(3), pp. 408–418.

[23] Carey, V. P., 1992, *Liquid-Vapor Phase-Change Phenomena*, Hemisphere, New York.

A Periodic-Transient Method for High-Resolution Heat Transfer Measurement on Two-Dimensional Curved Surfaces

M. Röger

German Aerospace Center (DLR),
Institute of Technical Thermodynamics,
Solar Research,
Pfaffenwaldring 38-40,
D-70569 Stuttgart, Germany
e-mail: marc.roeger@dlr.de

Measurement of heat transfer distribution is frequently required in engineering. However, some heat transfer techniques are not able to measure accurately on two-dimensional curved surfaces. In this field, periodic-transient measurement methods are advantageous. This paper describes the development of a periodic-transient technique for high-resolution heat transfer measurement and its application to multiple air-jet cooling of a concave solar receiver window. In contrast to other measurement techniques, the periodic-transient technique requires neither homogenous heating nor quantitative measurement of surface or fluid temperatures. The heat transfer coefficient is determined by periodically heating the substrate and evaluating the phase shift between the heat flux penetrating the substrate and the resulting temperature response. Equations for a hollow-sphere and flat-plate substrates are derived. The curved window surface is periodically heated by a simple device with standard light bulbs. A procedure for taking the transient heating characteristic into consideration is described. The distribution of surface temperature fluctuation is measured nonintrusively by thermography. For the sample application of air-jet cooling, a detailed uncertainty estimation is presented. The relative measurement uncertainty of the local, convective heat transfer coefficient ranges from −2.4% to +14.1% for $h=10 \ W/(m^2 \ K)$ and from −2.3% to +9.7% for $h=200 \ W/(m^2 \ K)$. The uncertainty of the spatially averaged heat transfer coefficient lies between +2.0% and +9.8% for $h_m=10 \ W/(m^2 \ K)$ and between +0.7% and +6.7% for $h_m =200 \ W/(m^2 \ K)$. The periodic-transient method described complements established techniques for high-resolution heat transfer measurements on two-dimensional curved surfaces. [DOI: 10.1115/1.2767677]

Keywords: high-resolution measurement, periodic transient, heat transfer coefficient, two-dimensional curved, concave surface, high spatial resolution, jet flow

1 Introduction

Despite excellent progress in computational fluid dynamics in recent years, convective heat transfer measurements are still indispensable. Knowledge of spatially resolved heat transfer is of great interest, especially in today's design optimization of complex flows. Two-dimensional curved surfaces, as frequently found in practice, complicate the measurement of heat transfer distribution. A heat transfer measurement technique should provide a fine spatial resolution, be highly accurate while requiring little calibration, be fast, allow automation, and be nonintrusive to the system being measured.

Reviews of different heat transfer measurement techniques may be found, for example, in Childs et al. [1] or Diller [2]. Moffat [3] concentrates on temperature and heat flux measurements. Some transient measurement methods are presented by Scott [4]. Most spatially distributed heat transfer measurements may be classified in stationary, transient, and analogy methods. Neither the references above nor the examples given below are exhaustive.

Stationary methods. Stationary methods may be distinguished by the imposed surface thermal boundary condition: constant temperature or constant heat flux. In the case of constant heat flux,

foil heaters are often used to homogenously heat the measurement surface, e.g., in Refs. [5,6]. Local heat transfer is the quotient of imposed heat flux minus losses and the difference between wall and fluid temperatures.

A constant temperature boundary condition can be imposed by temperature-controlled electric resistance heating devices [2]. In this case, the heat flux required to maintain a set temperature is measured. However, this implies an enormous number of resistance heaters and a control system to measure heat transfer distribution. Another heating device for a constant temperature boundary condition uses condensing vapor [7,8]. Here, heat flux is calculated by the thermal resistance and the difference between vapor saturation temperature and wall temperature. Local heat transfer is then calculated, as for constant heat flux.

Transient methods. Transient heat transfer measurement methods use the thermal system response to a change in boundary conditions. Either the heating boundary condition or the fluid temperature boundary condition can be changed. The heat transfer coefficient calculation then solves an inverse heat transfer problem. Different transient methods can be distinguished by the type of change in boundary conditions. In this paper, methods using a single, sudden change in a boundary condition are classified as step transients, while methods using a periodic boundary condition change are classified as periodic transients.

In the field of step transient methods, a boundary condition step is either produced by exposure of a preheated model to a cold fluid flow or by a sudden change in the fluid temperature. The heat transfer coefficient can be calculated by monitoring the tempera-

ture over time. If the internal resistance of the solid is negligible, i.e., for thin substrates with high thermal conductivity, the substrate can be approximated as isothermal. This assumption is valid within a few percent when the Biot number is lower than 0.1 ($Bi=h^*\delta/\lambda$, where δ is the substrate thickness) [1,2]. The time constant τ of the exponential temperature response is measured. The heat transfer coefficient h^* is the product of thermal inertia (ρc_p), substrate thickness (δ), and reciprocal of the time constant ($1/\tau$),

$$\frac{T_w(t) - T_f}{T_0 - T_f} = e^{-t/\tau} \quad h^* = \frac{\rho c_p \delta}{\tau} \tag{1}$$

At Bi numbers over 0.1, a non-negligible temperature profile develops inside the solid. For short times (Fourier number Fo $= at/\delta$ lower than $1/16$ [1,2]), the substrate can be treated as semi-infinite. Several solutions are given in Refs. [1,2] to calculate the heat flux transferred using temperature over time.

Using thermochromic liquid crystal thermography, the time required to reach a specific surface temperature $T_w(t)$ is measured. The heat transfer coefficient can be determined by using the following relationship:

$$\frac{T_w(t) - T_w(t_0)}{T_f - T_w(t_0)} = 1 - e^{\gamma^2} \operatorname{erfc}(\gamma) \quad \gamma = \frac{h^* \sqrt{t}}{\sqrt{\rho c_p \lambda}} \tag{2}$$

For long times (high Fourier numbers), heat transfer coefficients can also be measured if the substrate back is insulated. In this case, the substrate temperature can be approximated by the first term of an infinite series [9]. By measuring surface temperatures at two points of time t_1 and t_2, the heat transfer coefficient h^* can be determined by the following equations:

$$\mu = \sqrt{\frac{1}{Fo_2 - Fo_1} \ln\left[\frac{T_w(t_1) - T_f}{T_w(t_2) - T_f}\right]} \quad \text{where } Fo_i = \frac{at_i}{\delta^2} \tag{3}$$

$$h^* = \frac{\lambda}{\delta} \mu \tan \mu \tag{4}$$

The periodic-transient measurement techniques originate from Ångström's methods for determining the thermal conductivity of solid bodies [10]. They are used more rarely for heat transfer measurement than the other methods. Only point measurements are usually reported in the literature. Spatially resolved heat transfer measurements with a periodic-transient method are only reported by Baughn et al. [11].

In Refs. [11,4], the substrate is periodically excited by a variation in the fluid temperature. Kosky et al. [12,13] used a modulated electron beam, and Roetzel et al. [14] and Prinzen [15] used a periodically interrupted laser beam as the local heat source. All periodic-transient methods evaluate phase or amplitude response information to calculate the heat transfer coefficient. Further details are given in the following sections.

All thermal methods require the measurement of the surface temperature. Both infrared and liquid crystal thermography are nonintrusive temperature measurement techniques, which provide temperature maps. They are therefore ideally suitable for use in spatially resolved heat transfer measurements. While infrared thermography uses the thermal radiation emitted, liquid crystal thermography evaluates light intensity or color reflected off a coated surface. Examples of infrared and liquid crystal thermography for heat transfer measurement are given in Refs. [6,13,14,16] and Refs. [5,11,17–21], respectively.

Analogy methods. By analogy between mass and heat transfer, mass transfer measurements can be converted to heat transfer. Mass transfer methods can be classified into adsorption (e.g., ammonia on manganese chloride soaked substrate [21,22]), evaporation (e.g., water off a porous material [23]), and sublimation methods (e.g., naphthalene sublimation [24]). The amount of mass

transferred is frequently determined by optical, gravimetric, or surface profile scanning methods.

Stationary methods with a prescribed heat flux cannot generally be applied to two-dimensional curved surfaces because the foil heaters commonly used cannot be properly attached. Alternative heating devices that work by radiation usually do not provide a sufficiently homogeneous heat flux on the measurement surface. Therefore, the local heat flux cannot be calculated as for foil heaters by the ratio of electrical power and surface area. Moreover, high calibration standards are needed for accurate fluid and surface temperature measurements. The measurement uncertainty of stationary methods grows with rising heat transfer coefficient due to the decreasing temperature difference between fluid and surface temperatures.

A stationary method using a constant temperature boundary condition requires numerous temperature-controlled electric resistance heating devices, limiting the spatial resolution and complicating the measurement setup. Condensing vapor heating would overcome this, however, the challenge of accurate fluid and surface temperature measurement remains.

Step transient methods require a step change in one boundary condition. However, in practice, a good step change is not simple due to thermal inertia, mixing processes, etc. Furthermore, an accurate measurement of fluid and surface temperatures is also required in most step transient methods.

Mass transfer analogy methods offer both advantages and disadvantages. Most adsorption methods are not suitable for measuring on two-dimensional curved surfaces because the substrates cannot be properly attached. The naphthalene sublimation technique works well but involves, for example, high- and low-velocity limitations (temperature sensitivity and erosion) [24]. Another disadvantage of mass transfer experiments are their time-consuming model preparation and evaluation procedure.

The periodic-transient methods offer some advantages for measurement on two-dimensional curved surfaces. If the phase response is evaluated, neither the heat flux nor the wall or fluid temperatures have to be quantitatively measured. As a homogenous heat flux is no longer required, simpler heating methods are possible to heat two-dimensional curved surfaces. Periodic-transient methods also avoid a time-consuming calibration of thermography systems or temperature sensors without reducing measurement accuracy. In contrast to stationary methods, the measurement uncertainty remains small both for high and low heat transfer coefficients. However, there are also challenges of the periodic-transient method: A proper design and a transient thermal characterization of the heating system must be done. The substrate wall thickness must also be known for heat transfer measurement. Besides giving a theoretical background, this paper describes experiences and procedures to successfully apply the periodic-transient method.

For example, to design air-jet impingement cooling for a solar receiver window, heat transfer coefficients had to be measured on the concave surface of the window. The window is an axially symmetric piece that can be approximated by a hemisphere with a cylindrical extension (diameter of 0.31 m and height of 0.42 m). Further details may be found in Refs. [25,26]. Because of the above mentioned advantages, a periodic-transient measurement principle was used for this task. The following points had to be further developed [27]:

- Extension from a point measurement to a spatially resolved technique without using a step change in fluid temperature as in Ref. [11]. A fluid temperature step change is not possible in jet impingement measurements due to ambient air entrainment.
- Development of a low-cost heating system for the complete convex surface.
- Development of a method for transient thermal characterization of the heating system.
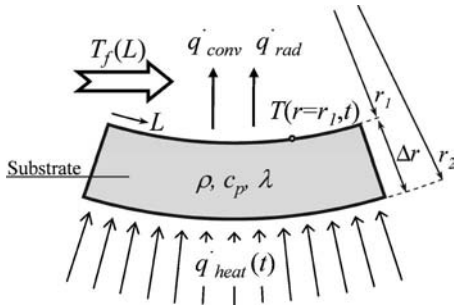
Fig. 1 Measurement principle and relevant quantities

- Achievement of a high measurement accuracy on two-dimensional curved surfaces.

2 Periodic-Transient Measurement Method

2.1 Theory. Figure 1 illustrates the transient measurement principle described in this paper. Sinusoidal modulated heat flux $\dot{q}_{\mathrm{heat}}(t)$ is applied to a substrate with thermal inertia ρc_p, thermal conductivity λ, and thickness Δr. The penetrating heat flux $\dot{q}_{\mathrm{in}}(t)$ can be calculated as described in Sec. 2.4. On the other side ($r = r_1$), the substrate is cooled with a fluid temperature $T_f(L)$, and the surface temperature over time ($T(r=r_1,t)$) is logged. The system along with its boundary conditions represents a continuous linear system with distributed parameters (see Fig. 2). It can be described by a partial differential equation (PDE) of position and time. The heat transfer coefficient can be calculated by the evaluation of the amplitude or phase response of the system.

Many two-dimensional curved surfaces with different curvature radii can be approximated by the basic geometries of a flat plate or a hollow sphere. Both solutions are given here. Much work has been done in the field of diffusion-wave fields and the solution of transient conduction problems, e.g., Refs. [10,12,13,28–31]. For the sake of completeness, the derivation of the amplitude and phase response of a hollow-sphere system is presented in the following section.

2.1.1 Hollow Sphere. The following assumptions are made for the analytical solution of the PDE problem:

- The substrate is part of a hollow sphere with wall thickness Δr. The external side (radius r_2) is heated while the internal side (radius r_1) is cooled convectively.
- The problem is assumed to be one dimensional (1D); that is, only radial heat flows are considered. Lateral heat flows are neglected (see Sec. 3.3).
- Physical properties through the wall thickness are assumed to be temperature independent (see Sec. 3.3).
- The fluid temperature change over time at a point P is neg-

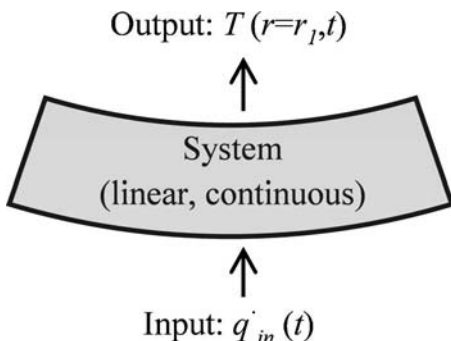**Fig. 2 System representation**

ligible; $\hat{T}_f(L_P,t) \approx 0$ (see Sec. 3.3).

With these assumptions, the transient equation of conduction with boundary and periodic conditions is,

differential equation:

$$\frac{\partial T}{\partial t} = a\left(\frac{\partial^2 T}{\partial r^2} + \frac{2}{r}\frac{\partial T}{\partial r}\right) \tag{5}$$

first boundary condition:

$$\lambda \left.\frac{\partial T}{\partial r}\right|_{r=r_1,t} = h^*[T(r_1,t) - T_f] \tag{6}$$

second boundary condition:

$$\lambda \left.\frac{\partial T}{\partial r}\right|_{r=r_2,t} = \dot{q}_{\mathrm{in}}(t) \tag{7}$$

periodic condition:

$$T(r,t) = T(r,t + k2\pi/\omega) \tag{8}$$

The substrate is heated periodically; that is, for $k = 1, \ldots, \infty$, the following relationship is valid: $\dot{q}_{\mathrm{in}}(t) = \dot{q}_{\mathrm{in}}(t + k2\pi/\omega)$.

Step 1: Elimination of mean quantities. All quantities can be expressed as the sum of a time-independent mean $\bar{x}$ and a time-dependent value $\hat{x}(t)$. The change in fluid temperature over time is assumed to be zero,

$$T(r,t) = \bar{T}(r) + \hat{T}(r,t) \tag{9}$$

$$T_f(L,t) = \bar{T}_f(L) + 0 \tag{10}$$

$$\dot{q}_{\mathrm{in}}(t) = \bar{\dot{q}}_{\mathrm{in}} + \hat{q}_{\mathrm{in}}(t) \tag{11}$$

Since the governing equation is linear, all mean quantities can be eliminated from the problem,

differential equation:

$$\frac{\partial \hat{T}}{\partial t} = a\left(\frac{\partial^2 \hat{T}}{\partial r^2} + \frac{2}{r}\frac{\partial \hat{T}}{\partial r}\right) \tag{12}$$

first boundary condition:

$$\lambda \left.\frac{\partial \hat{T}}{\partial r}\right|_{r=r_1,t} = h^*\hat{T}(r_1,t) \tag{13}$$

second boundary condition:

$$\lambda \left.\frac{\partial \hat{T}}{\partial r}\right|_{r=r_2,t} = \hat{q}_{\mathrm{in}}(t) \tag{14}$$

periodic condition:

$$\hat{T}(r,t) = \hat{T}(r,t + k2\pi/\omega) \tag{15}$$

Step 2: Creating dimensionless variables. With $\Delta r = r_2 - r_1$, it follows that

$$r_i \rightarrow r_i^+ = r_i/\Delta r \tag{16}$$

$$t \rightarrow \tau = t/T_{\mathrm{per}} \tag{17}$$

$$\hat{T}(r,t) \rightarrow \hat{\theta}(r^+,\tau) = \hat{T}(r,t)/\hat{T}_{\mathrm{max}}(r = r_1) \tag{18}$$

$$\omega \rightarrow \omega^+ = \omega T_{\mathrm{per}} \tag{19}$$

The Fourier and Biot numbers are

$$\mathrm{Fo} = \frac{aT_{\mathrm{per}}}{(\Delta r)^2} \tag{20}$$

$$\mathrm{Bi} = \frac{h^* \Delta r}{\lambda} \tag{21}$$

The dimensionless set of equations is,
   differential equation:

$$\frac{\partial \hat{\theta}}{\partial \tau} = \mathrm{Fo}\left(\frac{\partial^2 \hat{\theta}}{\partial r^{+2}} + \frac{2}{r^+} \frac{\partial \hat{\theta}}{\partial r^+} \right) \tag{22}$$

first boundary condition:

$$\left. \frac{\partial \hat{\theta}}{\partial r^+} \right|_{r^+ = r_1^+, \tau} = \mathrm{Bi}\,\hat{\theta}(r_1^+, \tau) \tag{23}$$

second boundary condition:

$$\left. \frac{\partial \hat{\theta}}{\partial r^+} \right|_{r^+ = r_2^+, \tau} = \frac{\Delta r}{\lambda \hat{T}_{\max}} \hat{q}_{\mathrm{in}}(\tau) \tag{24}$$

periodic condition:

$$\hat{\theta}(r^+, \tau) = \hat{\theta}(r^+, \tau + k) \tag{25}$$

Step 3: Laplace transform. The PDE transforms to an ordinary differential equation (ODE) with initial conditions included,
   differential equation:

$$s\hat{\vartheta} - \mathrm{Fo}\left(\frac{d^2 \hat{\vartheta}}{dr^{+2}} + \frac{2}{r^+} \frac{\partial \hat{\vartheta}}{\partial r^+} \right) = \hat{\theta}(r^+, 0^+) \tag{26}$$

first boundary condition:

$$\left. \frac{\partial \hat{\vartheta}}{\partial r^+} \right|_{r^+ = r_1^+, s} = \mathrm{Bi}\,\hat{\vartheta}(r_1^+, s) \tag{27}$$

second boundary condition:

$$\left. \frac{\partial \hat{\vartheta}}{\partial r^+} \right|_{r^+ = r_2^+, s} = \frac{\Delta r}{\lambda \hat{T}_{\max}} \hat{q}_{\mathrm{in}}(s) \tag{28}$$

periodic condition

$$\hat{\vartheta}(r^+, s) = e^{ks}\left[\hat{\vartheta}(r^+, s) - \int_0^k e^{-s\tau} \hat{\theta}(r^+, \tau) d\tau \right] \tag{29}$$

Step 4: Solution. With $\hat{\vartheta}^* = \hat{\vartheta} r^+$, the ODE is transformed to the following equation:

$$s\hat{\vartheta}^* - \mathrm{Fo}\frac{d^2 \hat{\vartheta}^*}{dr^{+2}} = \hat{\theta}(r^+, 0^+) \tag{30}$$

This equation can be solved by a further Laplace transform with respect to r^+. The following solution results from the inverse transform [9,30]:

$$\hat{\vartheta}(r^+, s) = A\frac{e^{pr^+}}{r^+} + B\frac{e^{-pr^+}}{r^+} + \frac{\hat{\theta}(r^+, 0^+)}{s} \tag{31}$$

$$p = \sqrt{\frac{s}{\mathrm{Fo}}} \tag{32}$$

Due to the periodic condition, the solution has to be independent of the initial condition $\hat{\theta}(r^+, 0^+)$. It can therefore be chosen arbitrarily, for example, $\hat{\theta}(r^+, 0^+) = 0$ for simplification. Coefficients A and B can be calculated with boundary conditions (27) and (28). Equation (39) then gives the temperature field.

Step 5: Transfer function. The transfer function can be calculated as the quotient of output and input signals, both written in the frequency domain. The input signal $X_{\mathrm{in}}(s)$ is the dimensionless change in the penetrating heat flux $\hat{q}_{\mathrm{in}}(s)$ Eq. (40). The output signal $X_{\mathrm{out}}(s)$ is the dimensionless change in wall temperature on
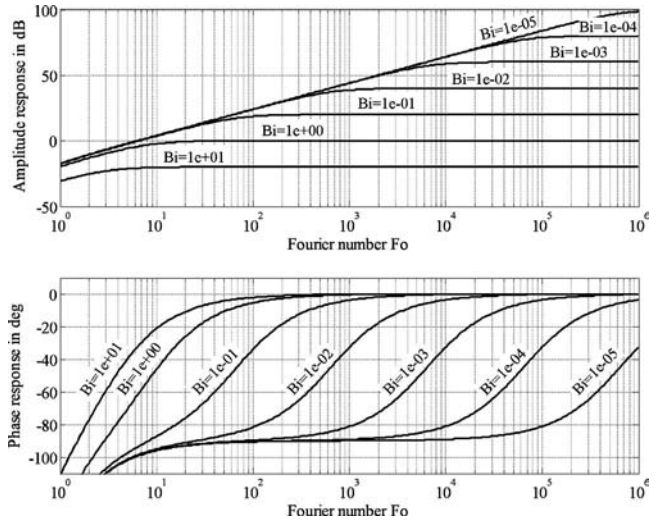

Fig. 3 Amplitude $A(\omega)$ and phase response $\varphi(\omega)$ for different Bi numbers (hollow sphere, $r_1 = 0.310$ m, $r_2 = 0.315$ m)

the cooled side $\hat{\vartheta}(r_1^+, s)$ (Eq. (41)), and is calculated by Eq. (39). Hence, transfer function $G(s) = X_{\mathrm{out}}(s)/X_{\mathrm{in}}(s)$ results in Eq. (42).

Step 6: Frequency response. Until now, the periodic condition (29) has not yet been used. The integral of this condition approaches zero as $\tau \to \infty$, that is, after the settling time. The periodic condition is then fulfilled for $s = i\omega^+ = i2\pi$. The frequency response is found by setting $s = i\omega^+$ in the transfer function. It is written as Eqs. (43) and (44).

Step 7: Amplitude and phase response. The complex frequency response can also be written with the amplitude response $A(\omega)$ and phase response $\varphi(\omega)$, resulting in the form $G(i\omega) = A(\omega)e^{i\varphi(\omega)}$,

$$A(\omega) = |G(i\omega)| = \sqrt{\mathrm{Re}^2[G(i\omega)] + \mathrm{Im}^2[G(i\omega)]} \tag{33}$$

$$\varphi(\omega) = \arg G(i\omega) = \arctan \frac{\mathrm{Im}[G(i\omega)]}{\mathrm{Re}[G(i\omega)]} \tag{34}$$

The amplitude response (Eqs. (45) and (47)), and phase response (Eqs. (46) and (47)), of the hollow-sphere system are found after several mathematical operations with $\sqrt{i\omega^+/\mathrm{Fo}} = \pm\sqrt{\omega^+/2\mathrm{Fo}}(1+i) = \pm\sqrt{\omega/2a}\Delta r(1+i) = \pm c(1+i)$. Figure 3 illustrates the Bode diagram for a hollow-sphere system.

2.1.2 Flat Plate. Similar amplitude and phase response results can be derived for a flat-plate system, cooled at $z = 0$ and periodically heated at $z = \delta$,

$$A(\omega) = \{[\mathrm{Bi} \cosh c \cos c + c(\sinh c \cos c - \cosh c \sin c)]^2$$
$$+ [\mathrm{Bi} \sinh c \sin c + c(\sinh c \cos c + \cosh c \sin c)]^2\}^{-1/2}$$
$$\tag{35}$$

$$\varphi(\omega) = -\arctan\left[\frac{\mathrm{Bi} \sinh c \sin c + c(\sinh c \cos c + \cosh c \sin c)}{\mathrm{Bi} \cosh c \cos c + c(\sinh c \cos c - \cosh c \sin c)} \right]$$
$$\tag{36}$$

where

$$c = \sqrt{\frac{\pi}{\mathrm{Fo}}} = \delta\sqrt{\frac{\omega}{2a}} \tag{37}$$

and

$$\mathrm{Bi} = \frac{h^* \delta}{\lambda} \tag{38}$$

$$\hat{\vartheta}(r^+, s) = \frac{\Delta r}{\lambda \hat{T}_{\max}} \hat{q}_{\mathrm{in}}(s) \left(\frac{(r_2^+)^2/r^+ \{pr_1^+ \cosh[p(r^+ - r_1^+)] + (r_1^+ \mathrm{Bi} + 1)\sinh[p(r^+ - r_1^+)]\}}{[r_1^+ r_2^+ p \mathrm{Bi} + p(r_2^+ - r_1^+)]\cosh[p(r_2^+ - r_1^+)] + (r_1^+ r_2^+ p^2 - r_1^+ \mathrm{Bi} - 1)\sinh[p(r_2^+ - r_1^+)]} \right) \tag{39}$$

$$X_{\mathrm{in}}(s) = \frac{\Delta r}{\lambda \hat{T}_{\max}} \hat{q}_{\mathrm{in}}(s) \tag{40}$$

$$X_{\mathrm{out}}(s) = \hat{\vartheta}(r_1^+, s) = \frac{\Delta r}{\lambda \hat{T}_{\max}} \hat{q}_{\mathrm{in}}(s) \left\{ \frac{p(r_2^+)^2}{[r_1^+ r_2^+ p \mathrm{Bi} + p(r_2^+ - r_1^+)]\cosh[p(r_2^+ - r_1^+)] + (r_1^+ r_2^+ p^2 - r_1^+ \mathrm{Bi} - 1)\sinh[p(r_2^+ - r_1^+)]} \right\} \tag{41}$$

$$G(s) = \frac{p(r_2^+)^2}{[r_1^+ r_2^+ p \mathrm{Bi} + p(r_2^+ - r_1^+)]\cosh[p(r_2^+ - r_1^+)] + (r_1^+ r_2^+ p^2 - r_1^+ \mathrm{Bi} - 1)\sinh[p(r_2^+ - r_1^+)]} \tag{42}$$

$$G(i\omega^+) = \frac{p'(r_2^+)^2}{r_1^+ r_2^+ p' \mathrm{Bi} + p'(r_2^+ - r_1^+)\cosh[p'(r_2^+ - r_1^+)] + (r_1^+ r_2^+ p'^2 - r_1^+ \mathrm{Bi} - 1)\sinh[p'(r_2^+ - r_1^+)]} \tag{43}$$

$$\text{where } p' = \sqrt{\frac{i\omega^+}{\mathrm{Fo}}} \tag{44}$$

$$A(\omega) = \sqrt{2}c(r_2^+)^2 \{2c^2(r_1^+ r_2^+ \mathrm{Bi} + 1)^2 \cosh^2 c \cos^2 c + 2c^2(r_1^+ r_2^+ \mathrm{Bi} + 1)^2 \sinh^2 c \sin^2 c - 2c(r_1^+ r_2^+ \mathrm{Bi} + 1)(r_1^+ \mathrm{Bi} + 1)\cosh c \sinh c + [(2c^2 r_1^+ r_2^+)^2$$
$$+ (r_1^+ \mathrm{Bi} + 1)^2](\sinh^2 c \cos^2 c + \cosh^2 c \sin^2 c) - 2c(r_1^+ r_2^+ \mathrm{Bi} + 1)(2c^2 r_1^+ r_2^+ + r_1^+ \mathrm{Bi} + 1)\cos c \sin c\}^{-1/2} \tag{45}$$

$$\varphi(\omega) = -\arctan\left\{ \frac{\mathrm{Bi}[2c \sinh c \sin c + 1/r_2^+(\sinh c \cos c - \cosh c \sin c)] + 2c^2(\sinh c \cos c + \cosh c \sin c) + 1/r_1^+ r_2^+[\sinh c \cos c + (2c \sinh c + \cosh c)\sin c]}{\mathrm{Bi}[2c \cosh c \cos c - 1/r_2^+(\sinh c \cos c + \cosh c \sin c)] + 2c^2(\sinh c \cos c - \cosh c \sin c) - \frac{1}{r_1^+ r_2^+}[\cosh c \sin c - (2c \cosh c - \sinh c)\cos c]} \right\} \tag{46}$$

$$\text{where } c = \sqrt{\frac{\pi}{\mathrm{Fo}}} = \Delta r \sqrt{\frac{\omega}{2a}} \tag{47}$$

$$\mathrm{Bi} = \frac{(2c^2 r_1^+ r_2^+ + 1)\sinh c \cos c + (2c^2 r_1^+ r_2^+ - 1)\cosh c \sin c + 2c \sinh c \sin c - \tan|\varphi|[(2c^2 r_1^+ r_2^+ - 1)\sinh c \cos c - (2c^2 r_1^+ r_2^+ + 1)\cosh c \sin c + 2c \cosh c \cos c]}{r_1^+[-2c r_2^+ \sinh c \sin c - \sinh c \cos c + \cosh c \sin c + \tan|\varphi|(-\sinh c \cos c - \cosh c \sin c + 2c r_2^+ \cosh c \cos c)]} \tag{48}$$

2.2 From Theory to Application

2.2.1 Hollow Sphere. Both amplitude and phase responses (Eqs. (45) and (46)) depend on the Biot number. By measuring either of the system responses and knowing wall thickness and thermal properties, the Biot number and hence the heat transfer coefficient can be calculated. Fluid temperature measurement is not necessary. The system can be excited by any periodic heating signal. However, the simplest way to determine the frequency response is by using a sinusoidal modulated heating signal: $\hat{q}_{\mathrm{in}}(t) = \hat{q}_{\mathrm{in,max}} e^{i\omega t}$. The dimensionless input signal is then

$$X_{\mathrm{in}}(t) = \frac{\Delta r}{\lambda \hat{T}_{\max}} \hat{q}_{\mathrm{in}}(t) = \frac{\Delta r \hat{q}_{\mathrm{in,max}}}{\lambda \hat{T}_{\max}} e^{i\omega t} \tag{49}$$

The dimensionless output signal is phase shifted (phase angle $\varphi < 0$),

$$X_{\mathrm{out}}(t) = \frac{1}{\hat{T}_{\max}} \hat{T}(r = r_1, t) = \frac{\hat{T}_{\max}}{\hat{T}_{\max}} e^{(i\omega + \varphi)t} = e^{(i\omega + \varphi)t} \tag{50}$$

A schematic graph of input and output signals over phase angle is shown in Fig. 4.

Evaluation by amplitude response. To determine the amplitude response $A(\omega)$, the heating amplitude $\hat{q}_{\mathrm{in,max}}$ and the temperature amplitude $\hat{T}_{\max}$ are measured. Provided that wall thickness Δr and thermal conductivity λ are known, the amplitude response is calculated by

$$A(\omega) = \frac{|X_{\mathrm{out}}(t)|}{|X_{\mathrm{in}}(t)|} = \frac{\lambda \hat{T}_{\max}}{\Delta r \hat{q}_{\mathrm{in,max}}} \tag{51}$$

However, as it is difficult to find the exact heating amplitude on the two-dimensional curved surface, evaluation by phase response is preferred.
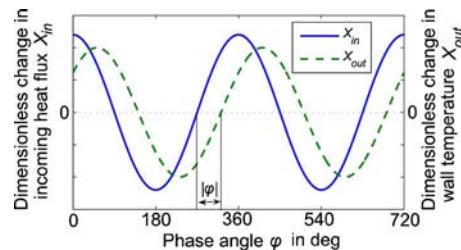
Evaluation by phase response. Phase angle φ can be extracted

Fig. 4 Schematic graph of input and output signals ($X_{\mathrm{in}}(t)$, $X_{\mathrm{out}}(t)$) and phase shift φ
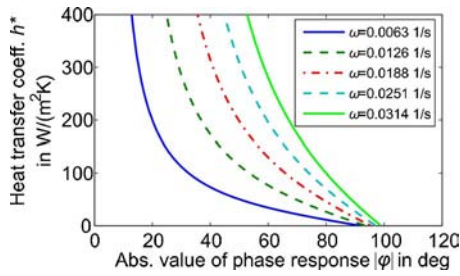
Fig. 5 Characteristic curves for heat transfer coefficient determination by phase response evaluation (hollow sphere, $r_1 = 0.310$ m, $r_2 = 0.315$ m, fused silica, $\lambda = 1.40$ W/(m K), $\rho = 2203$ kg/m^3, $c_p = 754$ J/(kg K))

directly from the oscillations of the substrate temperature and penetrating heat flux. The phase angle of the penetrating heat flux must be found by a special procedure accounting for the thermal inertia of the measurement setup (see Sec. 2.4). Nevertheless, phase response evaluation is clearly better suited for heat transfer calculation because neither the quantitative temperature amplitude nor quantitative heating amplitude need be known. Consequently, measurement is more accurate. Evaluation with both methods produces congruent results within their measurement accuracy. By solving Eq. (46) for the Biot number (see Eq. (48)), the heat transfer coefficient can be calculated by

$$h^* = \frac{\lambda}{\Delta r} \mathrm{Bi} \tag{52}$$

Figure 5 shows the characteristic curves of Eqs. (48) and (52) for different angular frequencies.

The Bode diagram of Fig. 3 shows that at low Fo numbers (high excitation frequencies), temperature oscillation is strongly damped. The optimum Fo number for a maximum phase response sensitivity depends on the Bi number. Table 1 lists the appropriate Fo numbers (excitation frequencies) for different Bi number ranges (heat transfer coefficient ranges) to be measured. In these ranges, the phase response is between −81 deg and −4 deg; the amplitude response is also sensitive. Bi numbers must be smaller than 10 or, even better, smaller than 1. Otherwise, the convective resistance, compared to the conductive, is too small to be measured appropriately.

The way from the measurement task to the experimental layout is shown in Fig. 6. Either low- or high-conductivity materials with different wall thicknesses may be chosen as substrates. The resulting Bi numbers should be smaller than 1. Then, the sensitive Fo number can be found by Table 1 or the Bode diagram (Fig. 3). The excitation cycle duration T_{per} can be calculated by

$$T_{\mathrm{per}} = \frac{\mathrm{Fo}(\Delta r)^2}{a} \tag{53}$$

If the cycle duration is too small (<100 s) or too high (>1000 s), another wall thickness or substrate material should be chosen and the iteration starts again. Moreover, one must pay attention to the required heat flux amplitude $\hat{q}_{\mathrm{in,max}}$. The greater the system damping is, the higher the heat flux amplitude $\hat{q}_{\mathrm{in,max}}$.

Table 1 Measurement sensitivity for different Bi number ranges

Bi number range	Approximate sensitive Fo number
0.1–10	10
0.01–1	100
0.001–0.1	1000
0.0001–0.01	10,000
0.00001–0.001	100,000

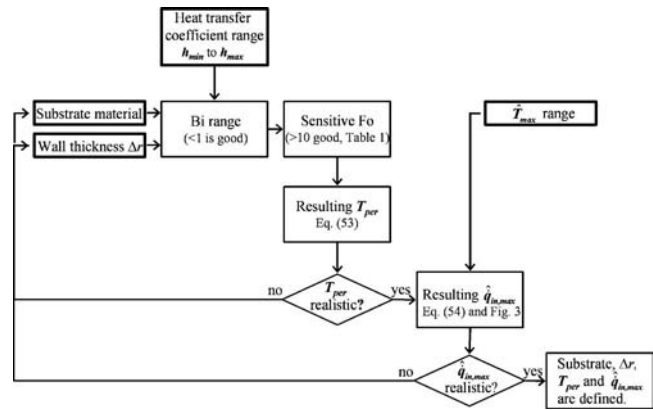**Fig. 6 The way from the measurement task to the experimental layout**

must be to get a measurable temperature response amplitude $\hat{T}_{\mathrm{max}}$. The required heat flux amplitude $\hat{q}_{\mathrm{in,max}}$ to get a measurable temperature response amplitude (depends on the temperature measurement system used) can be calculated by

$$\hat{q}_{\mathrm{in,max}} = \frac{\lambda \hat{T}_{\mathrm{max}}}{A(\omega)\Delta r} \tag{54}$$

If the heat flux amplitude, calculated by Eq. (54), can be easily applied by a heating system, an appropriate substrate and measurement parameter set has been found. If not, the iteration begins once again.

Table 2 lists examples of substrates, excitation periods, and penetrating heat flux amplitudes $\hat{q}_{\mathrm{in,max}}$ for different heat transfer coefficient ranges. The values and ranges are approximate and only serve for orientation. The penetrating heat flux amplitude is chosen in order that the temperature amplitude is between 0.5 K and 5 K for the high and low range of heat transfer coefficients, respectively. Examples with an excitation heat flux amplitude higher than 1000 W/m^2 are not listed. The 5-mm-thick fused-silica substrate is used in the application of this paper.

2.2.2 Flat Plate. For the flat-plate system, the heat transfer coefficient can be calculated by solving Eq. (36),

$$\mathrm{Bi} = \frac{c(\sinh c \cos c + \cosh c \sin c)}{\tan|\varphi|\cosh c \cos c - \sinh c \sin c}$$
$$- \frac{\tan|\varphi|c(\sinh c \cos c - \cosh c \sin c)}{\tan|\varphi|\cosh c \cos c - \sinh c \sin c} \tag{55}$$

$$\Rightarrow h^* = \frac{\lambda}{\delta} \mathrm{Bi} \tag{56}$$

2.2.3 Comparison Between Hollow Sphere and Flat Plate. The approximate evaluation of the exemplary hollow-sphere measurement setup (radius of 0.310 m and thickness of 0.005 m) with flat-plate equations leads to only slight deviations between 1.6% and 2.0% within the measurement range (10 W/(m^2 K) $< h^* < 200$ W/(m^2 K)) because the radius of curvature is large relative to Δr. For smaller radii of curvature, the difference between hollow-sphere and flat-plate evaluations evidently gets higher.

2.3 Application: Multiple Air-Jet Cooling and Measurement Setup. The periodic-transient measurement technique can be applied to a variety of convective heat transfer problems. Flat plates or surfaces with large radii of curvature relative to Δr can be approximated by the flat-plate equations. Two-dimensional curved surfaces with smaller radii of curvature can be frequently approximated by the hollow-sphere equations. As shown in Table

Table 2 Examples of substrate properties, measurement parameters, and appropriate heat transfer coefficient ranges

Material	Δr (mm)	T_{per} (s)	$\hat{q}_{in,max}$ (W/m²)	Fo	h^* (W/m² K)
Plexiglass	1.0	100	890	10	18–1800
	3.3	1000	280	100	5.6–560
Fused silica	5.0	1000	140	34	2.8–280
	2.9	1000	240	100	4.8–480
	0.9	100	760	100	15–1500
	0.9	1000	76	1000	1.5–150
V2a steel	2.0	100	380	100	76–7600
	2.0	1000	38	1000	7.6–760
	0.6	1000	120	10000	2.4–240
Aluminum	3.1	1000	390	10000	7.8–780
	1.0	1000	120	100000	2.5–250

2, a variety of heat transfer ranges can be covered.

The main purpose of the measurement setup presented in this paper was to determine the heat transfer distribution of multiple air-jet cooling on the concave fused-silica window of a solar receiver. Measurement setups for other applications of the periodic-transient measurement method would have to be adapted accordingly. However, the basic approaches can be transferred easily. Figure 7 shows the setup components: the forced-convection jet-cooling air supply and distribution systems, the domed fused-silica substrate, lamp heating, infrared thermography, and data acquisition systems. To ensure that the flow model emulates the real solar receiver, a secondary concentrator model was erected in front of the window.

2.3.1 Substrate. An old solar receiver window was used as the measurement substrate. Properties and dimensions of the domed substrate are listed in Table 3. The fused-silica window was painted mat black so the light from the heating lamps would be absorbed directly on the substrate surface. The paint was only about 30 μm thick. This is important because thick paint coating would change the thermal transient behavior of the substrate. The other side of the window was also painted black because thermography measurements without optical filters on opaque black bodies have a lower signal-to-noise ratio than direct measurement with optical filters on a semitransparent fused-silica window. Mat paint also reduces undesirable reflection. Materials other than

fused silica, for example, metals, could also have been used for the substrate. The fused-silica window was used only because it was at hand.

The substrate wall thickness is a very sensitive parameter using the periodic-transient measurement technique. Unfortunately, in this respect the fused-silica substrate at hand was of bad quality. Thickness variations up to 30% were measured (Wenzel 3D LH/computerized numerical control (CNC) measuring machine). The statistical uncertainty was ±12.3%. For future measurements, it is strongly recommended to use a substrate with a more homogenous wall thickness, for example, an aluminum, steel, or Plexiglass model, which may be produced on a CNC milling machine. Due to limited funding, we had to cope with the fused-silica substrate. By measuring the thickness and projecting the measured thickness data on the thermography images, the statistical thickness uncertainty could be reduced to ±0.8%. However, the thickness correction could not be done at the window top (7.6% of the total measurement surface) because the thickness gradients were too large there.

2.3.2 Heating System. The convex side of the spherical window is heated by 41 40-W lamps (light bulbs) arranged in such a way that substrate illumination is approximately uniform. However, more important than the uniformity in mean flux level is the
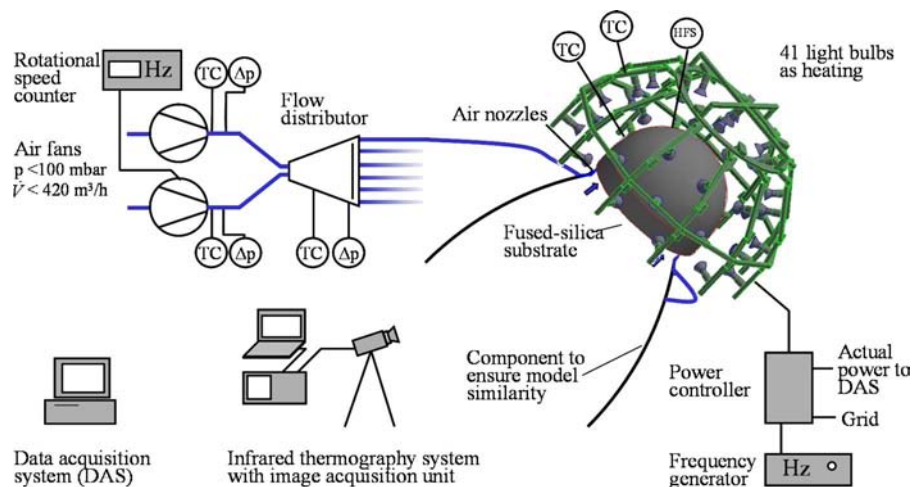

Fig. 7 Measurement setup (TC=thermocouple, Δp=differential pressure gage, HFS =heat flux sensor)

Table 3   Properties and dimensions of fused-silica window

Specifications	
Density[a] ρ (kg/m^3)	2203
Specific heat capacity[a] c_p (J/(kg K))	754
Thermal conductivity[a] λ (W/(m K))	1,40
Height[b]/Diameter[b] (mm)	447/315
Glass thickness[b] $\overline{\Delta r} \pm \sigma_{\Delta r}$ (mm)	4.8±0.6

[a]At 35°C [32].
[b]On the concave side, measurement at DLR (Wenzel 3D LH/CNC measuring machine).

uniformity in heat flux transients when heating power is modulated. High changes in thermal inertia in the heating structure should therefore be avoided.

The heated side of the substrate is protected from ambient influences such as forced convection by flexible, microporous insulating plates (Multitherm 550, Technophysik Engineering). The self-supporting insulating segments were arranged in this way that the heating structure, visible in Fig. 7, was outside and the lamps were inside the insulation cavity. To avoid heating, the insulating material is covered by aluminum foil, which reflects light passing by the substrate. The transient heat flux response to heating power modulation has been checked by an infrared camera. It could be demonstrated that the heat flux transients are uniformly distributed over the substrate surface and are not locally influenced by the heating structure (lamps, insulation). Hence, the standard light bulbs and the aluminum-coated insulation are suitable heating components.

A frequency generator and a thyristor power controller (JUMO TYA-110/3, 025, TR) modulate the lamplight intensity. Phase angle operation avoids jittering of the lamps. Electromagnetic compatibility of phase angle operation with measurement devices is achieved by appropriate shielding and filtering. The used thyristor has got a power level output that is logged by the data

Table 4   Omega HFS-4 heat flux sensor [33,34] and 3M 467MP adhesive transfer tape [35] technical data

Specifications	
Dimensions [34]	29×35 mm^2
Nominal thickness [34]	0.23 mm
Response time[a]	0.60 s
Nominal sensitivity	200 μV/(W/m^2)
Thermal resistance	0.002 K/(W/m^2)
Thermal capacitance	0.02 Btu/(ft^2 F)=409 J/(m^2 K)
Measurement accuracy	±10%
Adhesive transfer tape 3M, 467MP	<120°C; Thickness: 0.05 mm

[a]63%-step-function response.

acquisition system.

A thin-film heat flux sensor (HFS) [33,34] to measure the heat flux penetrating the substrate was mounted on the heated side of the window. A low sensor time constant is crucial for transient measurement. The HFS was glued onto the heated window surface with a thin adhesive transfer tape [35]. Sensor and adhesive tape details are given in Table 4. To ensure surface properties identical to the blackened window, the sensor surface was also painted.

2.3.3 Air Supply, Distribution System, and Nozzles. Two rotary piston blowers connected to a flow distributor supply air to the jet-cooling nozzles. The air volume flow rate is found by relating the blower rotational speed, pressure difference, and inlet air density (measurement accuracy ±5%). The maximum volume flow rate is 420 m^3/h at a maximum pressure difference of 100 mbars.

The flow distributor consists of a diffuser tube, which is closed by a plate with 18 orifices providing air to up to 18 nozzles. Optionally, a second rotating plate with up to 18 orifices is located inside the diffuser on the first plate. Some orifices may be closed. By rotation of the second plate, the nozzle air streams can be switched on and off.

The window-cooling nozzles are distributed equally over the circumference of the bottom edge of the window to avoid blocking sunlight entering the solar receiver. Both round-type and slot-type nozzles were used. The round-type nozzles are conical with a length of 30 mm. The slot-type nozzles have got a round inlet cross section (length 50 mm) with an intersection (length 30 mm) to a rectangular cross section (length of 78 mm). The slot-type nozzle geometry is adapted to the limited space in the solar receiver application. Further nozzle details can be found in Table 5.

Almost 50 experiments were done with the periodic-transient measurement method. Tables 6 and 7 give an overview of measurements and the parameters used. Different window-cooling designs, shown in Fig. 8, were tested. Symmetric configurations supply all active nozzles with the same mass flow. To enhance and smooth out heat transfer distribution, symmetric configurations with several different swirled flows were also studied. Finally, asymmetric configurations with pulsating mass flow were investigated. In this configuration, nozzles are only active on one side of the window, while the others are deactivated. By sequentially switching nozzles on and off, the well-cooled region is moved

Table 5   Nozzle types (r=round; s=slot: slot nozzle outlet: 35.0×6.0 mm^2)

Nozzle types	Round 16	Round 12	Round 8	Slot
Inlet/outlet type	r/r	r/r	r/r	r/s
d_h inlet/outlet (mm)	20.0/16.0	20.0/12.0	20.0/8.0	25.0/15.9
A inlet/outlet (mm^2)	314/201	314/113	314/50	491/198
Nozzle length (mm)	30	30	30	50+30+78

Table 6   Measurement overview

	Symmetric	Symmetric, swirled			Asymmetric				
Number of nozzles	6	6	3 of 18		4 of 18			5 of 18	6 of 18
Nozzle type	Round	Round	Slot	Slot	Round			Slot	Slot
Nozzle orientation	$\vartheta=0$ deg; $\varphi=0$ deg	$\vartheta=10$ deg; $\varphi=30/80$ deg	$\vartheta=0$ deg; $\varphi=0$ deg	$\vartheta=0$ deg; $\varphi=0$ deg	$\vartheta=10$ deg; $\varphi=0$ deg			$\vartheta=0$ deg; $\varphi=0$ deg	$\vartheta=0$ deg; $\varphi=0$ deg
Cycle duration[a] T_{rot} (s)	∞	∞	22	∞	22	30	22	∞	22	22
Nozzle Re number[b]	23,200–76,900	57,800–58,200	19,400–94,100	61,600–63,100	19,600–89,000	18,100–58,800	18,700–78,200	62,500–74,600	19,300–85,200	19,500–78,000
Number of measurements	7	2	5	6	5	2	4	6	5	3

[a]Cycle duration ∞ means no mass flow pulsation.
[b]Variation of Re number by varying volume flow rate or nozzle outlet diameter (Re=$\rho w d_h/\eta$).

Table 7 Parameter overview of periodic-transient measurements

Air supply system	
Volume flow rate $\dot{V}_0$	40–342 m²/h
Total pressure loss Δp	4–98 mbars
Nozzle Re number	18,100–94,070
Nozzle outlet velocity w	20–114 m/s
Heating system	
Heating frequency f	0.001 Hz ($\omega=0.0063$ s⁻¹, $T_{per}=1000$ s)
Electric heating power P_{el}	380±260 W
Mean penetrating heat flux $\dot{q}_{in}$	340±140 W/m²
Thermography system	
Number of frames per measurement	600
Image acquisition frequency	12 min⁻¹
Averaging	over 8 frames (0.27 s per frame)
Sensitivity	0.04–0.06 K
Substrate emittance	0.96
Maximum temperature	<44°C
Time	
To reach stationary state	2 h
To reach nontransient oscillation	>3 periods (>50 min)
Measurement duration	3 periods (50 min)

around the circumference of the window. The cycle duration T_{rot} gives the time needed for one rotation. More details are published in Refs. [25,26].

2.3.4 Thermography and Data Acquisition Systems. An infrared thermography system (Avio TVS-2100, Nippon Avionics Co., Ltd.) is used to nonintrusively measure temperature distribution on the substrate surface. InSb sensor sensitivity is between 3 μm and 5.4 μm. The thermography unit creates 256×200 pixel temperature maps with an 8 bit thermal resolution at a frequency of 30 Hz [36]. A temperature map sequence is automatically saved on a connected PC. To reduce noise, one frame is averaged over eight temperature maps, that is, over 0.27 s. The measurement took three heating periods (50 min). Acquiring images at a frequency of 12 frames/min, 600 frames were saved in each measurement.

The temperature range can be adapted to the actual test conditions. The relative temperature sensitivity of 0.04–0.06 K was achieved in the window-cooling measurement. In contrast, the accuracy of absolute temperature measurement (<120°C) is ±2.4 K, causing a prohibitively high heat transfer measurement uncertainty with stationary methods, not including in situ camera

calibration.

A Solartron integrated measurement pod (IMP) (3595 1C, Solartron) connected by S-Net to a PC is used to acquire the sensor data (HFS, thermocouple, electric power reading, etc.). The integration time was 20 ms. Data were logged every 5 s.

2.4 Transient Heating Characterization. Phase response evaluation uses the phase angle of the heat flux penetrating into the substrate ($\dot{q}_{in}(t)$). However, only the imposed heat flux phase angle is known a priori ($\dot{q}_{heat}(t)$ or $P_{el}(t)$). The issue in this section is whether there is a phase shift between the known imposed heat flux and the heat flux penetrating in the substrate, and, if so, how much. In Refs. [12,13], this matter receives no special treatment.

2.4.1 Physical Background. Due to the thermal inertia of the heating system and the substrate, heat flux penetrating into the substrate is phase shifted to the electric heating power $P_{el}(t)$. This phase shift must not be neglected; otherwise, this leads to wide errors in heat transfer calculation. The conditions on the heated side are illustrated in Fig. 9. Figure 10 shows the electric heating power (P_{el}) and the incident ($\dot{q}_{inc}$), outgoing ($\dot{q}_{out}$), and penetrating ($\dot{q}_{in}$) heat fluxes.

SYMMETRIC
→ 6 Nozzles
→ 9 Nozzles (alternative)

SYMMETRIC, SWIRLED
→ 6 Nozzles

ASYMMETRIC, PULSATING
→ 3 / 4 / 5 / 6 Nozzles
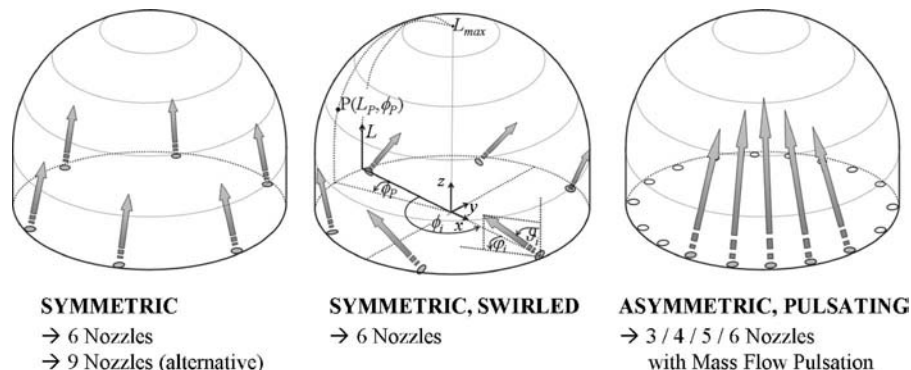with Mass Flow Pulsation

Fig. 8 Window-cooling designs and coordinate systems with nozzle orientation (center)
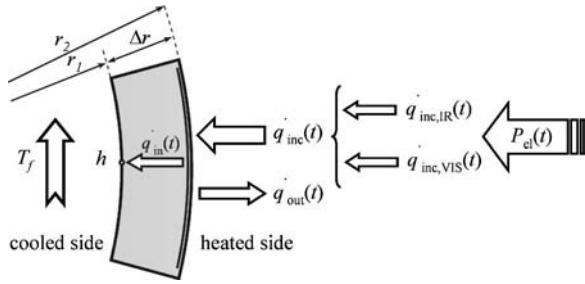
Fig. 9 Energy flows and heat fluxes on the heated side of the substrate

Fig. 11 Characteristic heating curve ($P_{el}=380\pm260$ W, $T_{per}=1000$ s)

Figure 10(a) shows the electric heating power, for which the phase is assumed to be 0 deg. The heat flux penetrating into the substrate volume is composed of (i) heat input by visible light, (ii) heat input by thermal radiation and convection, and (iii) heat losses from thermal emission and convection. The heat input by visible light ($\dot{q}_{inc,vis}$) is in phase with the electric heating power signal. The whole two-dimensional curved surface is radiated simultaneously by the lamps, regardless of the heat transfer coefficient on the other side. The insulation, lamps, and air are heated and transfer their heat to the substrate with a phase shift. It has been shown that the heat input by thermal radiation and convection ($\dot{q}_{inc,IR}$) is in phase over the whole substrate. The incident heat flux on the substrate is $\dot{q}_{inc}=\dot{q}_{inc,vis}+\dot{q}_{inc,IR}$, as shown in Fig. 10(b). There is a phase shift between the electric heating power and the incident heat flux. The phase shift is independent of the heat transfer coefficient on the other side. Heat loss from thermal emission and convection ($\dot{q}_{out}$) depends on the substrate surface temperature, i.e., on the heat transfer coefficient of the cooled side. Outgoing heat fluxes, therefore, vary in phase and amplitude over the substrate surface. Figure 10(c) shows the outgoing heat flux at two points, A and B, each having a different heat transfer coefficient h_A and h_B on the cooled side. At point A, with the lower heat transfer coefficient h_A, the outgoing heat flux and the phase shift to the electric heating power are higher than those at point B. The penetrating heat flux ($\dot{q}_{in}$), shown in Fig. 10(d), is the sum of incident ($\dot{q}_{inc}$) and outgoing ($\dot{q}_{out}$) heat fluxes. At a point with a low heat transfer coefficient (h_A), the penetrating heat flux
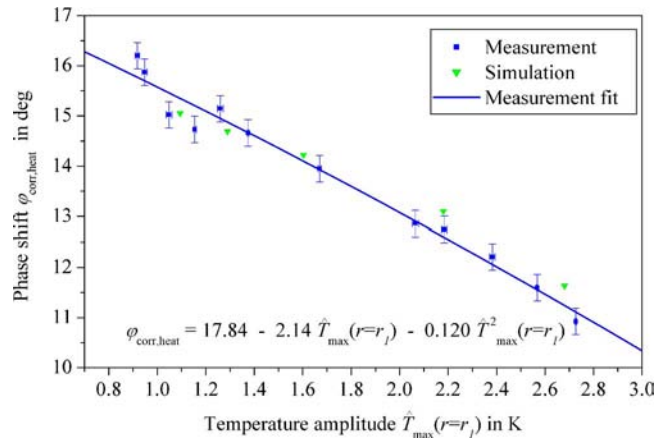
has a lower phase shift $\varphi_{corr,heat}$ to the electric heating power than at a point with a high heat transfer coefficient (h_B).

2.4.2 Characteristic Heating Curve. The required penetrating heat flux is measured locally by the HFS. As it is not feasible to install several HFSs to measure the penetrating heat flux distribution, the transient heating behavior was characterized once before measurement began. Different flow configurations were generated for this, causing varied heat transfer coefficients on the other side of the HFS without changing the heating conditions (mean, amplitude, frequency). The surface temperature amplitude on the cooled side $\hat{T}_{max}(r=r_1)$, which depends on the actual heat transfer coefficient, and the phase shift ($\varphi_{corr,heat}$) between the penetrating heat flux $\dot{q}_{in}$ and the electric heating power P_{el} are measured simultaneously. By repeating this procedure for different flow conditions, the characteristic curve shown in Fig. 11 can be plotted. There is a strong correlation ($r^2=0.98$) between the phase shift $\varphi_{corr,heat}$ and the surface temperature amplitude $\hat{T}_{max}(r=r_1)$. After correcting for the HFS influence on the phase shift measured (see below), the following relationship is calculated (valid for $P_{el}=380\pm260$ W and $T_{per}=1000$ s):
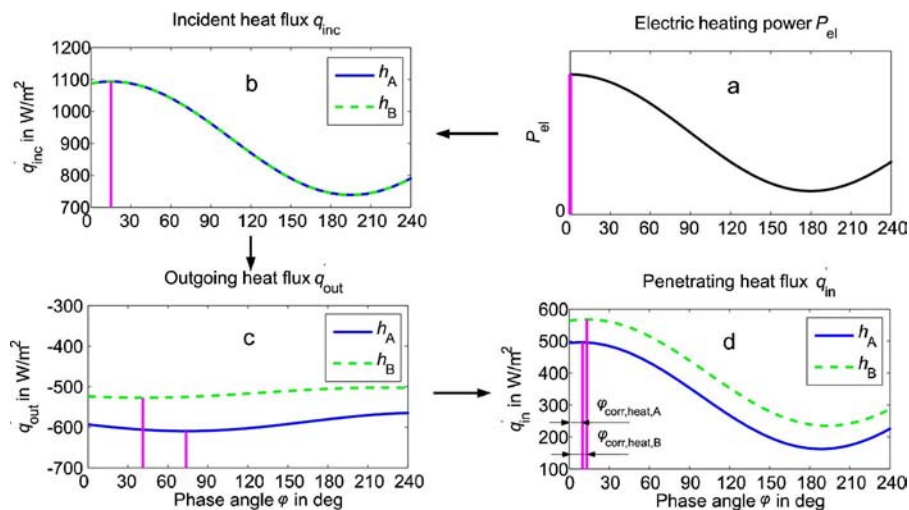

Fig. 10 (a) Electric heating power. (b)–(d) Heat fluxes at points A and B on the heated side for heat transfer coefficients $h_A=22$ W/m² K and $h_B=128$ W/m² K. Vertical lines point out the phase angles. Simulation: flat plate, $\delta=0.005$ m, fused silica, $\lambda=1.40$ W/(m K), $\rho=2203$ kg/m3, $c_p=754$ J/(kg K), $T_{per}=1000$ s ($\omega=0.0063$ s⁻¹).

$$\varphi_{\text{corr,heat}} = 17.84 - 2.14\hat{T}_{\max}(r = r_1) - 0.120\hat{T}^2_{\max}(r = r_1) \quad (57)$$

In a few words, once the characteristic curve is measured, it is possible to determine the phase shift between the electric heating power P_{el} and the penetrating heat flux $\dot{q}_{\text{in}}$ simply by evaluating the easily measurable temperature amplitude on the cooled side $\hat{T}_{\max}$.

The HFS thermal resistance changes the temperature field and the penetrating heat flux of the substrate. The question is how the measured transient quantities, which are input data for the heat transfer coefficient calculation, are biased (i.e., phase angles of penetrating heat flux $\dot{q}_{\text{in}}$ and the surface temperature amplitude $\hat{T}_{\max}(r = r_1)$). Although the sensor thermal capacitance (410 J/m^2 K) is only about 5% of the capacitance of the fused-silica substrate (7970 J/m^2 K), the influence on transient behavior should be evaluated and corrected. In experiments to evaluate the HFS influence on the temperature amplitude $\hat{T}_{\max}$, the lamplight intensity was modulated and the substrate was convectively cooled, as in the measurements. A sequence of IR images of the region was grabbed where, on the opposite window side, the HFS was glued. Then, the surface temperature amplitude was calculated for each pixel and plotted as a map. On these maps, no difference in amplitude was detected between the sensor region and the surrounding region. This analysis was repeated with different heat transfer coefficients. No measurable HFS influence on the temperature amplitude was found.

An experimental approach is not possible to evaluate the HFS influence on the phase angle of the penetrating heat flux $\dot{q}_{\text{in}}$. For this and to verify the characteristic curve, a transient simulation model was created. The model is comprised of the fused-silica substrate including the paint, insulation, aluminum foil, lamps, entrapped air mass, and, optionally, the HFS. The unbiased phase angle of the penetrating heat flux could be found by a transient simulation where the HFS is not modeled and could be compared to a transient simulation with the HFS modeled. It was found that the phase angle is distorted by only about 1.5% by the sensor. The data measured underlying the characteristic curve are corrected accordingly. The simulation results of the transient model are also shown in Fig. 11. There is a good agreement between measurements and simulation.

2.5 Evaluation Procedure. Figure 12 shows the evaluation procedure for finding the heat transfer coefficient by phase response evaluation.

Step 1. Phase shift evaluation. The phase shift ($\varphi_{\text{meas}} < 0$) between the electric heating power $P_{\text{el}}(t)$ and the surface temperature $T(r_1, t)$ measured by the thermography system can be evaluated using mean covariances,

$$\varphi_{\text{meas}} = -\arccos\frac{\overline{\hat{P}_{\text{el}}(t)\hat{T}(r_1, t)}}{[\hat{P}_{\text{el}}(t)\hat{P}_{\text{el}}(t)\hat{T}(r_1, t)\hat{T}(r_1, t)]^{0,5}} \quad (58)$$

Step 2. Phase shift correction. To find the phase shift required between the penetrating heat flux and surface temperature, the measured phase shift $\varphi_{\text{meas}}(<0)$ must be corrected for phase shift from the heating characteristics ($\varphi_{\text{corr,heat}} > 0$, Sec. 2.4) and paint ($\varphi_{\text{corr,paint}} > 0$). Phase correction for paint was estimated to 0.37 ± 0.10 deg by the simulation model (Sec. 2.4). Figure 13 shows the phase shift correction of the signals measured.

Step 3. Heat transfer coefficient calculation. The heat transfer coefficient h^* can be calculated by Eqs. (48) and (52) or Eqs. (55) and (56) for a hollow-sphere or a flat-plate substrate, respectively. The substrate thermal diffusivity a, thermal conductivity λ, heating frequency ω, glass thickness Δr, and corrected phase shift φ must be known for this. The thermal substrate data is considered temperature dependent (time averaged).

Step 4. Radiation correction of heat transfer coefficient. As the heat transfer coefficient h^* contains both convective and radiative
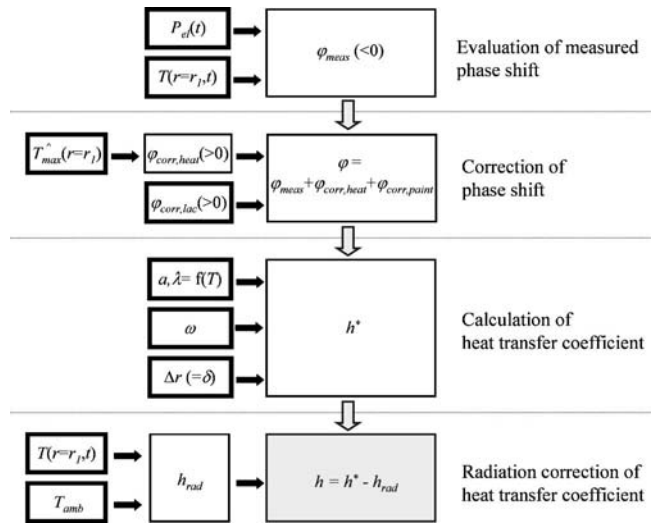

Fig. 12 Evaluation procedure for finding the heat transfer coefficient

components, the unknown convective heat transfer coefficient is obtained by the following radiation correction, where h_{rad} is the linearized radiative heat transfer coefficient,

$$h = h^* - h_{\text{rad}} \quad (59)$$

For the measurements with maximum substrate temperatures below 44°C, h_{rad} is between 6.0 W/m^2 K and 6.6 W/m^2 K.

3 Results

The high-resolution periodic-transient measurement technique was applied to the heat flux distribution of an air-jet-cooled receiver window. Some example measurements, verification of assumptions, and uncertainty estimation are given below.

3.1 Definitions

3.1.1 Heat Transfer Coefficient and Fluid Temperature. The convective heat transfer coefficient is defined as

$$h = \dot{q}_{\text{conv}}/(T_w - T_f) \quad \text{where } T_f = T_{f,\text{ad}} \quad (60)$$

The choice of an appropriate fluid temperature T_f is crucial for the application of heat transfer coefficients to situations with other boundary conditions. Moffat [3,20] recommended the use of a heat transfer coefficient defined in terms of the adiabatic wall temperature $T_{f,\text{ad}}$. The adiabatic wall temperature describes the
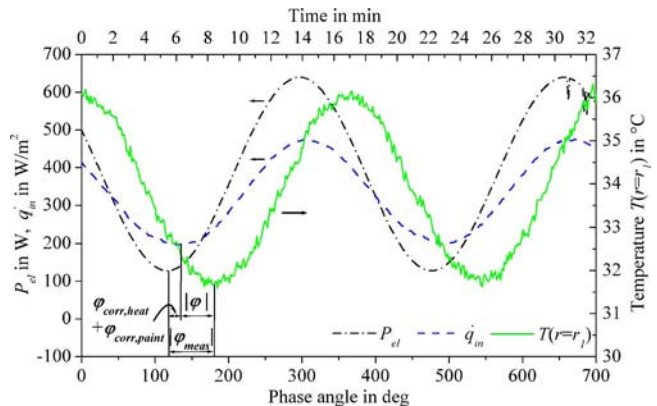

Fig. 13 Phase shift $|\varphi|$ found from measured phase shift $|\varphi_{\text{meas}}|$ and correction phase shifts $\varphi_{\text{corr,heat}}$ and $\varphi_{\text{corr,paint}}$ (measurement)
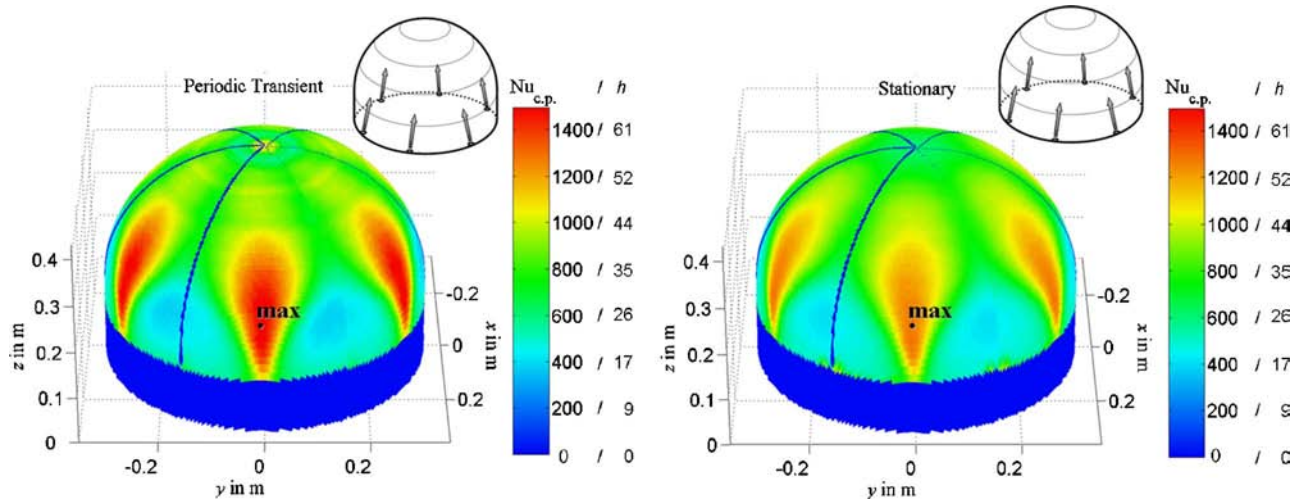
Fig. 14 Heat transfer distribution measured on the window surface with symmetric air-jet cooling (six round-type nozzles; d=0.008 m; ϑ=0 deg; φ=0 deg; $\dot{V}_0$=51 m³/h; w=47 m/s; Re=23,200; T_{rot}=∞; h in W/m² K (25°C)). Periodic-transient method, left; stationary method, right.

"effective fluid temperature," that is, the temperature the wall would have had if it had been locally adiabatic. With this definition, the heat transfer coefficient depends only on system geometry, fluid properties, and fluid mechanics and is independent of the thermal boundary condition, which frequently varies in different situations.

As may be seen in Eqs. (48) and (52), the fluid temperature need not be measured to calculate the heat transfer coefficient. This greatly simplifies the heat transfer measurement. However, if the heat transfer coefficient is used for calculation, the fluid temperature must be calculated at each position. As the driving force of heat transfer is the local temperature difference between wall and fluid, the adiabatic wall temperature $T_{f,ad}$ is the appropriate fluid temperature in the periodic-transient measurement. If the fluid temperature changes are smaller than the difference between the wall and fluid temperatures, the adiabatic wall temperature $T_{f,ad}$ can be approximated by a mean fluid temperature. In the air-jet window-cooling application, the mean fluid temperature $T_{f,m}$ can be calculated iteratively by [25]

$$T_f = T_{f,m} = T_{f,noz} + \frac{1}{2}\frac{\dot{Q}}{R\dot{M}_0 c_p} \tag{61}$$

where $T_{f,noz}$ is the nozzle outlet temperature, $\dot{Q}$ the transferred heat flow rate, $\dot{M}_0$ the total nozzle mass flow rate, c_p the specific heat capacity, and R the entrainment ratio. The entrainment ratio R is defined as the ratio of the total jet mass flow rate (nozzles and entrainment) to the mass flow rate of all active nozzles ($\dot{M}_0$). it was evaluated by computational fluid dynamics (CFD) simulations. The error of using $T_{f,m}$ instead of $T_{f,ad}$ was in the range of ±4.7% [25].

3.1.2 Nusselt Number. The Nusselt number for window cooling is defined by the maximum length of the window curve L_{max}=0.599 m and the thermal conductivity λ at the nozzle exit temperature (λ=0.0261 W/(m K) at 25°C),

$$Nu = hL_{max}/\lambda \tag{62}$$

The influence of variable air properties with temperature on heat transfer is very slight [37]. However, the given Nusselt numbers (Nu_{cp}) are corrected for variable fluid properties by the temperature ratio method [38]. For gases, the Nusselt number Nu_{cp} (constant properties) can be calculated with the measured Nusselt

number Nu (variable properties) using the following relationship:

$$Nu/Nu_{cp} = (T_w/T_f)^p \tag{63}$$

In a computational fluid dynamics study, the exponent p was determined to be p=−0.03 for a constant heat flux boundary condition. The correction factor for temperature-dependent properties $(T_w/T_f)^p$ is between 0.998 and 0.999 in the experiments.

3.1.3 Reynolds Number. The Reynolds number for the flow configurations is defined by the mean nozzle outlet velocity, the hydraulic diameter, and properties at nozzle outlet temperature. The hydraulic diameter d_h is calculated with the nozzle outlet cross section A to $d_h = 2\sqrt{A/\pi}$.

3.2 Sample Measurements

3.2.1 Symmetric Cooling Configuration. Figure 14 shows a heat transfer distribution with a six-nozzle symmetric window-cooling configuration. The lower window edge is assigned a value of zero because no measurement is possible there. As the thermography camera field of view is limited and the measurements are periodic, the plots in Fig. 14 are composed of six identical 60 deg slices. High heat transfer coefficients are observed where jets impinge, while between the jets, the heat transfer is lower. At the top of the window, a stagnation point causes only fair heat transfer.

3.2.2 Asymmetric Cooling Configuration. Figure 15 shows the heat transfer distribution of an asymmetric cooling configuration with 5 of the 18 nozzles simultaneously active. Due to the limited visibility, the plot is composed of three separate measurements. In contrast to the symmetric configuration, there is no stagnation point, thus enabling adequate cooling at the top of the window. While good heat transfer can be observed where the jets impinge, it is only poor on either side of this area. By sequentially switching nozzles on and off, the well-cooled region is moved around the window circumference to homogenize the heat transfer distribution [39]. The cycle duration is between 20 s and 30 s. The resulting time-averaged heat transfer distribution is shown in Fig. 16. Again, due to the limited camera field of view and the observed periodicity, the plot is composed of six identical 60 deg slices. The circular heat transfer distribution at the top of the window is due to measurement uncertainties caused by strong varia-
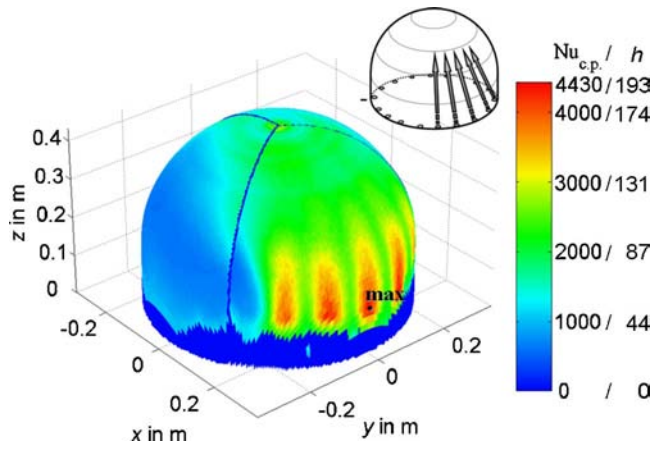
Fig. 15 Heat transfer with asymmetric air-jet cooling (5 of 18 slot-type nozzles; d_h=0.0159 m; ϑ=0 deg; φ=0 deg; $\dot{V}_0$ =245 m³/h; w=68 m/s; Re=65,800; h in W/m² K (25°C)). Nonpulsating cooling ($T_{rot}=\infty$).

Fig. 16 Heat transfer distribution with asymmetric air-jet cooling. Pulsating cooling (T_{rot}=22 s; for other parameters, see Fig. 15).

tions in quartz glass substrate thickness. Due to these strong gradients, the performed thickness correction was not successful there (7.6% of the total surface).

3.2.3 Comparison to Stationary Measurement. The right-hand plot in Fig. 14 shows the heat transfer distribution of the six-nozzle symmetric cooling configuration measured with the stationary method. As the measurement setup was not designed for a stationary method, some approximate assumptions had to be made. The heating power was assumed to be homogeneously distributed over the window surface. The penetrating heat flux was calculated by the electric heating power minus losses divided by the window area. The fluid temperature was measured right before the nozzle outlet and was assumed to be constant over the length of the window curve for calculation of the heat transfer coefficient. Neither the fluid temperature rise by upstream heating nor the change in fluid temperature due to air entrainment was considered. However, in most stationary measurements done, the air heated by the blowers significantly cooled over the curve length by the entrainment of cool ambient air leading to prohibitive measurement uncertainties (some over 100%). In addition to the high uncertainty in the heat flux and fluid temperature, the stationary measurements done with the setup designed for periodic-transient methods suffered from uncertainties in window temperature measurement by quantitative thermography.

By in situ calibration of the thermography system, calibration of the fluid temperature thermocouple, and the choice of a low-mass-flow cooling configuration with minimal air heating by the blowers, the heat transfer measurement uncertainty could be reduced to approximately 15% for the stationary measurement presented here. This stationary measurement compares reasonably well with the periodic-transient measurement.

The results performed with the periodic-transient and the stationary methods are in good agreement within the uncertainty of their measurement. The mean deviation of the local heat transfer is only about 6.3% and the peak deviation is about 15.8%, compared to the periodic-transient measurement. The deviation of the surface-averaged heat transfer is only 3.1%.

In contrast to stationary measurement methods, the periodic-transient method has the advantage of a simple heating device, which need not provide a uniform heat flux, and avoids quantitative measurements of surface and fluid temperatures. It can therefore facilitate spatially resolved heat transfer measurements, particularly for two-dimensional curved surfaces.
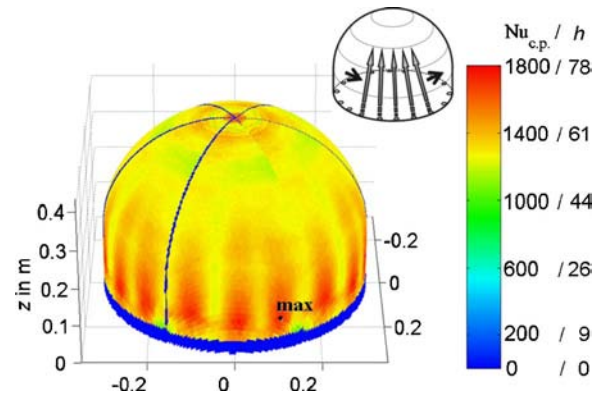
3.3 Verification of Assumptions

3.3.1 One-Dimensional Problem Without Lateral Heat Flows. Heat flows perpendicular to the radial direction (lateral heat flows) are assumed to be negligible in the derivation in Sec. 2. In the periodic-transient measurement, mean heat flows do not play a role. Only heat flows that vary over time are important. A detailed analysis showed that neglecting lateral heat flows is a very good assumption in areas with low and medium heat transfer gradients. In areas with higher gradients, the assumption has a slightly diffusing effect on heat transfer distribution. In Ref. [40], these effects were examined for a configuration with heat transfer gradients up to 3 W/(m² K mm). On 50% of the surface, the uncertainty due to this assumption is less than 1.1%; on 90% of the surface, it is less than 8.9%. The maximum uncertainty is 21.0%; the mean uncertainty is 3.5%. If a more accurate measurement of high heat transfer gradients is desired, a correction based on numerical methods may be applied. However, such correction was not required for the window-cooling application.

3.3.2 Constant Physical Properties Over Wall Thickness. For the solution of the transient heat conduction problem, constant physical properties of the substrate were assumed. In Ref. [40], it was shown that the changes in relevant physical properties due to varying temperatures are less than 1% and are therefore negligible.

3.3.3 Constant Fluid Temperature Over Time. The fluid temperature variation over time at a point P, defined as $\hat{T}_f(L_P,t)$ in this analysis, is assumed to be zero. However, in the experiment, the fluid temperature varies both with position and time. The variation is caused by periodic heating of the upstream fluid flow. Using the periodic-transient measurement technique, fluid temperature dependence on position need not be accounted for. Nevertheless, fluid temperature variation over time reduces the heat transfer coefficient measured in comparison to the actual. The reason for this behavior is that the fluid temperature increases with rising wall temperature and decreases with falling wall temperature. This has the same effect on the transferred heat as if the heat transfer coefficient was smaller than the actual. The reduction of the heat transfer measured compared to the actual is discussed in detail for a specific configuration in Ref. [40]. The fluid temperature amplitude is less than 0.1 K; the averaged substrate temperature amplitude is between 0.7 K and 2.4 K. The relative error in the heat transfer coefficient arises at positions with low substrate temperature amplitudes (i.e., for high heat transfer coefficients) and high fluid temperature amplitudes (i.e., for high curve length coordinates). However, it is increased less than 4% on 50% of the measurement surface due to the fluctuating fluid temperature. The maximum increase in the relative error is 6.5%.

Table 8 Quantities and their standard uncertainties

Quantity x_i	Type	Uncertainty	Remarks
Uncertainties in physical properties of substrate			
Density ρ	sys.	±0.1%	Estimated uncertainties in manufacturer's
Specific heat capacity c_p	sys.	±1.1%	data and uncertainties due to temperature gradient over
Thermal conductivity λ	sys.	±0.8%	substrate thickness
Uncertainties in substrate thickness			
Thickness Δr	stat.	±0.8%	Thickness measured because of
Thickness Δr	sys.	±0.6%	wide variation in surface thickness
Uncertainty in heating frequency			
Frequency ω	sys.	±0.1%	Uncertainty in heating frequency
Uncertainties in phase shift $\varphi(<0)$			
Measured phase shift φ_{meas}	stat.	±0.42 deg	Uncertainty varies over measurement surface (mean: ±0.42 deg; min: ±0.05 deg; max: ±1.08 deg [40])
Heating correction $\varphi_{\text{corr,heat}}$	sys.	±0.27 deg	Uncertainty in the correction of heating phase shift (Fig. 11)
Paint correction $\varphi_{\text{corr,paint}}$	sys.	±0.10 deg	Uncertainty in the correction of paint phase shift
Clock synchronization	sys.	$<±0.1$ deg	Clock synchronization error between DAS and thermography unit
Uncertainty by lateral heat flows (one dimensional assumption)			
Additional uncertainty in h^*	stat	±3.5%	Mean value of example in Ref. [40]
Uncertainty by nonconstant fluid temperature			
Boundary condition fluid temperature	sys.	+3.6%	Mean value of example in Ref. [40] Relative uncertainty defined as $\hat{T}_f(t)/[\hat{T}_w(r=r_1,t)-\hat{T}_f(t)]$
Uncertainty by radiation correction			
Radiative heat transfer coefficient h_{rad}	sys.	±1.7%	Uncertainty in the calculation of radiative heat transfer coefficient

3.4 Uncertainty Estimation. The uncertainty of periodic-transient measurements is influenced by uncertainties in the physical properties (ρ, c_p, λ), substrate thickness Δr, heating angular frequency ω, and phase shift φ. The uncertainties are increased by lateral heat flows, the nonconstant fluid temperature, and the radiation correction. Table 8 gives an overview of the absolute $(u(x_i))$ and relative $(u(x_i)/(x_i))$ standard uncertainties. In this paper, uncertainties are classified as statistical (stat.) if they are reduced by spatial averaging over several pixels. If reduction by averaging is not possible, the uncertainties are classified as systematic (sys.).

For the substrate thickness correction, it is assumed that the thickness projection on the thermography pixels is only correct up to two pixels. This causes a statistical thickness uncertainty of ±0.8%. The systematic uncertainty of the thickness measurement is ±0.6%. The sensitivity of the total measurement uncertainty to individual components is shown in Table 9. Assuming that the seven systematic uncertainties are not correlated and partially compensate for each other, the uncertainty is propagated as follows:

$$\frac{u(h_{\text{sq}})}{h} = \pm \sqrt{\left[\frac{\partial h}{\partial \rho}\frac{u(\rho)}{h}\right]^2 + \left[\frac{\partial h}{\partial c_p}\frac{u(c_p)}{h}\right]^2 + \left[\frac{\partial h}{\partial \lambda}\frac{u(\lambda)}{h}\right]^2 + \left[\frac{\partial h}{\partial \Delta r}\frac{u(\Delta r_{\text{sys}})}{h}\right]^2 + \left[\frac{\partial h}{\partial \omega}\frac{u(\omega)}{h}\right]^2 + \left[\frac{\partial h}{\partial \varphi}\frac{u(\varphi_{\text{sys}})}{h}\right]^2 + \left[1\frac{u(h_{\text{rad}})}{h}\right]^2} \quad (64)$$

The uncertainty due to the nonconstant fluid temperature only has an effect in one direction and so is only added linearly,

$$\frac{u(h_{\text{sys}})}{h} = \pm \frac{u(h_{\text{sq}})}{h} + \frac{u(h_{T_f \neq \text{const}})}{h} \quad (65)$$

The (statistical) uncertainty is

$$\frac{u(h_{\text{stat}})}{h} = \pm \sqrt{\left[\frac{\partial h}{\partial \Delta r}\frac{u(\Delta r_{\text{stat}})}{h}\right]^2 + \left[\frac{\partial h}{\partial \varphi}\frac{u(\varphi_{\text{stat}})}{h}\right]^2 + \left[1\frac{u(h_{\text{lat}})}{h}\right]^2} \quad (66)$$

Then, the relative combined standard uncertainty results in

Table 9 Relative measurement uncertainty of local convective heat transfer coefficient h subdivided into its components ($\pm \partial h / \partial x_i \cdot u(x_i)/h$)

Quantity x_i	$h=10$ W/(m² K)		$h=200$ W/(m² K)	
	sys.	stat.	sys.	stat.
Density ρ	±0.1%	—	±0.1%	—
Specific heat capacity c_p	±2.0%	—	±1.5%	—
Thermal conductivity λ	±0.2%	—	±0.3%	—
Glass thickness Δr	±1.3%	±1.7%	±1.1%	±1.5%
Angular frequency ω	±0.2%	—	±0.1%	—
Phase shift φ	±2.9%	±4.2%	±2.4%	±3.4%
Uncertainty lateral heat flows[a]	—	±5.7%	—	±3.6%
Heat transfer coefficient h_{rad}	±1.0%	—	± <0.1%	—
$u(h_{sq})/h$	±3.9%	±7.3%	±3.0%	±5.2%
$u(h_{Tf\neq const})/h$[a]	+5.9%	—	+3.7%	—
Relative sys./stat. uncertainty $u(h_{sys/stat})/h$	+2.0 to +9.8%	±7.3%	+0.7 to +6.7%	±5.2%
Relative, combined standard uncertainty $u_c^*(h)/h$	−2.4 to +14.1%		−2.3 to +9.7%,	

[a]Mean value of example in Ref. [40]

$$\frac{u_c^*(h)}{h} = + \frac{u(h_{Tf\neq const})}{h} \pm \sqrt{\left[\frac{u(h_{sq})}{h}\right]^2 + \left[\frac{u(h_{stat})}{h}\right]^2} \quad (67)$$

The relative measurement uncertainty of the local convective heat transfer coefficient h ranges from −2.4% to +14.1% for $h=10$ W/(m² K), and from −2.3% to +9.7% for $h=200$ W/(m² K).

By averaging N local heat transfer coefficients, the statistical uncertainty decreases by a factor of $1/\sqrt{N}$. For $N>200$, the statistical uncertainty is no longer significant. In that case, the relative measurement uncertainty of the mean convective heat transfer coefficient h_m ranges from +2.0% to +9.8% for $h_m=10$ W/(m² K) and from +0.7% to +6.7% for $h_m=200$ W/(m² K). The uncertainty margins are asymmetric to zero due to the varying fluid temperature over time (see Sec. 3.3.3). By correcting for the lateral heat flow, the periodic transient measurement uncertainty can be further reduced.

Figure 17 shows the uncertainty margin for heat transfer coefficients between 10 W/(m² K) and 200 W/(m² K). The gray area is for local heat transfer coefficients (systematic and statistical uncertainties), while the hatched area is for the mean heat transfer coefficients ($N>200$, systematic uncertainties only). A characteristic of the periodic-transient method is that the relative uncertainties have the same magnitude for both high and low heat transfers. A relative uncertainty rises because of radiation correction due to the decreased denominator only at very low heat transfer coefficients. In contrast to this, stationary methods usually show a strong increase in measurement uncertainty due to lower temperature differences at higher heat transfer coefficients.

4 Conclusion

In the field of the spatially resolved heat transfer measurement, periodic-transient methods offer many advantages, especially if applied to two-dimensional curved surfaces. In contrast to stationary methods, neither uniform heating of the measurement surface nor quantitative determination of the substrate or fluid temperature is required. As a consequence, simpler heating devices can be used and time-consuming calibration of temperature sensors and thermography unit can be avoided.

In the periodic-transient method described, the substrate is excited by a sinusoidal modulated heat flux. The heat transfer coefficient can be calculated by evaluating the phase shift between the penetrating heat flux and the resulting substrate temperature signal. Analytical equations for a flat-plate and a hollow-sphere substrate are derived.

The periodic-transient measurement method was further developed into an accurate high-resolution measurement technique. The proper operation of a simple, low-cost heating system made of commercial lamps (light bulbs) was demonstrated. A procedure for finding the transient penetrating heat flux signal from the applied heat flux by evaluating the measured surface temperature amplitude is described. This heating characterization is crucial for a correct application of the method and need to be done only once during measurement setup. The substrate temperature is measured nonintrusively by a thermography unit. The new measurement method was successfully applied to measure the heat flux distribution of a multiple-air-jet-cooled solar receiver window.

It was shown that the measurement uncertainty remains small both for high and low heat transfer coefficients. The relative measurement uncertainty of the local convective heat transfer coefficient ranges from −2.4% to +14.1% for $h=10$ W/(m² K), and from −2.3% to +9.7% for $h=200$ W/(m² K). The uncertainty of the spatially averaged heat transfer coefficient h_m is between +2.0% and +9.8% for $h_m=10$ W/(m² K) and between +0.7% and +6.7% for $h_m=200$ W/(m² K). Due to the varying fluid tempera-
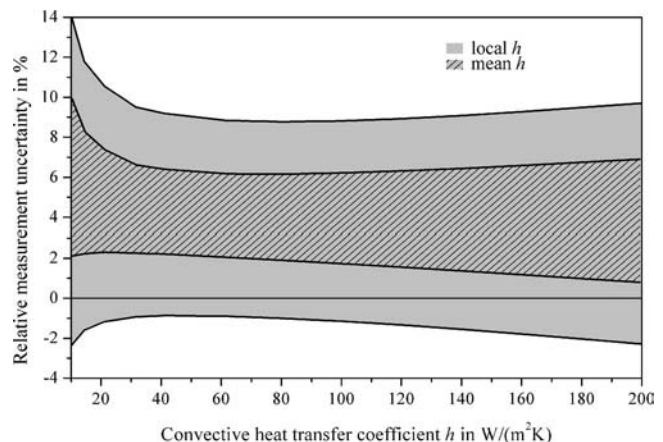

Fig. 17 Relative measurement uncertainty of convective heat transfer coefficient

ture over time, the uncertainty margins are asymmetric to zero. A further reduction in measurement uncertainty is possible with correction for lateral heat flow.

The air-jet cooling application verifies that the presented periodic-transient technique complements established techniques for a high-resolution, accurate heat transfer measurement on two-dimensional curved surfaces.

Acknowledgment

Nomenclature

A = nozzle cross section (mm^2)
$A(\omega)$ = amplitude response $(-)$
A, B = coefficients in Eq. (31), points on cooled surface $(-)$
a = thermal diffusivity (m^2/s)
Bi = Biot number $\text{Bi}=h^*\delta/\lambda$ or $\text{Bi}=h^*\Delta r/\lambda$ $(-)$
c = variable in Eq. (47) $(-)$
c_p = specific heat capacity (J/kg K)
d = diameter (m)
d_h = hydraulic diameter $d_h=2\sqrt{A/\pi}$ (m)
Fo = Fourier number $(-)$
f = frequency (1/s)
G = transfer function, frequency response $(-)$
h = convective heat transfer coefficient $(\text{W}/\text{m}^2\,\text{K})$
h^* = measured heat transfer coefficient (convective and radiative, $\text{W}/\text{m}^2\,\text{K}$)
i = complex number $\sqrt{-1}$ $(-)$
k = period number, $k=1,\dots,\infty$ $(-)$
L = curve length coordinate (m)
$\dot{M}_0$ = nozzle mass flow rate of all active nozzles (kg/s)
N = number of heat transfer coefficient to average
Nu = Nusselt number $\text{Nu}=hL_{\max}/\lambda$ $(-)$
P_{el} = electric heating power (W)
p = exponent in Eq. (63) $(-)$
p, p' = variables in Eqs. (32) and (44) $(-)$
$\dot{Q}$ = heat flow rate (W)
$\dot{q}$ = heat flux rate (W/m^2)
Re = Reynolds number $\text{Re}=\rho w d_h/\eta$ $(-)$
R = entrainment quotient; ratio of total jet mass flow to nozzle mass flow $(-)$
Re = Reynolds number $\text{Re}=\rho w d_h/\eta$ $(-)$
r = radial coordinate (m)
r^2 = coefficient of determination $(-)$
s = parameter of Laplace transform (s^{-1})
T = temperature $(°\text{C})$
T_{per} = cycle duration of heating modulation (s)
T_{rot} = cycle duration of mass flow modulation (s)
t = time (s)
u = standard uncertainty
$\dot{V}$ = volume flow rate (m^3/h)
w = mean nozzle exit velocity (m/s)
$X_{in/out}$ = dimensionless input/output signal $(-)$
x, y, z = Cartesian coordinate (m)

Greek Symbols

γ = dimensionless number $\gamma=h^*\sqrt{t}/\sqrt{\rho c_p\lambda}$ $(-)$
Δ = difference
δ = substrate thickness (m)

η = dynamic viscosity (kg/m s)
θ = dimensionless temperature $(-)$
ϑ = Laplace transformed dimensionless temperature $(-)$
ϑ_i = orientation polar angle of nozzle i (deg)
ϑ^* = dimensionless substitution parameter, $\vartheta^*=\vartheta r^+$ $(-)$
λ = thermal conductivity (W/m K)
μ = eigenvalue in Eqs. (3) and (4) $(-)$
ρ = density (kg/m^3)
σ = standard deviation
τ = time constant (s)
ϕ_i = position azimuth angle of nozzle i (deg)
φ = phase response, phase shift, phase angle (deg)
φ_i = orientation azimuth angle of nozzle i (deg)
ω = angular frequency (s^{-1})

Subscripts and Superscripts

A, B = points on cooled surface
ad = adiabatic
amb = ambient
c = combined
conv = convective
cp = constant properties
corr, heat = heating correction
corr, paint = paint correction
f = fluid
heat = heating
IR = infrared radiation
in = penetrating, input
inc = incident
lat = lateral
m = mean
max = maximum
meas = measured
noz = nozzle
out = outgoing, output
P = at point P
rad = radiative
sq = root of sum of squared values
stat = statistical
sys = systematic
$Tf \neq$ const = nonconstant fluid temperature
vis = visible radiation
w = wall
$+$ = dimensionless
0 = initial
$-$ = mean value
$\hat{}$ = time-dependent value

References

[1] Childs, P. R. N., Greenwood, J. R., and Long, C. A., 1999, "Heat Flux Measurement Techniques," Proc. Inst. Mech. Eng., Part C: J. Mech. Eng. Sci., **213**(7), pp. 655–677.
[2] Diller, T. E., 1993, "Advances in Heat Flux Measurements," *Advances in Heat Transfer*, Academic, New York, Vol. 23, pp. 279–368.
[3] Moffat, R. J., 1988, "Experimental Methods in Heat Transfer," *Experimental Heat Transfer, Fluid Mechanics, and Thermodynamics*, R. K. Shah, E. N. Ganić, and K. T. Yang, eds., Elsevier, New York, pp. 13–31.
[4] Scott, C. J., 1976, "Transient Experimental Techniques for Surface Heat Flux Rates," *Measurements in Heat Transfer*, 2nd ed., E. R. G. Eckert and R. J. Goldstein, eds., Hemisphere, Washington, DC, pp. 375–396.
[5] Lee, D. H., Chung, Y. S., and Kim, D. S., 1997, "Turbulent Flow and Heat Transfer Measurements on a Curved Surface With a Fully Developed Round Impinging Jet," Int. J. Heat Fluid Flow, **18**, pp. 160–169.
[6] Sargent, S. R., Hedlund, C. R., and Ligrani, P. M., 1998, "An Infrared Thermography Imaging System for Convective Heat Transfer Measurements in Complex Flows," Meas. Sci. Technol., **9**, pp. 1974–1981.
[7] Hofmann, H., Martin, H., and Kind, M., 2003, "Experimental Setup for Heat Transfer Measurements in Pulsating Impinging Jet Flow," *Proceedings of the International Symposium on Transient Convective Heat and Mass Transfer in Single and Two-Phase Flow*, Cesme, Turkey, Aug. 17–22.

[8] Hofmann, H., 2005, "Wärmeübergang beim pulsierenden Prallstrahl," Ph.D. thesis, Universität Karlsruhe (TH), Universitätsverlag Karlsruhe.

[9] Baehr, H. D., and Stephan, K., 1996, "Wärme- und Stoffübertragung," 2nd ed., Springer-Verlag, Berlin.

[10] Ångström, A. J., 1861, "Neue Methode, das Wärmeleitungsvermögen der Körper zu bestimmen," Ann. Phys. Chem., **114**(12), pp. 513–530.

[11] Baughn, J. W., Anderson, M. R., Mayhew, J. E., and Butler, R. J., 1997, "A Periodic Transient Method Using Liquid Crystals for the Measurement of Local Heat Transfer Coefficients," *Proceedings of the ASME Heat Transfer Division*, ASME, New York, HTD-Vol. 353, pp. 73–80.

[12] Kosky, P. G., Maylotte, D. H., and Gallo, J. P., 1999, "Ångström Methods Applied to Simultaneous Measurements of Thermal Diffusivity and Heat Transfer Coefficents: Part, 1, Theory," Int. Commun. Heat Mass Transfer, **26**(8), pp. 1051–1059.

[13] Kosky, P. G., Maylotte, D. H., and Gallo, J. P., 1999, "Ångström Methods Applied to Simultaneous Measurements of Thermal Diffusivity and Heat Transfer Coefficents: Part, 2, Experimental," Int. Commun. Heat Mass Transfer, **26**(8), pp. 1061–1068.

[14] Roetzel, W., Prinzen, S., and Wandelt, M., 1993, "Temperature Oscillation Technique for Determination of Local Convective Heat Transfer Coefficients Without Fluid Temperature Measurement," Chem. Eng. Technol., **16**, pp. 89–93.

[15] Prinzen, S., 1991, "Experimentelle Bestimmung örtlicher Wärmeübergangskoeffizienten mittels Temperaturschwingungen der Wand," Fortschritt-Berichte, VDI, Reihe, 19, Nr. 51.

[16] Carlomagno, G. M., and De Lucca, L, 1989, "Infrared Thermography in Heat Transfer," *Handbook of Flow Visualization*, W. J. Yang, ed., Hemisphere, Washington, DC, pp. 531–553.

[17] Anderson, M. R., and Baughn, J. W., 2005, "Liquid Crystal Thermography: Illumination Spectral Effects. Part 1-Experiments," ASME J. Eng. Gas Turbines Power, **127**(5), pp. 581–587.

[18] Anderson, M. R., and Baughn, J. W., 2005, "Thermochromic Liquid Crystal Thermography: Illumination Spectral Effects. Part 2-Theory," ASME J. Eng. Gas Turbines Power, **127**(5), pp. 588–597.

[19] Campbell, R. P., and Molezzi, M. J., 1996, "Applications of Advanced Liquid Crystal Video Thermography to Turbine Cooling Passage Heat Transfer Measurement," GE Research & Development Center, Technical Information Series No. 96CRD036.

[20] Moffat, R. J., 1990, "Experimental Heat Transfer," *Heat Transfer*, G. Hestroni, ed., Hemisphere, Washington, DC, Vol. 1, pp. 187–205.

[21] Fiebig, M., and Schulz, K., 1999, "Ammonia Absorption Method and Liquid Crystal Thermography for Accurate Local Mass and Heat Transfer Measurements," *Applied Optical Measurements*, M. Lehner and D. Mewes, eds., Springer-Verlag, Berlin, pp. 19–33.

[22] Kottke, V., and Schmidt, K.-G, 1985, "Measuring Techniques for Determination of Local Mass and Heat Transfer in Industrial Scale," *Measurement Techniques in Heat and Mass Transfer*, R. I. Soloukhin and N. H. Afgan, eds., Hemisphere, Washington, DC, pp. 325–335.

[23] Schlünder, E. U., and Gnielinsky, V., 1967, "Wärme- und Stoffübertragung zwischen Gut und aufprallendem Düsenstrahl," Chem.-Ing.-Tech., **39**(9/10), pp. 578–584.

[24] Goldstein, R. J., and Cho, H. H., 1995, "A Review of Mass Transfer Measurements Using Naphthalene Sublimation," Exp. Therm. Fluid Sci., **10**, pp. 416–434.

[25] Röger, M., Buck, R., and Müller-Steinhagen, H., 2005, "Numerical and Experimental Investigation of a Multiple Air Jet Cooling System for Application in a Solar Thermal Receiver," ASME J. Heat Transfer, **127**(8), pp. 863–876.

[26] Röger, M., Pfänder, M., and Buck, R., 2006, "Multiple Air-Jet Window Cooling for High-Temperature Pressurized Volumetric Receivers: Testing, Evaluation, and Modeling," ASME J. Sol. Energy Eng., **128**(3), pp. 265–274.

[27] Röger, M., 2006, "Verfahren und Vorrichtung zur ortsaufgelösten Bestimmung des Wärmeübergangskoeffizienten an einem Messgegenstand," German Patent No. 102004026520.

[28] Mandelis, A., 2001, *Diffusion-Wave Fields: Mathematical Methods and Green's functions*, Springer, New York.

[29] Mandelis, A., 2000, "Diffusion Waves and their Uses," Phys. Today, **53**(8), 29–34.

[30] Tautz, H., 1971, *Wärmeleitung und Temperaturausgleich*, Chemie, Weinheim/Bergstr.

[31] Doetsch, G., 1970, *Einführung in Theorie und Anwendung der Laplace-Transformation*, 2nd ed., Birkhäuser, Basel, Stuttgart.

[32] Heraeus Quarzschmelze, 1985, *Quarzglas und Quarzgut*, Heraeus Quarzschmelze GmbH, Hanau, Germany.

[33] Omega, 2003, Omega Engineering, Inc. Calibration Report No. HFS-4.

[34] Omega, 2001, User's Guide Thin Film Heat Flux Sensor HFS-1, HFS-2, HFS-3, HFS-4, Omega Engineering, Inc., Stamford, USA.

[35] 3M, 1998, 3M 467MP, 467MPF, 468MP Klebstoff-Filme ohne Träger, Product information 08/98, 3M Deutschland GmbH, Neuss.

[36] Goratec, Manual Thermgraphy Camera TVS-2000 Series (in German), GORATEC Technology GmbH & Co KG, Erding, Germany.

[37] Schlichting, H., and Gersten, K., 1997, *Grenzschicht-Theorie*, 9th ed., Springer-Verlag, Berlin.

[38] Herwig, H., 1985, "Asymptotische Theorie zur Erfassung des Einflusses variabler Stoffwerte auf Impuls- und Wärmeübertragung," Fortschritt-Berichte VDI, Reihe, 7, Nr. 93.

[39] Röger, M., and Uhlig, R., 2005, "Cooling Device for Curved Window Subjected to Radiation, Solar Receiver and Process for Cooling a Curved Window," European Patent No. EP 1598608 A2.

[40] Röger, M., 2005, "Fensterkühlung für solare Hochtemperatur-Receiver," Fortschritt-Berichte VDI, Reihe 6, Nr. 534.

Optically Based Rapid Heat Transfer Measurements in Complex Internal Flows

Charles W. Booten[1]
e-mail: booten@alum.mit.edu

John K. Eaton
e-mail: eatonj@standard.edu

Mechanical Engineering Department,
Stanford University,
Stanford, CA 94305

An optically based technique was developed that involves fabrication of a thin-walled plastic model with laser heating applied to a small section of the outer surface. The heat flux distribution applied to the model by the laser was measured first using a short-duration, transient experiment. The external temperature distribution was then recorded using infrared thermography with steady laser heating. The measured heat flux and temperature distributions were used as thermal boundary conditions in a finite-element code to solve an inverse heat conduction problem for the heat transfer coefficient on the internal passage wall. Hydrodynamically fully developed turbulent flow in a round tube was used as a test case for the development of the new optical method. The Reynolds numbers used were 30,000 and 60,000. This flow was chosen because accurate computational tools were available to calculate the internal heat transfer coefficient for a variety of thermal boundary conditions. In addition, this geometry simplified both the model fabrication and the implementation of a finite-element model for the inverse heat conduction problem. Heat transfer coefficient measurements agreed with numerical simulations and semi-analytical solutions within 1.5% and 8.5% for the low and high Reynolds numbers, respectively. Additional simulations suggest that the method can be accurate with thermal boundary conditions more complex than in these experiments.
[DOI: 10.1115/1.2767751]

1 Introduction

This study was undertaken to develop a technique for quickly and accurately measuring heat transfer coefficients in complex internal flows. One of the primary applications of this technique is for analysis of turbine blade cooling systems. These blades have extremely complicated internal cooling passages, making it very difficult to measure heat transfer coefficients accurately or to predict them with computational fluid dynamics (CFD) codes. However, the full mean velocity field can be acquired in a short time using magnetic resonance velocimetry as demonstrated by Elkins et al.[1]. Experimental techniques are necessary that can provide cooling-passage designers with heat transfer coefficients on real geometries within a design-cycle time frame. The data from this technique also must be useful for benchmarking CFD codes to improve numerical heat transfer predictions.

The measurement concept involves steady-state laser heating of a thin-walled plastic model with a measured heat flux distribution applied to a section of the surface. The external temperature distribution on the model is then measured using infrared thermography. These measured quantities are used as thermal boundary conditions in a finite-element code to solve an inverse heat conduction problem for the heat transfer coefficient on the internal passage wall.

Some of the original work on numerical solutions of inverse heat conduction problems (IHCPs) was done by Beck [2]. The majority of the subsequent work in this area focuses on the stability of solving transient problems within this basic framework as in Ref. [3–5]. The focus on transient solutions is due to the nature of measurement techniques that often lead to ill-posed heat transfer problems. Typically, a material is heated transiently from one

surface and a point measurement device records the temperature at a different location. The heat flux and/or temperature distribution on another surface is inferred using IHCP solution techniques.

A steady-state experimental technique is preferable so the test apparatus can be as simple as possible. Some work has been done on the analysis of steady-state IHCPs, particularly in a hollow cylinder, by Yang et al. [6]. They constructed the problem solution utilizing the knowledge of the geometry to simplify the method. Extending that technique to complex geometries would be difficult. The current solution technique, based on the use of a commercial FEA code, can be viewed as a practical method to solve the IHCP in more generic geometries.

There has been work in applying IHCP transient solution techniques to gas-turbine cooling research. Nirmalan et al. [7] used a transient IHCP solution technique for determining the Nusselt number inside turbine cooling passages. The model was allowed to come to equilibrium at a uniform temperature and then the inlet air temperature was abruptly heated to induce the thermal transient that was recorded on the outside surface using an infrared camera. An initial estimate of the heat transfer coefficient on the inside of the passages was used along with the measured external surface temperature distribution to solve for the temperature in the wall numerically. A commercial finite-element code (ANSYS) was used to solve the problem. The heat transfer coefficient was then updated using an algorithm that takes into account the difference between the measured and calculated temperatures.

Bunker [8] used this method, referred to by the author as thermal inertia heat transfer coefficient (HTC), on a generic turbine blade cooling passage that used a latticework structure rather than turbulators for heat transfer enhancement. The initial guess for h was based on the assumption of one-dimensional conduction through the channel wall. The author did not attempt to quantify the heat transfer coefficients in the latticework, instead the overall effect of the latticework was characterized using a fin effectiveness.
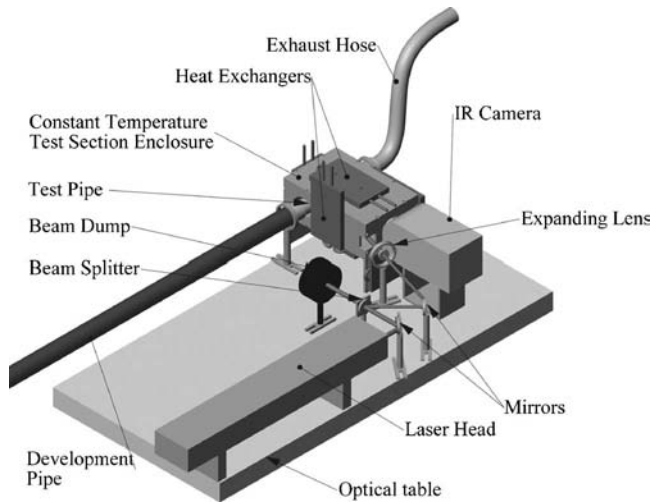
Fig. 1 Infrared thermography experimental apparatus

Fig. 2 Copper calibrator

Freund et al. [9] have used temperature oscillation infrared thermography measurements as boundary conditions to solve an IHCP. They measure h on a flat surface with impinging jets using a laser to supply a periodic heat flux and an infrared camera to measure surface temperature. This method uses the phase shift between the applied laser heat flux and surface temperature measurements on one surface to determine h on the opposing surface that has the impinging jets. They achieved agreement within 10–25% of traditional methods of measuring h.

This paper presents the development of an alternative, steady-state technique that may be simpler to implement for routine measurements during design cycles. Hydrodynamically fully developed turbulent flow in a round tube was used as a test case during the development of the new method. This flow was chosen because accurate computational tools are available to calculate the internal heat transfer coefficient for a variety of thermal boundary conditions.

2 Equipment and Procedures

A schematic of the experimental setup is given in Fig. 1. The flow enters at the left through the hydrodynamic development pipe. The mass flow was measured upstream of the pipe using a Meriam 50MH10-4T laminar flow meter with an uncertainty of $\pm 1 \times 10-4$ kg/s. The inlet air temperature to the test section was measured using a thermocouple mounted flush with the inside wall of the pipe with an uncertainty of $\pm 0.1 \,^{\circ}C$. All of the instrumentation and measurements for the flow up to the end of the development pipe are described in greater detail by Booten and Eaton [10]. The test section, comprised of a thin-walled PVC tube, was connected to the development pipe at its inlet and to a flexible exhaust hose at its outlet. The infrared camera was pointed directly at the center of the test section. The CO_2 laser and its associated optical components directed a high-power infrared laser beam onto the surface.

The entire test section was mounted inside an actively cooled, uniform temperature enclosure to minimize the effects of background radiation on the infrared temperature measurements. The enclosure walls were 6.4 mm thick aluminum plates to minimize temperature nonuniformity. The entire enclosure was held at $20\,^{\circ}C \pm 1\,^{\circ}C$.

2.1 Test Section. The test section was made from a section of PVC pipe because the thermal characteristics are similar to the stereolithography resins that will likely be used to fabricate more complex models. The inner diameter of the pipe was bored to the same diameter as the development pipe (32.8 mm) and the outer diameter was turned to 36.8 mm, giving a wall thickness of
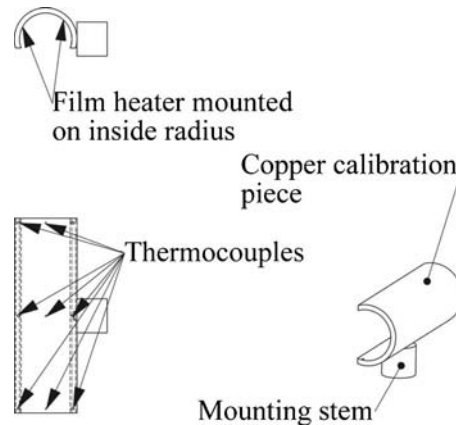
2.0 mm. The thin wall minimizes lateral conduction. An even thinner wall could have been produced easily for the cylindrical geometry, however, that would leave some doubt as to how well this technique would work in more complex shapes fabricated using stereolithography. An important point to note is that there is no temperature measurement or other instrumentation attached to the test model.

The exterior surface of the model was painted with Krylon 1602 ultraflat black spray paint to maximize absorbance of the laser beam heat source and to ensure uniform emissivity for temperature measurement. This paint has tabulated data on the spectral reflectivity for an incidence angle of 30 deg in Touloukian et al. [11]. It is approximately 0.014 for a 10.6 μm wavelength at the temperatures in this study. If the transmissivity is assumed to be zero, the absorbance is 0.986. The majority of the beam power was at a lower incidence angle than 30 deg and so the absorbance was conservatively considered constant at that value.

2.2 IR Camera and Calibration. The temperature distribution on the pipe outer surface was measured using an Indigo Systems Merlin MWIR infrared camera with a 256×256 charge coupled device (CCD) array sensitive in the $3-5$ μm wavelength range. It was not sensitive at 10.6 μm wavelength; therefore, reflected power from the laser did not interfere with temperature measurements. The optical magnification was set such that each camera pixel corresponded approximately to a 0.22 mm^2 on the pipe surface. The camera measured infrared light intensity at each pixel and therefore required calibration for the particular emissivity and geometry to measure the surface temperature distribution.

The simplest way to accomplish this was to replace the test section with a temperature controlled surface that had the identical geometry and emissivity as the test section. A drawing of the calibration apparatus is given in Fig. 2. It was made from a thick-walled oxygen-free high conductivity (OFHC) copper pipe to ensure uniform temperature. The outer surface was painted with the same ultraflat black paint as the test section. The outer diameter was identical to that of the test model within ± 0.025 mm. The piece was slightly more than one-half of a pipe because the camera can only image one-half of the pipe surface. A film heater was placed across the inside surface of the copper so that heating was uniform. The Biot number for the calibration piece was roughly

$$\mathrm{Bi} \equiv \frac{hL_{\mathrm{ch}}}{k_{\mathrm{copper}}} = \frac{10(\mathrm{W/m^2K})0.00305(\mathrm{m})}{400(\mathrm{W/mK})} = 7.6 \times 10^{-5} \quad (1)$$

The characteristic length L_{ch} is the thickness of the copper wall in the radial direction. The heat transfer coefficient h was estimated from natural convection correlations on a heated horizontal cylinder from Mills [12]. The copper calibration piece was assumed to be isothermal as is standard for objects with $\mathrm{Bi} < 0.01$.
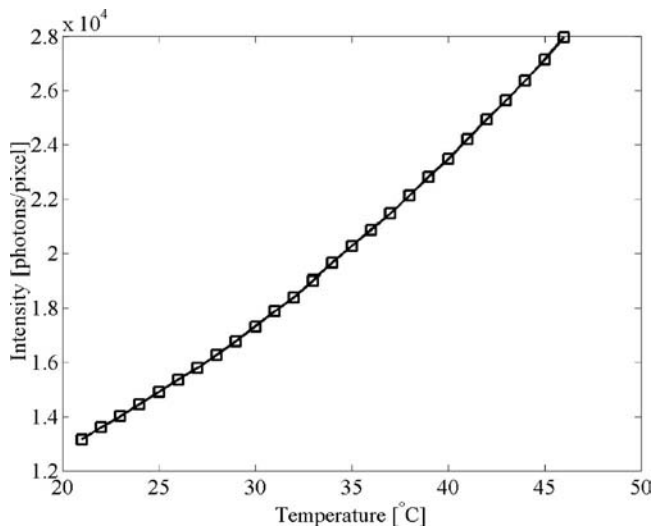
Fig. 3 Spline interpolation at the center pixel location in the copper calibrator
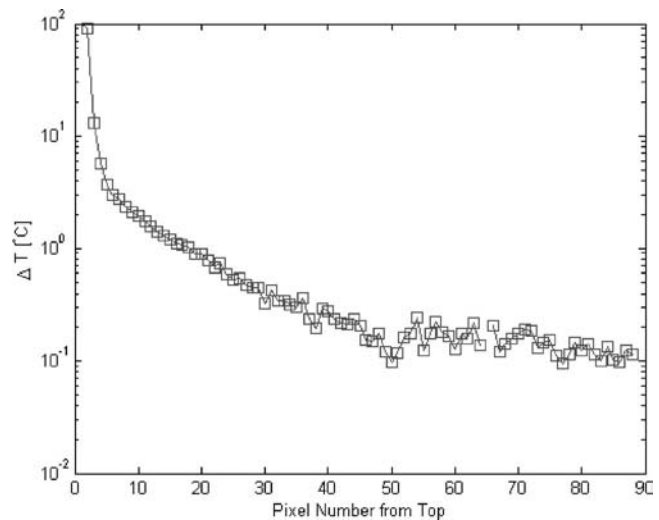

Fig. 4 Comparison of the interpolated temperature at each pixel to the interpolated temperature that would be calculated if the spline at that location were the same as the spline at the pipe centerline (i.e., normal to the CCD array). The pixels are in the middle of the image horizontally and form a vertical line from the top of the calibrator (pixel 0) to the centerline (pixel 90). The copper calibrator temperature was 44°C.

Careful positioning of the calibrator in the identical location as the test section was critical to the accuracy of the temperature measurements. The test piece was first positioned carefully by eye, and then the pipe was heated with a heat gun to produce a sharp contrast between the warm pipe and the cool background in the infrared images. The test piece position was adjusted until the edges were in the identical pixel locations as the calibrator. The imaged pipe diameter was checked to ensure that it was the same as the diameter of the calibrator. This procedure guaranteed that the pipe and calibrator positions were the same to within half of a pixel (~0.1 mm).

Eight 36-gauge K-type thermocouples were distributed throughout the calibrator, as shown in Fig. 2, to measure the temperature distribution. The mean temperature among the thermocouples was used in calculating the spline fits for converting pixel intensity to temperature at each pixel location. Temperature steps of approximately 1°C were used to make the spline fits. When steady state was reached, images and thermocouple readings were taken simultaneously. A total of 2000 images and 30 sets of 32-sample averages at each thermocouple were taken at each temperature step.

A sample of calibration data and a spline fit for the center pixel location in the calibration piece is given in Fig. 3. This calibration curve is similar to that from Cooper and Eaton [13] for a calibration of the same camera on a planar, black-painted calibration surface. The calibration for all other pixels looked qualitatively similar to this. Pixels that were near the top and bottom of the pipe had lower overall intensity values because of the high angle of the surface with respect to the camera.

Fabrication and calibration were time consuming because of the curved calibration surface and very tight tolerances. In more complex models, these two steps might be the time-limiting factors for this type of experiment. Therefore, it was useful to look at how sensitive the calibration was to the angle of the measured surface relative to the CCD array. Figure 4 compares the temperature difference calculated using two methods of creating spline fits. The first method was based on the mean temperature of the copper, 44°C, and the local pixel intensity. A separate spline fit was generated for each pixel location on the vertical axis. The second method used the same mean copper temperature but the intensity was for the pixel on the pipe centerline (the surface at that location was normal to the camera) so that only one spline fit was generated but was applied to pixels at every location on the vertical axis. The temperature difference obtained using these two methods is compared in the figure for all pixels along a vertical

line from the top of the pipe (pixel 0) to the centerline (pixel 90).

The difference in temperature calculated was less than 0.2°C for pixels that were less than 8 mm (40 pixels) from the centerline. This distance corresponded to an angle of 51 deg from normal to the CCD array. At angles as high as 63 deg, the difference was less than 1°C. This is encouraging because it means that accurately replicating complex external features does not significantly increase the accuracy of the calibration, as long as the incidence angles of the surface relative to the camera are moderate. Note that at higher angles the error increases dramatically; therefore, calibration at these angles does require local intensity data. It is also important to note that the full geometry calibration (first method) was used for the results presented in this paper.

2.3 Laser Heater. The heat source was a Synrad Evolution 100 CO_2 laser. It emitted at 10.6 μm wavelength and could supply up to 100 W continuously. The amount of power applied to the test section in this study was 0.11–0.17 W, corresponding to a bulk temperature rise of the fluid of 0.006–0.008°C. This power was at the extreme low end of what the laser could output, making the beam intensity quite noisy. This was remedied using a ZnSe beam splitter that reflected 3% of the beam power while operating the laser at a much higher power (>3.5 W) where it was more stable. The reflected part of the beam was used as the power source for the test section and the much larger transmitted portion was directed into a beam dump.

The optical path is shown in detail in Fig. 5. The portion of the beam reflected by the beam splitter was redirected through an expanding lens so that the nominally 4 mm diameter beam was expanded to approximately 15 mm diameter when it impinged on the surface of the test section. The expansion was necessary to input enough power into the model for a measurable temperature rise over a reasonable section of the pipe without damaging it. The angle of the beam relative to the pipe axis was approximately 70 deg, or 20 deg from normal to the pipe centerline. This angle resulted in a maximum incidence angle between the laser and the pipe of 26 deg.

2.4 Beam Power Absorption Measurement. A custom laser beam profiling system was used in the preliminary measurements to measure the beam intensity profile, but this turned out to be
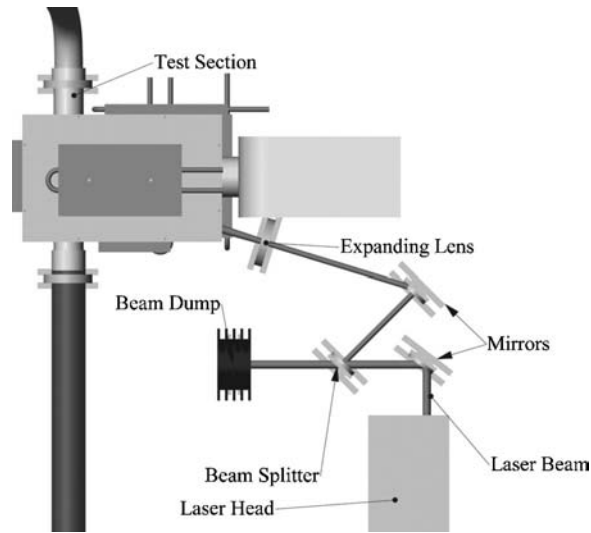
Fig. 5 Top view of optical path

Fig. 6 Beam power taken at vertical centerline of profile. Each profile was measured at a different laser power.

inadequate. What was needed was a measure of the full distribution of absorbed power on the surface of the test model. This was acquired by taking images of the pipe surface with the infrared camera during transient laser heating. The pipe was initially at room temperature, and then was impulsively exposed to laser heating. An infrared image of the pipe surface was acquired 2 s after initiation of heating. This process was repeated 30 times to get an average, transiently heated surface temperature distribution. The distribution of absorbed heat flux from the laser was assumed to be proportional to the temperature rise. This assumed linear, one-dimensional transient heating of the pipe wall. For this technique to work, the time from the laser startup to recording of the images needed to be much less than the thermal diffusion time scale t_d:

$$t_d = \frac{w^2}{\alpha} = \frac{0.002(m)^2}{1.1 \times 10^{-7}(m^2/s)} = 36 \text{ s} \qquad (2)$$

where w is the wall thickness of the pipe and α is the thermal diffusivity of PVC. The diffusion length sets the best possible spatial resolution. This length L_d is the characteristic length that heat diffuses from the time the laser was impulsively started until the profile image was recorded, t. It is given by

$$L_d = \sqrt{\alpha t} = \sqrt{1.1 \times 10^{-7}(m^2/s)2.0(s)} = 0.46 \text{ mm} \qquad (3)$$

This length is approximately 2 pixels wide and was less than the thickness of the pipe (2 mm) so that a semi-infinite body approximation was appropriate.

This transient method gives only the relative distribution of absorbed laser power. It was desirable for one laser beam profile to be used to calculate the heat flux distribution for all power settings by scaling the heat flux values from a single beam profile. This required that the relative power distribution in the beam profile not change with the laser power. Figure 6 shows the vertical beam profile slices taken through the maximum intensity portion of the beam on the surface of the test section. There were four applied laser powers (measured after the beam passed through the beam splitter) 0.12, 0.17, 0.46, and 0.78 W. The four profiles match quite well in most areas, with the three higher power profiles matching extremely well over the entire beam.

The total laser power was measured separately from the beam profile by placing a power meter just downstream of the last optical component, the expanding lens. At this location, the beam was small enough (~4 mm diameter) that the power meter could capture the entire beam.
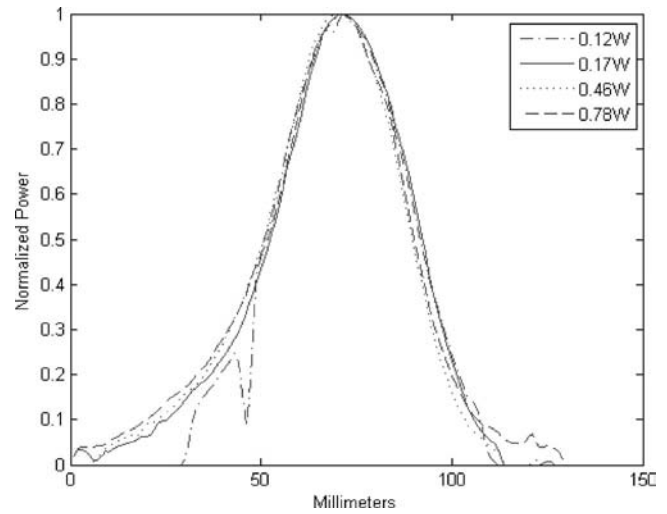
3 Inverse Heat Conduction Problem Solution

The experimental test pipe was first modeled in COMSOL, a commercial finite-element code. Only the half of the pipe viewed by the camera was modeled. The pipe wall was discretized using a 3D, unstructured mesh with a maximum element size in the wall-normal direction of less than 0.32 mm, which was 1/6th of the wall thickness and less than 1 mm in the other directions. The thermal conductivity of the pipe was assumed to be 0.18 W/m K.

The edges of the model were well away from strong temperature gradients and were considered to be adiabatic in the finite-element model. The inside of the pipe had a convective boundary condition characterized by h, which was the quantity to be measured. The external surface had a temperature boundary condition.

The present steady-state experiment avoids or reduces the severity of some of the pitfalls commonly associated with IHCP's. The analysis begins by taking the net experimental heat flux $\dot{q}''_{expt}$ and temperature T_{expt}, distributions on the outside of the geometry and importing these into the finite-element program. The measured external surface temperature and heat flux data were both filtered before being mapped to the outer surface of the model. The filter for both was a 3×3 (0.65×0.65 mm^2) Gaussian matrix with the distance from the center to the edges of the matrices being two standard deviations long. The filter was normalized so that there was no dc component added to the heat flux or temperature distributions by the filter. Additional quantities that were needed were the ambient temperature T_∞ the fluid bulk temperature T_{bulk}, and the temperature that the outside surface of the model radiates to $T_{enclosure}$. The latter can be the same as T_∞, but in this study it was at a controlled value very close to but distinct from T_∞.

If the surface temperature is fixed, the heat transfer due to radiation $\dot{q}''_{rad}$ and natural convection $\dot{q}''_{nc}$ can be considered separately from the measured laser power applied to the test section $\dot{q}''_{laser}$ and then combined to get the net, experimental surface heat flux

$$\dot{q}''_{expt}(x_o, y_o) = \dot{q}''_{laser}(x_o, y_o) + \dot{q}''_{rad}(x_o, y_o) + \dot{q}''_{nc}(x_o, y_o) \qquad (4)$$

The heat fluxes from radiation and natural convection in Eq. (4) can be estimated at each pixel location in the temperature distribution using

$$\dot{q}''_{rad}(x_o, y_o) = \epsilon\sigma[T^4_{expt}(x_o, y_o) - T^4_{enclosure}] \qquad (5)$$

$$\dot{q}''_{nc}(x_o, y_o) = \frac{k_{air}[T_{expt}(x_o, y_o) - T_\infty]}{L_{ch}} \left\{ 0.36 + \frac{0.518 Ra_{L_{ch}}^{1/4}}{[1 + (0.559/Pr)^{9/16}]^{4/9}} \right\}$$

$$(6)$$

Equation (6) is an empirical correlation for natural convection on a horizontal cylinder taken from Mills [12]. The characteristic length scale L_{ch} is taken to be the width of the laser beam rather than the pipe diameter because of the relatively small size of the heated area on the pipe. This is a significant source of uncertainty that is quantified later.

Computing h using iterative techniques requires an initial guess for h. This is obtained using experimental data assuming one-dimensional conduction radially through the pipe wall as

$$h_{guess,initial}(x_i, y_i) = \frac{1}{[T_{expt}(x_o, y_o) - T_{bulk}]/\dot{q}''_{expt}(x_o, y_o)} \quad (7)$$

where

$$R_{cond} = \frac{A_{av} \ln(r_o/r_i)}{2\pi k L} \quad (8)$$

is the radial thermal resistance in the wall and A_{av} is the surface area corresponding to the external experimental heat flux at a given location (x_o, y_o). Equation (7) relies only on geometrical parameters, material properties, and experimental data and so can be calculated before any optimization for h.

The problem was constrained by the guess for h, along with the adiabatic boundary conditions applied to the edges of the pipe and the external temperature boundary condition. The temperature distribution throughout the model was solved using COMSOL. The resulting heat flux distribution on the outside of the model was then compared to the experimentally measured heat flux distribution. The difference was used to update the guess for h using

$$h_{guess}(x_i, y_i) = h_{guess,old}(x_i, y_i) + C[\dot{q}''_{expt}(x_o, y_o) - \dot{q}''_{it}(x_o, y_o)] \quad (9)$$

where C is an arbitrary constant that allowed for more or less damping in updating h_{guess}. For the heat transfer coefficients in this study, $-0.02 \lesssim C \lesssim -0.9$ was usually sufficient, with larger values being more useful closer to convergence or if more filtering was necessary. Equation (9) is by no means the only optimization algorithm that can be used and should be considered a guideline that captures the important physics rather than a definitive formula for this type of optimization.

Note that Eq. (9) updates h_{guess} using the values on the outside of the pipe (x_o, y_o), corresponding to the same surface coordinates on the inside of the pipe (x_i, y_i). This is a convenient way to couple the exterior heat flux data to the interior heat transfer coefficient, but it is not always physically correct. There is three-dimensional conduction in the wall so that Eq. (9) is a reasonable approximation for thin-walled geometries; however, it limits the applicability of this algorithm to situations where heat transfer is predominately normal to the wall. The values of h throughout this example, and in the experiment, are strongly dependent on heat fluxes normal to the surface. Therefore, measurements of h are expected to be most accurate near the center of the heated spot where wall-normal heat fluxes dominate.

4 Results

The experiment was performed at Reynolds numbers of 30,000 and 60,000, corresponding to bulk velocities of approximately 14.3 and 28.6 m/s, respectively. The bulk flow and ambient temperatures were in the range of 20–23 °C. The maximum heat flux applied to the surface of the model was approximately 1300 W/m².

A typical image of the pixel intensity when recording beam absorption profiles for an applied power of 0.12 W is given in Fig. 7. This image was acquired 0.4 s after the beam was turned on. The "dead" pixels in the camera show up as white dots randomly
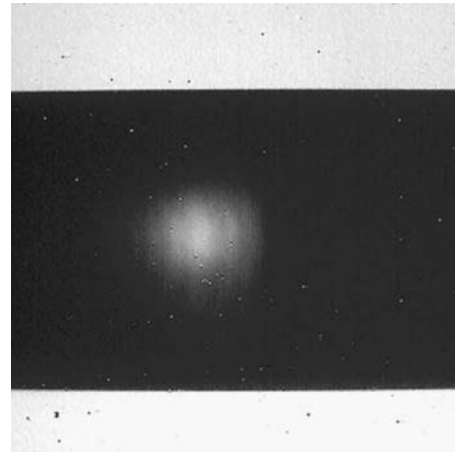

Fig. 7 Single image of beam profile intensity at 0.12 W power applied. Randomly distributed, single, white pixels are dead pixels and do not represent the laser beam. The dark background is the unheated area of the pipe, and the gray, background is the wall behind the pipe. Flow in the pipe is left to right.

distributed throughout the image. The most obvious feature is the non-Gaussian profile. The low intensity regions of the beam are clearly visible and extend far beyond the core of the beam to the left and bottom of the image. The stripes that occur are diffraction patterns resulting from the apertures used to block a satellite beam generated by the square cross section of the CO_2 laser cavity. While it was desirable to eliminate as much nonuniformity in the beam as possible, accurate knowledge of the beam was more important for calculating h than having a clean, Gaussian profile. The pixel intensity recorded in Fig. 7 was converted to temperature and then normalized by the total measured power input of the laser to get the power distribution over the surface of the pipe.

4.1 Thresholding and Filtering. The measured beam profile required processing to eliminate noise. The beam profile test was repeated 30 times and the resulting temperature distributions were averaged. A threshold and Gaussian filter were then applied to the average beam profile.

The image was first filtered using a 3×3 (0.65×0.65 mm) Gaussian kernel. Then a threshold level was set at 3% of the maximum value. This level was chosen to eliminate background noise without significantly reducing the size of the beam profile. The diffraction patterns were not attenuated significantly from Fig. 7. The overall shape of the beam and the high intensity region were very close to the raw image, while dead pixels and noise were largely eliminated. A larger filter matrix would easily smooth the beam profile more; however, filtering spread the profile out as well as smoothing it and so the smallest practical filter size was used.

4.2 Heat Losses. The total heat flux absorbed by the pipe was corrected for losses from the pipe surface due to radiation and natural convection as discussed in the previous section. The heat flux loss to the environment from these factors together is given in Fig. 8 for Re=30,000 and laser power 0.12 W. These losses essentially reflect the local temperature on the surface because they depend on a temperature difference between the pipe and the environment. The heat loss, was roughly 12% of the laser power in the hottest part of the beam. Outside of the beam, where the applied heat flux was zero, the losses were still non-negligible because the surface was heated by the thermal wake to the right (downstream) of the beam. These losses were subtracted from the applied laser power to get the net heat flux into the pipe shown in Fig. 9.
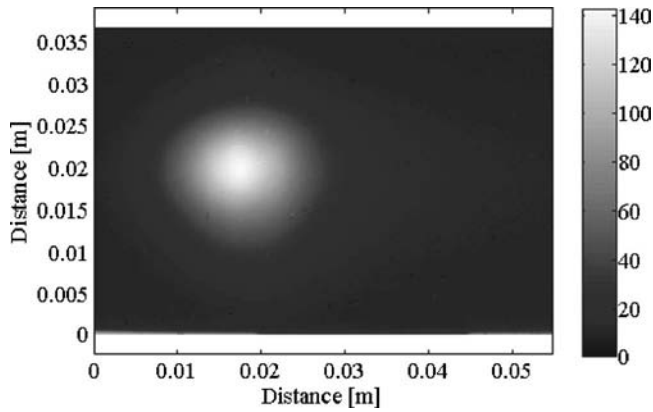
Fig. 8 Heat flux loss, through natural convection and radiation ($\dot{q}''_{nc} + \dot{q}''_{rad}$ in Eq. (4)). Scale is W/m².

Fig. 10 Beam power taken at vertical centerline of profile on multiple days

The beam location in the image is clear and there is a relatively smooth transition from far upstream where the heat flux was approximately zero to the core of the beam where the heat flux into the pipe was high. Downstream of the core, the heat flux quickly dropped and became negative, indicating that heat exited the surface of the pipe. This was due to the sharp drop in applied laser power combined with the thermal wake caused by the fluid convecting heat downstream.

It was important to ensure that the profile could be repeated at different times, on different days for comparisons of results. Figure 10 shows four profiles, taken with the same laser power, measured on different days. The profiles were taken up to 2 weeks apart, demonstrating that the alignment of the optics was stable and that the system did not need to be realigned over time. Therefore, profiles taken on different days were considered interchangeable as long as none of the optics were deliberately changed between measurements.

Figure 11 shows the final temperature distribution that was used as a boundary condition when solving for h at Re=30,000. The thermal wake is clearly defined and the discontinuities in temperature caused by the dead pixels are eliminated completely. The top and bottom of the image show slight increases in temperature. This is an artifact of the calibration. The high curvature and angle of incidence of the pipe surface relative to the camera cause the calibration to be less accurate near the top and bottom of the pipe. A shift between the location of the calibration piece and the test model by a single pixel produces a dramatic effect on the measured temperature. These erroneous temperatures are limited to
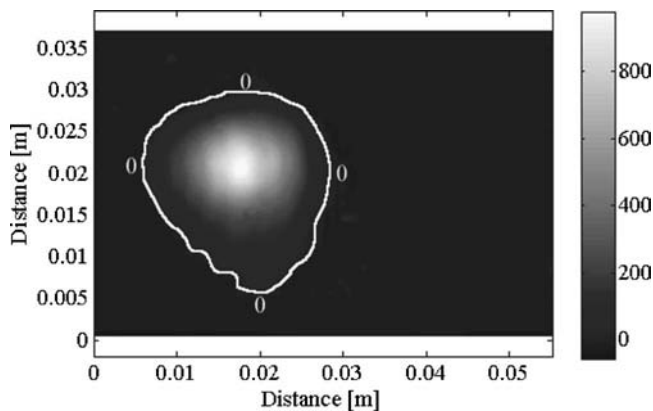
the few pixels nearest ($\lesssim 1$ mm) the top and bottom of the image, which are well away from the important temperature gradients in the image and are readily filtered away or ignored. These create errors in the IHCP solution so that calculated values of h are unreliable near the edges of the domain.

The measured heat flux and temperature distributions on the outer wall of the pipe were used in COMSOL to determine h and temperature on the inside of the pipe. The convergence criteria for the iteration on the difference in heat flux were set at ±5 W/m² within the laser beam, which corresponded to less than 0.5% of the maximum heat flux. The convergence criterion was applied after the heat fluxes were subtracted and the difference had been filtered. On the edges of the domain, noise and less accurate calibration as well as small heat fluxes and temperature rises occasionally caused the difference in the calculated and experimental heat flux to exceed this limit. This was allowed because these areas were not critical to the final calculation of h.

The distribution of h on the inside of the pipe measured with this technique is given in Fig. 12. The h distribution had a tail that extended somewhat to the left and a more pronounced tail toward the bottom of the domain. The temperature rise in these areas was small, as can be seen in Fig. 11. The heat fluxes were also small in these regions because they were near the edge of the beam. There were inflection points in the heat flux as the beam power went to zero and the heat flux started to exit the surface of the pipe due to

Fig. 9 Net heat flux into the test section ($\dot{q}''_{expt}$, in Eq. (4)) at laser power 0.12 W (used for Re=30,000) with 3% threshold applied. The zero heat flux contour is labeled in the plot. Scale is W/m².
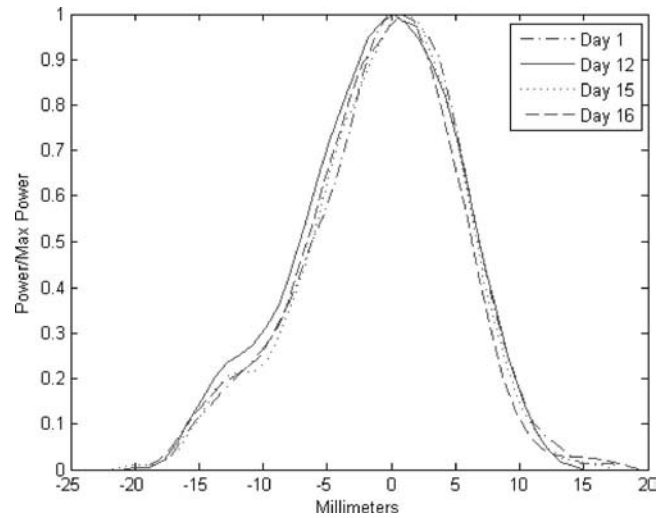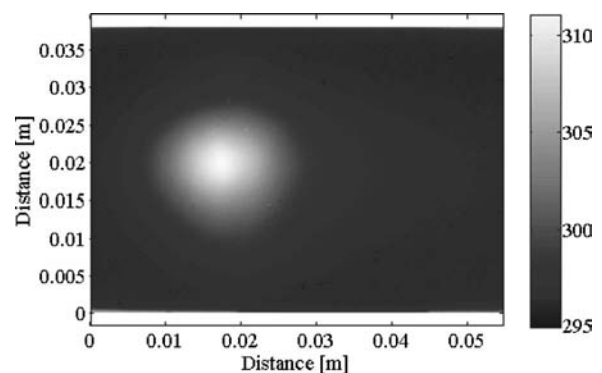

Fig. 11 Measured, filtered temperature distribution on the external surface of the test section for Re=30,000. Flow is from left to right, and scale is K.
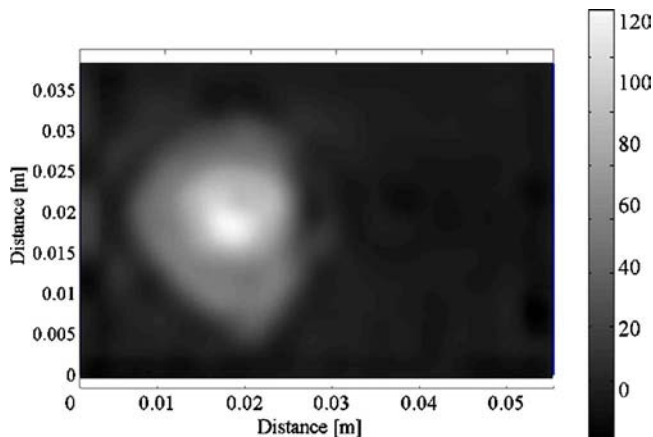
Fig. 12 Measured heat transfer coefficient distribution for Re =30,000 on the inside of the pipe. Scale is W/m² K.

Fig. 14 Temperature contours with heat fluxes shown as arrows as determined in COMSOL. The top is the outside of the pipe, and the flow on the inside is from left to right. Scale is K.

natural convection and radiation. The combined effects of low temperature rise and heat flux made obtaining h outside of the core of the beam were very difficult.

The calculated temperature distribution on the inner wall of the pipe is shown in Fig. 13. This distribution looks qualitatively similar to the externally measured temperatures, with a concentrated high temperature region and a lower temperature wake extending downstream, to the right. The temperatures are much lower than on the outside of the pipe, up to $13\,°C$, due to the high thermal resistance through the plastic wall.

The low heat fluxes also meant that the lateral component of the heat conduction became larger relative to the radial heat conduction, thus reducing the accuracy of the optimization technique for h. This can be seen more clearly in Fig. 14, which shows a cross section through a short length of the pipe wall. The contours are of wall temperature in the pipe; the arrows represent heat flux vectors. The plane is a horizontal slice through the pipe near the center of the laser beam. The top is the outside pipe wall, and the bottom is the inside wall where the flow is from left to right. In the center of the beam, where the temperatures were highest, the conduction was almost purely radial (vertical in the figure), creating a strong relation between h on the inside wall and the heat flux on the outside wall at the same axial and circumferential location. Near the edges of the figure, the lateral conduction through the wall was of the same order of magnitude as the radial conduction. The lateral component dominated at distances farther away from the beam than is shown in the figure.
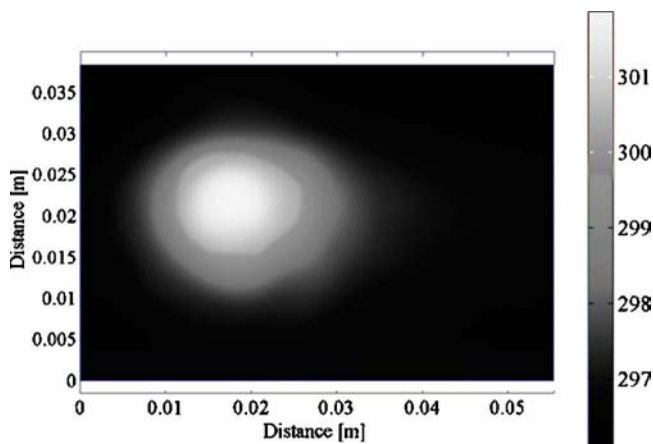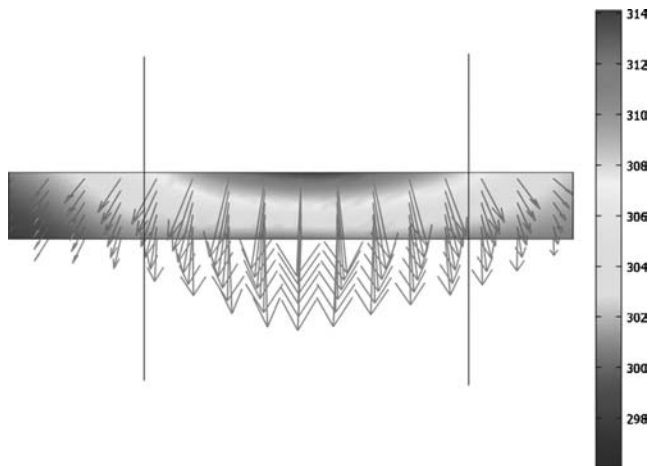

Fig. 13 Temperature distribution calculated on the inside wall of the pipe using COMSOL. Scale is K.

4.3 FLUENT Comparison. One of the most difficult aspects in the development of this new measurement technique was finding a suitable standard against which to compare the measured results. The fully developed round pipe geometry was chosen because the flow is well understood and a modern CFD code should be able to compute the heat transfer rate accurately. However, this calculation is made difficult by the relatively complex thermal boundary conditions in which the wall temperature varies circumferentially and axially. Therefore, a semianalytical solution for h based on the discrete Green's function (DGF) analysis presented by Booten and Eaton [10] is also used for comparison of the results.

The commercial CFD code FLUENT was chosen as one basis for comparison. The FLUENT model was the same half pipe that was used in COMSOL except that only the fluid was modeled, instead of only the pipe wall. The Spalart–Allmaras turbulence model was used. It employed a two-layer near-wall model rather than wall functions allowing a more accurate resolution of near-wall effects, such as heat transfer, see Refs. [14,15]. The boundary conditions on the FLUENT model were hydrodynamically fully developed flow at the inlet, a pressure boundary at the outlet, a specified temperature distribution on the inside pipe wall, and a symmetry boundary at the pipe center plane. The temperature boundary condition was the inner wall temperature distribution shown in Fig. 13.

Only locations well inside the laser beam were considered when making a quantitative assessment of h. The cutoff in the beam intensity that was chosen for measuring and calculating h was 60% of the maximum. This area is encompassed by the vertical lines in Fig. 14 and is shown on the outer pipe surface in Fig. 15. The h that was obtained using FLUENT is compared to the h obtained (using COMSOL) from the experimental data in Fig. 16. The agreement was within 4% for both Reynolds numbers measured.

The second basis for comparison was the semianalytical solution for h in thermally developing pipe flow obtained using the DGF analysis. The solution was only approximate for these thermal boundary conditions because the DGF formulation that was used assumed circumferentially uniform boundary conditions. The horizontal, centerline temperature-rise distribution from Fig. 11 was applied as the approximate thermal boundary condition to obtain h using the DGF technique. This h agreed with the experimental h within 1.5% and 8.5% for Re=30,000 and 60,000, respectively, despite the approximation in the thermal boundary condition.
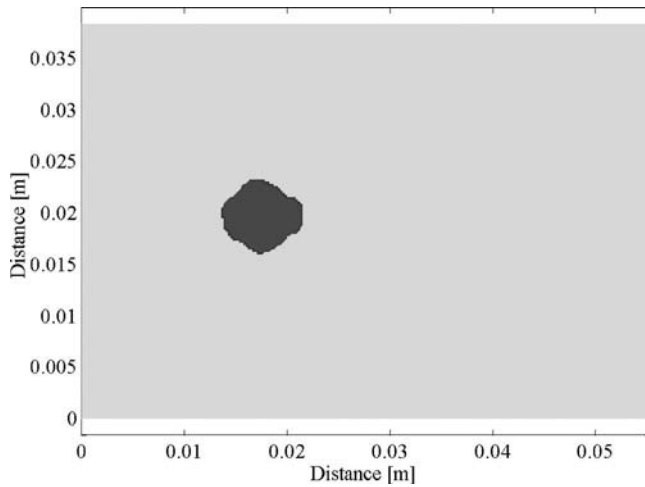
Fig. 15 The high intensity area of the beam where *h* was averaged

The dashed line in Fig. 16 represents the thermally fully developed value for *h* in a round pipe from the well known Dittus–Boelter equation

$$Nu = 0.023\,Re^{0.8}\,Pr^{0.4} \tag{10}$$

The measured values of *h* were approximately 50–80% higher than what was predicted using Eq. (10). This was within the expected range given that *h* was averaged over a relatively small area and so could not approach the fully developed value. The somewhat Gaussian temperature distribution lowered *h* by gradually increasing the wall temperature in the streamwise direction rather than introducing a sharp step that would create a very high *h*. The peak *h* within this area was up to 30% higher than the average *h* but only in a small subsection of the area.

The agreement between the experimental and FLUENT results was a function of the beam intensity cutoff level used to determine the area over which *h* was evaluated. This is shown graphically in Fig. 17. The best agreement was for a cutoff power intensity of 50%–60%. A lower cutoff, corresponding to a larger averaging area, led to worse agreement because the distributions of *h* were qualitatively different in the measured results and the FLUENT calculations. FLUENT predicted a more even *h* distribution than was found in the measurements. The latter shows a more abrupt drop
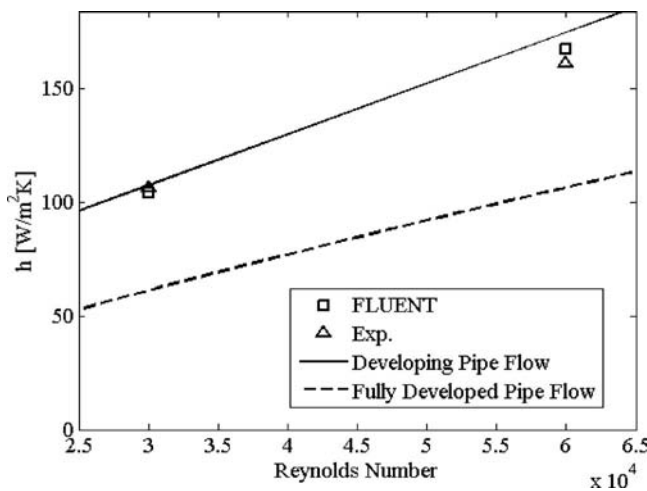

Fig. 16 Comparison of heat transfer coefficients calculated (using COMSOL) from experimental data and from FLUENT simulations
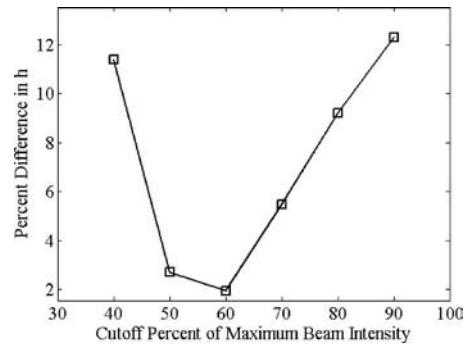
Fig. 17 Difference in measured *h* and that calculated in FLUENT as a function of the cutoff beam intensity level used to determine the area over which *h* was calculated.

near the edges of the laser beam. The difference in the average *h* at the higher cutoff was in part due to the same qualitative difference in the *h* distribution. There was also a slight difference in the peak *h* location between the two results. A small area meant that slight differences in this location had a large impact in the average value of *h*.

5 More Complex Boundary Conditions

A test case was used to assess the ability of the new experimental technique to be extended to solve for *h* with large spatial gradients and complex thermal boundary conditions. Synthetic boundary conditions were generated and used in the same fashion as the experimental data were used in the actual experiment. The modeled geometry was half of a circular pipe, the same as for the experiment. The boundary condition on the inside of the pipe was a specified *h* distribution h_{spec}. This made the problem well defined so that the wall temperature could easily be determined using COMSOL. This solution was treated as "experimental" data; the resulting heat flux and the temperature on the outside of the pipe were treated as if they had been measured using the infrared camera and were known. The internal *h* that was used as a boundary condition was treated as an unknown, because it was unknown in the experiments. An initial guess was used to iterate on *h* and the final result was compared to h_{spec} to determine the accuracy of the technique.

The particular application of this test case was turbine blade serpentine cooling passages; the boundary conditions tested were meant to closely resemble potential *h* distributions in those types of passages. The external temperature and internal h_{spec} boundary conditions are given in Fig. 18. The temperature distribution was Gaussian to simulate approximately the effect of using an idealized, Gaussian laser beam as a heat source. The h_{spec} heat transfer coefficient distribution varied in a sinusoidal fashion at a 45 deg angle to the main flow, similar to the distribution that could be expected in a turbulated cooling passage. Note that although a very complicated *h* was specified, the actual wall shape on the inside of the pipe was not changed. Therefore, the specified h_{spec} was certainly unphysical in this case but was still useful as a demonstration of the ability of this technique to handle complex boundary conditions.

The converged solution for *h* was within 1.5% of the maximum value of h_{spec} at all locations on the surface. The agreement between the specified and calculated *h* was significantly better than what was achieved experimentally. Even in locations well outside the hottest area of the pipe, where the temperature rise was small and the heat flux had a significant lateral component, *h* was obtained accurately. This demonstrated that, even with an extremely complex *h* distribution in the pipe, this method has the potential to accurately measure *h*. The key was a lack of noise that would cause numerical instabilities. Therefore, extremely accurate mea-
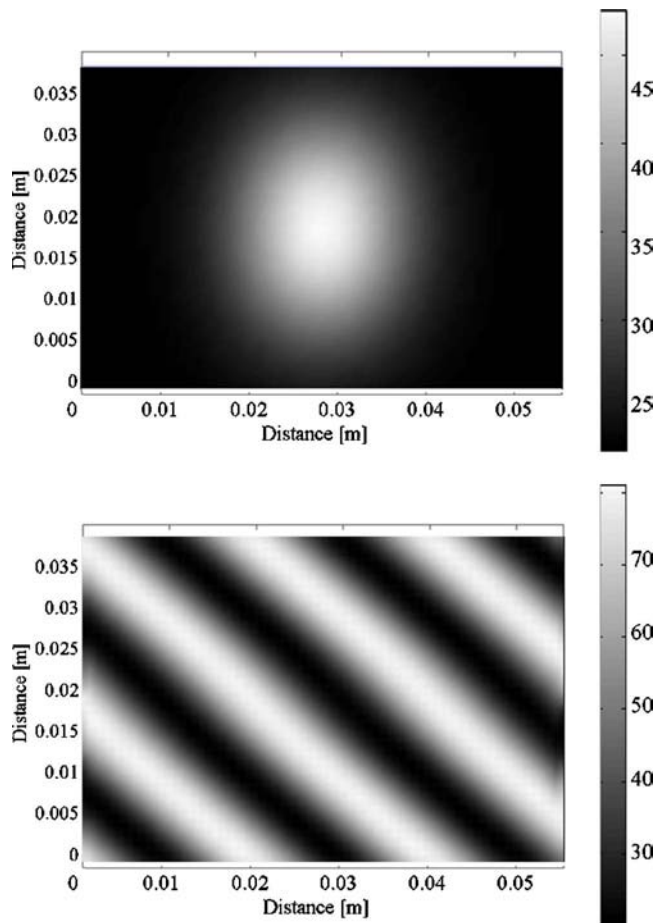
Fig. 18 External temperature distribution (left) in °C and internal *h* distribution (right) in W/m² K specified to generate experimental data for the test case. The *h* distribution was created to resemble that inside a turbulated passage.

surement techniques would be necessary to measure *h* with this accuracy over a large area with such a complicated distribution.

6 Uncertainty Analysis

Uncertainties in experimental results were calculated using the single-sample uncertainty analysis put forth by Kline and McClintock [16] and Moffat [17]. The important parameters and their effect on the measurement uncertainty of *h* are presented in Table 1. A range in uncertainty is given for most parameters because they are field variables (i.e., they were obtained from images)

whose value and uncertainty changed with location. The range represents typical uncertainties around the mean value at all locations.

The largest uncertainty was from the beam profile images. A more Gaussian beam, with no diffraction patterns, could dramatically reduce the overall uncertainty in *h*. Another major factor was the uncertainty in the pixel intensity from the calibration images. A planar calibration surface rather than the semicircular pipe calibration piece would probably reduce this uncertainty as well as make the calibration faster and easier. The uncertainty in the estimate of the natural convection was also quite high. The maximum temperature rise in the Re=30,000 test was approximately 16°C, whereas it was approximately 21°C, for Re=60,000. The extra temperature rise on the model significantly increased natural convection on the outer surface, almost doubling the effect that the uncertainty in L_{ch} had on *h*. Lowering the maximum temperature rise on the model is certainly the simplest and most effective way of reducing natural convection and the uncertainty it causes in *h*.

7 Advantages and Disadvantages of Technique

This optical heat transfer measurement method has several useful advantages over traditional techniques for measuring heat transfer coefficients. All of these advantages ultimately lead to the potential for significant time savings. This can lead to true, rapid experimentation on time scales of days so that measurements performed with this optical technique could be used directly in product design.

The most important advantage is that there is no instrumentation on the model. Other techniques require drilling holes for thermocouples or applying a paint along with needing optical access to the measured surface. Drilling holes and installing thermocouples requires a small thermocouple when good spatial resolution is desired and also requires direct access to any measured surface (i.e., holes cannot curve around corners, etc.). Intermediate spatial resolution thermocouple experiments therefore can be quite time consuming to prepare. Models that require optical access to the surface where *h* is measured are more complicated and time consuming to design. They often have imaging windows installed, which could be nonplanar, or need external illumination, which typically results in models that are fabricated in several parts that must be assembled. A rapid prototyping process, such as stereolithography, can be used to fabricate even complex passage geometries as one piece with ease.

The outer surface of the model might require a high emissivity coating that should also be applied to the calibration piece. However, coating of an external surface, which in general will be planar, is straightforward compared to coating internal surfaces. This small amount of model preparation means that interchanging geometries can be accomplished rapidly as well. If the external surfaces of the two models have the same shape, no recalibration is necessary when changing models. This could be useful in investigating different internal turbulence enhancement devices.

Table 1 Parameters included in uncertainty analysis and their effect on the uncertainty in the measurement of *h*

		% uncertainty in *h*	
Parameter	Uncertainty	Re=30,000	Re=60,000
Thermocouple temperature in calibration piece	0.04−0.06°C	1.2	1.0
Pixel intensity count in calibration images	40−250	5.8	6.6
Measured wall temperature from images	0.1−0.4°C	0.5	0.2
Heat flux in beam profile images	10−80 W/m²	9.0	10.8
Krylon 1602 ultraflat black paint emissivity	0.01	0.1	0.2
Total laser power	$(1.1-2.4)\times10^{-4}$ W	0.4	0.7
Characteristic length for natural convection	15 mm	5.4	9.0
RSS		12.1	13.5

The size and location of the measurement of h also can be easily adjusted with this technique. A larger or smaller measurement area can be achieved by adjusting the size of the laser beam used to heat the model. An expanding lens with a different focal length can be used or simply adjust the location of the lens. It is much more difficult to adjust the resolution when performing thermocouple type measurements.

There are, however, some disadvantages of measuring h using this method rather than traditional methods. The measurements of h are a function of the thermal conductivity of the material, so that accurate knowledge of this property is more important than for measurement techniques where the thermal conductivity is important only in estimating conduction losses. Quantifying the applied heat flux from the infrared laser is also more difficult than if a simple electrical film heater is used as is common in other measurement systems. Wall thicknesses less than 2 mm are also desirable. Thicker walls that allow for more lateral diffusion of the applied heat or complex wall shapes that result from turbulence enhancement devices could reduce the accuracy significantly or require more sophisticated and computationally expensive algorithms for solving the IHCP. Further experimentation will be required to determine how robust this technique is.

The calibration can be time consuming if the imaged surface of the model is not planar. A nonplanar external surface requires that a calibration piece be fabricated that replicates the model surface shape. This technique is best suited to situations where a planar external surface can be used while still maintaining thin walls ($\leqslant$2 mm) throughout the region of interest.

The thermal boundary conditions are also complicated; this makes comparison with CFD difficult. The applied heat flux can, in general, be very nonuniform and non-Gaussian as well. Supplying a constant wall temperature boundary condition (by making the measured surface from a high thermal conductivity material, such as copper) is relatively straightforward and is much easier to compare with literature and numerical results.

8 Discussion and Conclusions

There are many engineering applications where designs could be substantially improved using knowledge of the distribution of the heat transfer coefficient in a complex internal flow. For the information to be useful, it must have a relatively low and quantifiable uncertainty, and it must be available on design-cycle time scales that are typically measured in days or weeks. Accurate flow models of complex passages can be manufactured quickly using a range of commercial, rapid prototyping technologies. However, conventional heat transfer measurement techniques involving the application of heaters, temperature sensors, heat flux gauges, or complex unsteady flow systems have not kept pace.

This work has demonstrated that external laser heating and external infrared-camera based temperature measurement can be used with a thin-walled, plastic model to measure the internal heat transfer coefficient with an accuracy of a few percent in the central part of the heated area. The fixed equipment is relatively complex and expensive, but once this equipment is in place, a new flow geometry can be measured quickly. In particular, no instrumentation is attached to the flow model. The only modification required for a typical stereolithography model would be to spray it with high emissivity black paint.

The wall thickness for the test model was chosen to provide a reasonable representation of typical models that could be fabricated using rapid prototyping techniques. Some manufacturing techniques and flow geometries would allow even thinner walls that would provide for more accurate results. Thicker walls adversely affect the accuracy of the inner wall temperature calculation when a plastic model is used. This is due to the larger temperature drop between the inner and outer walls of the passage.

Hydrodynamically fully developed pipe flow was chosen as a test case because of the ability of commercial CFD packages to compute the heat transfer coefficient distribution accurately and provide a basis of comparison. The simple geometry made the setup of the heat conduction program simpler, but commercial finite-element codes can handle more complex geometries easily. Therefore, it should be possible to extend the present approach to more complex passage geometries as long as the external surface can be imaged successfully. A follow-on experiment using a more complex geometry would be useful in extending this technique for use in more practical flow configurations.

It is also important to note that the heat transfer coefficient in the fully developed pipe flow is lower than it would be in most complex internal passages where secondary flows and higher turbulence levels usually result in higher values of h. In this regard, the pipe flow is a very challenging test case because the lower value of h on the inner passage wall increases the relative importance of lateral conduction in the wall and radiative and convective losses from the outer surface of the model.

An analytical test of the method using a varying internal heat transfer coefficient showed that the method is capable of resolving relatively rapid variations in h that would be caused by passage features, such as ribs, separation bubbles, or internal impingement jets. This capability has not been verified experimentally, and it is likely to be degraded somewhat by measurement noise.

Finally, we address a significant remaining issue with this technique, namely, the complex thermal boundary condition. In the present work, the thermal boundary condition on the inside surface of the pipe was dictated by the specific geometry of the pipe model, the characteristics of the laser cavity, and the optical system. Clearly, this boundary condition was not as simple as would be desired. It may be possible to improve the optical system and/or the external surface characteristics of the model to produce a more easily defined thermal boundary condition. For example, the model could be thinned dramatically in a specific area. Illuminating this area with a uniform laser beam would produce a specific area of almost constant heat flux. However, this would involve more complex model manufacturing and an improved optical system. It is important to note that the present test flow is relatively more sensitive to the specific thermal boundary condition than other flows of interest. Booten and Eaton [18] studied a ribbed serpentine passage using conventional heat transfer measurement techniques. They showed that the flow was quite insensitive to the specific thermal boundary condition due to the strong secondary flows and turbulent mixing, which acted to rapidly disperse the concentrated thermal wake of a heated spot. This insensitivity could mean the present experimental technique might be applicable to more realistic geometries even with complex thermal boundary conditions.

Acknowledgment

Nomenclature

A_{av} = surface area, m^2
Bi = Biot number
C = constant used in optimization of h
h = heat transfer coefficient, W/m^2 K
k = thermal conductivity, W/m K
L_{ch} = characteristic length, m
L_d = diffusion length scale
Nu = Nusselt number, hL_{ch}/k
Pr = Prandtl number, ν/α
$\dot{q}''$ = heat flux, W/m^2
r = radius, m

$\mathrm{Ra}_{L_{\mathrm{ch}}}$ = Rayleigh number,
$2g(T_{\mathrm{expt}}-T_\infty)L_{\mathrm{ch}}^3/(T_{\mathrm{expt}}+T_\infty)\alpha^2$

Re = Reynolds number, $\bar{V}D/\nu$

t_d = diffusion time scale

t = time, s

T = temperature, K

w = thickness of pipe, m

x = axial location

y = circumferential location

Subscripts

bulk = mean value for fluid

enclosure = referring to the constant temperature enclosure around the optical heat transfer measurement test section

expt = experimental data

i = inner surface of pipe

it = iterative solution from COMSOL

guess = used as an initial guess when optimizing h

nc = natural convection.

o = outside surface of pipe

rad = radiation

∞ = ambient value

Greek

α = thermal diffusivity, $\mathrm{m^2/s}$

ϵ = surface emissivity

σ = stephan–Boltzmann constant, $5.6705\times10^{-9}\ \mathrm{W/m^4\,K^4}$

References

[1] Elkins, C. J., Marki, M., Iyengar, A., Wicker, R., and Eaton, J. K., 2004, "Full Field Velocity and Temperature Measurement Using Magnetic Resonance Imaging in Turbulent Complex Internal Flows," Int. J. Heat Fluid Flow, **25**(5), pp. 702–710.

[2] Beck, J. V., 1970, "Nonlinear Estimation Applied to the Nonlinear Inverse Heat Conduction Problem," Int. J. Heat Mass Transfer, **13**, pp. 703–716.

[3] Liu, J., 1996, "A Stability Analysis on Beck's Procedure for Inverse Heat Conduction Problems," J. Comput. Phys., **123**, pp. 65–73.

[4] Sassi, M., and Raynaud, M., 1998, "New Space-Marching Method for Solving Inverse Boundary Problems," Numer. Heat Transfer, Part B, **34**, pp. 21–38.

[5] Ling, X., Cherukuri, H. P., and Keanini, R. G., 2005, "A Modified Sequential Function Specification Finite Element-Based Method for Parabolic Inverse Heat Conduction Problems," Comput. Mech., **36**, pp. 117–128.

[6] Yang, Y. T., Hsu, P. T., and Chen, C. K., 1997, "A Three-Dimensional Inverse Heat Conduction Problem Approach for Estimating the Heat Flux and Surface Temperature of a Hollow Cylinder," J. Phys. D, **30**, pp. 1326–1333.

[7] Nirmalan, N. V., Bunker, R. S., and Hedlund, C. R., 2003, "The Measurement of Full-Surface Internal Heat Transfer Coefficients for Turbine Airfoils Using a Nondestructive Thermal Inertia Technique," ASME J. Turbomach., **125**, pp. 83–89.

[8] Bunker, R. S., 2004, "Latticework (Vortex) Cooling Effectiveness—Part 1: Stationary Channel Experiments," *Proceedings of ASME Turbo Expo 2004*, Vienna, Austria, June 14–17, ASME, New York.

[9] Freund, S., Pautsch, A. G., Shedd, T. A., and Kabelac, S., 2007, "Local Heat Transfer Coefficients in Spray Cooling Systems Measured With Temperature Oscillation IR Thermography," Int. J. Heat Mass Transfer, **50**, pp. 1953–1962.

[10] Booten, C. W., and Eaton, J. K., 2005, "Discrete Green's Function Measurements in Internal Flows," J. Heat Transfer, **127**(7), pp. 692–698.

[11] Touloukian, Y. S., DeWitt, D. P., and Hernicz, R. S., 1972, *Thermophysical Properties of Matter*, TPRC Data Series, IFI/Plenum, New York, Vol. 9.

[12] Mills, A. F., 1995, *Heat and Mass Transfer*, 3rd ed., Irwin, Chicago, IL.

[13] Cooper, S. R., and Eaton, J. K., 2002, "Spatially Resolved Surface Temperature Control Using Scanned Laser Heating," Report No. TSD-148, Stanford University, Stanford, CA.

[14] FLUENT 5 Manual, FLUENT Inc., Lebanon, NH, 1999.

[15] Durbin, P. A., and Pettersson Reif, B. A., 2001, *Statistical Theory and Modeling for Turbulent Flows*, Wiley, New York.

[16] Kline, S. J., and McClintock, F. A., 1953, "Describing Uncertainties in Single-Sample Experiments," Mech. Eng. (Am. Soc. Mech. Eng.), pp. 53–57.

[17] Moffat, R. J., 1988, "Describing the Uncertainties in Experimental Results," Exp. Therm. Fluid Sci., **1**(1), pp. 3–17.

[18] Booten, C. W., Elkins, C. J., and Eaton, J. K., 2006, *Rapid Heat Transfer Measurements in Complex Internal Flows*, Stanford University, Stanford, CA.

Internal Cooling in 4:1 AR Passages at High Rotation Numbers

Fuguo Zhou

Jonathan Lagrone

Sumanta Acharya

Turbine Innovation and
Energy Research (TIER) Center,
College of Engineering,
Louisiana State University,
Baton Rouge, LA 70803

Heat transfer and pressure drop measurements are reported for a rotating 4:1 aspect ratio (AR) smooth two-pass coolant passage for Reynolds number in the range of 10,000–150,000, rotation number in the range of 0–0.6, and density ratios in the range of 0.1–0.2. The measurements are performed for both 90 deg *and* 45 deg *orientations of the coolant passage relative to the rotational axis. A large-scale rotating heat transfer rig is utilized, with the test section consisting of segmented foil-heated elements and thermocouples. Results for the 4:1 AR indicate that beyond specific Ro values (different values for the inlet and outlet passages), the expected trends of heat transfer enhancement on the destabilized surface and degradation on the stabilized surface are arrested or reversed. Unlike the 1:1 AR, the inlet-leading surface for the 4:1 AR shows enhancement with Ro at low Re (less than 20,000) and shows the expected degradation only at high Re. Increasing the density ratio enhances the heat transfer on all walls. Orientation of the coolant passage relative to the rotational axis has an important effect, with the 45 deg orientation reducing the heat transfer on the destabilized surface and enhancing it on the stabilized surface.* [DOI: 10.1115/1.2767676]

Keywords: turbine blade, internal cooling, heat transfer, rectangular channel, rotation, aspect ratio

1 Introduction

Efforts to increase the efficiency of turbines often involve increasing the turbine inlet temperature. In order to combat the higher temperatures experienced by the first-stage vanes and blades, more effective and innovative cooling techniques have been studied. One of the most common techniques for blade cooling involves circulating coolant air through internal-cooling passages within the turbine blade. Maximizing the cooling efficiency of such passages and attempting to accurately quantify the performance of these passages for parameters relevant to engine operating conditions have been the primary focus of many researchers for several decades. As a result, many studies have focused attention on different cross-sectional geometries, different turbulator configurations, and different flow parameters for both stationary and rotating internal coolant passages. These studies have provided insights on the effect of Coriolis and centrifugal-buoyancy forces on the flow and heat transfer characteristics for specific geometries and have provided guidelines for implementing reliable and/or improved internal-cooling strategies.

The early research focused mainly on straight, smooth, tubes with a circular cross-section [1–3]. Later, square smooth cross-section ducts received extensive attention. For example, Wagner et al. [4] reported detailed measurements in a rotating smooth, square cross-section channel. Their study investigated the effects of rotation, density ratio (DR), and Reynolds number. The results showed that rotation has a significant effect on heat transfer. By varying the rotation number from 0 to 0.48, the heat transfer ratio on the pressure side (trailing wall) steadily increased, and at a rotation number of 0.48, the heat transfer ratio was 350% higher than the stationary case. However, the heat transfer ratio on the suction side (leading wall) demonstrated a more complex behavior. Initially, the heat transfer ratio decreased as the rotation number increased, but beyond a critical rotation number (depending on

the DR and streamwise location), the heat transfer ratio increased with rotation number. Heat transfer on sidewalls experienced only slight changes. Increases in DR were found to enhance heat transfer ratios of both leading and trailing walls. Wagner et al. [5] further studied a serpentine, smooth, square cross-section rotating channel. The heat transfer ratio in the bends was found to nearly double the value in the fully developed straight sections. Mochizuki et al. [6] also conducted experiments in a smooth serpentine square channel with rotation. Their results also showed that the heat transfer ratios in the bend regions were about twice the values in the straight legs of the channel. In addition, their results showed that the heat transfer ratios in the second and third legs were higher than in the first leg due to the bend effects.

The cross section in the coolant passages of a turbine blade airfoil ranges from tall passages (low aspect ratio (AR)) in the thickest portion of the turbine blade airfoil to wide rectangular passages (high AR) in the trailing edge. Most of the early reported studies have focused attention on square passages. However, recently, several studies have reported measurements in rectangular cross-section internal passages. Guidez [7] first studied a radial straight channel of AR=2:1 for Reynolds numbers from 17,000 to 41,000 and rotation numbers up to about 0.2, and found the trends to be similar as those described in Wagner et al. [4]. Morris and Ghavami-Nasr [8] also studied a straight rectangular channel with AR=2:1, covering Re from 10,000 to 25,000 and Ro from 0 to 0.2, but noted weaker rotation effects than those reported by Wagner et al. [4]. Iacovides and Launder [9] performed a numerical study on an AR=2:1 straight rectangular rotation channel. Their results revealed that at low rotation numbers Coriolis forces induced a pair of symmetric streamwise vortices. The vortex pair could be transitioned to a more complex four-vortex structure at high rotation numbers due to the flow instability on the pressure wall. Soong et al. [10] conducted a series of tests on square and rectangular channels with different aspect ratios, but mainly focused attention in the laminar flow regime, and rotation numbers were less than 0.05 for the turbulent flow cases. Griffith et al. [11] experimentally studied a straight, smooth, rectangular model of AR=4:1 in the parameter range of Ro=0.305 at Re=5000 to Ro
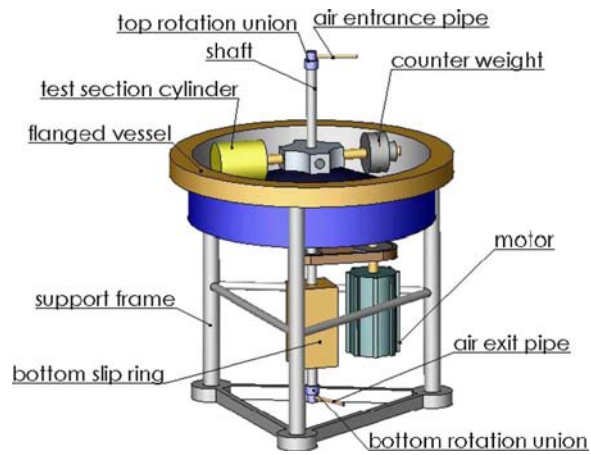
Fig. 1   Rotating rig

=0.038 at Re=40,000. Their results showed that the heat transfer ratio on both leading and trailing walls increased with rotation number. This observation was different from that reported for square channels [4–6].

The configuration of interest in the present study is that of a rectangular coolant channel with AR=4:1. This configuration has received limited attention, and only for limited parameter ranges. For example, at Re=40,000, a maximum Ro of 0.038 has been reported [11]. With the development of modern advanced turbine systems, realistic parameter ranges of interest include Reynolds number up to 75,000 and Ro up to 0.3–0.4. Higher parameter ranges are possible in closed-loop steam cooled blades. While for the 1:1 AR geometry, Wagner et al. [5] reported data for Ro up to 0.48 (at Re=25,000), no comparable data are available for the 4:1 AR coolant passages encountered closer to the trailing edge of the blades. The objectives of the present study are to investigate the effects of rotation, DRs, Reynolds number, and the orientation angle on the heat transfer and pressure drop characteristics in a two-pass 4:1 AR channel over a wide range of parameter values. The parameter ranges studied for both 90 deg and 45 deg orientations of the passage relative to the rotational axis include Reynolds numbers from 10,000 to 150,000, rotation numbers from 0 to 0.6, and DRs from 0.1 to 0.2. The highest Ro (0.6) is achieved only at the lowest Re (10,000), at intermediate Re of 40,000 the highest Ro achieved is 0.2, while at high values of Re (70,000) the maximum Ro is 0.1. No data at these high parameter values have been reported in the literature for a 4:1 AR geometry; these are the primary motivation and contribution of the present work.

2   Experimental Details

2.1   Rotating Heat Transfer Facility. The rotating rig shown in Fig. 1, and originally used by Wagner et al. [4,5], has been utilized in the present study. The facility has two major components: the containment vessel and the rotating arm assembly. The containment vessel is 1.83 m (6 ft) in diameter and consists of two symmetrical flanged sections. The upper section (not shown in Fig. 1) of the vessel is removable to allow access to the rotating arm, and the lower section is anchored and supported by a steel support frame shown in Fig. 1. The vessel is designed for operation at a 5 mm Hg absolute pressure to reduce the viscous heating and the power requirement of the rotating arm.

The arm assembly consists of the vertical shaft and the horizontal arm, which are driven by a 15 hp dc motor. The rotational speed of the shaft can be varied from 0 to a maximum tested speed of 1500 rpm by a feedback electronic controller. The vertical shaft consists of the main outer shaft and an inner concentric shaft. Together, the shafts provide dual fluid paths for the rotary unions mounted on each end of the main shaft. In the present

experiments, only the inner shaft is used as the air path. The rotary unions and the paths in the shafts were designed to sustain 1034 kPa (about 10 atm).

On the exterior surface of the main shaft, recessed grooves allow signal and power leads to run from the rotating arm assembly to two slip rings, one located on the upper end of the main shaft (not shown in the figure) and the other on the lower end. The two slip rings provide a total of 240 channels for power and instrumentation wires between the stationary and rotating frames. A cylindrical pressure vessel containing the test section is mounted on one end to the horizontal arm. On the other end, a counterweight, with variable mass and positioning capabilities, is mounted to allow for static and dynamic balancing of different test sections. Stainless steel tubing along the arm provides an air passage from the test section to the shaft. A Kulite and a Scani-valve pressure transducer are mounted on the arm to measure the absolute pressure and differential pressure inside the test section, respectively.

Air entering the test section is circulated through a refrigerant cooling loop to alter and maintain the temperature of the inlet airflow in order to achieve the desired DR. The air is provided by a compressor-dryer-reservoir system, with a maximum mass flow rate and pressure of 0.5 kg/s and 20 atm (300 psi (absolute)), respectively. The power supply unit has 72 independent channels for providing the 0–45 V of dc power for the heaters inside the test section. The data are acquired through Hewlett-Packard data acquisition systems (HP 3497 and HP 3497A), which are connected to a Dell computer through a general purpose interface bus (GPIB) port and controlled by a custom-C program. The pressure signals, shaft speed, thermocouple readings, and heater power readings are all recorded by this system. The mass flow rate of the airflow is read separately through a Rosemount mass flow unit.

2.2   Heat Transfer Model. Figure 2(a) shows a section view of the lower portion of the test model, which consists of a 6.35 mm (0.25 in.) thick G-10 Garolite bottom plate, a 0.794 mm (0.031 in.) thick silicon rubber sheet between the bottom plate and the frames, 12.7 mm (0.5 in.) thick G-10 Garolite central and outer frames, and 11 copper elements (10 rectangular plates plus a bend) 3.175 mm (0.125 in.) thick. The copper elements rest on shoulders on both the central and outer frames and are flushed with the bottom surfaces of the frames. The copper elements on the upper portion (not shown in Fig. 2(a)) are flushed with the top of the frames. Together they form a U-shaped channel with a rectangular cross section and dimensions of 25.4 mm (1 in.) wide by 6.35 mm (0.25 in.) tall (AR of 4:1 and hydraulic diameter of 10.16 mm (0.4 in.)). An addition silicon rubber sheet and a G-10 Garolite top plate, identical to the bottom ones, rest on the top of the frames, and, finally, the whole unit is held together by screws through the smaller holes shown on the frames.

The straight inlet and outlet sections of the test channel are 117.48 mm (4.625 in.) long, and the outer diameter of the bend is 69.85 mm (2.75 in.). The smooth inner and outer sidewalls are formed by the G-10 frame surfaces. In the inlet channel, two pressure taps are installed to measure the inlet static pressure and pressure drop across the length of the first straight leg of the channel.

A steel two-channel transition section is inserted between the top and bottom G-10 plates and aligned with the inlet and exit planes of the test section. This section provides the transition between the test channel and the air-feeds on the rotation rig. The transition section is also equipped with screens to stabilize the flow and two K-type thermocouples to measure the inlet and outlet flow temperatures.

The typical copper element configuration is shown in Fig. 2(b). Each copper plate has the dimensions of 27.432 mm (1.08 in.) by 21.59 mm (0.85 in.) by 3.175 mm (0.125 in.). On the back of each copper plate, a Minco Kapton aluminum-backed foil heater is installed using thermally conductive adhesive film. Two K-type
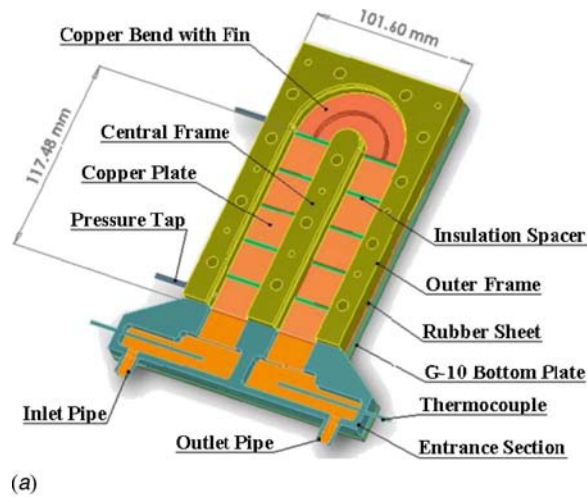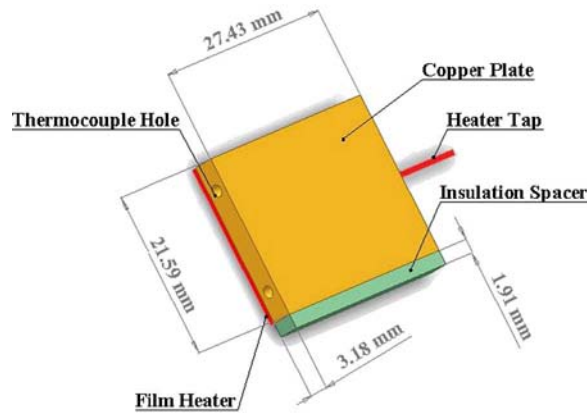
Fig. 2 (*a*) **Lower portion of the smooth model;** (*b*) **copper element with heater and spacer**

thermocouples are installed into two blind holes inside each copper plate using thermally conductive glue. Each copper plate is isolated by a G-10 Garolite spacer with dimensions of 1.905 mm (0.075 in.) by 21.59 mm (0.85 in.) by 3.175 mm (0.125 in.) to impede heat conduction between different copper plates. The inner surfaces of the spacers are carefully flush mounted with the surfaces of the copper elements in the channel. A total of 20 copper plates separated by spacers collectively form the top and bottom of inlet and outlet straight channels. In addition, a continuous copper element is used to form each bend. Each bend plate (top and bottom) is equipped with a foil heater with the same surface area as the bend and two *K*-type thermocouples.

The whole unit is bolted between two steel support plates, and the assembly is mounted inside a cylindrical pressure vessel. The thermocouple leads, power wires, and pressure transducer tubes are routed out of the vessel through sealed plugs on one of the cylinder's planar faces.

2.3 Data Reduction. During each run of the experiments, the wall temperature T_w of each copper plate is maintained at a constant value. In order to achieve the uniform wall temperature condition, the current supplied to each individual heater is adjusted. By varying T_w and inlet flow temperature T_{in}, different DRs are obtained. The local heat transfer coefficient h_i at the ith copper plate is calculated from the net heat flux $q''_{\text{net},i}$ from the heated plate to the cooling air, the measured surface temperature of the plate, T_w, and the local bulk mean air temperature $T_{b,i}$ at the midpoint of the plate, as follows:

$$ h_i = \frac{q''_{\text{net},i}}{(T_w - T_{b,i})} $$

where

$$ q''_{\text{net},i} = \frac{(q'_i - q'_{\text{loss},i})}{A} $$

and

$$ q'_i = I_i^2 R_i $$

In the above equation, I_i and R_i are the current and the resistance of the ith copper plate, respectively, $q'_{\text{loss},i}$ is the heat loss from the ith plate, and A is the projected area of the copper plate. The maximum temperature reached by the plates over the range of test conditions is 323 K, and the resistance of the heaters are constant for temperatures less than 383 K as per data sheets provided by Minco Inc. The heat loss is determined by a series of stationary tests, without flow, where under equilibrium conditions, the heat input is balanced by the heat loss and the heat loss can be calibrated to the wall temperature. The magnitude of the heat loss is typically less than 10% of the total heat input.

The local bulk mean air temperature $T_{b,i}$ is given by

$$ T_{b,i} = T_{in} + \left[\sum_{j=1}^{i} (q'_j - q'_{\text{loss},j}) \right] \Big/ (\dot{m} C_p) $$

where $\dot{m}$ is the mass flow rate and C_p is the specific heat. The Nusselt number Nu is then obtained from

$$ \text{Nu}_i = h_i D_h / k $$

where D_h is the hydraulic diameter of the test channel (0.4 in.) and k is the air conductivity. Then, Nu_i is normalized by the Dittus–Boelter correction [12]: $\text{Nu}_0 = 0.023 \, \text{Re}^{0.8} \text{Pr}^{0.4}$. Thus,

$$ \text{Nu}_i / \text{Nu}_0 = h_i D_h / (k 0.023 \, \text{Re}^{0.8} \text{Pr}^{0.4}) $$

The frictional factor f is calculated by

$$ f = (\Delta P D_h) / \left(4 L \tfrac{1}{2} \rho V^2 \right) $$

where L is the distance between the two pressure taps, ΔP is the pressure drop, ρ is the flow density, and V is the mean velocity of the flow. Then, f is normalized by $f_0 = 0.046 \, \text{Re}^{-0.2}$,

$$ f / f_0 = (\Delta P D_h) / \left(4 L \tfrac{1}{2} \rho V^2 0.046 \, \text{Re}^{-0.2} \right) $$

Using Kline and McLintock's [13] method for estimating uncertainties, the maximum error in the calculated heat transfer coefficient was estimated to be approximately 7% for the current test conditions. The uncertainty in the friction factor, at the Reynolds number reported, was calculated to be less than 10%. Uncertainties in the Reynolds number and rotation number are about 2.5%.

3 Results and Discussions

During the experiments, the pressure in the test section was maintained at 1034 kPa (150 psi (absolute)). The inlet air temperature varied from 25 °C (stationary) to 35 °C (at high rotational speeds), while the wall temperature was varied between 58 °C and 112 °C to achieve different DRs. As noted earlier, the experimental test matrix covered Reynolds number Re from 10,000 to 150,000, rotation number Ro from 0 to 0.6, and density ratio DR from 0.1 to 0.2.

3.1 Stationary Tests. A series of stationary tests were initially performed in order to validate the experimental procedures and to serve as a basis for comparison. For each Re number, the stationary tests were repeated three to six times. The repetition showed that the results for a given Re number were very consistent. Typically, the variations in the results were no more than 2% in the fully developed region.

Figure 3 shows the streamwise Nu/Nu_0 distributions in the
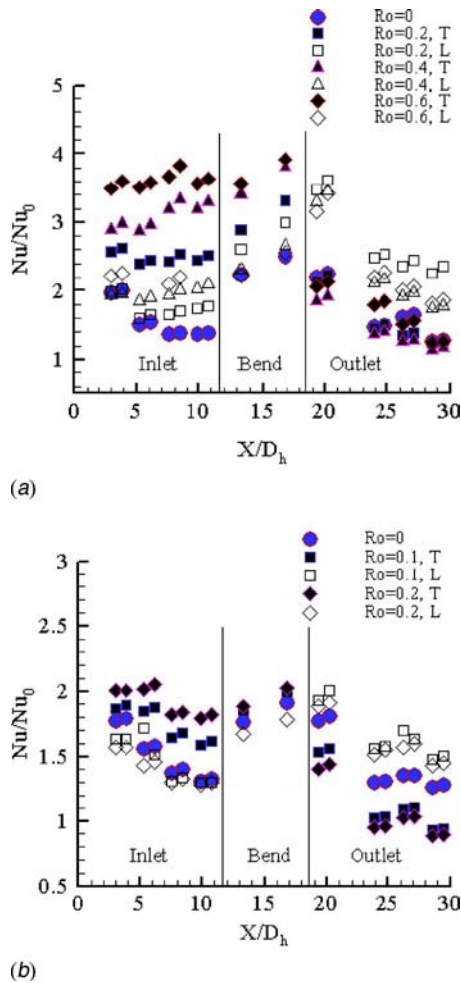
(a)

(b)

Fig. 3 Rotation effects in the two-pass channel for DR=0.1 at *(a)* **Re=10,000 and** *(b)* **Re=40,000. L-leading wall, T-trailing wall.**

two-pass channel for Re=10,000 and 40,000. Stationary results are identified as Ro=0. The bend is located between $10.5 < X/D_h < 14.5$. The inlet channel (radially outward flow) is upstream of the bend ($X/D_h < 10.5$), and the outlet channel (radially inward flow) is downstream of the bend ($X/D_h > 14.5$).

The results show almost no Reynolds number effects in the fully developed regions of the inlet or outlet channel, and the heat transfer ratio Nu/Nu_0 is approximately 1.25–1.3 in the fully developed regions. The 25% enhancement of Nu/Nu_0, with respect to the smooth circular tube value, is due to the higher AR of the coolant passage [14,15] and due to the two unheated sidewalls (asymmetric wall heating) due to which the thermal boundary-layer thickness on the heated surfaces are lower, leading to higher heat transfer coefficients. The bend has the highest Nu/Nu_0 (1.8–2.0) due to the secondary flows and turbulence induced in the 180 deg bend. The two copper elements immediately downstream of the bend also have a higher Nu/Nu_0 due to the bend-induced secondary flows. Close to the entrance of the inlet channel, due to the thermal development of the boundary layers, higher heat transfer ratios (1.8–2.0) are observed.

3.2 Rotation Effects. Rotation effects for square (AR of 1:1) cross-section passages have been well documented in the literature [11]. Coriolis-driven secondary flows, in the form of a two-roll eddy, are directed from the middle of the leading surface to the trailing surface in the inlet duct, while the flow direction is reversed in the outlet duct. Based on this understanding of the secondary flow motion, heat transfer is expected to be enhanced

on the inlet-trailing and outlet-leading walls (called destabilized surfaces), while they are expected to be reduced along the stabilized inlet-leading and outlet-trailing surfaces. Recent numerical calculations in 4:1 AR passages have, however, shown that the flow field in a 4:1 AR is different than that in a 1:1 AR, and has a complex multicellular flow pattern, and that both the trailing and leading surfaces experience a downwash of the core fluid [15]. The differences between 1:1 AR and higher AR (10:1) channels, under conditions of rotation, have also been studied by Willet and Bergles [16].

Figure 3 shows the streamwise Nu/Nu_0 distribution at Re =10,000 for Ro up to 0.6 and at Re=40,000 for Ro values up to 0.2. At the lower Re, the stabilized surfaces do not exhibit any significant degradation in heat transfer with rotation; rather, in the inlet duct, all surfaces experience an increase in heat transfer with Ro. Such a behavior is consistent with the experimental results in Ref. [11] and the numerical study in Ref. [15]. In Ref. [15], it was shown that a multicellular flow pattern exists in the coolant passage and that even the leading surface experiences a downwash over certain regions of the surface leading to enhanced heat transfer on the surface. However, the enhancements along the trailing surface are higher than the leading surface in the inlet channel. At a Ro=0.6, Nu/Nu_0 reaches values of 3.6 on the trailing surface of the inlet duct, and 4 in the bend regions, while the corresponding enhancement along the leading surface in the inlet duct is in the range of 2.2–2.4. In the outlet duct, similar trends are observed with three notable exceptions. First, the enhancement levels are lower with a maximum Nu/Nu_0 value of about 2.4 along the leading surface. Second, along the trailing surface, no enhancement is observed in the fully developed region, and the Nu/Nu_0 values remain relatively unchanged. Third, the leading surface enhancement does not exhibit a monotonic dependence with Ro; rather, the maximum Nu/Nu_0 value is attained at Ro=0.2, beyond which the Nu/Nu_0 values decrease with Ro. This nonmonotonic behavior will be discussed further later. The lower enhancements obtained in the outlet duct are linked to the bend-induced flows that delay or mitigate the establishment of the Coriolis-induced secondary flows.

At Re=40,000 and at higher Re, the Nusselt number distributions and their dependence on Ro are different than those described above for lower Re and conform more to the expected trends of enhancement along the destabilized surface and degradation along the stabilized surface. In the inlet region, the degradation levels are, however, rather low. For example at X/D_h =8.0 (the fully developed region in the inlet) and at Ro=0.2, the Nu/Nu_0 on the trailing wall increases to 1.8 from the stationary passage value of 1.25, while the corresponding decrease in Nu/Nu_0 on the leading wall is negligible. In the bend region, the effect of rotation is similar to that in the inlet although degradation effects are more significant. In the outlet, the Nu/Nu_0 on the leading wall increases with Ro and correspondingly decreases on the trailing wall; however, the degradation effect on the stabilized-trailing wall is more pronounced in the outlet channel compared to that observed on the stabilized wall in the inlet channel.

The rotation effects can be seen more clearly in Fig. 4 (for destabilized surfaces, i.e., inlet trailing and outlet leading) and Fig. 5 (for stabilized surfaces, i.e., inlet leading and outlet trailing), which focus attention on a fixed X/D_h location in the fully developed inlet and outlet regions. For each surface, the figures are plotted separately for the lower Re ($\leq$40,000) and higher Re ($\geq$70,000) ranges for clarity.

Figure 4 shows the Nu/Nu_0 values along the destabilized surfaces where an increase with Ro is expected. Along the outlet-leading surface (Figs. 4(c) and 4(d)), increase in Nu/Nu_0 is observed with Ro until a critical Ro is reached, beyond which Nu/Nu_0 decreases or plateaus. This nonmonotonic behavior was earlier noted in Fig. 3. The AR 1:1 data reported by Wagner et al. [5] at Re=25,000 are also shown in Fig. 4(c) and also display a similar behavior with an increase in the Nu ratio up to a Ro of

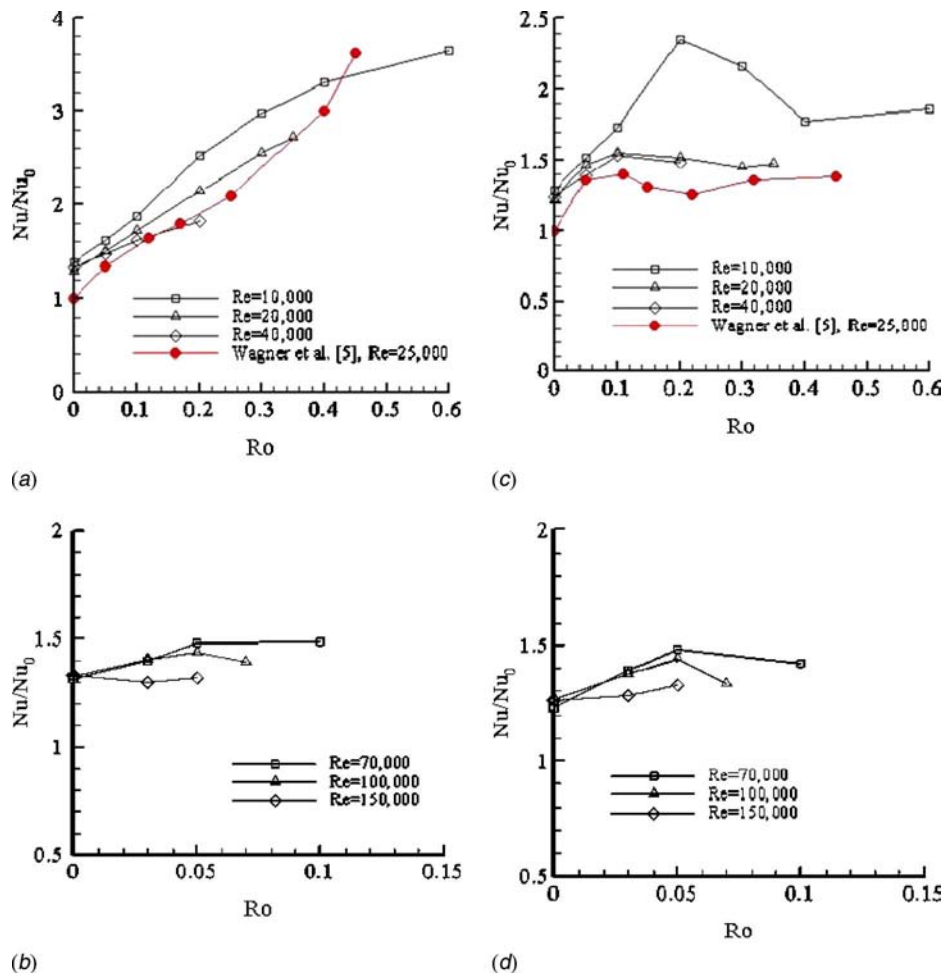**Fig. 4** Rotation effects on destabilized surfaces at DR=0.1. (*a*) and (*b*) inlet-trailing wall at X/D_h=8.0; (*c*) and (*d*) outlet-leading wall at X/D_h=26.7.

about 0.1. The critical Ro appears to be lower for higher Re and is 0.25 for Re=10,000 and 0.05 for Re=100,000. Along the inlet-trailing surface (Figs. 4(*a*) and 4(*b*)), evidence of a similar behavior can also be seen, except that the critical Ro is considerably higher. For Re=10,000, 20,000, and 40,000, this critical Ro does not appear to be reached in our measurements, but at Re =70,000 and 100,000, a plateau in the profile develops around Ro=0.05. At Re=150,000, the plateau in the profile is essentially observed at all Ro, with little or no change in the Nu ratio with Ro. The 1:1 AR data [5] at Re=25,000 shows a monotonic increase with Ro along the inlet-trailing wall. For Ro<0.3, the Nu ratio for the 1:1 AR is less than the Nu ratio for the 4:1 AR (at Re=20,000), as expected based on previously reported measurements [11] and computations [15]. However, at higher Ro, it appears that the 1:1 AR values of the Nu ratio exceed those of the 4:1 AR, implying a greater rotational effect for the 1:1 AR case.

For the stabilized surface (Fig. 5), the inlet-leading wall shows an enhancement with Ro at low Re ($\leqslant$20,000), consistent with the experimental observation in Ref. [11], while the outlet-trailing wall shows reduction in Nu/Nu_0 until a critical Ro, beyond which Nu/Nu_0 increases again. The increase in Nu/Nu_0 along the stabilized surface is linked to the multicellular flow patterns obtained in rotating 4:1 AR ducts [15], which produce a downwash of core fluid even along the stabilized surface. However, this effect is limited to low Re since as observed in Fig. 5, for Re$\geqslant$70,000, Nu/Nu_0 along the stabilized surfaces decrease with Ro, in contrast to the low-Re experimental observations in Ref. [11]. This

strong Re dependence of the effect of rotation on the Nu/Nu_0 ratio has not been previously reported and should clearly be taken into consideration by the turbine heat-transfer designer.

Along the inlet-leading stabilized surface, the present data for 4:1 AR show enhancement with Ro at low Re, while the 1:1 AR data show degradation until Ro=0.25 (Fig. 5(*a*)). This difference in behavior in the present data, with enhancement along the stabilized surface at low Re, was explained earlier and attributed to strong multicellular secondary flow patterns that enhance the heat transfer on the inlet-leading surface. In the 1:1 AR data, enhancement along the stabilized surface is also observed but only at high Ro(Ro$\geqslant$0.25). Saha and Acharya [15] also reported enhancements of the inlet-leading-wall heat transfer for 1:1 AR at Ro $\geqslant$0.25 and linked these to the development of large-wavelength unsteadiness in the flow and the development of two additional counter-rotating vortex pairs, which increased the recirculation. Iacovides and Launder [9] also performed a numerical study and noted the important role of Ro. Their results show that at lower Ro numbers, Coriolis forces produce a single vortex pair. As Ro increases, the vortex pair becomes unstable and breaks into two pairs of vortices. This change in flow pattern was seen to alter the heat transfer characteristics.

Figure 6 presents the averaged Nu/Nu_0 value in the bend region as a function of the rotation number. Data are presented for the leading and trailing surfaces of the bend, and the low- and high-Re plots are separated out for clarity. Rotation number effects in the bend are significant only at the lower Re (10,000 and
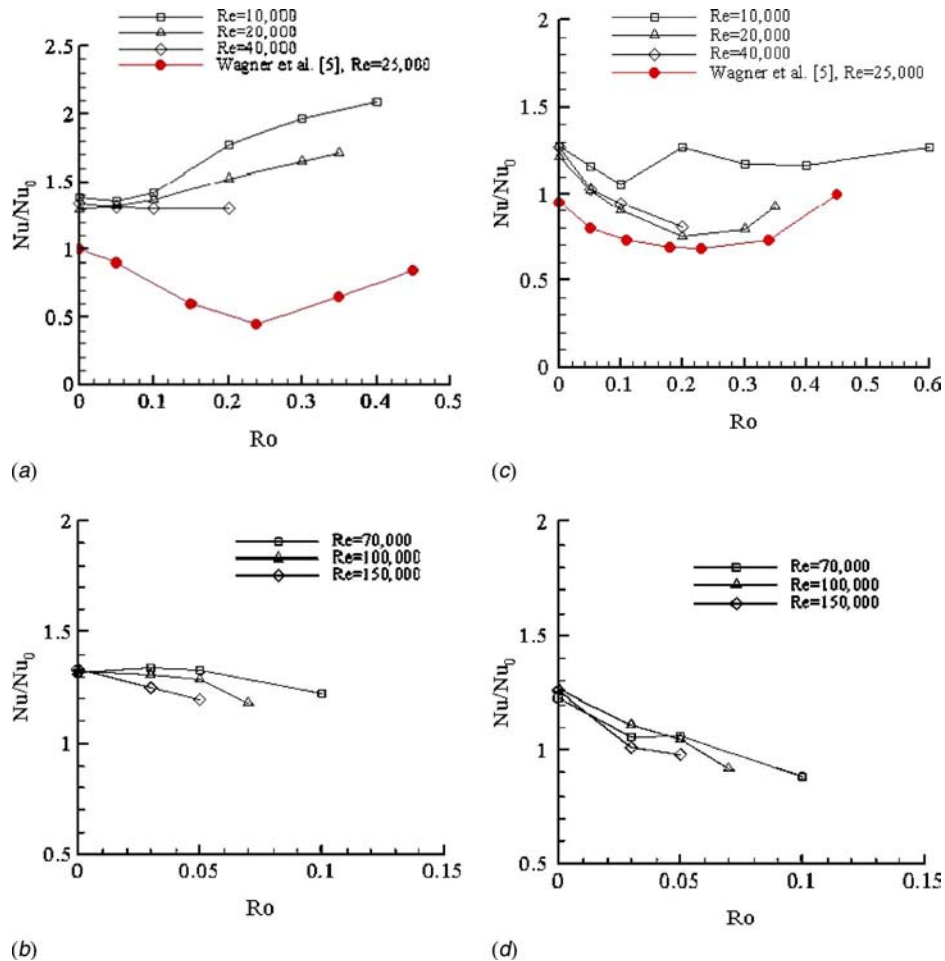
Fig. 5 Rotation effects on stabilized surfaces at DR=0.1. (a) and (b) inlet-leading wall at X/D_h=8.0; (c) and (d) outlet-trailing wall at X/D_h=26.7.

20,000) and behave as in the inlet (radially outward flow) channel. Thus, the trailing surfaces see significant enhancement (Nu/Nu_0 =3.8 at Rp=0.6 and Re=10,000), while the leading surfaces see moderate enhancements up to a Ro of about 0.2 (Nu/Nu_0=2.8 at Re=10,000), beyond which there is a small decrease in the Nu/Nu_0 value. At higher Re values ($\geq$40,000), Nu/Nu_0 values along the trailing and leading surfaces are in the range of 1.8–2, and it would appear that at these higher Re, the bend-induced secondary flows begin to play a more important role, and the primary Coriolis forces that arise from the radial velocity diminish. Note that as the flow turns in the bend, the mean radial velocities (and the primary Coriolis-force component) decrease and reach zero at the 90 deg turning point and then increase again as the flow turns radially inwards in the outlet.

3.3 Density Ratio Effects. To investigate the effects of buoyancy on the Nu/Nu_0, a series of test were conducted, varying the DR, where DR is defined by DR=$(T_w-T_{in})/T_w$. The wall temperature T_w of the copper plates was adjusted for a specific measured inlet air temperature T_{in} to achieve different density ratios DRs at Re=10,000 and 20,000. The buoyancy parameter is proportional to both DR and Ro. Therefore, higher DR or higher Ro imply higher buoyancy parameter values.

Figure 7 shows the average Nu/Nu_0 distribution at Re =20,000 and Ro=0.3 and for three different values of DR. As the DR increases, centrifugal-buoyancy forces are larger. In the inlet duct, the centrifugal-buoyancy opposes the radially outward flow, while in the outlet duct, the centrifugal-buoyancy force aids the radially inward flow. However, as seen in Fig. 7, increasing DR

enhances Nu/Nu_0 in both the inlet and outlet ducts. Centrifugal buoyancy produces opposed/aiding flow effects in the inlet/outlet channel and also influences turbulence through countershear enhancement (in opposed flow situations) or through boundary-layer modifications. Therefore, either through turbulence enhancement (inlet channel) or boundary-layer thinning with aided flow (outlet channel) there is an increase in Nu/Nu_0 with DR.

As seen in Fig. 7, DR does not alter any of the trends observed earlier in Figs. 4 and 5; rather, with increasing DR, Nu/Nu_0 values are enhanced and the trends accentuated. For example, along the inlet-leading surface (Fig. 7(a)), the enhancement observed earlier in Fig. 5 is increased further at the higher DR. Along the outlet duct (Fig. 7(c)) a critical Ro had been observed for DR =0.1, where the enhancement along the destabilized surface and the degradation along the stabilized surface were either reversed or arrested (Fig. 5). At a higher DR of 0.2, the critical Ro, where the change in trend takes place, is lower.

DR effects in the bend region are shown in Fig. 7(b), which indicates that DR has a considerable effect on the leading surface of the bend. Note that DR=0.1 data in Figs. 6 and 7(b) are the same. At a Ro=0.3, the leading-bend surface Nu/Nu_0 increases by nearly 40% when the density ratio increases from 0.1 to 0.2. The effect of DR on the trailing-bend surface is, however, considerably lower.

The centrifugal-buoyancy effects are often presented by plotting Nu/Nu_0 as a function of the buoyancy parameter Bo (=DR*Ro$^{2*}R/D_h$), which contains the centrifugal acceleration term $\Omega^2 R$ and the driving density/temperature ($\Delta\rho$ or ΔT) in the
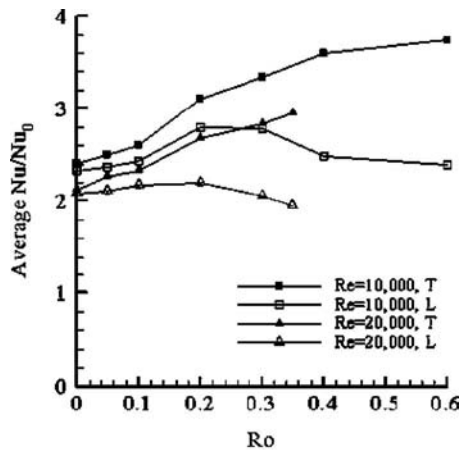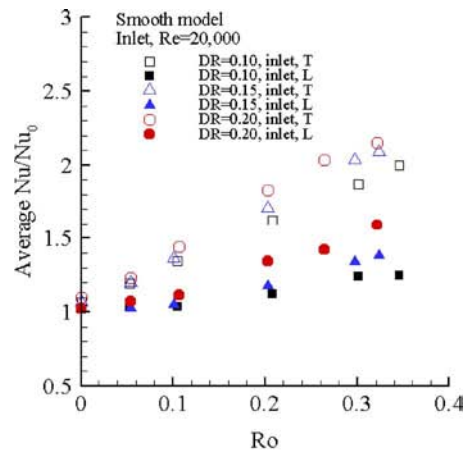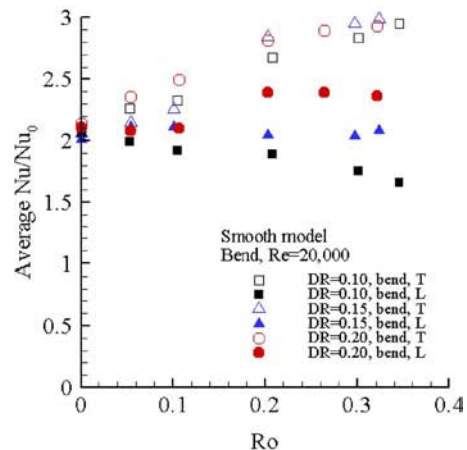
(a)
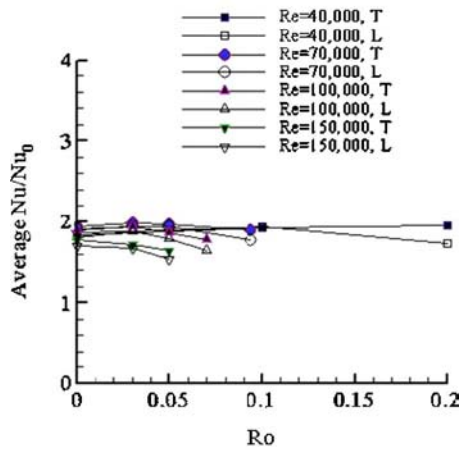
(b)

Fig. 6 Rotational effects on the heat transfer in the bend at DR=0.1.

(a)

(b)

(c)

Fig. 7 Density ratio effects at Re=20,000. (a) Inlet, (b) bend, and (c) outlet.

numerator. This parameter is equivalent to the conventionally used mixed-convection parameter Gr/Re^2, where Gr is the Grashof number containing the gravitational acceleration term g and the driving temperature difference ΔT in the numerator. The centrifugal-buoyancy effects at Re=20,000 are shown in Fig. 8 for both the inlet and outlet channels. Figure 8 has the same data set as that used in Figs. 7(a) and 7(c), but the former plotted as a function of the combined buoyancy parameter (Bo).

In general, the data at different DR collapse quite well. In the inlet channel, the average Nu/Nu_0 along the leading and trailing walls increases monotonically and becomes asymptotic with Bo on both walls (Fig. 8(a)). These are similar to the results of Wagner et al. [5] on the trailing wall in a square channel at Re =25,000. However, along the leading wall, Wagner et al. [5] observed a decrease in Nu/Nu_0 with Bo up to 0.2. The difference is likely caused by the fact that the Coriolis force is stronger in the square channel than in the AR 4:1 rectangular channel. In the inlet channel with a radially outward flow, the rotational buoyancy force aids the heat transfer on both leading and trailing walls, while the Coriolis force enhances heat transfer on the trailing wall, but degrades the heat transfer on the leading wall. On the inlet-trailing walls of square and AR 4:1 rectangular channels, heat transfer is enhanced by both the rotational buoyancy force and the Coriolis force, so Nu/Nu_0 on the inlet-trailing walls increases monotonically with Bo. However, on the inlet-leading walls, the Coriolis force weakens the heat transfer, while, the rotational buoyancy force still enhances the heat transfer. On the leading wall of square channel, the Coriolis effect is stronger and
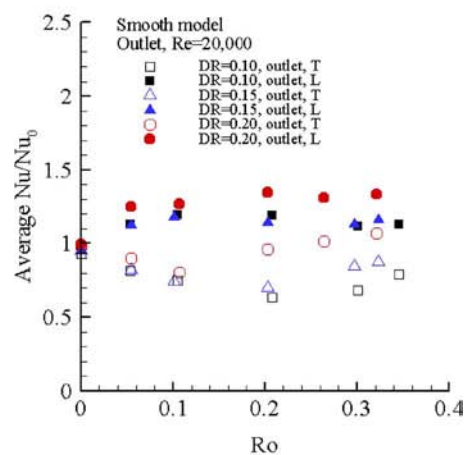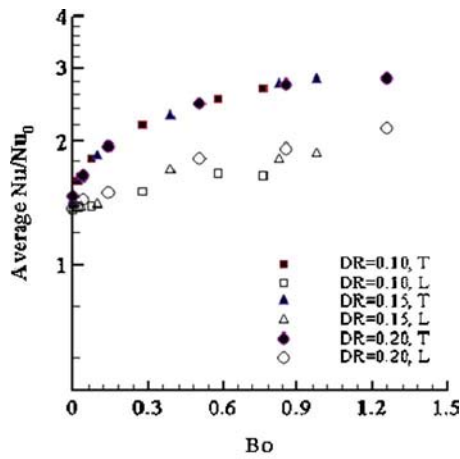
Nu/Nu_0 decreases as Bo increases when Bo is less than 0.2 [5]. However, as Bo exceeds 0.2, the rotational buoyancy effect becomes significant and overcomes the Coriolis effect. Thus, beyond this point, the heat transfer is enhanced on the inlet-leading wall, and Nu/Nu_0 begins to rise with Bo. For the AR 4:1 channel, the Coriolis effect is weaker and rotational buoyancy effects are stronger even at small Bo values. Therefore, the heat transfer is enhanced on the inlet-leading wall in the AR 4:1 channel due to the
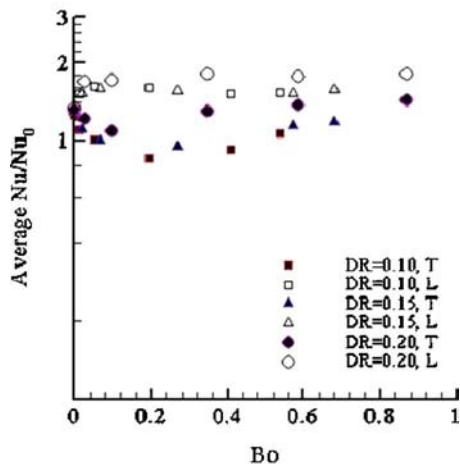
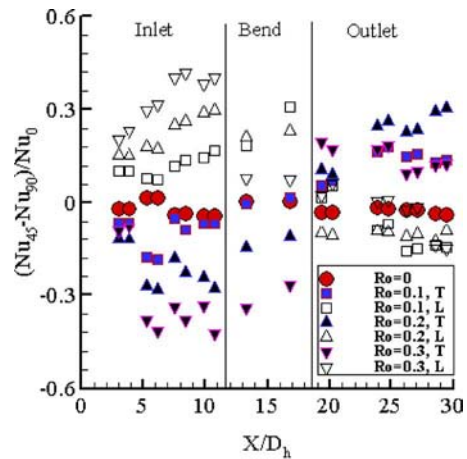Fig. 8 Average Nu/Nu_0 versus buoyancy parameter at Re =20,000. (a) Inlet and (b) outlet.

Fig. 9 Orientation effects with orientation angles 90 deg and 45 deg, DR=0.1, and (a) Re=20,000 and (b) Re=70,000

coupled effects of Coriolis and rotational buoyancy forces. Hence, a monotonic increase of Nu/Nu_0 with Bo is observed for the 4:1 AR in contrast to the 1:1 AR.
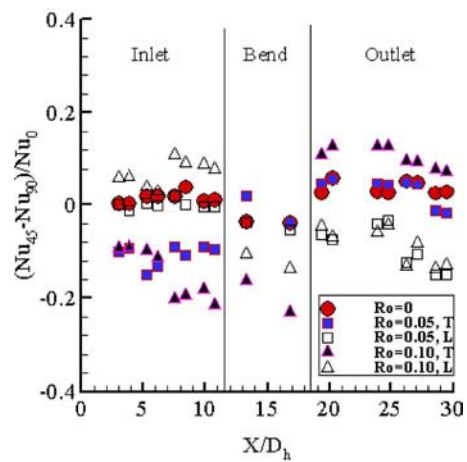
In the outlet channel (Fig. 8(b)), the observed behavior is qualitatively similar to that observed for a square channel [5]. The heat transfer on the outlet-leading wall of the AR 4:1 channel increases initially with Bo and then quickly asymptotes beyond Bo of 0.05. Along the outlet-trailing wall, the heat transfer first decreases due to the Coriolis effect, but beyond a Bo of 0.2, the heat transfer increases with Bo due to the increasingly important role of the centrifugal buoyancy. For a square channel, this turning point is about 0.15 [5].

3.4 Orientation Effects. Results shown previously were obtained for the 90 deg orientation angle, where the orientation angle is defined as the counterclockwise angle between the plane parallel to the leading or trailing wall and the plane of rotation. To examine orientation effects, the test model was turned to an orientation angle of 45 deg. Two Re values Re=20,000 and Re =70,000 were investigated at this orientation angle with DR =0.1.

With a 90 deg orientation, the Coriolis force is orthogonal to the flow direction, and, as discussed earlier, the resulting secondary flows are directed from the leading (stabilized) to the trailing (destabilized) surface in the inlet duct and in the opposite direction in the outlet duct. With a 45 deg orientation, the Coriolis force is no longer orthogonal to the leading and trailing surfaces.

Instead, it is directed at a 45 deg angle to the leading/trailing surfaces. Thus, the secondary flows are expected to be directed from the outer-stabilized side to the inner-destabilized side, where outer and inner refer to the position of the side walls. In view of the altered secondary flow pattern, the leading surface of the inlet duct and the trailing surface of the outlet duct can no longer be viewed as stabilized surfaces since flow lifts off near one corner and impinges near the other corner (assuming a counter-rotating secondary vortex pair).

Figure 9 shows the orientation effects at Re=20,000 and 70,000. The results are presented in the form of Nu/Nu_0 change $(=(Nu_{45}-Nu_{90})/Nu_0)$ versus X/D_h at different Ro numbers. Thus, a positive value for the Nu/Nu_0 change implies enhancement in Nu in the 45 deg orientation, while a negative value implies a corresponding reduction in Nu.

The Nu/Nu_0 change is nearly zero for the stationary case (Ro =0), as expected. The orientation effects become more significant as Ro increases. In the inlet duct, as Ro is increased, the trailing surface is associated with negative Nu/Nu_0 change values, implying a reduction in heat transfer relative to the 90 deg orientation. This reduction is directly linked to the fact that the secondary flows no longer impinge orthogonally onto the midspan of the surface, but instead impinge at an angle closer to the inner-trailing surface corner. On the leading surface of the inlet duct, the positive values of the Nu/Nu_0 change obtained imply higher values of Nu/Nu_0 in the 45 deg orientation and are again linked to the
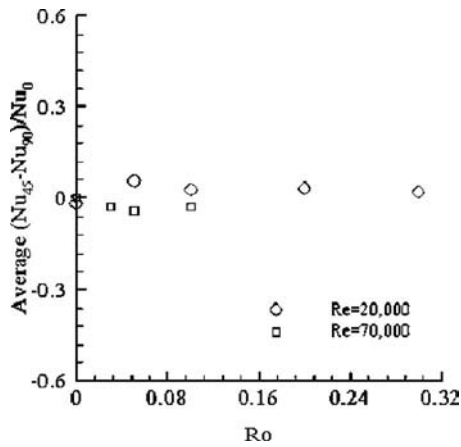
Fig. 10 Total average of $(Nu_{45} - Nu_{90})/Nu_0$ on the four walls (inlet leading and trailing and outlet leading and trailing)

altered secondary flow patterns. In the outlet duct, with the 45 deg orientation higher values of Nu/Nu_0 are again obtained on the stabilized-trailing surface, while lower values are obtained on the destabilized-leading surface. The orientation-induced changes are seen to be quite significant $Re = 20,000$, with a maximum change of about $\pm 30\%$ at $Ro = 0.3$, which decrease with Re. At $Re = 70,000$, the maximum Nu/Nu_0 change is $\pm 20\%$.

In the bend region, orientation effects are also seen to be important with degradation levels of the order of 30% on the leading side of the bend. Figure 9 shows that the 45 deg orientation reduces Nu/Nu_0 on the leading side and enhances it on the trailing side. At a lower Re (20,000), in the bend region, degradation in Nu/Nu_0 is primarily observed with the 45 deg orientation.

Averaging $(Nu_{45} - Nu_{90})/Nu_0$ on both walls shows that the orientation angle had almost no effect on the overall Nu/Nu_0 of the channel (Fig. 10). This implies that orientation effects on the stabilized walls and on the destabilized walls nearly cancel each other out.

3.5 Frictional Factors. During the experiments, the absolute pressure in the entrance of the test section and the pressure drop in the inlet were measured. Figure 11 shows the friction factor values in the range of 1.2–1.4 for $Re = 70,000$, 100,000, and 150,000 with $DR = 0.1$ and an orientation angle of 90 deg, and shows that Ro does not produce significant changes in the friction factor. No significant changes in the friction factors were observed with a variation of density ratio or change of orientation, and are therefore not presented here.
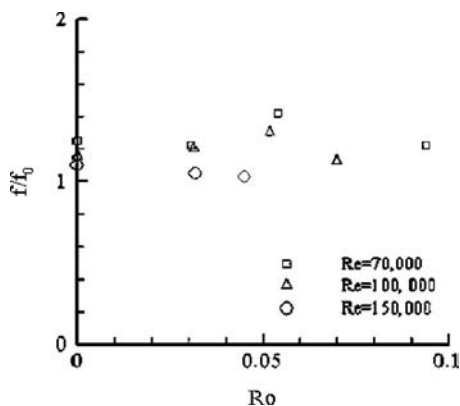

Fig. 11 Frictional factors in the inlet at $DR = 0.1$

4 Concluding Remarks

An experimental study has been undertaken in a rotating heat-transfer rig to provide heat-transfer measurements in a 4:1 AR smooth coolant passage for a wide range of Reynolds number and rotation numbers. A maximum Reynolds number of 150,000 and a maximum rotation number of 0.6 are achieved in the study. These maximum parameter values are considerably higher than those previously reported for the 4:1 AR geometry and provide data for parameter ranges that may be representative of certain modern engines. The following are the main conclusions reached.

1. On the destabilized surfaces of the inlet channel (trailing wall) and outlet channel (leading wall), rotation enhances the heat transfer up to a certain Ro, beyond which the enhancement is flat or reduced. Ro, where the expected trends alter, are different in the outlet and inlet channels and are higher at lower Re.
2. On the stabilized surface of the inlet channel (leading wall), rotation produces an enhancement of heat transfer at low Re but exhibits a degradation at high Re ($\geqslant 40,000$). For the trailing wall of the outlet channel, rotation also enhances the heat transfer at low Re but only at higher Ro.
3. Rotational effects are important in the bend region at lower Re (Re $\leqslant 20,000$), with significant enhancement along the bend-trailing surface.
4. Higher density ratio enhances heat transfer on both leading and trailing walls of the inlet, bend, and outlet. In the bend region, the enhancement is more significant on the leading surface. The enhancement also becomes stronger as the rotation number increases.
5. The Nusselt number ratio appears to correlate well with the buoyancy parameter Bo, particularly in the inlet channel where Nu/Nu_0 increases with Bo along both leading and trailing surfaces, and to indicate an important role of centrifugal buoyancy. In the outlet channel, nonmonotonic effects of Nu/Nu_0 with Bo can be seen due to the relative effects of buoyancy and Coriolis forces, but the variations in Nu/Nu_0 with Bo are small.
6. Orientation has an important effect on the heat transfer from the leading and trailing surfaces with peak changes of the order of 30% between the 90 deg and 45 deg orientations. In the 45 deg orientation, the heat transfer from the destabilized surfaces reduces while the heat transfer from the stabilized surface increases relative to the 90 deg orientation. The channel-averaged heat transfer is, however, insensitive to orientation.

Acknowledgment

Nomenclature

$$A = \text{area}$$
$$Bo = \text{buoyancy parameter, } DR^*Ro^{2*}R/D_h$$
$$C_p = \text{specific heat}$$
$$D = \text{diameter}$$
$$DR = \text{coolant to wall density ratio at the inlet, } (\rho_w - \rho_b)/\rho_w = (T_w - T_b)/T_w$$
$$F = \text{force}$$
$$f = \text{average friction factor}$$
$$H = \text{the height of the channel cross section}$$
$$h = \text{heat-transfer coefficient}$$
$$I = \text{current applied to heater}$$
$$k = \text{heat conductivity of air, or 1000 in representing Re values}$$
$$L = \text{channel length}$$
$$\dot{m} = \text{mass flow rate}$$

Nu = Nusselt number
P = pressure or rib pitch
Pr = Prandtl number
ΔP = pressure drop
q = heat transferred through copper element
q'' = heat flux per unit area
R = resistance of heater or rotational radius
Re = Reynolds number, $\rho V D / \mu$
Ro = Rotation number, $\Omega D_h / V$
T = temperature
TPF = thermal performance factor, $(\mathrm{Nu}/\mathrm{Nu}_0)/(f/f_0)^{1/3}$
V = average velocity
W = the width of the channel cross section; ribs are located on these two walls
X = distance along the streamwise direction
Ω = rotational speed
ρ = density of air
ν = kinematics viscosity

Subscripts

0 = smooth conditions
b = bulk value
h = hydraulic
i = the ith copper plate
w = wall

References

[1] Mori, Y., Fukada, T., and Nakayama, W., 1971, "Convective Heat Transfer in a Rotating Circular Pipe (Second Report)," Int. J. Heat Mass Transfer, **14**, pp. 1807–1824.

[2] Metzger, D. E., and Stan, R. L., 1977, "Entry Region Heat Transfer in Rotating Radial Tubes," J. Energy, **1**(5), pp. 297–300.

[3] Morris, W. D., and Ayhan, T., 1979, "Observations on the Influence of Rotation On Heat Transfer in the Cooling Channels of Gas Turbine Rotor Blades," Proc. Inst. Mech. Eng., **193**, pp. 303–311.

[4] Wagner, J. H., Johnson, B. V., and Hajek, T. J., 1991, "Heat Transfer in Rotating Passages With Smooth Walls and Radial Outward Flow," ASME J. Turbomach., **113**, pp. 42–51.

[5] Wagner, J. H., Johnson, B. V., and Kopper, F. C., 1991, "Heat Transfer in Rotating Serpentine Passages With Smooth Walls," ASME J. Turbomach., **113**, pp. 321–330.

[6] Mochizuki, S., Takamura, J., Yamawaki, S., and Yang, W.-J., 1994, "Heat Transfer in Serpentine Flow Passages With Rotation," ASME J. Turbomach., **116**, pp. 133–140.

[7] Guidez, J., 1989, "Study of the Convective Heat Transfer in a Rotating Coolant Channel," ASME J. Turbomach., **111**, pp. 43–51.

[8] Morris, W. D., and Ghavami-Nasr, G., 1991, "Heat Transfer Measurements in Rectangular Channel With Orthogonal Mode Rotation," ASME J. Turbomach., **113**, pp. 339–345.

[9] Iacovides, H., and Launder, B. E., 1991, "Parametric and Numerical Study of Fully Developed Flow and Heat Transfer in Rotating Rectangular Ducks," ASME J. Turbomach., **113**, pp. 331–338.

[10] Soong, C. Y., Lin, S. T., and Hwang, G. J., 1991, "An Experimental Study of Convective Heat Transfer in Radially Rotating Rectangular Ducts," ASME J. Heat Transfer, **113**, pp. 604–611.

[11] Griffith, T. S., Al-Hadhrami, L., and Han, J. C., 2002, "Heat Transfer in Rotating Rectangular Cooling Channels (AR=4) With Angled Ribs," ASME J. Heat Transfer, **124**, pp. 1–9.

[12] Kays, W. M., and Crawford, M. E., 1993, *Convective Heat and Mass Transfer*, 3rd ed., McGraw-Hill, New York.

[13] Kline, S. J., and McClintock, F. A., 1953, "Describing Uncertainties in Single-Sample Experiments," Mech. Eng. (Am. Soc. Mech. Eng.), **75**(1), pp. 3–8.

[14] Han, J. C., Park, J. S., and Ibrahim, M. Y., 1986, "Measurement of Heat Transfer and Pressure Drop in Rectangular Channels With Turbulence Promoters," NASA Contractor Report No. CR 4015.

[15] Saha, A., and Acharya, S., 2004, "Unsteady RANS Simulations of Turbulent Flow and Heat Transfer in Ribbed Coolant Passages of Different Aspect Ratios," Int. J. Heat Mass Transfer, **48**(23–24), pp. 4704–4725.

[16] Willett, F. T., and Bergles, A. E., 2001, "Heat Transfer in Rotating Narrow Rectangular Ducts With Heated Sides Oriented at 60 deg to the R-Z Plan," ASME J. Turbomach., **123**, pp. 288–295;

Mass (Heat) Transfer Downstream of Blockages With Round and Elongated Holes in a Rectangular Channel

H. S. Ahn

S. W. Lee

S. C. Lau[1]

D. Banerjee

Convective Heat and Mass Transfer Laboratory,
Department of Mechanical Engineering,
Texas A&M University,
College Station, TX 77843-3123

Turbulent forced convective mass (heat) transfer downstream of blockages with round and elongated holes in a rectangular channel was studied. The blockages and the channel had the same 12:1 (width-to-height ratio) cross section, and a distance equal to twice the channel height separated consecutive blockages. The diameter of the holes was either 0.5 or 0.75 of the height of the channel. Naphthalene sublimation experiments were conducted with four hole aspect ratios (hole-width-to-height ratios) between 1.0 and 3.4, two hole-to-channel area ratios (ratios of total hole cross-sectional area to channel cross-sectional area) of 0.2 and 0.3, and Reynolds numbers (based on the channel hydraulic diameter) of 7000 and 17,000. The effects of the hole aspect ratio, for each hole-to-channel area ratio, on the average mass (heat) transfer and the local mass (heat) transfer distribution on the exposed primary channel wall between consecutive blockages were examined. The results of the study showed that the blockages with holes caused the average mass (heat) transfer to be as high as about eight times that for fully developed turbulent flow through a smooth channel at the same mass flow rate. The elongated holes caused higher overall mass (heat) transfer and larger spanwise variation of the local mass (heat) transfer on the channel wall than round holes. [DOI: 10.1115/1.2767748]

Keywords: forced convection, heat transfer enhancement, turbulent flow, naphthalene sublimation

Introduction

To protect the vanes and the blades in gas turbine engines from the hot combustion gases, air from the compressors is forced to flow through shaped internal cooling passages. The cooling air leaves the airfoils through strategically located film cooling holes on the pressure and suction walls, and at the tips of the airfoils, and through slots along the trailing edges of the airfoils. Along the internal cooling passages, there may be holes for impingement cooling of the airfoil leading edges, which are subjected to very high heat fluxes. There may be turbulators on the surfaces of the straight or serpentine internal cooling channels, and pin fins in the channels near the trailing edges, to enhance the heat transfer to the cooling air. Han et al. [1] presented a comprehensive survey of published experimental and numerical studies of internal cooling of gas turbine airfoils. Other recent studies, such as Refs. [2–8], gave the latest accomplishments of several research groups that have conducted research on internal cooling of gas turbine airfoils.

In a design concept for protecting the trailing edge region of an airfoil, cooling air is forced to flow through two to three blockages with staggered holes, before it exits the airfoil through the trailing edge slots. Each blockage has the same cross section as the flow cross section between the pressure and suction walls. After passing through the holes along a blockage, the cooling air impinges onto the next blockage and is deflected toward the suction and pressure walls of the airfoil before it passes through the staggered holes along the next blockage.

In Ref. [9], the tail region of an airfoil with these blockages was modeled as two converging rectangular channels. Air flowed through elongated holes with rounded edges along two blockages in each channel, after the air made a right-angled turn in an entrance channel. Downstream of the second blockage, the air exited through slots separated by lands with rounded leading edges. Two different entrance channels and two exit slot configurations were considered. Naphthalene sublimation experiments were conducted to determine the overall mass transfer coefficients and the distributions of the local mass transfer coefficient on the walls between the two blockages and between the second blockage and the exit slots. The analogy between heat transfer and mass transfer was used to relate the experimentally determined mass transfer enhancement to heat transfer enhancement.

Moon and Lau [10] conducted experiments with thermochromic liquid crystals to obtain the average heat transfer coefficients and the local heat transfer distributions on one of the channel walls between two blockages with round holes, and the overall pressure drops across the blockages, for nine different staggered configurations of holes in the blockages. Lau et al. [11] conducted naphthalene sublimation experiments to study heat transfer enhancement by blockages with staggered round holes and square holes with rounded corners for turbulent airflows through a wide rectangular channel.

There have been a number of other heat transfer studies on turbulent flows through channels with perforated blockages or blockages with various openings for flows to pass through, such as Kukreja and Lau [12], Hwang et al. [13], Liou and Chen [14], and Buchlin [15]. However, the blockages in these studies had cross sections that were much smaller than the cross sections of the channels such that air flowed over the blockages as well as through the openings in the blockages.

The objective of this study was to examine, for turbulent airflow through holes in blockages, the effects of the aspect ratio (width-to-height ratio) of the holes and the hole-to-channel area ratio on the overall heat transfer and local heat transfer distribu-
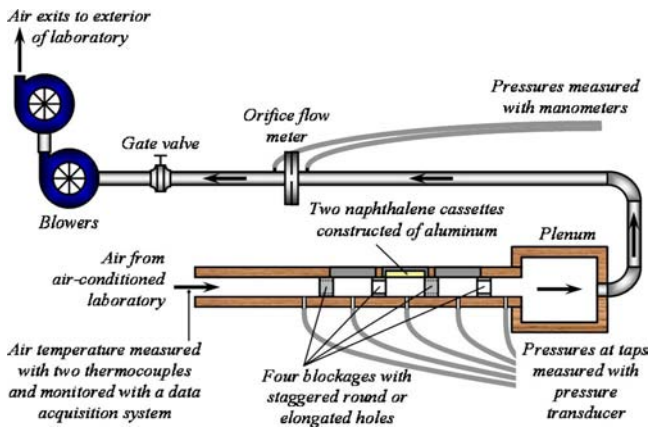

Fig. 1 Schematic of test apparatus for mass transfer experiments (not to scale)

tions on the two principal walls between consecutive blockages, and the pressure drops across the blockages. These blockages were oriented perpendicular to the main flow direction in a wide rectangular channel and had the same cross section as the flow channel. Naphthalene sublimation experiments were conducted to obtain the overall mass transfer and local mass transfer distributions for two flow rates corresponding to Reynolds numbers (based on the channel hydraulic diameter) of 7000 and 17,000. The heat and mass transfer analogy was used to relate the mass transfer enhancement to heat transfer enhancement. This parametric study was different from Lau et al. [9] in which blockages with two specific hole configurations (elongated holes with rounded edges) in two converging rectangular channels with specific dimensions and entrance and exit configurations were considered.

Test Apparatus

The main components of the test apparatus for this study are the test section, a settling chamber, an orifice flow meter, a control valve, and two centrifugal blowers (Fig. 1). The test section is a rectangular channel that has a cross section of 30.5 cm (width) $\times$ 2.54 cm (height), and thus, an aspect ratio of 12:1. The walls of the test section are constructed of 1.27-cm-thick oak plywood. As shown in the schematic of the top view of the test section with the top wall removed in Fig. 2, there are four blockages with round or elongated holes in the test section. These blockages have the same cross section as the cross section of the test section. They are constructed of acrylic and are 1.14 cm thick, and the distance between consecutive blockages is equal to 5.08 cm, or, two times the height of the channel. Figure 2 also shows that the holes in
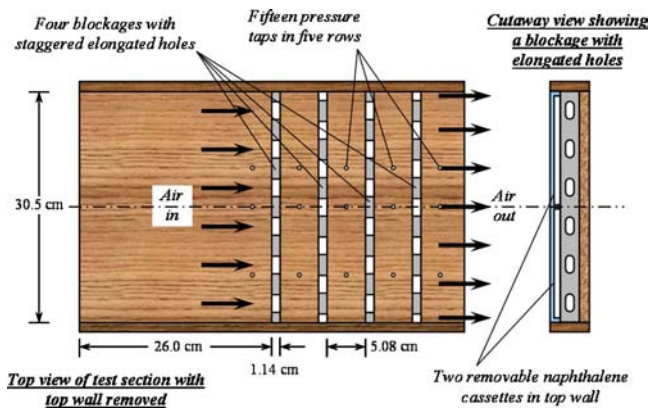

Fig. 2 Schematic of test section showing four blockages with elongated holes and naphthalene cassettes in top wall
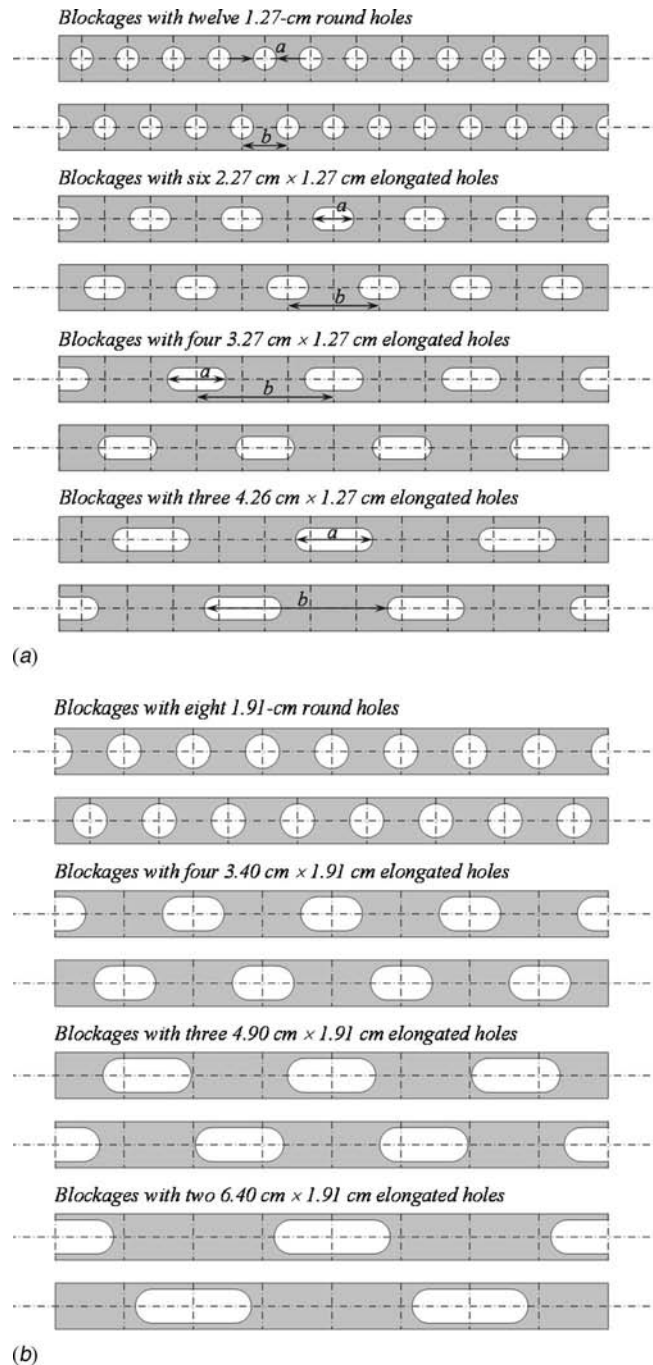
Fig. 3 (a) Blockages with round or elongated holes; diameter of holes equals $\frac{1}{2}$ of channel height. (b) Blockages with round or elongated holes; diameter of holes equals $\frac{3}{4}$ of channel height.

consecutive blockages are staggered to induce secondary flows, as air passes through the blockages during an experiment, to enhance the mass transfer on the exposed surfaces of the primary walls of the test channel.

For this study, the round or elongated holes in the four blockages have a diameter of either 1.27 cm or 1.91 cm, or, $\frac{1}{2}$ or $\frac{3}{4}$ of the height of the channel. There are eight sets of blockages with different hole configurations. Figures 3(a) and 3(b) show the blockages with holes that have diameters of 1.27 cm and 1.91 cm, respectively. Table 1 lists the dimensions of the holes and the spacings between holes in the various blockages. While the aspect

Table 1 Dimensions of holes in blockages

Smaller holes, $d=1.27$ cm	Case S-1	Case S-2	Case S-3	Case S-4
Number of holes in each blockage	12	6	4	3
Shape of holes	Round	Elongated	Elongated	Elongated
Width of holes, a	1.27 cm	2.27 cm	3.27 cm	4.26 cm
Center-to-center spacing between holes, b	2.54 cm	5.08 cm	7.62 cm	10.16 cm
Cross-sectional area of each hole	1.27 cm^2	2.53. cm^2	3.80 cm^2	5.07 cm^2
Aspect ratio of holes	1.00	1.79	2.57	3.36
Total hole-to-channel area ratio	0.196	0.196	0.196	0.196

Larger holes, $d=1.91$ cm	Case L-1	Case L-2	Case L-3	Case L-4
Number of holes in each blockage	8	4	3	2
Shape of holes	Round	Elongated	Elongated	Elongated
Width of holes, a	1.91 cm	3.40 cm	4.90 cm	6.40 cm
Center-to-center spacing between holes, b	3.81 cm	7.62 cm	10.66 cm	15.24 cm
Cross-sectional area of each hole	2.85 cm^2	5.70 cm^2	8.55 cm^2	11.40 cm^2
Aspect ratio of holes	1.00	1.79	2.57	3.36
Total hole-to-channel area ratio	0.295	0.295	0.295	0.295

ratio of the holes ranges from 1.00 (round holes) to 3.36, and the total number of holes varies from 2 to 12, the ratios of the total hole-to-channel cross-sectional areas are kept constant and are equal to about 0.2 and 0.3, respectively, in the $d=1.27$ cm and $d=1.91$ cm cases.

Measurements of Average and Local Mass Transfer

The top wall of the test channel consists of three rectangular slots into each of which a removable section of the top wall may be inserted (Fig. 1). To facilitate the measurements of the overall mass transfer coefficient and the distribution of the local mass transfer coefficient on the exposed surface of one of the primary walls between two blockages, two naphthalene cassettes are inserted into the slot between the two blockages in the top wall. Each cassette is constructed of aluminum and is about half as wide as the test channel. Each cassette has a 2.0-mm-deep cavity that is filled with naphthalene during a casting process. Once installed, the two cassettes rest side by side in the slot, on top of the two blockages and the test channel sidewalls, exposing a smooth, flat, naphthalene surface. During an experiment, mass is transferred from the naphthalene surfaces of the two cassettes to the air that flows through the test channel and the holes in the blockages, but all other surfaces exposed to the air are mass transfer inactive.

The two naphthalene cassettes are designed such that they can be quickly inserted into and removed from one of the three slots in the top wall. At the beginning and at the end of an experiment for determining the average mass transfer coefficient, the cassettes are weighed one at a time with a Sartorious electronic balance, which has a range of up to 160.0 g and a resolution of 0.1 mg.

To determine the distribution of the local mass transfer coefficient in an experiment, the elevations at a grid of 1100 points (50×22) on the naphthalene surface and on the top surface of the rim of each cassette are measured with a Starrette electronic depth gage at the beginning and at the end of the experiment. The depth gage has a lever type LVDT head, a range of ± 0.2 mm, and a resolution of 0.002 mm. A Velmax NF90 controller, two stepper motors, a desktop computer, National Instruments data acquisition hardware, and a LABVIEW computer program are used to move the cassette on a coordinate table into position to facilitate the elevation measurements and to record the output from the electronic depth gage. The elevation measurements on the top surface of the rims of the cassette are needed to determine two reference planes of the naphthalene surface for calculating the elevation changes at the almost 1000 points on the naphthalene surface.

During an experiment, air is drawn into the test channel from the air-conditioned laboratory and exits the test apparatus to the outside of the building in which the laboratory is located. The temperature of the air is measured with two thermocouples and

monitored with the computer controlled data acquisition system throughout the duration of the experiment. These thermocouples are calibrated with a constant temperature bath against a calibrated standard that is traceable to NIST. Also, before each experiment, the electronic depth gage or the electronic balance is calibrated with calibration standards that are supplied by the respective manufacturer.

To ensure the accuracy of the measured mass transfer data, each experiment is repeated multiple times. Supplementary experiments are conducted to check the calibration of the orifice flow meter (along with the manometers) and to determine the amounts of mass transfer during blower startup and shutdown for the experiments. The mass transfer corrections are needed because the duration of an experiment is defined as the period of time during which air flows steadily through the test channel.

Data Reduction

The overall and local mass transfer coefficients are defined, respectively, as

$$\bar{h}_m = \frac{\Delta M_n / \Delta t}{A_s(\rho_{v,w} - \bar{\rho}_{v,b})} \tag{1}$$

$$h_m = \frac{\dot{M}''_n}{\rho_{v,w} - \rho_{v,b}} = \frac{\rho_s \Delta z / \Delta t}{\rho_{v,w} - \rho_{v,b}} \tag{2}$$

where ΔM_n is the net mass transfer from a naphthalene surface to the air, $\dot{M}''_n$ is the local naphthalene mass flux, Δz is the local change of elevation on the naphthalene surface, Δt is the duration of the experiment, and ρ_s is the density of solid naphthalene. In the above equations, $\rho_{v,w}$ is the local vapor density of naphthalene at the wall and is evaluated using the ideal gas law, in which the vapor pressure is determined using the vapor pressure-temperature correlation for naphthalene by Ambrose et al. [16].

$$T_w \log(p_{v,w}) = \frac{a_0}{2} + \sum_{s=1}^{3} a_s E_s(x) \tag{3}$$

with

$$E_1(x) = x \quad E_2(x) = 2x^2 - 1 \quad \text{and} \quad E_3(x) = 4x^3 - 3x \tag{4}$$

where $a_0 = 301.6247$, $a_1 = 791.4937$, $a_2 = -8.2536$, and $a_3 = 0.4043$, and $x = (2T_w - 574)/114$.

The average bulk vapor density of naphthalene, $\bar{\rho}_{v,b}$, in Eq. (1) is the average of the bulk vapor densities at the upstream and downstream edges of the naphthalene surface and is calculated as

$$\bar{\rho}_{v,b} = \frac{1}{2}\left[\left(\frac{\dot{M}_n}{\dot{V}}\right)_{upstream} + \left(\frac{\dot{M}_n}{\dot{V}}\right)_{downstream}\right] \qquad (5)$$

The bulk vapor density is equal to zero upstream of the naphthalene surface, because there is no naphthalene vapor in the air passing through the holes in the upstream blockage. The local bulk vapor density, $\rho_{v,b}$, in Eq. (2) for determining the local mass transfer coefficient at a point on the naphthalene surface is the rate of total mass transfer from the naphthalene surface upstream of the point divided by the air volumetric flow rate.

The average and local Sherwood numbers are defined, respectively, as

$$\overline{Sh} = \frac{\bar{h}_m D_h}{\sigma} \qquad (6)$$

$$Sh = \frac{h_m D_h}{\sigma} \qquad (7)$$

where σ is the mass diffusion coefficient for naphthalene vapor in the air. A correlation suggested by Goldstein and Cho [17] is used to determine the mass diffusion coefficient.

$$\sigma = 0.0681\left(\frac{T}{298.16}\right)^{1.93}\left(\frac{1.013 \times 10^5}{p}\right) \times 10^{-4} \qquad (8)$$

According to the analogy between heat transfer and mass transfer described in Ref. [18],

$$\frac{\overline{Nu}}{Nu_0} = \frac{\overline{Sh}}{Sh_0} \qquad (9)$$

$$\frac{Nu}{Nu_0} = \frac{Sh}{Sh_0} \qquad (10)$$

where the reference Nusselt number and Sherwood number are based on the Dittus-Boelter correlation that is for a fully developed turbulent flow at the same Reynolds number through a smooth channel with the same hydraulic diameter as the test channel.

$$Nu_0 = 0.023 Re^{0.8} Pr^{0.4} \qquad (11)$$

$$Sh_0 = 0.023 Re^{0.8} Sc^{0.4} \qquad (12)$$

where Pr is the Prandtl number and Sc is the Schmidt number determined by

$$Sc = 2.28\left(\frac{T}{298.16}\right)^{-0.1526} \qquad (13)$$

The Reynolds number for the airflow through the test section is

$$Re = \frac{4\dot{m}}{\mu P_w} = \frac{2\dot{m}}{\mu(W+H)} \qquad (14)$$

where $\dot{m}$ is the mass flow rate of air, μ is the dynamic viscosity of air, P_w is the wetted perimeter of the test section, and W and H are the width and the height of the test section, respectively.

Based on the average pressure drop across two consecutive blockages, the friction factor is determined as

$$f = \frac{(\Delta p/\Delta x)D_h}{\rho \bar{u}^2/2} = 2\rho\left(\frac{\Delta p}{\Delta x}\right)D_h\left(\frac{A_c}{\dot{m}}\right)^2 \qquad (15)$$

where Δx is the distance between pressure taps for measuring the pressure drops across two consecutive blockages, $\bar{u}$ is the average air velocity, and A_c is the cross-section area of the test channel. The friction factor is compared with a reference friction factor that is for fully developed turbulent flow in the channel with smooth walls.

$$f_0 = [0.79 \ln(Re) - 1.64]^{-2} \qquad (16)$$

The calculations of the uncertainty values of the Reynolds number, the Sherwood number, and the friction factor are based on a confidence level of 95%, uncertainty values of ±1.0% for all properties of the air, and ±0.5% for all physical dimensions [19]. Based on the maximum uncertainties for pressure at the orifice flow meter, the pressure drop across the orifice, and the Reynolds number for flow through the orifice flow meters of ±2.0%, ±3.9%, and ±2.4%, respectively, the maximum uncertainty of the air mass flow rate is calculated to be ±2.2%. The corresponding maximum uncertainty of the Reynolds number is ±2.5%.

Based on the uncertainty values of ±6.3% for ΔM_n, ±4.3% for $\rho_{v,w}$, and ±6.5% for $\rho_{v,b}$, the maximum uncertainty of the average mass transfer coefficient is found to be ±7.9%. Similarly, using uncertainty values of ±1.0% for ρ_s, ±9.5% for Δz, and ±0.1% for Δt, the maximum uncertainty of the local mass transfer coefficient is calculated to be ±10.4%. With the uncertainty value of ±2.0% for the diffusion coefficient of naphthalene vapor in air using the equation suggested by Goldstein and Cho [17], the estimated values of the maximum uncertainties for the average and local Sherwood numbers are ±8.2% and ±10.6%, respectively.

Using the maximum uncertainty values of ±6.8% for Δp and ±2.2% for $\dot{m}$, the maximum value of the uncertainty of the friction factor is estimated to be ±8.4%.

Presentation and Discussion of Results

According to the heat/mass transfer analogy [18], local and average heat transfer coefficients, and heat transfer enhancement, are related to, respectively, local and average mass transfer coefficients, and mass transfer enhancement, by $Nu/Nu_0 = Sh/Sh_0$ and $\overline{Nu}/\overline{Nu_0} = \overline{Sh}/\overline{Sh_0}$ (Eqs. (9) and (10)). In this section, we will present local and average mass transfer results in terms of Sh/Sh_0 and $\overline{Sh}/\overline{Sh_0}$, respectively, and it is understood that we may apply the presentation and discussion of these results to heat transfer, and replace Sh/Sh_0 and $\overline{Sh}/\overline{Sh_0}$ by Nu/Nu_0 and $\overline{Nu}/\overline{Nu_0}$ throughout.

Local Mass Transfer. In this study, the local mass transfer coefficient distributions on one of the two primary channel walls between two consecutive blockages were determined by measuring the changes of the elevations at a regular grid of 960 points (20×48) on the naphthalene surface of one of two cassettes during an experiment. Recall that the two naphthalene cassettes were installed side by side in a slot in the top channel wall between two blockages, exposing a smooth, flat, naphthalene surface to the airflow during an experiment. Local mass transfer results were obtained for eight different hole configurations, with aspect ratios between 1.0 and 3.36, and for two Reynolds numbers of 7000 and 17,000.

We will first discuss the variations of the local Sh/Sh_0 distribution downstream of the first, second, and third blockages, in the two cases of round holes and elongated holes with the largest aspect ratio of 3.36. We will then present the local Sh/Sh_0 distributions downstream of the second blockage only and examine the effect of the configuration of the holes on the local Sh/Sh_0 distribution. In subsequent sections, we will present the results on the effects of the hole configuration on the average mass transfer and the pressure drop.

Variation of Sh/Sh_0 Downstream of Three Consecutive Blockages. In Figs. 4 and 5, the local Sh/Sh_0 distributions downstream of the blockages are presented for the case of the smaller round holes (Case S-1) and in the case of the smaller elongated holes with the largest aspect ratio of 3.36 (Case S-4), respectively. In these figures, arrows indicate the direction of the main flow, which is from left to right, and the unshaded portions of the four blockages indicate the locations of the staggered holes. Also, only half of each of the Sh/Sh_0 distributions is shown—a broken line shows a symmetry plane.

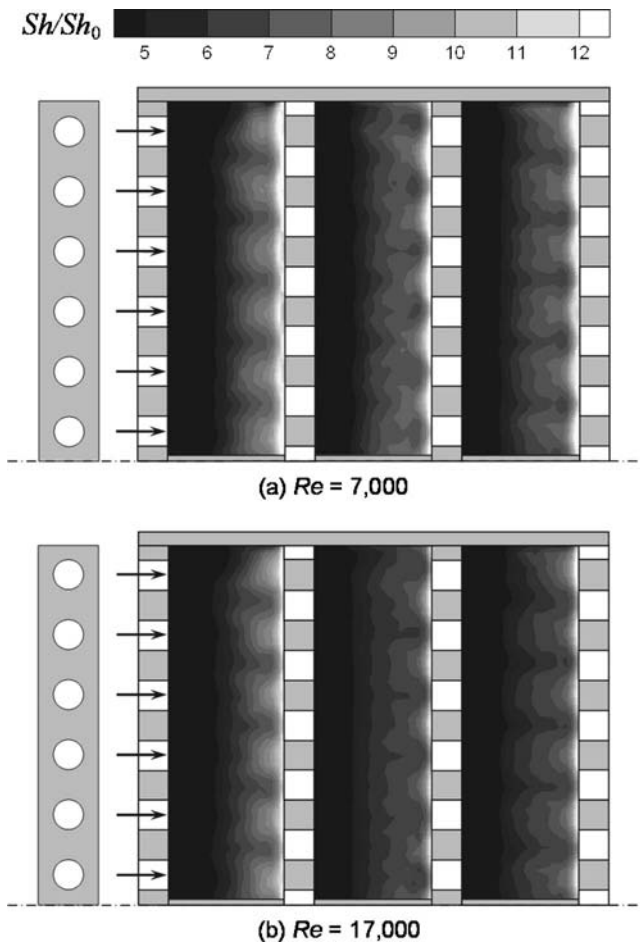In the case of the round holes (Case S-1, Fig. 4), there is a

Fig. 4 Local mass transfer distributions on three wall segments downstream of blockages with the smaller round holes, Case S-1

Fig. 5 Local mass transfer distributions on three wall segments downstream of blockages with the smaller elongated holes, Case S-4

monotonic increase of the Sh/Sh_0 value from less than 5.0 to over 12.0 between two blockages along the main flow direction. The local mass transfer is quite low immediately downstream of a blockage but is very high immediately upstream of a blockage. The spanwise variation of Sh/Sh_0 is much smaller than the streamwise variation. Immediately upstream of a blockage, the Sh/Sh_0 value is slightly lower at a hole than between two adjacent holes. The Sh/Sh_0 distributions on the three segments of the channel wall are quite similar, with Sh/Sh_0 values of 5.0 or less over 40–50% of each wall segment, and values of over 12 over only small discrete regions upstream of a blockage between two holes. Comparing Figs. 4(a) and 4(b), it appears that the blockages cause slightly higher Sh/Sh_0 distributions when Re=7000 than when Re=17,000.

After the air flows through the round holes in a blockage, a large portion of the jet impinges onto the upstream face of the downstream blockage, because the holes in consecutive blockages are staggered. There does not appear to be any reattachment of the air jets. The air is then deflected toward the two primary channel walls, causing the very high local mass transfer immediately upstream of the downstream blockage. The deflected airflow toward each channel wall may turn tangential to the wall before it is lifted from the wall and is forced to flow through the holes along the downstream blockage. A portion of the deflected airflow may turn upstream along the wall and is drawn into the recirculation zones with relatively slow moving flow between the air jets passing through the holes in the upstream blockage and the wall. The individual jets of air cause a periodic spanwise variation of the
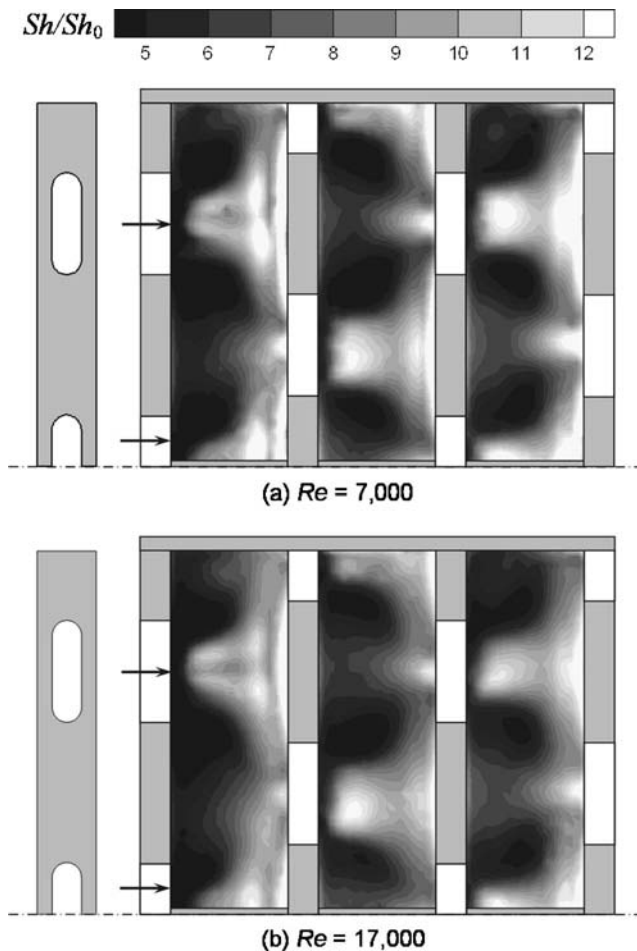
local mass transfer over each wall segment between consecutive blockages, although the spanwise variation is small compared with the streamwise variation between the blockages.

In the case of the elongated holes with an aspect ratio of 3.36 (Case S-4, Fig. 5), the spanwise variation of Sh/Sh_0 is quite large, although it is not as large as the streamwise variation. The local mass transfer is still very high immediately upstream of a blockage, with Sh/Sh_0 values of over 12.0. However, the local mass transfer is also quite high in an isolated region downstream of a hole, with Sh/Sh_0 values of over 12.0, while the values may be as low as less than 5.0 downstream of a blockage between two holes. The Sh/Sh_0 distribution downstream of the first blockage is slightly different than the similar distributions downstream of the second and third blockages. Comparing Figs. 5(a) and 5(b), while corresponding Sh/Sh_0 distributions are similar, the blockages with the elongated holes again cause slightly higher Sh/Sh_0 distributions when Re=7000 than when Re=17,000.

After the air flows through the wide opening of an elongated hole in a blockage, a portion of the flow impinges onto the upstream face of the downstream blockage between two staggered holes. The deflected airflow toward each channel wall again causes the high mass transfer immediately upstream of the downstream blockage between two holes. The local mass transfer distributions in Fig. 5 show that there is reattachment of the air jet on the channel wall, causing the isolated region of high mass transfer downstream of the hole. Also, the low mass transfer region that is sandwiched between two regions of even lower mass transfer regions (with Sh/Sh_0 values below 5.0), downstream of a blockage,
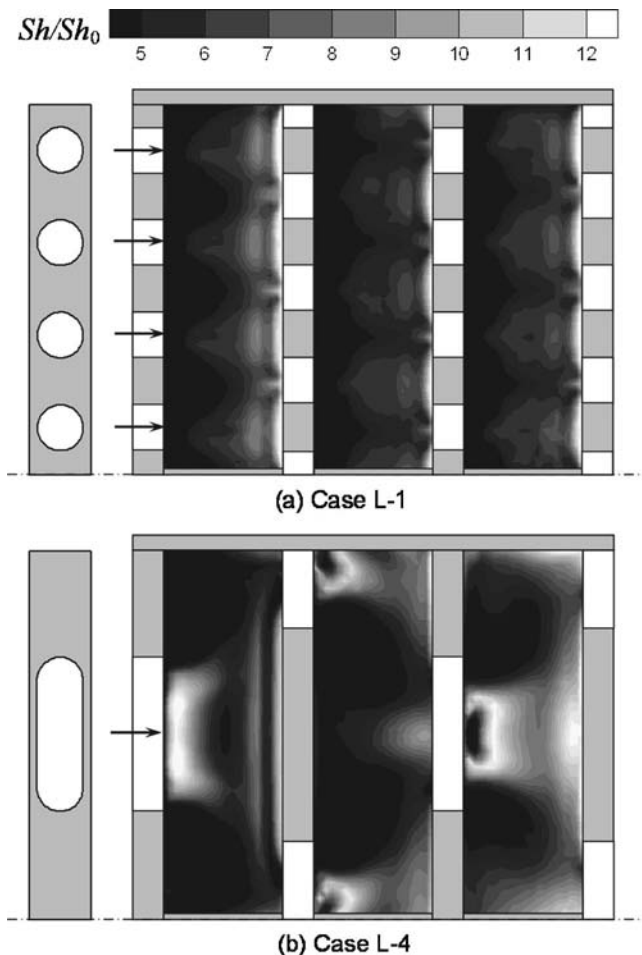
Fig. 6 Local mass transfer distributions on three wall segments downstream of blockages with the larger round and elongated holes, Re=7000

Fig. 7 Local mass transfer distributions on second wall segment downstream of second blockage with the smaller holes, Cases S-1–S-4, for Re=17,000

may indicate the existence of two counter-rotating vortices downstream of the blockage between two holes. The differences between the mass transfer distribution on the first wall segment and the similar mass transfer distributions on the two downstream wall segments may be the results of the airflow approaching the first blockage from an open wide channel while the airflow leaves an upstream blockage as individual jets before it approaches the second and third blockages. The effect of the entrance on the mass transfer distribution is more evident in Fig. 5 for Case S-4 with elongated holes than in Fig. 4 for Case S-1 with round holes.

In Figs. 6(a) and 6(b), the local Sh/Sh_0 distributions are presented for the cases of the larger round holes (Case L-1) and the larger holes with the largest aspect ratio of 3.36 (Case L-4), respectively, and for Re=7000. The Sh/Sh_0 distributions in Fig. 6(a) are similar to those in Fig. 4(a), except that the Sh/Sh_0 values are higher immediately downstream of the larger holes, resulting in larger periodic spanwise variations of the Sh/Sh_0 distributions in Case L-1 for the larger holes than in Case S-1 for the smaller holes. In Fig. 6(a), distinctive local high mass transfer regions upstream of a blockage indicate that there may be flow reattachment of the air jets from the holes along an upstream blockage. The Sh/Sh_0 values in these reattachment regions, however, are much smaller than those in the very high mass transfer region immediately upstream of a blockage resulting from the deflection of the jets off the upstream face of the blockage. Flow reattachment downstream of the large round holes is not as evident for Re=17,000 (Ahn [20]). These results are consistent with those for round holes obtained in an earlier study in Ref. [11].
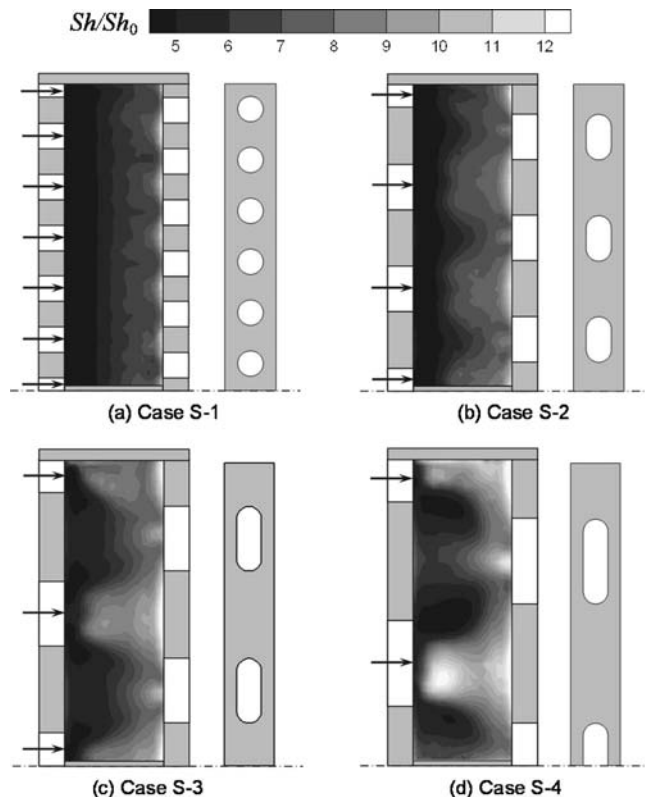
In the case of the larger holes with the largest aspect ratio of 3.36 (Case L-4), there are only two holes along each blockage and there is a rather wide section of the blockage between two holes that does not allow the flow to pass. Figure 6(b) shows that the Sh/Sh_0 values are large downstream of the holes, where flow reattachment is clearly evident, and in a wide region upstream of a blockage between two holes, where the flow is deflected toward the channel wall. However, there are large regions of very low Sh/Sh_0 values downstream of the blockage between two holes and between a hole and the channel sidewall. Because of the geometry of the blockages in Case L-4, with two large "slots" separated from each other and from the sidewalls by very wide sections of the blockage, the spanwise variation of Sh/Sh_0 may be larger than the streamwise variation, and the Sh/Sh_0 distributions are different on the three wall segments between consecutive blockages. Figure 6(b) also shows that the Sh/Sh_0 distribution is the lowest on the first wall segment and the highest on the third and last wall segment.

Effect of Hole Configuration on Sh/Sh_0 *Distribution Downstream of Second Blockage.* To examine the effect of the hole aspect ratio on the local mass transfer distributions downstream of blockages with holes, the Sh/Sh_0 distributions on the second wall segment, between the second and third blockages, for the four cases with the smaller holes (Cases S-1–S-4) are presented in Fig. 7 for Re=17,000. In the case of the round holes, Fig. 7(a) again shows that the monotonic variation of Sh/Sh_0 in the main flow direction is much larger than the spanwise Sh/Sh_0 variation. It can be seen from Fig. 7 that increasing the hole aspect ratio increases the spanwise Sh/Sh_0 variation. Increasing the hole aspect ratio appears to increase the overall mass transfer on the wall segment, since there are larger regions of higher mass transfer in the larger hole aspect ratio cases. In Cases S-3 and S-4, there are regions with relatively high mass transfer downstream of the holes in the
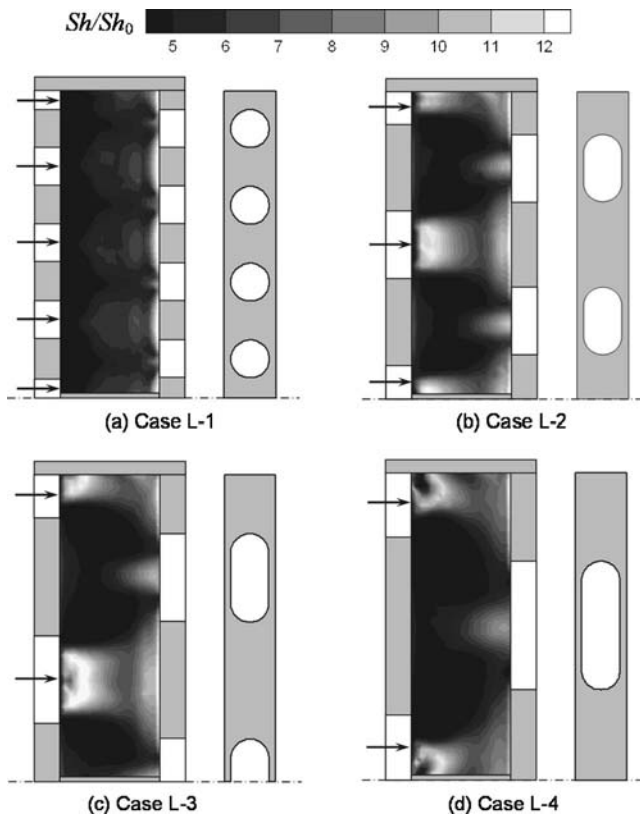
Fig. 8 Local mass transfer distributions on second wall segment downstream of second blockage with the larger holes, Cases L-1–L-4, for Re=17,000

second blockage. There are also regions with clearly very high mass transfer upstream of the third blockage between two holes, and the size of these regions increases with increasing hole aspect ratio.

For airflow through the smaller round holes in a blockage, a large portion of each jet either impinges onto the upstream face of the downstream blockage, and is then deflected toward the two primary channel walls, or passes straight through the two staggered holes in the downstream blockage. The deflection of the jet toward the walls causes the high local mass transfer immediately upstream of the downstream blockage.

For a given total hole-to-channel area ratio, increasing the aspect ratio of the holes reduces the number of holes and increases the distance between adjacent holes. The elongated holes with a larger aspect ratio cause a larger spanwise variation of the local mass transfer coefficient, with larger values immediately downstream of the holes in the upstream blockage but larger regions with small values of the local mass transfer coefficient downstream of the upstream blockage between adjacent holes. The larger values of the mass transfer coefficient downstream of the wider holes are the results of the shapes of the wider jets leaving the elongated holes, flow reattachment immediately downstream of the elongated holes, and the deflection of the wider jets toward the walls upstream of the downstream blockage. The mass transfer coefficient is small over larger regions downstream of the upstream blockage with the wider holes because there are larger counter-rotating vortices with relatively slow moving flow downstream of the wider section of the blockage where the flow is blocked.

The Sh/Sh_0 distributions on the second wall segment for the four cases with the larger holes (Cases L-1–L-4) are presented in Fig. 8 for Re=17,000. To maintain the same total hole-to-channel area ratio of 0.295 in these four cases, doubling the area of a round hole reduces the number of holes from 8 in Case L-1 to 4 in Case L-2. In Case L-3, for the holes with an aspect ratio of 2.57, there are only three holes in each blockage, while in Case L-4, for the holes with an aspect ratio of 3.36, there are only two holes in a blockage. These large elongated holes, or slots, are spaced rather far apart along the blockages. Figure 8 shows that the mass transfer is very low downstream of the wide sections of the upstream blockage between holes, and the size of the low Sh/Sh_0 regions increases with an increase of the distance separating the holes. As a result, for the three cases with larger elongated holes, the mass transfer distribution appears to be lower when the distance separating the holes is larger. It will be shown in the next section that the average mass transfer is lower in Case L-3 than in Case L-2 and is lower in Case L-4 than in Case L-3.

The flow reattaches on the channel wall downstream of the larger elongated holes in Cases L-2–L-4. The spanwise Sh/Sh_0 variation is larger in these three cases than in Case L-1 for the round holes, as a result of the large Sh/Sh_0 values in the regions of flow reattachment downstream of the elongated holes and upstream of the downstream blockage where the flow is deflected toward the channel wall, and the very low Sh/Sh_0 values downstream of the upstream blockage between the holes.

Based on the local mass transfer results presented in Figs. 7 and 8, the smaller elongated holes with the largest aspect ratio of 3.36 in Case S-4 appear to enhance the mass transfer the most. The mass transfer may be enhanced further by increasing the number of these holes in the blockages, since the mass transfer is quite high downstream of the holes and decreasing the spacing between two holes also reduces the size of the low mass transfer regions downstream of the blockages between two holes. Also, increasing the number of holes, which increases the hole-to-channel area ratio, should reduce the pressure drop across the blockages.

Average Mass Transfer. The average mass transfer on a wall segment was obtained both by weighing the two naphthalene cassettes, located side by side in a slot in the top channel wall between two blockages, before and after each experiment, and by determining the area-weighted average of the 960 local Sh/Sh_0 values, on the naphthalene surface of one of the two cassettes, that were measured in a separate experiment. For all of the experiments, the Sh/Sh_0 values obtained by weighing the two cassettes differed by less than 2.1% (the average of the variations was 0.4%, with a standard deviation of 1.1%), while the $\overline{Sh}/Sh_0$ values obtained by weighing the cassettes and by averaging the local Sh/Sh_0 values differed by not more than 4.9% (the average of the variations was 1.9% and the standard deviation was 2.2%). These variations were well within the estimated uncertainty value of 8.2% for $\overline{Sh}/Sh_0$.

In Ref. [20], supplementary heat transfer experiments were conducted to obtain the average heat transfer coefficients on three wall segments downstream of the same blockages in this study, using the test section of this study, three copper blocks as the wall segments between blockages, three flexible electric heaters to supply heat to the copper blocks, and small-gage thermocouples (seven in each copper block) to measure the wall and air temperatures, for the same two airflow rates. The effect of the hole configuration on $\overline{Nu}/Nu_0$ based on the heat transfer measurements was found to be consistent with the effect on $\overline{Sh}/Sh_0$ in this study. The $\overline{Nu}/Nu_0$ values in the heat transfer study were lower than corresponding $\overline{Sh}/Sh_0$ values in this study by not more than 9.9%. For all eight hole configurations studied, the heat transfer data were lower than the mass transfer data by 4.9% on average, with a standard deviation of 2.7%.

In Fig. 9, the average Sherwood number ratios on the three wall segments for Cases S-1, S-4, L-1, and L-4 are presented. These four cases are for round holes and elongated holes with the largest aspect ratio of 3.36. The corresponding local mass transfer distri-
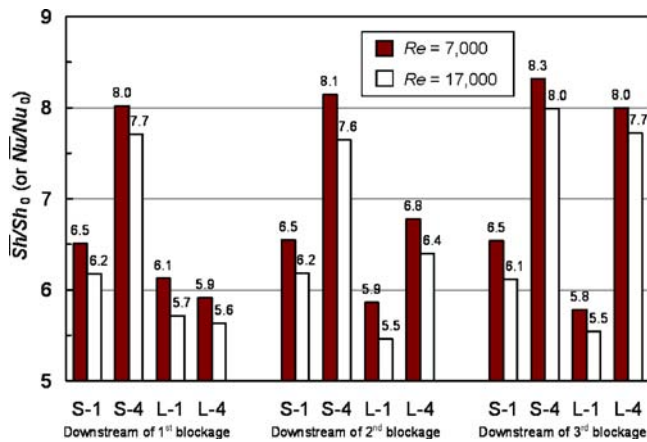
Fig. 9 Mass (heat) transfer enhancement on three wall segments between blockages with round holes and elongated holes with the largest aspect ratio

Fig. 10 Mass (heat) transfer enhancement on second wall segment between second and third blockages with round and elongated holes

butions for these cases have already been given in Figs. 4–6 and discussed earlier. Based on the results presented in Fig. 9, the following trends can be observed.

- In all cases, the average mass transfer enhancement is lower when the airflow rate is higher. The $\overline{Sh}/Sh_0$ value is lower when Re=17,000 than when Re=7000—by 3.5–6.8%.
- For the smaller holes, the average mass transfer is about the same on all three wall segments. In Case S-1, for the round holes, the $\overline{Sh}/Sh_0$ values on the three wall segments are within 1.1% of one another, with values of about 6.5 and 6.2, respectively, for Re=7000 and 17,000. In Case S-4, for the wide elongated holes, the $\overline{Sh}/Sh_0$ values on the two upstream wall segments are within 1.5% of each another but are slightly higher by 2.1–4.5% on the third wall segment. The $\overline{Sh}/Sh_0$ values are 25% and 26% higher in Case S-4 than in Case S-1, for Re=7000 and 17,000, respectively.
- For the larger round holes (Case L-1), the average mass transfer is the highest on the first wall segment and the lowest on the last wall segment, but the differences between the $\overline{Sh}/Sh_0$ values on the two wall segments are less than 5.6%. The $\overline{Sh}/Sh_0$ values of between 5.5 and 6.1 on the wall segments in this case (for the larger round holes) are lower than values of between 6.1 and 6.5 in Case S-1, for the smaller round holes.
- In Case L-4, there are only two large elongated holes along each blockage and it has been shown that the Sh/Sh_0 distributions on the three wall segments were very different and that there were very large regions of low Sh/Sh_0 values in the distribution on the first wall segment. Figure 9 shows that the $\overline{Sh}/Sh_0$ values are small on the first wall segment, but are 14–15% larger on the second wall segment, and are the highest on the last wall segment, with values of about 36% over those on the first wall segment.

In Fig. 10, the average Sherwood number ratios on the second wall segment for all hole configurations are compared. The figure shows that the average mass transfer on the second wall segment is higher in the four cases for the smaller holes than in the corresponding cases for the larger holes. Again, in all cases, the $\overline{Sh}/Sh_0$ value is lower when Re=17,000 than when Re=7,000—with a maximum difference of 6.8%. For the smaller holes, the average mass transfer increases as the aspect ratio of the holes is increased. The maximum $\overline{Sh}/Sh_0$ values for the widest holes (Case S-4) are about 24% higher than those for the round holes (Case S-1). The local Sh/Sh_0 distributions in Fig. 7 showed that there was significant mass transfer enhancement downstream of the
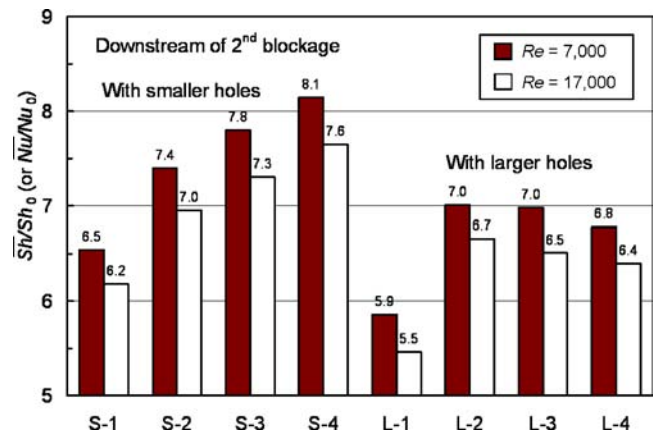
wider holes, because of flow reattachment, and in regions upstream of the wide sections of the downstream blockage between staggered holes, as a result of the deflection of the flow from the downstream blockage toward the channel wall.

For the larger holes, the average mass transfer is again the lowest for the round holes (Case L-1) but is the highest for the elongated holes with an aspect ratio of 1.79 (Case L-2). With a further increase of the hole aspect ratio, the $\overline{Sh}/Sh_0$ value decreases. The increase of the size of the large low mass transfer regions downstream of the wide sections of a blockage between holes may contribute to the decrease of the average mass transfer with an increase of the aspect ratio of the larger holes (see Fig. 8).

Friction Factor. The pressure drops across the blockages were measured with five rows of static pressure taps, along with a calibrated pressure transducer with a digital readout. Three pressure taps were installed in a spanwise row in the bottom wall at a distance of 2.54 cm (half the distance between the blockages) upstream of the first blockage. Nine pressure taps were installed in three rows in the bottom channel wall halfway between the consecutive blockages. Three additional pressure taps were located at a distance of 2.54 cm downstream of the last blockage (see Fig. 2). The friction factor that is to be reported here was calculated based on the average of the three pressure drops across two consecutive blockages—between the pressure taps in the first and third rows, the second and fourth rows, and third and fifth rows.

As expected, with the flow cross section reduced by about 70% and 80% by the blockages with holes of two sizes in this study, the pressure drops across the blockages are much larger than the pressure drop for airflow through an open rectangular channel at the same flow rate. Figure 11 shows that the smaller holes in Cases S-1–S-4 cause larger pressure drops than the larger holes in Cases L-1–L-4. The friction factor ratio, f/f_0, increases as the hole aspect ratio is increased, with values ranging from 780 to 1810 for the blockages with the smaller holes and from 330 to 1030 for the blockages with the larger holes, although the hole-to-channel area ratio is the same (and equal to 0.196) in all four cases with the smaller round and elongated holes and in the four cases with the larger holes (equal to 0.295). The wider sections of the blockages between staggered holes with a larger aspect ratio appear to increase the resistance to the airflow through the channel more than the blockages that have more holes with a smaller aspect ratio and a smaller spacing between holes.

In all cases, the friction factor ratio, f/f_0, is larger when Re=17,000 than when Re=7000.

Thermal Performance. The thermal performance was evaluated based on the average mass (heat) transfer enhancement on the
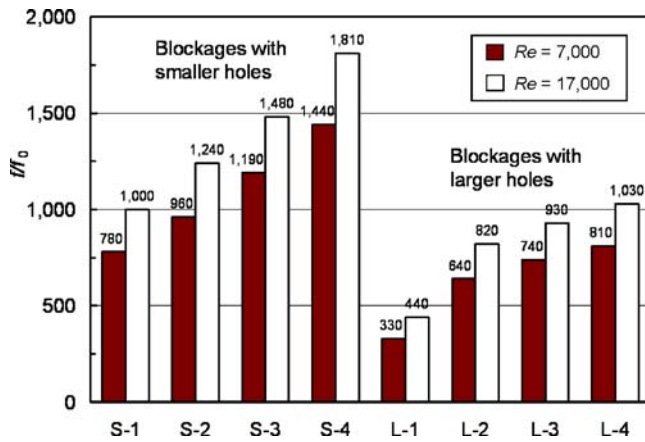
Fig. 11 Pressure drop across two consecutive blockages with round and elongated holes

wall segment between the second and third blockages and pressure drop across the second and third blockages. Although the smaller holes enhance more mass (heat) transfer than the larger holes, they also cause a larger increase of the pressure drop than the larger holes. While $\overline{Sh}/Sh_0$ ($\overline{Nu}/Nu_0$) decreases with increasing Re, f/f_0 increases (see Figs. 10 and 11). Figure 12 compares the thermal performances of the blockages with the smaller and the larger holes. In all cases, the thermal performance (TP) value decreases with an increase of the Reynolds number. The blockages with the larger holes outperform those with the smaller holes slightly, with TP values ranging from 0.63 to 0.85 versus values from 0.62 to 0.75. For the blockages with the smaller holes, the TP values for the three elongated hole cases are about the same and are slightly higher than those for the round hole case. For the blockages with the larger holes, the TP decreases with an increase of the hole aspect ratio while keeping the total hole-to-channel cross-sectional area ratio constant.

Concluding Remarks

Naphthalene sublimation experiments were conducted to study mass (heat) transfer enhancement by blockages with round and elongated holes in a wide rectangular channel that modeled the cooling channel in the trailing edge region of an internally cooled gas turbine blade. Local and average mass (heat) transfer results were obtained for eight configurations of staggered holes with two sizes and four aspect ratios in the blockages and for two Reynolds
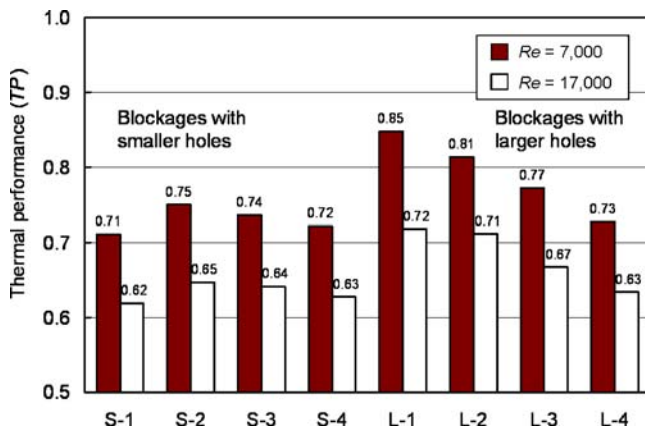
numbers. For the conditions under which the experiments were conducted and the geometries of blockages and the test sections that were studied, the results are summarized as follows.

- The distribution of the local mass (heat) transfer is very much dependent on the configuration of the holes in the blockages. For the blockages with round holes in this study, the mass (heat) transfer on the wall segment between two blockages is low downstream of the upstream blockage and is high upstream of the downstream blockage, with much larger streamwise variation than spanwise variation. For the blockages with elongated holes in this study, the mass (heat) transfer is high downstream of the holes, as a result of flow reattachment, but is very low downstream of the wide section of the blockage between holes, and the spanwise variation of the local mass (heat) transfer may be as large as the streamwise variation. The local mass (heat) transfer distribution is not significantly affected by changing the airflow rate.
- Blockages with holes may cause the average mass (heat) transfer on the wall segments between two blockages in a channel to be much higher than that for a fully developed flow through an open channel with no blockages at the same flow rate, but they also significantly increase the pressure drop. The blockages with round and elongated holes in this study increase the average mass (heat) transfer by 4.5–7.3 times over the corresponding fully developed channel flow value. The blockages with the smaller holes enhance the average mass (heat) transfer more than those with the larger holes, but also increase the pressure drop more than the blockages with the larger holes, by as much as 136%, for the same hole aspect ratio.

Based on the results of this study, blockages with elongated holes and a small spacing between holes are recommended for a cooling channel near the trailing edge of an internally cooled gas turbine airfoil. Additional parametric studies are needed to obtain local and average heat transfer data to optimize the size and the aspect ratio of the holes in the blockages, the spacing between the holes, and the spacing between two blockages, relative to the channel height. Heat transfer data are also needed on the upstream surfaces of the blockages and on the surfaces of the holes, where the heat transfer is expected to be very high, and also on the downstream surfaces of the blockages since a substantial amount of heat may be conducted from the pressure and suction walls to the blockages and is then transferred from these surfaces to the air in a cooling channel near the trailing edge of an airfoil. The total area of the surfaces of the blockages may be comparable with the area of the surfaces of the pressure and suction walls that are exposed to the cooling air.

Nomenclature

a = width of round or elongated holes in blockages, m
A_c = flow cross-sectional area of test channel, m^2
A_s = surface area, m^2
b = center-to-center spacing between adjacent holes in blockages, m
d = diameter of holes in blockages, m
D_h = hydraulic diameter of test channel, m
f = friction factor based on pressure drop across two consecutive blockages and distance between pressure taps
f_0 = reference friction factor for fully developed turbulent flow in smooth channel
h_m = local mass transfer coefficient, m/s
$\overline{h}_m$ = average mass transfer coefficient, m/s
H = height of test channel
$\dot{m}$ = air mass flow rate, kg/s

Fig. 12 Thermal performance based on mass transfer enhancement downstream of second blockage and pressure drop across two consecutive blockages

$\dot{M}_n$ = rate of total mass transfer from upstream naphthalene surface, kg/s

$\dot{M}_n''$ = local naphthalene mass flux, kg/(m^2 s)

$\underline{\text{Nu}}$ = local Nusselt number

$\overline{\text{Nu}}$ = average Nusselt number

Nu_0 = reference Nusselt number for fully developed turbulent flow in smooth channel

p = pressure, N/m^2

$p_{v,w}$ = vapor pressure on naphthalene surface, N/m^2

P_w = perimeter of test channel, m

Re = Reynolds number

Sc = Schmidt number

$\underline{\text{Sh}}$ = local Sherwood number

$\overline{\text{Sh}}$ = average Sherwood number

Sh_0 = reference Sherwood number for fully developed turbulent flow in smooth channel

T = temperature, K

T_w = wall temperature, K

TP = thermal performance, defined as $(\overline{\text{Nu}}/\text{Nu}_0)/(f/f_0)^{1/3}$

$\bar{u}$ = average velocity, m/s

$\dot{V}$ = volumetric flow rate of air, m^3/s

W = width of the test channel, m

Greek Symbols

ΔM_n = total mass transfer from naphthalene surface to air, kg

Δp = pressure drop across two consecutive blockages, N/m^2

Δt = duration of experiment, s

Δx = distance between two pressure taps for measuring pressure drop across two blockages, m

Δz = local change of elevation on naphthalene surface, m

μ = dynamic viscosity of air, N s/m^2

ρ = density of air, kg/m^3

$\rho_{v,b}$ = local bulk vapor density of naphthalene, kg/m^3

$\bar{\rho}_{v,b}$ = average bulk vapor density of naphthalene, kg/m^3

ρ_s = density of solid naphthalene, kg/m^3

$\rho_{v,w}$ = vapor density of naphthalene on naphthalene surface, kg/m^3

σ = mass diffusion coefficient of naphthalene vapor in air, m^2/s

References

[1] Han, J. C., Dutta, S., and Ekkad, S. V., 2000, *Gas Turbine Heat Transfer and Cooling Technology*, Taylor & Francis, New York, pp. 251–529.

[2] Park, C. W., Yoon, C., and Lau, S. C., 2000, "Local Heat (Mass) Transfer in a Diagonally-Oriented Rotating Two-Pass Channel With Rib-Roughened Walls," ASME J. Heat Transfer, **122**(1), pp. 208–211.

[3] Taslim, M. E., Pan, Y., and Bakhtari, K., 2000, "Experimental Racetrack Shaped Jet Impingement on a Roughened Leading-Edge Wall With Film Holes," ASME Paper No. GT-2002–30477.

[4] Ligrani, P. M., and Mahmood, G. I., 2003, "Spatially Resolved Heat Transfer and Friction Factors in a Rectangular Channel With 45 Deg Angled Crossed-Rib Turbulators" ASME J. Turbomach., **125**, pp. 575–584.

[5] Wright, L. M., Lee, E., and Han, J. C., 2003, "Influence of Entrance Geometry on Heat Transfer in Narrow Rectangular Cooling Channels (AR=4:1) With Angled Ribs," ASME Paper No. IMECE2003-42572.

[6] Tafti, D., 2003, "Large-Eddy Simulations of Heat Transfer in a Ribbed Channel for Internal Cooling of Turbine Blades," ASME Paper No. CT2003-38122.

[7] Acharya, S., Agarwal, P., and Nikitopoulos, D. E., 2004, "Heat/Mass Transfer in a 4:1 AR Smooth and Ribbed Coolant Passage With Rotation at 90-degree and 45-degree Orientations," ASME Paper No. GT2004–53928.

[8] Lee, D. H., Rhee, D.-H., and Cho, H. H., 2006, "Heat Transfer Measurements in a Rotating Equilateral Triangular Channel With Various Rib Arrangements," ASME Paper No. GT-2006–90973.

[9] Lau, S. C., Cervantes, J., Han, J. C., and Rudolph, R. J., 2006, "Internal Cooling Near Trailing Edge of a Gas Turbine Airfoil With Cooling Airflow Through Blockages With Holes," ASME Paper No. GT2006–91230.

[10] Moon, S. W., and Lau, S. C., 2003, "Heat Transfer Between Blockages With Holes in a Rectangular Channel," ASME J. Heat Transfer, **125**, 587–594.

[11] Lau, S. C., Cervantes, J., Han, J. C., Rudolph, R. J., and Flannery, K., 2003, "Measurements of Wall Heat (Mass) Transfer for Flow Through Blockages With Round and Square Holes in a Wide Rectangular Channel," Int. J. Heat Mass Transfer, **46**, pp. 3991–4001.

[12] Kukreja, R. T., and Lau, S. C., 1998, "Distributions of Local Heat Transfer Coefficient on Surfaces With Solid and Perforated Ribs," J. Enhanced Heat Transfer **5**(1), pp. 9–21.

[13] Hwang, J. J., Lia, T. Y., and Liou, T. M., 1998, "Effect of Fence Thickness on Pressure Drop and Heat Transfer in a Perforated-Fenced Channel," Int. J. Heat Mass Transfer **41** (4–5), pp. 811–816.

[14] Liou, T. M., and Chen, S. H., 1998, "Turbulent Heat and Fluid Flow in a Passage Distributed by Detached Perforated Ribs of Different Heights," Int. J. Heat Mass Transfer **41**(12), pp. 1795–1806.

[15] Buchlin, J. M., 2002, "Convective Heat Transfer in a Channel With Perforated Ribs," Int. J. Therm. Sci. **41**, pp. 332–340.

[16] Ambrose, D., Lawrenson, I. J., and Sprake, C. H. S., 1975, "The Vapor Pressure of Naphthalene," J. Chem. Thermodyn. **7**, pp. 1172–1176.

[17] Goldstein, R. J., and Cho, H. H., 1995, "A Review of Mass Transfer Measurements Using Naphthalene Sublimation," Exp. Therm. Fluid Sci. **10**, pp. 416–434.

[18] Eckert, E. R. G., 1976, "Analogies to Heat Transfer Processes," in *Measurements in Heat Transfer*, E. R. G. Eckert, and R. J. Goldstein, eds., Hemisphere, New York, pp. 397–423.

[19] Coleman, H. W., and Steele, W. G., 1889, *Experimentation and Uncertainty Analysis for Engineers*, Wiley, New York.

[20] Ahn, H. S., 2006, "Heat and Mass Transfer Enhancement for Flow Through Blockages With Round and Elongated Holes in a Rectangular Channel," Ph.D. thesis, Texas A&M University, College Station, TX.

Discrete Green's Function Measurements in a Serpentine Cooling Passage

Charles W. Booten
Protonex Technology Corporation,
Bloomfield, CO 80020
e-mail: booten@alum.mit.edu

John K. Eaton
Mechanical Engineering Department,
Stanford University,
Stanford, CA 94305
e-mail: eatonj@stanford.edu

The inverse discrete Green's function (IDGF) is a heat transfer coefficient that is valid for arbitrarily complex thermal boundary conditions. It was measured using a rapid experimentation technique in a generic serpentine turbine-blade cooling passage with rib turbulators for Reynolds numbers from 15,000 to 55,000. The model was designed to adhere closely to industry design practice. There were four square cross-section passages with ribs on two opposing walls at 45 deg to the main flow. The rib pitch-to-height ratio was 8.5:1 and the blockage ratio was 0.1. The IDGF was measured with an element length of one rib pitch and was used to determine Nusselt numbers that were then compared to the literature. An increase in Nusselt number over thermally fully developed pipe flow of 2.5–3.0 is common in the literature and was consistent with the results in this work. The results showed that the heat transfer coefficient in such complex passages is weakly affected by the thermal boundary condition, which simplifies measurement of this quantity. [DOI: 10.1115/1.2767749]

1 Introduction

Modern gas turbine engines use active cooling in key components of the turbine to prevent failure under the extreme operating conditions they face. There are two primary mechanisms to accomplish this, film cooling and internal passage cooling. This study focuses on internal passage cooling, where a series of passages is cast into the turbine blades for cooling using compressed air. Inaccurate knowledge of internal passage heat transfer rates is a major factor in the uncertainty of turbine-blade life-span prediction, resulting in more conservative, and less efficient, internal cooling passage designs.

Figure 1 shows a sample turbine blade with internal cooling passages. The air that flows through these passages is bled from the high pressure compressor, bypassing the combustor, and enters through the root of the blades. In modern turbine blades, there are typically three to four sets of cooling passages, one each for the leading and trailing edges and one to two sets of mid-chord passages. These serpentine passages are extremely complicated including multiple separation regions, strong secondary flows, and substantial roughness in the form of ribs (also referred to as turbulators).

The complicated geometry makes detailed measurements and CFD simulations difficult. Experimentally, it is difficult to install instrumentation to provide spatially resolved measurements in complex internal flows. In the case of CFD, the grid must be extremely complex to resolve the separation regions behind each of the many ribs and both flow separation and strong secondary flows offer significant challenges for turbulence models. Because detailed heat transfer information is rarely available, turbine analysis systems often assign a single value of the heat transfer coefficient for the entire passage using empirical correlations.

To accurately describe steady-state heat transfer with variable boundary conditions, a heat transfer coefficient that is valid for a variety of thermal boundary conditions (for a given geometry and hydrodynamic conditions) is necessary. The discrete Green's function (DGF) technique provides this capability. A DGF approach to characterizing heat transfer was first used in external flows by Batchelder and Eaton [2] and Hacker and Eaton [3]. Mukerji and Eaton [4] showed that it can be easier to measure the DGF than h in complex external flows where it is difficult to achieve constant wall temperature or heat flux. Booten and Eaton [5] and Booten et al. [6] demonstrated a technique for measuring the IDGF in internal flows using a fully developed turbulent pipe flow. This method was shown to be very accurate for measuring the IDGF and is the basis for the experiments performed in this work.

The specific objectives of the present work are to provide detailed heat transfer measurements of a generic ribbed serpentine passage that captures much of the complexity of a real passage but eliminates such effects as variable passage cross section, passage twist, and film cooling discharge. A body of literature exists dealing with measurements in ribbed passages such as this. Generally, the ribs are square or rectangular in cross section although many shapes have been investigated. Trapezoidal cross sections were compared in Han et al. [7] to square cross-section ribs between parallel plates with a substantial effect on the friction factor but only a modest effect on heat transfer. Liou and Hwang [8] looked at square, triangular, and semicircular ribs and found Nusselt number enhancements of up to 2.7, 2.2, and 2.1, respectively.

Astarita et al. [9] reported Nusselt numbers on a square serpentine passage with one 180 deg bend with ribs that had pitch-to-height ratios of 10 and 20. Peak Nusselt number enhancements of more than 4 were reported on the rib tops with enhancements of 1.5–2.0 between ribs. Carlomagno et al. [10] measured Nusselt numbers in a similar geometry for blockage ratio 0.1 and two different pitch-to-height ratios, 10 and 20. Localized Nusselt number enhancements of more than 5 were reported on ribs downstream of the turn; however, the locations of these high heat transfer rates were limited to the tops of the ribs.

Different rib angles have been studied ranging from 90 deg to 20 deg relative to the passage axis, although 90–45 deg is more typical. Most studies found that 60 deg ribs have the highest heat transfer enhancement for a given increase in friction factor followed by 45 deg and 90 deg ribs, respectively, according to Chandra et al. [11]. Wright et al. [12] found that for a channel aspect ratio of 4:1, discrete W- and V-shaped ribs (with rib angle=45 deg) have higher thermal performance than angled or continuous ribs, followed closely by continuous W-shaped ribs.
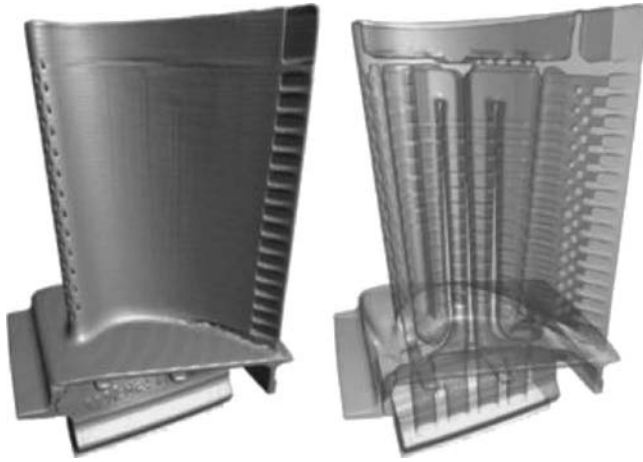
Fig. 1 Turbine blade with serpentine cooling passages. Reproduced from Lindstrom [1].

Lau et al. [13] showed that discrete angled ribs also outperform more conventional full ribs by 5–32% depending on the Reynolds number and rib angle.

Ribs on opposite walls can be either parallel or crossed as well as staggered or un-staggered. Han et al. [14] reported that parallel ribs tend to have higher Nusselt number enhancement than crossed ribs, although this is somewhat confined to the region just upstream of each rib where the parallel rib geometries can have significantly higher Nusselt numbers according to Won and Ligrani [15]. Similarly, staggered ribs have a higher thermal performance than unstaggered ribs. The Nusselt numbers are slightly higher for the unstaggered rib placement in Chandra et al. [16] but the increase in friction factor more than offset this for a lower thermal performance.

Some studies have focused on the effect of having different numbers of walls with ribs. The heat transfer enhancement for an aspect ratio 2:1 channel with four ribbed walls has been shown to be a modest 4% more than the same channel with ribs only on the wider two walls, but the enhancement was 14% higher than the case with only one ribbed wide wall, as reported by Chandra et al. [17]. Chandra et al. [18] found that the relative results for different numbers of ribbed walls were very similar for an aspect ratio 1:1 channel except that the overall Nusselt number enhancement over a smooth wall was 8% higher than the aspect ratio 2:1 geometry.

The measurements presented here were conducted in the same geometry and in the same Reynolds number range as used by Elkins et al. [19] for fluid mechanics measurements. They used magnetic resonance velocimetry (MRV) to provide three-component mean velocity measurements throughout four-passage ribbed serpentine geometry. Although MRV provides very high spatial resolution mean velocity data, the heat transfer experiments in this work provide intermediate spatial resolution. Typical heat exchanger type tests supply a single average heat transfer coefficient for the entire passage while spatially resolved tests use a constant heat flux surface and optical temperature measurement. Fabricating a constant heat flux surface for this entire geometry would be very difficult. Hacker and Eaton [3] and Booten and Eaton [5] have shown that measurement of the heat transfer rate from discrete elements along with simultaneous measurement of the thermal wake of the heated element provides sufficient information to characterize the heat transfer over the entire surface. The advantage of this approach over other methods is the ability to make accurate heat transfer measurements quickly that are capable of predicting the thermal characteristics for a variety of thermal boundary conditions. Previously mentioned procedures typically have only one of those characteristics.

2 Formulation of the Discrete Green's Function

The DGF is essentially a heat transfer coefficient that provides a relationship between the wall temperature and heat flow. The inverse of this relationship is called the inverse discrete Green's function (IDGF). Measuring the IDGF is the focus of this work, but the DGF is presented first for clarity. The formulation represents the surface as a set of N discrete elements each of which has an average, steady-state temperature rise above a suitable reference and a heat transfer rate to the flow. The DGF is an $\mathbf{N} \times \mathbf{N}$ matrix, $\mathbf{G}$, with units of W/K, which relates the vector of heat transfer rates into the fluid $\dot{\mathbf{q}}$ to the steady-state wall temperature rise vector $\Delta \mathbf{T}$ as

$$\dot{\mathbf{q}} = \mathbf{G} \Delta \mathbf{T} \qquad (1)$$

Equation (1) shows that the DGF relates the heat transfer to the fluid from a given element to the applied wall surface temperature rise on every element. Thermal boundary condition effects are accounted for directly through $\Delta \mathbf{T}$.

In most instances, it is easier to measure the IDGF, which is defined by

$$\Delta \mathbf{T} = \mathbf{G}^{-1} \dot{\mathbf{q}} \qquad (2)$$

$\mathbf{G}^{-1}$ is an $\mathbf{N} \times \mathbf{N}$ matrix with units of K/W. A column in $\mathbf{G}^{-1}$ can be determined by heating a single element with a known heat flow, $\dot{q}$, while keeping all other elements adiabatic. The resulting temperature on each element, ΔT_i, is measured and used to obtain each element in a single column of $\mathbf{G}^{-1}$, $\mathbf{g}^{-1}$,

$$g_i^{-1} = \frac{\Delta T_i}{\dot{q}} \qquad (3)$$

Simplifications can be made in the measurement of $\mathbf{G}^{-1}$ for certain flow situations. In fully developed pipe flow, each column is the same except shifted down by one element relative to the previous column (Booten and Eaton [5]). We expect a serpentine cooling passage with turbulators to have similar behavior except near the corners where the passages turn 180 deg. $\mathbf{G}^{-1}$ is a lower triangular matrix in fully attached flows; however, there are some nonzero elements above the main diagonal in ribbed passages because recirculation between the ribs causes upstream heating. In principle, each element must be heated independently to determine the full $\mathbf{G}^{-1}$ matrix. In practice, interpolation can often be used between columns.

Typical formulations of h for internal flows use the mixed mean temperature as the appropriate reference temperature. The DGF technique was developed for external flows where T_∞ is the appropriate reference temperature. The fixed inlet temperature is commonly used as a reference for developing pipe flow problems as in Refs. [20,21]. In this study, the adiabatic wall temperature $\mathbf{T}_{aw}$ is used as a reference to account for Mach number effects on the unheated wall temperature. The vector $\Delta \mathbf{T}$ in Eq. (1) is therefore defined as

$$\Delta \mathbf{T} = \Delta \mathbf{T}_{aw} = \mathbf{T}_{wall} - \mathbf{T}_{aw} \qquad (4)$$

3 Experimental Equipment and Procedures

The experimental facility is the same as that used in Booten and Eaton [5] with the addition of the serpentine test section. A detailed view of the model, called the Stanford generic turbine internal passage (SGTIP), is given in Fig. 2. The manifold acted as a nozzle to smoothly transition from the 32.8 mm diameter round pipe to a square cross-section 20 mm × 20 mm passage over a length of 38 mm. The passages of the model were designed to adhere as closely as possible to industry design practice while eliminating certain complexities such as twist, variable cross section, and film cooling. Each of the four passages had ten rib turbulators on each of the two opposing walls; Fig. 2 only shows the ribs on the top wall for clarity. The bottom ribs were staggered so they were directly in between the top turbulators from the view of
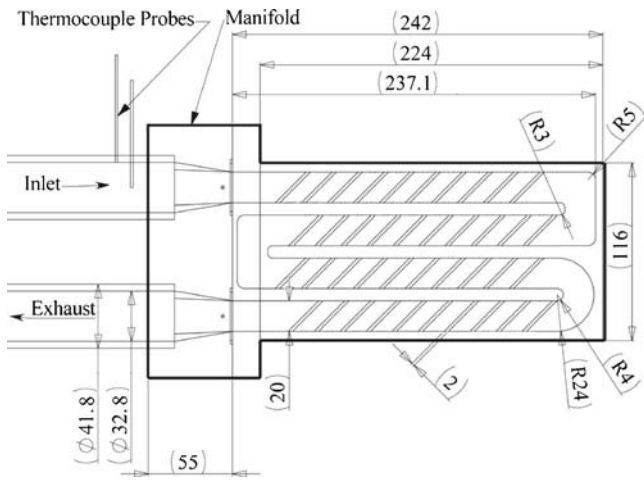
Fig. 2 Top view of the test section. Only the ribs on the top wall are visible. Dimensions are in millimeters.

Fig. 3 Heated element locations. Each shaded element represents the location of the heated copper element in the instrumented plug.

Fig. 2. All ribs had a square cross section of 2 mm×2 mm and were angled at 45 deg to the flow. The rib pitch-to-height ratio was 8.5:1. This was defined by using a rib width of 2 mm (at 45 deg to the passage axis) but measuring the pitch along the axis of the passage as is standard in the literature. The blockage ratio was 0.1.

There were two types of corners in this model that were representative of the corners seen in actual passages. Figure 1 shows a range of corner configurations in a real passage with some corners clearly being more square and others more rounded. The first two corners of the SGTIP model were almost square with very little rounding of the actual corner. The last corner was circular with a constant cross section.

Two versions of the model were built with identical flow geometry using stereolithography. This allowed for single step fabrication of the complex geometry with a resolution of approximately ±0.05 mm. The first version was used for velocity field measurements using MRV by Elkins et al. [22]. The second version of the model was manufactured with cutouts to allow insertion of heat transfer measurement instrumentation. One cutout shape was replicated seven times to provide measurements in the straight sections of the passage. In addition, there were cutouts for one of the square corners and for the round corner. All cutouts were sealed with plugs that replicated the internal geometry of the passage.

The basic experimental procedure that was used in the pipe flow tests by Booten and Eaton [5] was applied here as well. The passage surface was conceptually discretized into elements, and one of these elements was replaced with a heated copper piece that was geometrically identical to the section of wall that it replaced. Figure 3 shows the 13 locations where heated elements were placed for measurement. The heated straight section locations were chosen for comparisons of h between passages as well as to try and get a complete picture of how the thermal characteristics vary over the entire model. There were heated elements near both types of corners, near the inlet and exits of the model, and in the middle section of one of the passages.

The element size for the straight section elements was based on the rib pitch of the model, as illustrated by the shaded region in Fig. 3. This means that one rib plus one "floor" between ribs constituted an element.

The experiment was simplified considerably by designing a removable instrumented section so that data could be acquired at multiple locations without building and instrumenting a new model. The SGTIP model is well suited to this because of the repetitive nature of the wall shape. A four-rib-pitch section of one passage wall was instrumented and mounted in a movable plug
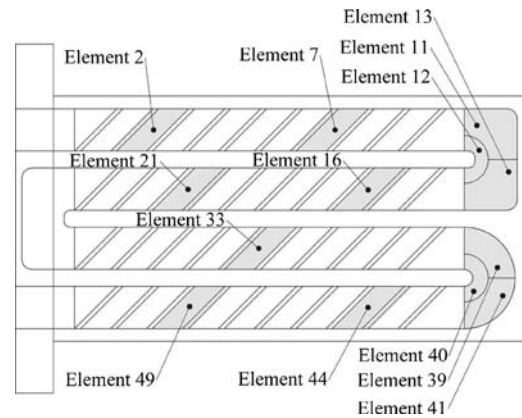
shown in Fig. 4. Noninstrumented plugs made completely from stereolithography resin were used whenever the instrumented plug was removed from a particular location. This kept the model sealed without altering the passage shape or thermal boundary condition. The dimensions of the plug itself are given in Figs. 5 and 6. Each heated copper element was sealed in place using epoxy and was heated using a kapton-coated thermofoil heater with a known heat flow. The steady-state thermal response was measured using embedded thermocouples. Temperature measurements were taken on one element upstream and two elements downstream of the copper element.

The air gap behind the instrumented elements, shown in Fig. 6, allowed room for installing the thermocouples and heaters and insulated the copper from conduction back losses. The 3 mm gap was small enough so that natural convection was negligible (Rayleigh number ~50). The thermocouple numbering scheme is given in Fig. 7. Numbers 1–8 are the "upstream" column because
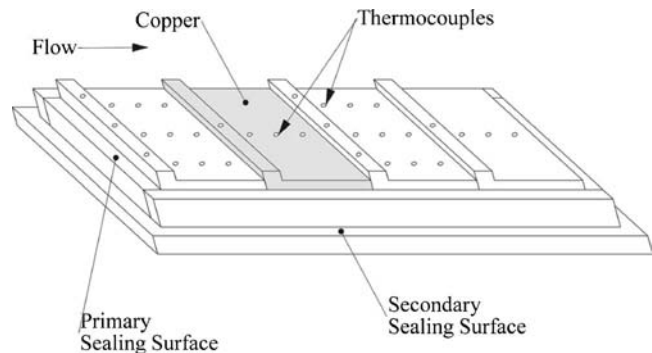

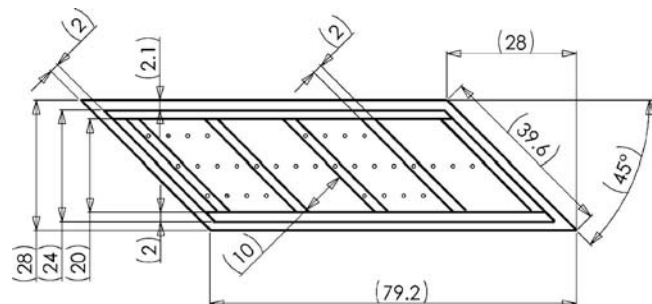**Fig. 4 Instrumented plug for straight sections of SGTIP model**

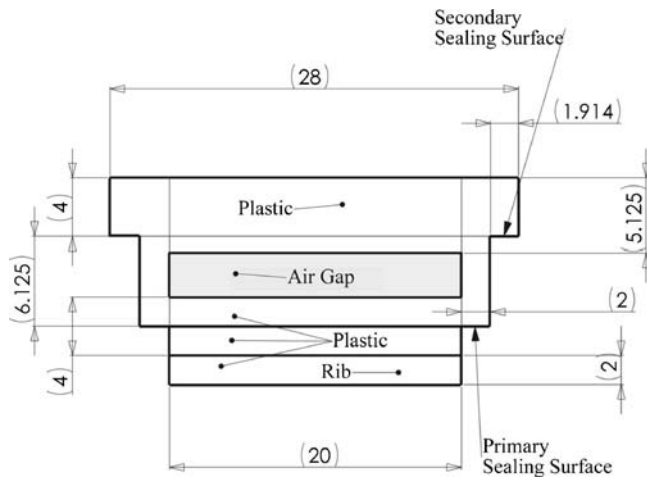**Fig. 5 Dimensions of straight section plug in millimeters**

Fig. 6 End view of straight section instrumented plug. Dimensions are in millimeters.

Fig. 8 Comparison between mean velocity vectors from PIV (white) and MRV (black) in the centerplane of the first corner. Reproduced from Elkins et al. [19].

it is near the upstream edge of the rib, numbers 9–24 are the "center" column, and numbers 25–32 are the "downstream" column. Having three columns of thermocouples allowed for some resolution of spanwise variation in the temperature distributions.

The element sizes for the corners were a design choice based roughly on flow characteristics and practical geometric constraints. The corners have significantly different flow and thermal characteristics than the straight sections and the element sizes were chosen to correspond roughly to different flow conditions over the corner surface, while maintaining an ability to easily instrument and heat the pieces. Figure 8, reproduced from Elkins et al. [19], shows the velocity around the square corner as measured using MRV and particle image velocimetry (PIV). The mean velocity magnitude increases near the inside radius of the corner. Therefore, heat transfer measurements in the corners were separated into inner and outer components. The outer section was separated into upstream and downstream elements because the Reynolds number affected the separation around the corner, causing the flow to impinge on the outer wall at different locations; two elements allowed for reasonable resolution of the effect this had on heat transfer. The corner measurement sections are shown in Fig. 9. The shaded areas represent the location of the copper element for each plug and the small circles represent the thermocouple placements in the plastic. The thermocouple placements in the copper elements were distributed around the film heaters in approximately the same fashion as the thermocouples installed in the plastic in Fig. 9. An expanded view of one of the instrumented plugs is given in Fig. 10.

In addition to the two ports for the instrumented corner plugs, there were 30 thermocouples embedded in the upper surface of the
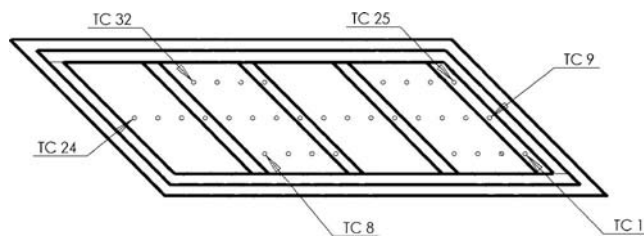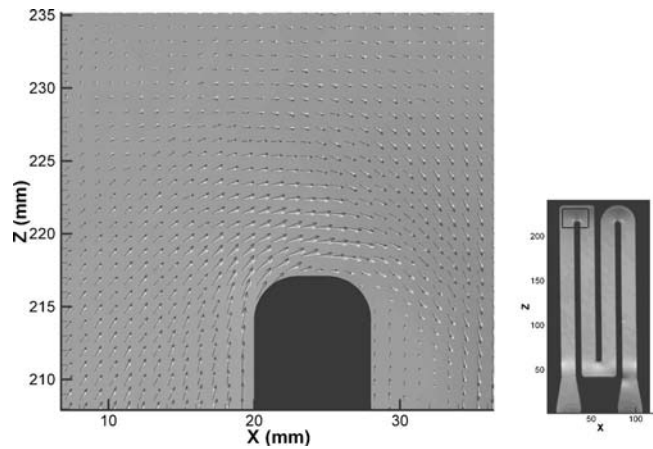

Fig. 7 Thermocouple numbers on the surface of instrumented plug. Only selected thermocouples are numbered for clarity. Numbers 1–8 are near the "upstream" side wall (column 1), 9–24 are in the centerline (column 2), and 25–32 are near the "downstream" side wall (column 3).

four passages. These were included to help estimate the upstream and downstream heating effects, if any, of applying heat in the corners.

The hydrodynamic development pipe was encompassed by 19 mm of polyethylene insulation. Surrounding this was between 38 mm and 89 mm of polystyrene ($k \approx 0.04$ W/mK). The model itself was insulated with 19 mm of plywood on top and bottom ($k \approx 0.15$ W/mK) surrounded by 76 mm of polystyrene.

4 Results

4.1 Adiabatic Wall Temperature. The adiabatic wall temperature can differ significantly from the test section inlet temperature. This is especially important for the highest Reynolds numbers where the local Mach numbers can exceed 0.2 according to Elkins et al. [19]. Therefore, the adiabatic wall temperature was measured with no heat addition at all locations and Reynolds numbers to provide a correct reference temperature for heat transfer calculations. A sample of the adiabatic wall temperature, with the copper located at element 44, is shown in Fig. 11. The thermocouple numbers correspond to those listed in Fig. 7. The adiabatic wall temperature was within $\pm 0.06\,^\circ$C of the inlet stagnation temperature at all measurement locations for the lowest Reynolds number. However, it drops below the inlet temperature by around $0.2\,^\circ$C for the intermediate Reynolds number case and by as much as $0.6\,^\circ$C for the high Reynolds number case.

This drop in adiabatic wall temperature can be explained with the use of the recovery factor

$$\frac{T_0}{T} = 1 + r_c \frac{\gamma - 1}{2} \mathrm{Ma}^2 \qquad (5)$$

where T_0 is the stagnation temperature, Ma is the freestream Mach number, and γ is the specific heat ratio. The recovery factor is not a fundamental property of a flow but is rather an empirical factor that can be measured and used to describe the thermal behavior of a flow near a boundary. A typical relation for the recovery factor in turbulent flow over a flat plate, as well as a thorough discussion, is given in White [23],

$$r_c \approx \mathrm{Pr}^{1/3} \qquad (6)$$

This empirical relation is often applied to other turbulent boundary layers as well. The inlet Mach numbers in this study were 0.033, 0.077, and 0.121. If a freestream Mach number of 0.12 is used in Eq. (5), a reduction in the adiabatic wall temperature of about $0.75\,^\circ$C below stagnation temperature is expected. This rough calculation confirms that the measured $T_w - T_{aw}$ in the non-heated cases was in the expected range.
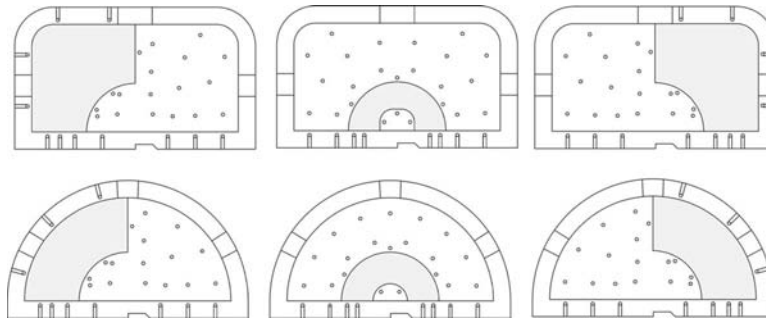
Fig. 9 The six corner measurement sections. Shaded areas represent copper elements; circles represent thermocouple locations.

4.2 Straight Section Wall Temperature Distribution. The measurements were performed with only one element heated at a time. The power for the heated element was set between 0.6 W and 2.0 W to obtain a maximum temperature rise around 20°C. Figure 12 shows the steady-state thermal "footprint" on element 33 at a Re=35,000. Each column represents a line of thermocouples parallel to the axis of the passage, as shown in Fig. 7. The axial position corresponding to $x=0$ is at the upstream edge of the
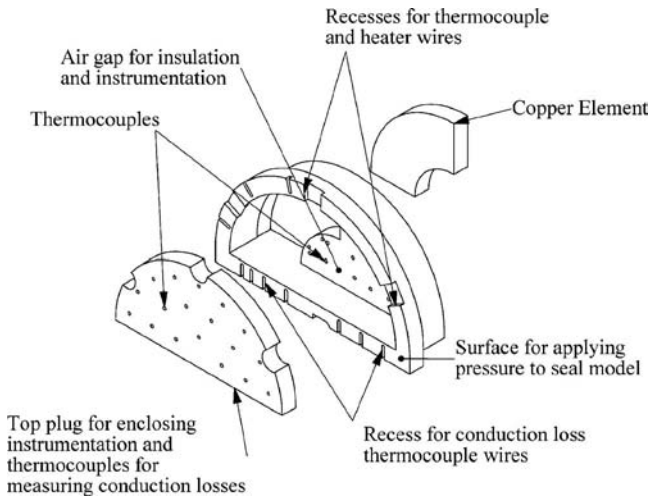

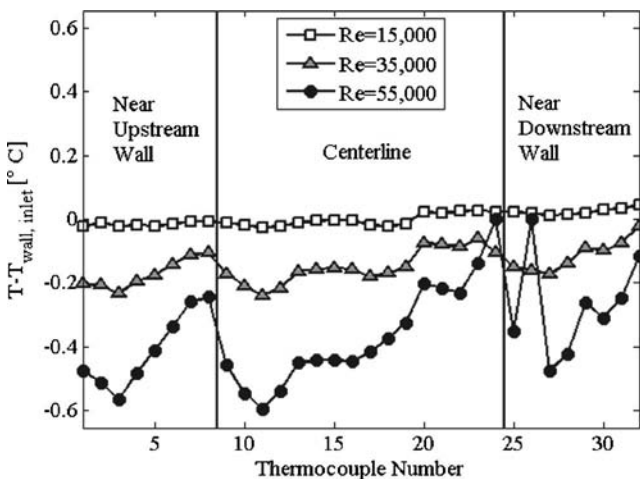**Fig. 10** Expanded view of corner plug in SGTIP model

Fig. 11 Adiabatic wall temperature with respect to the fluid inlet temperature on surface mounted thermocouples. Thermocouple numbers are given in Fig. 7.

rib (which is angled 45 deg to the flow). This coordinate system means that thermocouples 1, 9, and 25 all have the same x location, as do thermocouples 2, 10, 26, etc. The x location of the thermocouples is nondimensionalized in Fig. 12, and the heated copper element is located in the range of $1.6 \times 10^{-4} \leq x^{+} \leq 3.2 \times 10^{-4}$.

The two most interesting characteristics of Fig. 12 are that there was very little downstream temperature rise past the first element downstream of the heated copper element and that there was significant heating upstream of the copper element. The mean temperature rise two elements downstream of the copper was approximately 3.5% of that on the copper over the range of Reynolds numbers studied. This rapid decrease was caused by the strong secondary flows and turbulence that dispersed the heat throughout the mainstream flow very quickly.

The rapid decrease in wall temperature rise downstream of the heated element greatly simplified the measurement of the IDGF. To measure one column of $\mathbf{G}^{-1}$, only four elements needed to be measured. The $\mathbf{G}^{-1}$ obtained by measuring only elements with large values in each column is called $\mathbf{G}_{\text{reduced}}^{-1}$. Booten and Eaton [5] showed the discrepancy in predicted heat flow using $\mathbf{G}^{-1}$ and $\mathbf{G}_{\text{reduced}}^{-1}$ to be quite small for sinusoidal thermal boundary conditions. It will be even less for serpentine passages than for the pipe flow because the off diagonals drop to zero more quickly; in other words, the secondary flows and turbulence reduce the length of the thermal footprint for a given amount of heating.

There was also substantial heating upstream of the copper element even after subtracting out conduction from the copper to the upstream element. This was caused by recirculation drawing heat from the rib on the copper element and transferring it to the wall upstream.

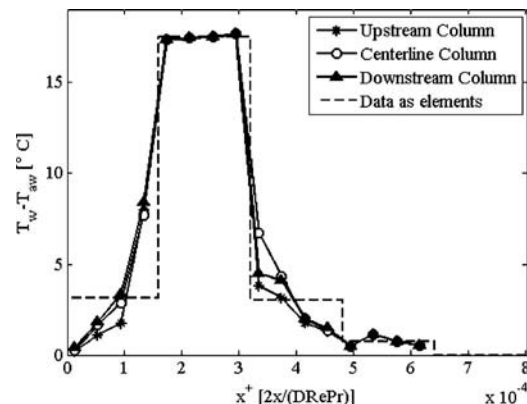A further experimental simplification can be made by noticing

Fig. 12 Experimental centerline temperature rise on element 33, Re=35,000
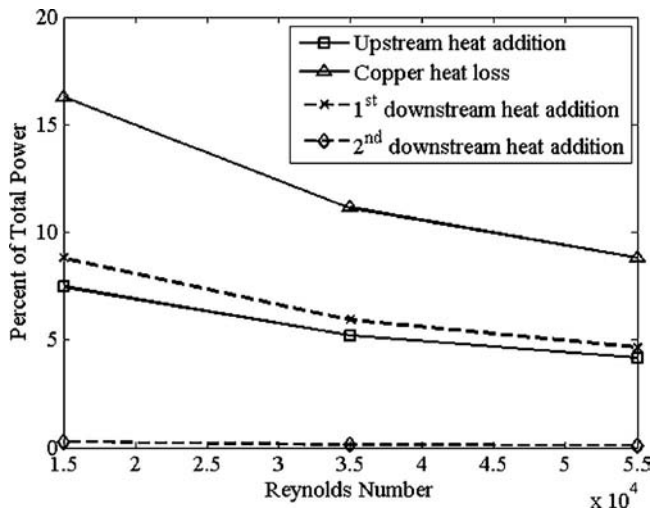
Fig. 13 Comparison of the relative heat losses on the copper element and the corresponding heat gains on the adjacent upstream and two downstream elements on the pipe flow and for heating on element 2

Fig. 14 G^{-1} in straight section locations, Re=15,000

that the thermal response for the model is nearly uniform parallel to the rib direction. There was very little temperature variation parallel to the ribs. Small variations immediately upstream and downstream of the heated element were probably due to the complex three dimensional flow field.

4.3 Conduction Losses and Data Reduction. A relatively large fraction of the heat applied to the copper element was lost to conduction due to its small size. Most of the heat was conducted into the plastic elements on either side, but a small fraction was conducted into either the flow or the environment without flowing through the adjacent elements. To correct for this, the heat conduction was modeled in FLUENT using an unstructured mesh representation of the measurement insert shown in Fig. 5. The model included the copper ($k=400$ W/mK), the stereolithography plastic ($k=0.2$ W/mK), and the air gap behind the heated surface ($k=0.026$ W/mK). The air was treated as solid due to the small Rayleigh number in the gap (~50). The outer surfaces of the test insert were well insulated and were treated as adiabatic in the model. The experimental temperature distribution in the copper element was used as a boundary condition. The other parts of the surface exposed to the flow used a prescribed heat transfer coefficient to avoid singularities where they adjoined the copper. The heat transfer coefficient was estimated from literature values and preliminary measurements, so the uncertainties were fairly large. However, variations in the prescribed heat transfer coefficient produced only small changes in the calculated conduction losses.

Figure 13 shows the calculated heat loss from the heated element and conduction heat transfer into the adjacent elements. The values are plotted for heating of element 2, but they are representative of all the straight section measurement positions. Clearly, the conduction losses are too large to ignore in the calculation of the IDGF.

The calculation of the IDGF begins using the nominal power input on the copper, $\dot{q}_{Cu}$, and the steady-state wall temperature rise on each element, $\Delta T_{uncorrected}$. These are used to create column k of $\mathbf{G}^{-1}_{uncorrected}$ using

$$g^{-1}_{ik} = \frac{\Delta T_{uncorrected,i}}{\dot{q}_{Cu,k}} \qquad (7)$$

$\mathbf{G}^{-1}_{uncorrected}$ is used along with the conduction loss estimates to obtain a correction to $\Delta T_{uncorrected}$ that accounts for heating of
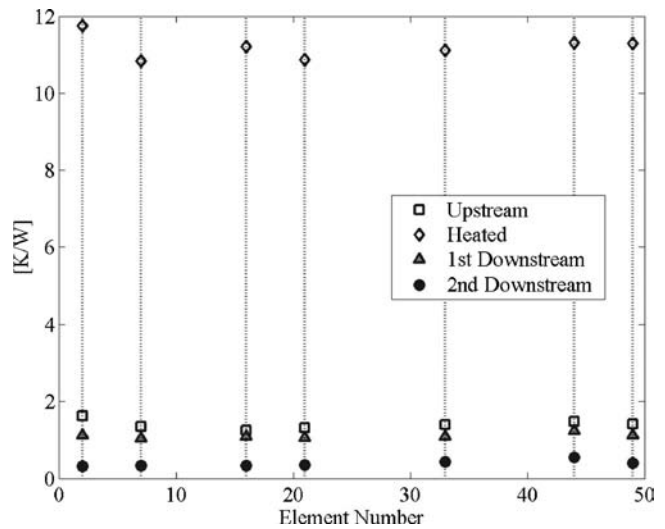
other elements by conduction. The new temperature rise on each element is then

$$\Delta T_{corrected,i} = \Delta T_{uncorrected,i} - \sum g^{-1}_{ij} \cdot \dot{q}_{corrected,j}(1 - \delta_{jk}) \qquad (8)$$

where $\dot{q}_{corrected,j}$ is the net heat flow to each element j, including all losses. The second term in Eq. (8) subtracts the temperature rise on element i due to heating on all other elements, using the current estimate for g^{-1}_{ij}. This process is used for all elements where conduction losses are calculated, but the effect is most important close to the heated element. An iterative procedure is then used to solve for $\mathbf{G}^{-1}$. The new temperature rise vector, $\Delta T_{corrected}$, is used in conjunction with the estimated heat flow supplied to the copper given in $\dot{q}_{corrected,j}$, where j is the heated copper element, to calculate $\mathbf{G}^{-1}$ via Eq. (7). In practice, this process required two to four iterations to converge.

4.4 Measured IDGF for Straight Sections. The measured straight section IDGF is shown for the low and high Reynolds number cases in Figs. 14 and 15. Each column in these figures corresponds to one column of a complete $\mathbf{G}^{-1}$ matrix.

An important feature of the plots is that for a fixed Reynolds number the values are nearly constant over all the elements mea-
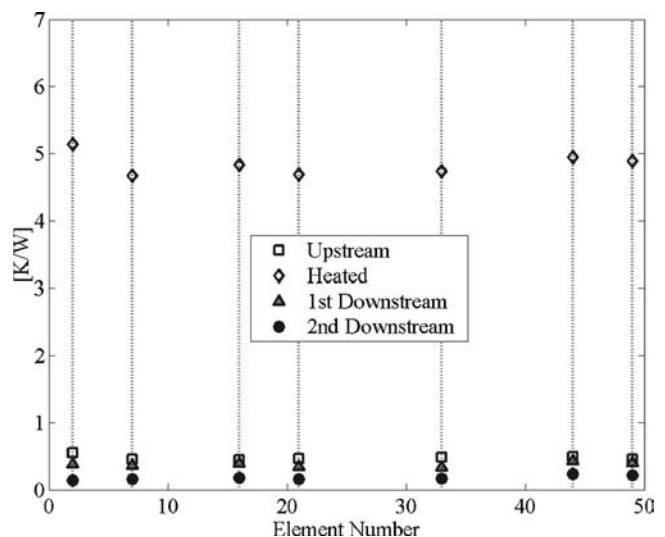

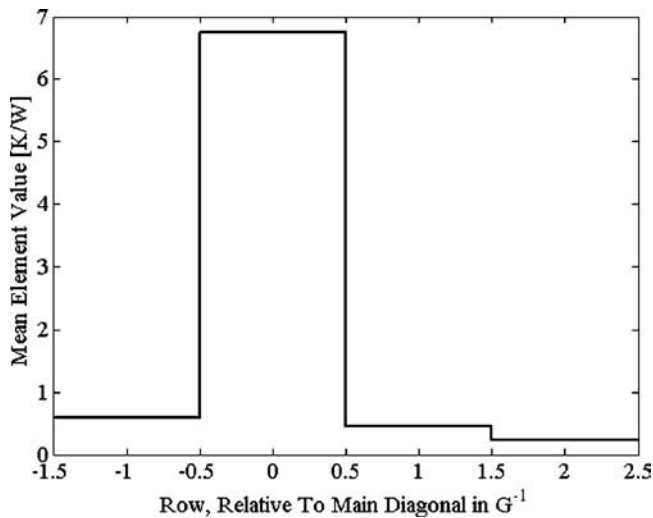**Fig. 15 G^{-1} in straight section locations, Re=55,000**

Fig. 16 Mean of measured elements in $\mathbf{G}^{-1}$ Re=35,000

Fig. 17 Fully developed Nusselt number. Values from this experiment, $\mathrm{Nu}_{\Delta T_{aw}}$ and $\mathrm{Nu}_{\Delta T_{bulk}}$, are averages over all measured straight section elements.

sured. The maximum difference between any two measured elements is less than 8%. This suggests that interpolation could be used to fill in the missing columns with a reasonable uncertainty. The intermediate Reynolds number data are presented in a different form in Fig. 16 where the data are averaged over all of the measured elements. Element "0" corresponds to the heated copper element, element "−1" to the element just upstream of the heated element, element 1 corresponds to the element immediately downstream of the heated element, etc. This plot shows clearly that the off-diagonal elements of $\mathbf{G}^{-1}$ are much smaller than the diagonal elements. The first downstream element is only 6.8% of the diagonal element for Re=35,000 compared to 28.4% for the first downstream element for fully developed turbulent pipe flow. This is due to the strong secondary flows and the high turbulent mixing in the ribbed passage. The thermal wake of the heated element spreads rapidly through the flow. The small off-diagonals indicate that the heat transfer coefficient is relatively insensitive to the thermal boundary condition for this type of flow.

The small off-diagonals greatly simplify the task of measuring the IDGF in similar passages with strong secondary flows and turbulent mixing. It is only necessary to measure the off-diagonal terms for the two elements immediately adjacent to the heated element. In fact, beyond the second element downstream of the heated element, the off-diagonal terms are too small to measure accurately. The only effect the heat transfer near the heated element has on the elements far downstream of the heated element is to raise the bulk mean temperature. This temperature rise can be calculated easily using an energy balance.

For the purpose of comparing the present data to literature values, the Nusselt number for a constant heat flux case was calculated using $\mathbf{G}^{-1}$. The temperature rise for a uniform heat flux boundary condition on element i was calculated using

$$\Delta T_i = \sum_{j=1}^{51} G_{ij}^{-1} \dot{q}_j \qquad (9)$$

where the heat flow vector is

$$\dot{\mathbf{q}} = \begin{bmatrix} \dot{Q} \\ \vdots \\ \dot{Q} \end{bmatrix} \qquad (10)$$

which applies a constant heat flow, $\dot{Q}$, on all 51 elements. The Nusselt number was calculated from
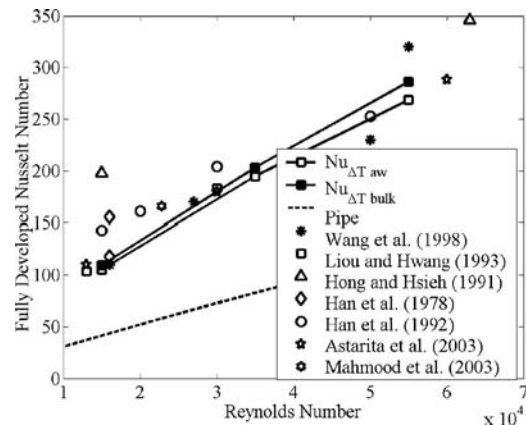
$$\mathrm{Nu}_i = \frac{hD}{k} = \frac{(\dot{Q}/A_s \Delta T_i)D}{k} \qquad (11)$$

at all seven straight passage locations.

The data from Hong and Hsieh [24] presented in Fig. 17 show significantly higher Nusselt numbers than the other studies, which is easily explained given the high blockage ratio and low pitch-to-height ratio relative to the other studies. Han et al. [14] normalized the heat transfer by using the projected surface area on the ribbed surface in Eq. (11); this results in a decrease in area over the total surface area on the ribbed wall by 23%. The Nusselt numbers presented in Fig. 17 are adjusted to reflect the total surface area on the ribbed walls.

There are two methods for calculating the Nusselt number in Fig. 17; they differ by how ΔT is defined in Eq. (11). It is common in the literature to use

$$\Delta T = \Delta T_{bulk} = (T_{wall} - T_{bulk}) \qquad (12)$$

The Nusselt number defined using this ΔT is $\mathrm{Nu}_{\Delta T_{bulk}}$. However, it is more appropriate to use

$$\Delta T = \Delta T_{aw} = (T_{wall} - T_{aw}) \qquad (13)$$

to calculate the Nusselt number denoted as $\mathrm{Nu}_{\Delta T_{aw}}$. This allows easier use of the superposition technique reported in Booten and Eaton [5] to characterize heat transfer in internal passages. Both methods for calculating the Nusselt number are used in Fig. 17 for comparison and show that the present results are within the range of Nusselt numbers found in similar geometries.

4.5 Corner Sections. The corners of the model have significantly different flow and thermal characteristics than the straight sections. Figure 18 shows the location of the "columns" that the thermocouples are grouped into. Each column was at a constant radius that was concentric with the outer surface of element 12 in the square corner that is shown in the figure and also with the outer surfaces of elements in the round corner. A sample of the steady-state thermal response in the corners is given in Fig. 19. The particular case shown is for the upstream, outside element of the square corner (element 11) being heated at Re=35,000. The x^+ direction was measured along a constant radius for each column beginning from the upstream edge of the corner. Therefore, the total x^+ that was covered was different for each column.

There was significant heating in all directions. As in the straight sections, much of this was from conduction through the plastic, which was corrected for when calculating Nusselt numbers and $\mathbf{G}^{-1}$. In particular, there was heating radially inward toward columns 1.5 and 1 (element 12) and downstream toward the outer element (element 13) that was not a result of conduction, as will
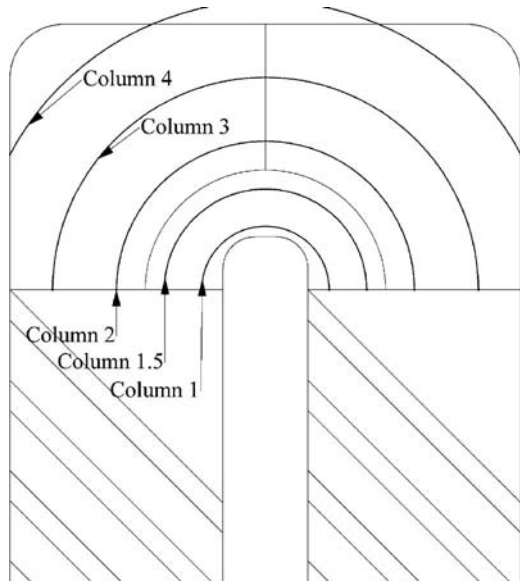
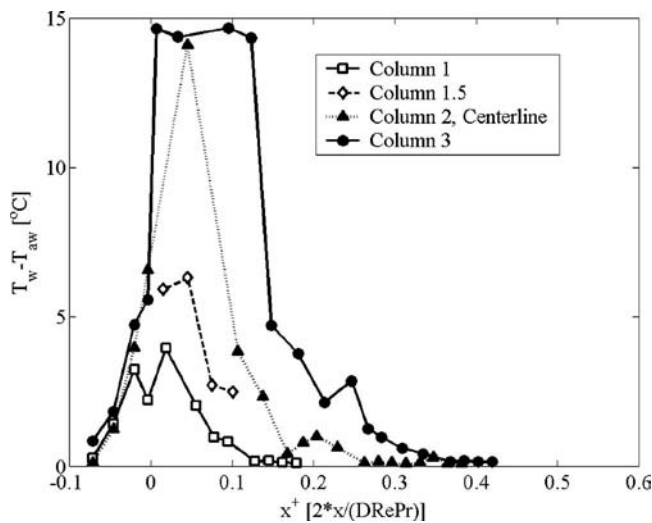**Fig. 18 Locations of "columns" of thermocouples in the square corner**

Fig. 19 Experimental temperature rise on the square corner, element 11 is heated, Reynolds number=35,000

be seen later. The general trend of strongly two dimensional surface temperature distribution that is seen in Fig. 19 holds true for all corner positions being heated and at all Reynolds numbers measured even though the relative amounts of heating can change.

The procedure for estimating conduction losses and calculating $\mathbf{G}^{-1}$ in the two corners was similar to that in the straight section; however, the geometry was more complicated. Each of the elements around the corners (elements 10–14 in the square corner and 38–42 in the round corner) can conduct heat to three to four elements directly plus lose heat through the top of the model, normal to the passage surface.

Table 1 compares the relative heat losses on the elements in both the square and round corners for Re=35,000. Table 1 shows that the conduction losses in the corners were in general a much higher percentage of the applied power than for the straight sections. This was due primarily to the small element sizes, especially in elements 12 and 40, and because of the relatively low heat transfer coefficients on the outer corner elements.

The measurement of $\mathbf{G}^{-1}$ around the corners follows the same methodology as in the straight sections. The conduction loss estimation was similar to that for the straight sections but the corrections for upstream and downstream surface heating were not. This was because in the straight sections, the upstream and downstream elements had similar thermal characteristics to the measured element. Therefore, uncorrected data from the measured element could be approximated as holding true for the adjacent elements and used in the iterative analysis needed to find the IDGF. On the corner elements, this was not possible. The thermal response to heating must be measured on all elements, then the data from the complete set of tests were used to calculate the up and downstream heating effects for each element.

There were no direct measurements of columns 10 and 14. The same is true for the corresponding elements near the round corner. The only data available on those elements are the temperature rise caused by the corner elements being heated. The columns of $\mathbf{G}^{-1}$ that correspond to these elements are left empty. This creates errors when using $\mathbf{G}^{-1}$ to calculate heat transfer rates in the corners and adjacent elements, but has no effect outside of those areas. Therefore, the corrections to $\mathbf{G}^{-1}$ are less accurate than with the straight passage locations where the effects of adjacent elements can be estimated more accurately.

A plot of $\mathbf{G}^{-1}$ for all measured elements is given in Fig. 20. The two most important trends in Fig. 20 are the rapid decrease in the elements of $\mathbf{G}^{-1}$ when moving away from the heated (main diagonal) element and the significantly higher values of $\mathbf{G}^{-1}$ around the corners when compared to the straight sections. The rapid decrease in the elements of $\mathbf{G}^{-1}$ is caused by the strong secondary flows that mix the warmed fluid near the wall with the mainstream flow very quickly. The higher values of $\mathbf{G}^{-1}$ in the corner represent the effects of heat transfer rates and surface area differences

Table 1 Comparison of the heat addition as a percentage of total power supplied to the heated element for all measured corner elements in the SGTIP model, Re=35,000

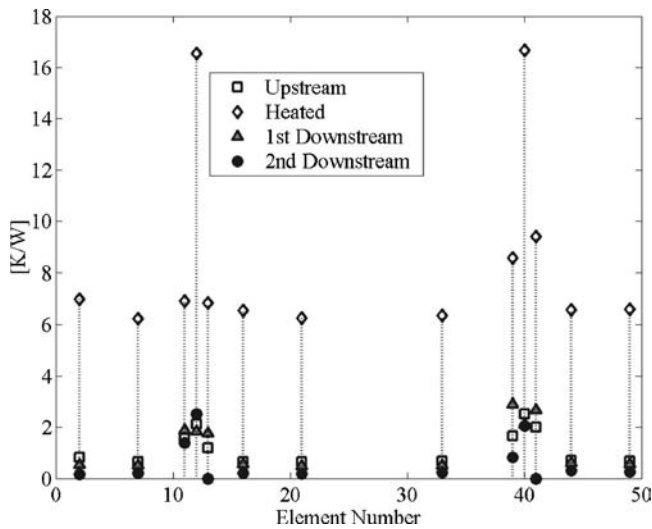| Element	Heated element					
	11	12	13	39	40	41
10	2.63	3.43				
11	−15.89	8.17	3.23			
12	3.77	−28.30	4.20			
13	2.81	7.92	−18.12			
14		3.42	2.95			
38				3.55	3.47	
39				−19.80	8.46	4.20
40				4.83	−28.57	5.52
41				3.54	8.16	−22.57
42					3.48	4.03

Fig. 20 G^{-1} for all measured locations, Re=35,000

with the straight section passages. G^{-1} is analogous to $1/hA_s$; a higher heat transfer coefficient and lower surface area A_s, therefore, have offsetting effects.

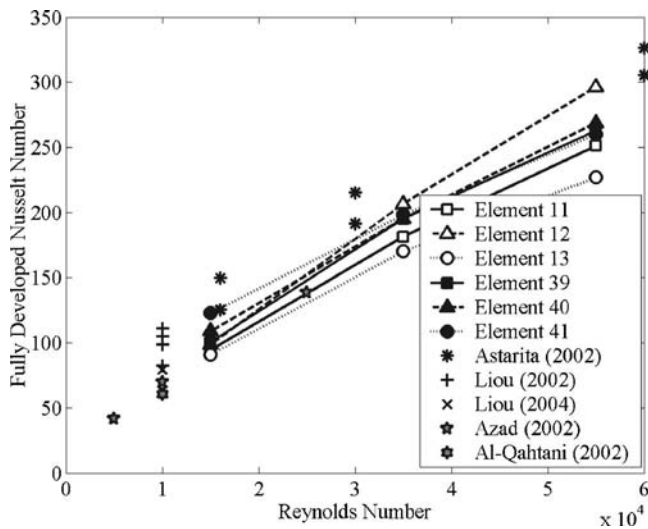The fully developed Nusselt numbers on the corner elements,

Fig. 21 Fully developed Nusselt numbers on corner elements versus Reynolds number

obtained using Eqs. (9)–(11), are given in Fig. 21. It is clear that the element near the inside corner has a much higher heat transfer rate, due to the higher freestream velocities. The Nusselt number on the downstream outer element on the square corner (element 13) increases significantly more slowly than the upstream outer element (element 11) with Reynolds number. This is because the higher Reynolds number flow tends to separate earlier when turning the corner than the lower Reynolds number flow. This causes the impingement of the flow to be more directly on the upstream outer element than the downstream. A similar trend is seen with the round corner (elements 41 and 39, respectively), except that it is less extreme because the rounded outer surface tends to sweep the flow around the round corner better than the square corner.

The agreement with the literature is striking considering that the geometries vary so widely. All of the studies compared in Fig. 21 used square corners but have different inner radii in the corners, they also have very different rib configurations, and most have ribs extending into the corners and sometimes in the middle of the corner as well. The values are all approximate average values of either the upstream or downstream halves of the corner except Azad et al. [25], which is an average over the entire corner.

5 Uncertainty Analysis

Uncertainties in experimental results were calculated using the single-sample uncertainty analysis put forth by Kline and McClintock [26] and Moffat [27]. The uncertainty associated with the conduction loss estimates was relatively large. This was in part due to the complex geometry and in part due to the lack of data on the heat transfer coefficients that were supplied as boundary conditions in the conduction loss models. The important parameters included in the uncertainty analysis are the accuracy of the thermocouple temperature difference readings ($\pm 0.05\,^{\circ}$C), power input ($\pm 0.0083 - 0.0093$ W), thermal conductivity of the stereolithography resin (± 0.05 W/mK), and the estimates of h on the nonheated surfaces. The resulting contributions of the individual parameters to the overall uncertainty in G^{-1} are given in Table 2. Note that only the nonzero entries in one column of G^{-1} (representing the straight section and the corner, respectively) are given. Other columns in G^{-1} had similar uncertainties.

6 Summary and Conclusions

The purpose for the experiments performed was to develop experimental techniques for measuring heat transfer coefficients in complex internal flows, specifically gas-turbine blade-cooling passages. The present technique can be used directly to aid in the design of turbine-blade serpentine cooling passages and to provide CFD qualification data. Current measurement techniques are often time consuming and difficult to perform, making them unwieldy and difficult to incorporate into the design of turbine-blade cool-

Table 2 Percent contributions to the overall root-sum-square uncertainty of G^{-1} for one square corner plug (element 12 heated) and one straight section plug (element 33 heated), Re=35,000. Element locations are shown in Fig. 3.

IDGF element	Power input	TC temperature	SLA thermal conductivity	h on nonheated surfaces in conduction model	RSS
$G^{-1}_{(32,33)}$	0.12	5.5	20	7.0	28.9
$G^{-1}_{(33,33)}$	0.31	0.5	4.4	1.8	5.4
$G^{-1}_{(34,33)}$	0.01	6.4	20.1	5.8	21.3
$G^{-1}_{(35,33)}$	0.36	15.4	2.8	1.7	15.8
$G^{-1}_{(10,12)}$	0.57	4.5	5.5	2.4	7.4
$G^{-1}_{(11,12)}$	0.27	4.8	6.1	2.4	8.1
$G^{-1}_{(12,12)}$	0.62	0.6	7.7	3.3	8.1
$G^{-1}_{(13,12)}$	0.12	7.7	20.6	8.6	23.1
$G^{-1}_{(14,12)}$	0.57	3.1	5.4	2.4	6.5

ing passages. The measurement techniques explored here have the advantage of being fast, accurate, and able to handle variable thermal boundary conditions.

This method for measuring heat transfer coefficients used discrete, heated copper elements with embedded thermocouples located in a passage wall to measure steady-state temperatures for a known applied heat flux. The data were converted to heat transfer coefficients using a DGF analysis. The DGF analysis uses superposition to combine the thermal response of the wall at all locations for a given boundary condition into a matrix. This matrix relates the wall temperature rise to the heat flux for any arbitrarily complex set of boundary conditions down to the size of the heated copper elements.

A generic serpentine passage model, dubbed the SGTIP model, was designed to adhere closely to industry design practice for mid-chord type cooling passages. It had four straight sections with rib turbulators on two opposing walls. There were two types of corners, one with a roughly square shape and the other with a circular shape to mimic the extremes in the types of corners on actual cooling passages.

There are no analytical comparisons for the heat transfer in this type of passage, but there is a significant body of experimental literature on similar types of passage geometries. An increase in Nusselt number over thermally fully developed pipe flow of 2.5–3.0 is common in the previous experiments and is consistent with the results in the present work. An important result was that the high turbulence levels in the straight sections of the model caused the flow to become thermally fully developed quickly so that the heat transfer characteristics were relatively constant over all the passages. The heat transfer characteristics in the corners varied significantly depending on the location and the corner shape. The inner side of the corners had much higher heat transfer and mean velocity than the outer side, which had large stagnant regions. The geometry of the corners had a large effect on the heat transfer coefficients. The different corner shapes and features in the literature resulted in a much larger distribution in heat transfer coefficients than in the straight sections. This makes heat transfer measurements in the corners even more important when qualifying CFD codes or designing new cooling passages.

There is a more general conclusion from this work that is probably applicable to a wide range of complex passage flows. Most such flows contain strong secondary flows and, if there are separated flow zones, the turbulence levels are also high. The present experiment has shown that the rapid mixing in complex passages leads to small values of the off-diagonal terms of the IDGF. The off diagonals decay very rapidly moving away from a heated element and can be accurately estimated knowing only the bulk temperature rise due to that element. Practically, this means that the conventionally defined heat transfer coefficient h is only weakly affected by the applied thermal boundary conditions. This is the opposite of simpler flows, such as straight pipes, where the upstream wall temperature profile has a strong influence on h. This is important because a careful heated element experiment is considerably easier than an experiment where the full passage temperature or heat flux distribution is controlled.

Acknowledgment

Nomenclature

aspect ratio = width of channel side with ribs to width of channel side without ribs

A_s = cross-sectional area of serpentine passage (m^2)
α = thermal diffusivity of fluid (m^2/s)
β = expansion coefficient, for ideal gases, it is one over the film temperature ($2/(T_{\text{bulk}}+T_{\text{wall}})$).
δ_{jk} = Kronecker delta
DGF = discrete Green's function $\mathbf{G}$ (W/K)
D = hydraulic diameter (m)
$\Delta\mathbf{T}$ = temperature difference vector for calculating Nusselt number (°C)
$\Delta T_{\text{uncorrected}}$ = measured temperature rise on each element (°C)
IDGF = inverse discrete Green's function $\mathbf{G}^{-1}$ (K/W)
$\mathbf{G}^{-1}_{\text{uncorrected}}$ = $\mathbf{G}^{-1}$ before correcting for conduction losses (K/W)
$\mathbf{G}^{-1}_{\text{reduced}}$ = reduced $\mathbf{G}^{-1}$ where all elements in diagonals more than a certain distance away from the main diagonal are considered zero (K/W)
$\mathbf{g}^{-1}$ = a single column of $\mathbf{G}^{-1}$ (K/W)
h = heat transfer coefficient, (W/m^2 K)
k = thermal conductivity (W/m^2 K)
Ma = Mach number
Nu = Nusselt number hD/k_{fluid}
ν = kinematic viscosity of fluid (m^2/s)
pitch = axial distance between ribs
Pr = Prandlt number (ν/α)
$\dot{Q}$ = constant heat flow applied to determine Nusselt number (W)
$\dot{\mathbf{q}}$ = vector of heat transfer rates into fluid (W)
$\dot{q}_{\text{corrected},j}$ = net heat flow into fluid on element j (W)
Ra = measure of natural convection ($g\beta\Delta T L_{\text{ch}}^2/\nu\alpha$)
Re = Reynolds number ($\bar{v}L_{\text{ch}}/\nu$).
r_c = recovery factor
ribs = protrusions from the passage walls into the flow stream. Also called turbulators.
SGTIP = Stanford generic turbine internal passage
T = static temperature (°C)
T_∞ = reference temperature for external flows (°C)
T_{bulk} = bulk temperature of fluid (°C)
T_o = stagnation temperature (°C)
T_{wall} = wall temperature (°C)
T_{aw} = adiabatic wall temperature (°C)
x = axial distance along serpentine passage (m)
x^+ = nondimensional axial distance along passage ($2x/D$ Re Pr)

References

[1] Lindstrom, P., "Out-of-Core Simplification of Large Polygonal Models," 2000, *ACM SIGGRAPH*, ACM SIGGRAPH, New Orleans, LA, pp. 259–262.

[2] Batchelder, K., and Eaton, J. K., 2001, "Practical Experience With the Discrete Green's Function Approach to Convective Heat Transfer," J. Heat Transfer, **123**, pp. 70–76.

[3] Hacker, J., and Eaton, J., 1997, "Measurements of Heat Transfer in a Separated and Reattaching Flow With Spatially Varying Thermal Boundary Conditions," Int. J. Heat Fluid Flow, **18**, pp. 131–141.

[4] Mukerji, D., and Eaton, J., 2002, "Spatially-Resolved Measurements of Heat Transfer in Turbomachinery Applications," Stanford University Technical Report No. TSD-145.

[5] Booten, C., and Eaton, J., 2005, "Discrete Green's Function Measurements in Internal Flows," J. Heat Transfer, **127**, pp. 692–698.

[6] Booten, C., Elkins, C., and Eaton, J., 2006, "Rapid Heat Transfer Measurements in Complex Internal Flows," Stanford University Technical Report No. TF-99.

[7] Han, J., Glicksman, L., and Rohsenow, W., 1978, "An Investigation of Heat Transfer and Friction for Rib-Roughened Surfaces," Int. J. Heat Mass Transfer, **21**, pp. 1143–1156.

[8] Liou, T., and Hwang, J., 1992, "Developing Heat Transfer and Friction in a Ribbed Rectangular Duct With Flow Separation at Inlet," J. Heat Transfer, **114**, pp. 565–573.

[9] Astarita, T., Cardone, G., and Carlomagno, G., 2002, "Convective Heat Transfer in Ribbed Channels With a 180° Turn," Exp. Fluids, **33**, pp. 90–100.

[10] Carlomagno, C., Astarita, T., and Cardone, G., 2002, "Convective Heat Trans-

fer and Infrared Thermography," Ann. N.Y. Acad. Sci., **972**, pp. 177–186.

[11] Chandra, P., Han, J., and Lau, S., 1988, "Effect of Rib Angle on Local Heat/Mass Transfer Distribution in a Two-Pass Rib-Roughened Channel," J. Turbomach., **110**, pp. 233–241.

[12] Wright, L., Fu, W., and Han, J., 2004, "Thermal Performance of Angled V-Shaped and W-Shaped Rib Turbulators in Rotating Rectangular Cooling Channels (AR=4:1)," J. Turbomach., **126**, pp. 604–614.

[13] Lau, S., McMillin, R., and Han, J., 1991, "Heat Transfer Characteristics of Turbulent Flow in a Square Channel With Angled Discrete Ribs," J. Turbomach., **113**, pp. 367–374.

[14] Han, J., Zhang, Y., and Lee, C., 1992, "Influence of Surface Heat Flux Ratio on Heat Transfer Augmentation in Square Channels With Parallel, Crossed, and V-Shaped Angled Ribs," J. Turbomach., **114**, pp. 872–880.

[15] Won, S., and Ligrani, P., 2004, "Comparisons of Flow Structure and Local Nusselt Numbers in Channels With Parallel- and Crossed-Rib Turbulators," Int. J. Heat Mass Transfer, **47**, pp. 1573–1586.

[16] Astarita, T., and Cardone, C., 2003, "Convective Heat Transfer in a Square Channel With Angled Ribs on Two Opposite Walls," Exp. Fluids, **34**, pp. 625–634.

[17] Chandra, P., Niland, M., and Han, J., 1997, "Turbulent Flow Heat Transfer and Friction in a Rectangular Channel With Varying Numbers of Ribbed Walls," J. Turbomach., **119**, pp. 374–378.

[18] Chandra, P., Alexander, C., and Han, J., 2003, "Heat Transfer and Friction Behaviors in Rectangular Channels With Varying Number of Ribbed Walls," Int. J. Heat Mass Transfer, **46**, pp. 481–495.

[19] Elkins, C., Markl, M., Iyengar, A., Wicker, R., and Eaton, J., 2004, "Full Field Velocity and Temperature Measurements Using Magnetic Resonance Imaging in Turbulent Complex Internal Flows," Int. J. Heat Fluid Flow, **25**, pp. 702–710.

[20] Hsu, C., 1968, "Exact Solution to Entry-Region Laminar Heat Transfer With Axial Conduction and the Boundary Condition of the Third Kind," Chem. Eng. Sci., **23**, pp. 457–468.

[21] Notter, R., and Sleicher, C., 1971, "A Solution to the Turbulent Graetz Problem by Matched Asymptotic Expansions—II. The Case of Uniform Wall Heat Flux," Chem. Eng. Sci., **26**, pp. 559–565.

[22] Elkins, C., Markl, M., Pelc, N., and Eaton, J., 2003, "4D Magnetic Resonance Velocimetry for Mean Flow Measurements in Complex Turbulent Flows," Exp. Fluids, **34**, pp. 494–503.

[23] White, F., 1991, *Viscous Fluid Flow*, 2nd ed., McGraw-Hill, New York.

[24] Hong, Y., and Hsieh, S., 1991, "An Experimental Investigation of Heat Transfer Characteristics for Turbulent Flow Over Staggered Ribs in a Square Duct," Exp. Therm. Fluid Sci., **4**, pp. 714–722.

[25] Azad, G. S., Uddin, M., Han, J., Moon, H., and Glezer, B., 2002, "Heat Transfer in a Two-Pass Rectangular Rotating Channel With 45–deg Angled Rib Turbulators," J. Turbomach., **124**, pp. 251–259.

[26] Kline, S., and McClintock, F., 1953, "Describing Uncertainties in Single-Sample Experiments," Mech. Eng. (Am. Soc. Mech. Eng.), pp. 53–57.

[27] Moffat, R., 1988, "Describing the Uncertainties in Experimental Results," Exp. Therm. Fluid Sci., **1**, pp. 3–17.

Effects of Fin Shapes and Arrangements on Heat Transfer for Impingement/Effusion Cooling with Crossflow

Sung Kook Hong

Dong-Ho Rhee

Hyung Hee Cho[1]
e-mail: hhcho@yonsei.ac.kr

Department of Mechanical Engineering,
Yonsei University,
Seoul 120-749, Korea

The present paper has investigated the effects of fins on the flow and heat/mass transfer characteristics for the impingement/effusion cooling with crossflow. The circular or rectangular fins are installed between two perforated plates, and the crossflow occurs between these two plates. The crossflow blowing ratio is varied from 0.5 to 1.5 for a fixed jet Reynolds number of 10,000. A naphthalene sublimation method is used to obtain local heat/mass transfer coefficients on the effusion plate. A numerical calculation is also performed to investigate the flow characteristics. The flow and heat/mass transfer characteristics are changed significantly due to the installation of fins. In the injection hole region, the wall jet spreads more widely than in the case without fins because the fins prevent the wall jet from being swept away by the crossflow. In the effusion hole region, a higher heat/mass transfer coefficient is obtained due to the flow disturbance and acceleration by the fin. As the blowing ratio increases, the effect of fins against the crossflow becomes more significant and subsequently the higher average heat/mass transfer coefficients are obtained. In particular, the cases with rectangular fins show an approximately 40–45% enhancement at the high blowing ratio of $M=1.5$. However, the increase in the blockage effect results in increased pressure loss in the channel.
[DOI: 10.1115/1.2767727]

Keywords: impingement/effusion cooling, fin, crossflow, heat/mass transfer

1 Introduction

The demand for improvements in the efficiency and power output of gas turbines has led to a continuous increase in the turbine inlet temperature, which increases thermal loads on the hot components of the gas turbine as well. Therefore, a variety of cooling techniques has been developed to preserve components such as combustor liner and turbine blade. Among the cooling schemes, impingement/effusion cooling is a very efficient cooling technique that combines array jet impingement with film cooling. In this cooling scheme, the system structure is consisted of injection plate and effusion plate, which have a lot of small hole. The cooling air issues through the injection hole and the inner surface of effusion plate (effusion surface) are cooled by the impingement of cooling air. The spent cooling air is discharged through the effusion hole into the outside and the outer surfaces of effusion plate exposed to hot gases are protected by film cooling.

Owing to this advantage, investigations on the impingement/effusion cooling technique have been performed for the past two decades. Hollwarth and Dagan [1] measured average heat transfer coefficients on the effusion surface and reported that array jets with staggered vents yield higher heat transfer rates than do the impinging jets on the solid plates. Hollwarth et al. [2] continued their work measuring local heat transfer along two symmetry lines and providing flow visualization. Nazari and Andrews [3] reported the film cooling performance with a variety of number of holes for impingement/effusion cooling. Cho and Goldstein [4] studied the local heat/mass transfer characteristics inside the effusion plate.

They found that the high transfer rate is induced by strong secondary vortices and flow acceleration, and the averaged Sherwood value is approximately 45–55% higher than that for the impingement cooling alone. Cho and Rhee [5], Rhee et al. [6], and Cho et al. [7] showed flow and heat/mass transfer characteristics of impingement/effusion cooling system with a variety of conditions, such as hole-to-plate spacing, Reynolds number, and hole arrangement.

In actual combustor liner and turbine parts cooling, an initial crossflow may occur in the internal passages and it significantly affects the heat transfer characteristics. Thus, several studies have been performed on the crossflow effects although most of them have been focused on array jet impingement cooling. Florschuetz et al. [8], Metzger and Korstad [9], Huang et al. [10], Haiping et al. [11], Hwang and Chang [12], Bailey and Bunker [13], Rhee et al. [14], Gao et al. [15], and Chambers et al. [16] performed examinations of the effects of crossflow on array jet impingements with various conditions and showed that an adverse effect on jet impingement cooling occurs by crossflow. For the impingement/effusion cooling, Ekkad et al. [17] studied the influence of crossflow orientation. They showed that high heat transfer appears in the crossflow orientation with a small crossflow rate among the various orientations. Rhee et al. [18] reported that the overall heat/mass transfer rates on the effusion (target) plate decrease as the velocity of crossflow increases and that locally low transfer regions are formed between the adjacent effusion holes.

It is necessary to reduce the adverse effects generated by the crossflow and to enhance the cooling performance. For this purpose, studies using ribs on the target plate have been carried out by Haiping et al. [19] and Andrews et al. [20]. Rhee et al. [21] applied various rib configurations to an impingement/effusion cooling system and showed that the averaged heat transfer was

enhanced by 4–15% as compared to a system without ribs. However, the rate of increase in heat transfer decreases as the crossflow effect becomes strong.

To obtain a more efficient cooling performance and increased durability, the usage of fins is considered to be one of the possible options. Further, the fins provide additional advantages such as heat conduction through the fins and enhancement of the structural strength in the system. However, there have been few studies on the fins with respect to the impingement/effusion cooling. Andrews et al. [22] and Annerfeldt et al. [23] carried out the experiments with fins but those were focused on the jet impingement cooling. Funazaki et al. [24] and Yamawki et al. [25] reported the effects of fins on the impingement/effusion cooling; however, they did not consider the crossflow. Therefore, we have studied the effects of fins in a combined cooling technique to reduce the adverse effect of the crossflow and to augment the cooling performance for an impingement/effusion cooling system with crossflow.

In the present study, the flow and heat/mass transfer characteristics have been investigated for impingement/effusion cooling with various fin shapes and arrangements when the initial crossflow is applied. These results are compared with those for the cases without fins and array jet impingement cooling with fins. Further, the influence of the crossflow blowing ratio (crossflow rate) has been examined.
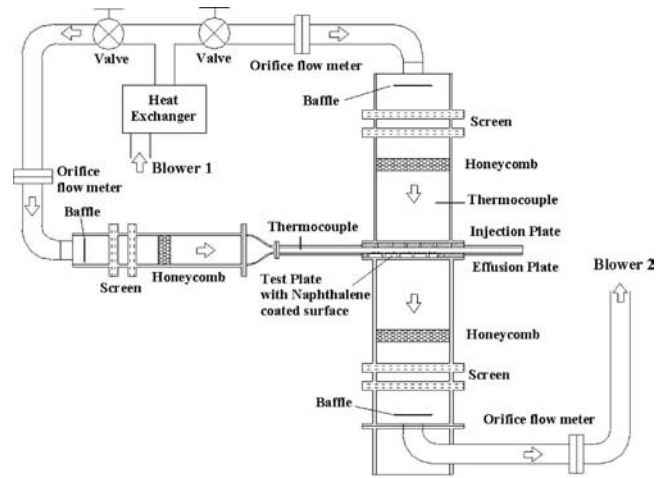
2 Experimental Apparatus and Conditions

2.1 Experimental Apparatus. The experimental apparatus is shown in Fig. 1(a). This is composed of three parts such as impinging jet, flow effusion, and crossflow supply parts. One blower (Blower 1) supplies the crossflow and impinging jet flow and the other blower (Blower 2) makes effusion flow through the effusion plate. The flow rates of the air supplied to each part are measured by orifice flow meters and controlled.

Figure 1(b) presents the schematics of test section and effusion plate. The crossflow channel is positioned between the injection and the effusion plenum chambers. It is noted that the injection hole is on the plate above the naphthalene coated plate (effusion plate). For simulating the impingement/effusion cooling, the jets from injection holes impinge on the effusion plate and then discharge through the effusion holes. The effect of mainstream, i.e., the flow passing the outer surface of effusion plate, is not considered because heat/mass transfer coefficients on the inner surface of the effusion plate are the same with and without mainstream in film cooling, as reported by Cho and Goldstein [26]. In order to obtain the turbulent channel flow, sand paper and trip wire are installed at the inlet of channel after the contraction section with a 6:1 area ratio. The inlet of duct is 400 mm ($10.7D_h$) away from the first row of injection holes. The cross section of the channel is 300 mm (W) × 20 mm (H), and the hydraulic diameter of the channel (D_h) is 37.5 mm.

The diameters of the injection and the effusion holes are 10 mm, and the thickness of plates is 20 mm ($t/d=2.0$). The gap distance (H/d) between the injection and the effusion plate is fixed to 2.0. The 25 (5×5) holes of square array are positioned at each plate, and the ratio of hole spacing to the diameter (P_{hole}/d) is 6.0. A naphthalene coated test plate ($8.4d \times 28d$) is installed on the effusion plate for local mass transfer measurements. Using a T-type thermocouple, the naphthalene surface temperature is measured during the experiment.

For measurement of the pressure drop through crossflow channel, inlet and outlet pressure taps are positioned at the sidewall 100 mm away from the first row of injection holes and the last row of effusion holes, respectively. The differential static pressure is measured by using a low differential pressure sensor (LPE 9145 model, Druck).

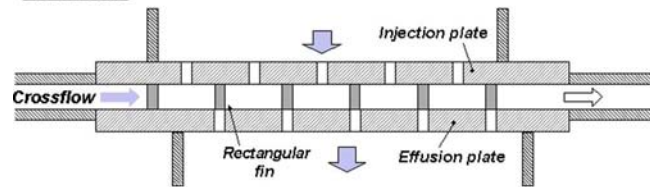**2.2 Fin Shapes and Arrangements.** The fins are installed in

(a)
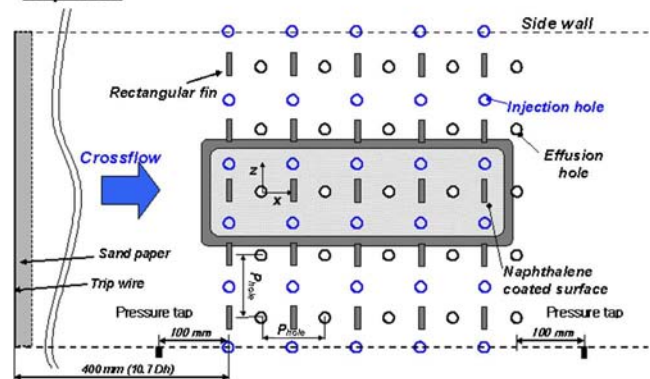
(b)

Fig. 1 Schematic view of experimental facility: (a) experimental apparatus and (b) test section

the channel, as shown in Fig. 1(b). In the present study, we consider a total of five cases, which can be classified into two groups: two cases with circular pin fins and three with rectangular fins. Figure 2 shows the schematic diagram of each case that is referred to as CP1, CP2, RF0, RF1, and RF2 and the notations "CP" and "RF" represent circular pin fin and rectangular fin, respectively. The geometry and arrangement parameters of the fins in each case are listed in Table 1. The height of a fin is equal to the channel height.

In the case of CP, the CP fins are installed along the centerline of the effusion holes, as shown in Figs. 2(a) and 2(b). In the case of CP1, an additional row of the CP fins is installed along the centerline of the injection holes. In the case of CP2, two additional rows of CP fins are positioned 1d away from the centerline of the injection holes.

Figures 2(c)–2(e) show the three cases with RFs in which there are no fins along the centerline of the effusion holes. In the case of RF0 and RF1, the RFs are installed along the centerline of the injection holes. In the case of RF2, the positions of the fins are the
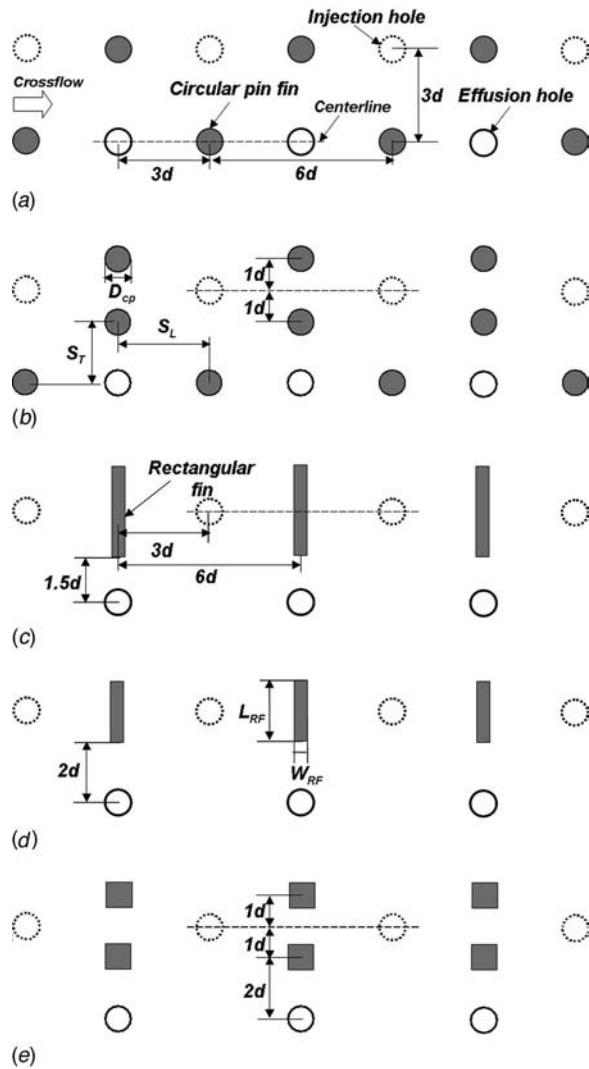
Fig. 2 Schematic view of various fin shapes and arrangements: (a) CP1, (b) CP2, (c) RF0, (d) RF1, and (e) RF2

same as that in the CP2 case except that there is no installation of fins between the effusion holes. Hence, S_T is set as $2d$ and $4d$ in the injection and effusion regions, respectively.

By installing the fins, the cross-sectional area of the channel is changed. In the present study, the blockage area ratio is defined as the ratio of the the windward area of the installed fin to cross-sectional area of the channel. The ratio for each case is listed in Table 1.

2.3 Operating Conditions. In the present study, a crossflow blowing ratio has been used to represent the influence of crossflow on the cooling system. The blowing ratio is a ratio of total flow rate of crossflow to the impinging jets and defined as

Table 1 Fin geometry and arrangement parameters

Case	Fin shape	S_L (mm)	S_T (mm)	D_{CP} (mm)	L_{rf} (mm)	W_{rf} (mm)	B (%)
CP1	Circular	30	30	10	—	—	16.7
CP2	Circular	30	20	10	—	—	33.3
RF0	Rectangular	60	60	—	30	5	50.0
RF1	Rectangular	60	60	—	20	5	33.3
RF2	Rectangular	60	20,40	—	10	10	33.3

Table 2 Operating conditions

M	MR	I	Re_d	Re_{D_h}
0.5	0.164	0.027	10,000	6130
1.0	0.327	0.107	10,000	12,270
1.5	0.491	0.241	10,000	18,400

$$M = Q_c/Q_i \tag{1}$$

The experiments were performed for the blowing ratio from 0.5 to 1.5, and the desired conditions were obtained by changing the flow rate of the crossflow with the fixed flow rate of impinging jets. For the impingement/effusion cooling, the flow rate of air through the effusion holes is set to be the same as that through the injection holes to catch the effects of crossflow precisely. The operating conditions are summarized in Table 2.

From a different point of view, a mass flux ratio of the crossflow to the jet flow ($\mathrm{MR} = \rho_c V_c / \rho_i V_i$) or momentum ratio ($I = \rho_c V_c^2 / \rho_i V_i^2$) may be a more important parameter than the blowing ratio (i.e., a ratio of total flow rate) to design the cooling system. These values corresponding to a given value of blowing ratio are also presented in Table 2.

2.4 Data Reduction. Equation (2) shows the local mass transfer coefficient as

$$h_m = \frac{\dot{m}}{\rho_{v,w} - \rho_{v,\infty}} = \frac{\rho_s(dy/d\tau)}{\rho_{v,w}} \tag{2}$$

Note that incoming flow contains no naphthalene: $\rho_{v,\infty}$ is zero in the present study. Thus, the mass transfer coefficient is calculated from the local sublimation depth of naphthalene (dy), run time ($d\tau$), density of solid naphthalene (ρ_s), and naphthalene vapor density ($\rho_{v,w}$). The naphthalene vapor pressure is obtained from a correlation of Ambrose et al. [27]. Then, the naphthalene vapor density $\rho_{v,w}$ is calculated from the perfect gas law. The details of the measuring system are described in Ref. [18]. The Sherwood number (Sh) can be expressed as

$$\mathrm{Sh} = h_m d/D_{\mathrm{naph}} \tag{3}$$

Note that for the channel flow cases (the simple channel cooling), the hydraulic diameter of the channel was used as a characteristic length ($\mathrm{Sh}_{D_h} = h_m D_h / D_{\mathrm{naph}}$). D_{naph} is the diffusion coefficient of naphthalene vapor in air and the properties of naphthalene suggested by Goldstein and Cho [28] are used in the present study. The mass transfer coefficients can be converted to the heat transfer coefficients using the heat and mass transfer analogy by Eckert [29]. Prandtl number is 0.71 for air and the Schmidt number is 2.28 for the naphthalene vapor in air at 25°C. The experiments were conducted at room temperature, and the Lewis number (Pr/Sc) for this study is about 0.31.

$$\mathrm{Nu}/\mathrm{Sh} = (\mathrm{Pr}/\mathrm{Sc})^{0.4} \quad \mathrm{Nu} = 0.624 \, \mathrm{Sh} \tag{4}$$

The comparison between heat transfer and mass transfer results is reported by Rhee et al. [14,18]. Uncertainty of the Sherwood numbers using the method of Kline and McClintock [30] for single sample experiments is within ±7.1% in the entire operating range of the measurement, based on a 95% confidence level as listed in Table 3. This uncertainty is mainly caused by the uncer-

Table 3 Uncertainty of main parameter

$\rho_{v,w}$	ρ_s	dy	h_m	d	D_{naph}
3.8%	1.1%	0.7%	4.9%	0.4%	5.1%

$$\frac{\Delta \mathrm{Sh}}{\mathrm{Sh}} = \left[\left(\frac{\Delta h_m}{h_m} \right)^2 + \left(\frac{\Delta d}{d} \right)^2 + \left(\frac{\Delta D_{\mathrm{naph}}}{D_{\mathrm{naph}}} \right)^2 \right]^{1/2} = 7.1\%$$
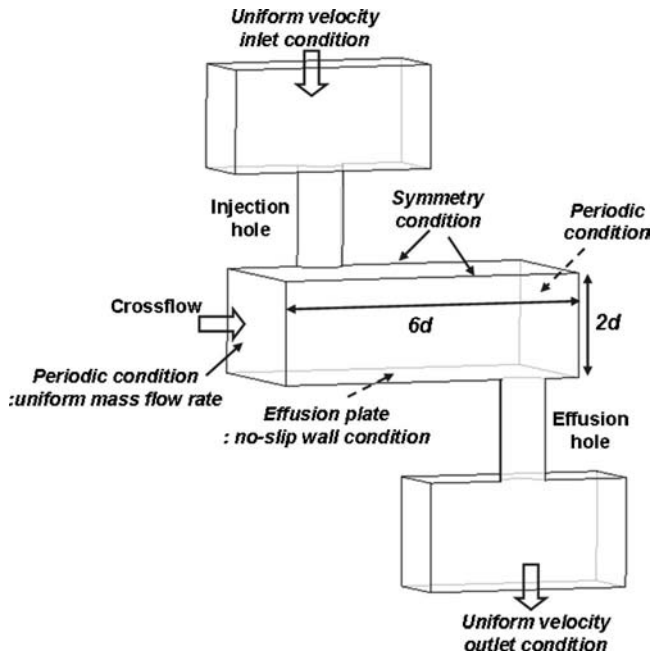
Fig. 3 Calculation domain and boundary conditions for the impingement/effusion cooling system

tainty of the properties of naphthalene (i.e., $\rho_{v,w}$, D_{naph}), which are estimated by the previous measurement studies. The details of calculation of uncertainty are described in Refs. [28,31].

3 Numerical Simulation

In order to understand the flow characteristics, numerical simulations were performed for the impingement/effusion cooling with different fin shapes (without fins, CP1, and RF1 case) at $M=1.0$.

A commercial code, FLUENT (version 6.1), was used to calculate flow fields and computation domain grids were created using GAMBIT solid modeling. Figure 3 shows the calculation domain and boundary conditions for the impingement/effusion cooling system. Since the interested calculation domain has a periodic geometry as shown in Fig. 1(b), one pitch including an injection hole, an effusion hole and fins are considered by using a periodic boundary condition. Symmetric boundary conditions were imposed on the injection/effusion planes to reduce grid size and calculation time.

To simulate the flow conditions corresponding to $M=1.0$, a uniform flow with a velocity of 0.327 m/s and a turbulence intensity of 10% was applied to the inlet of the injection chamber. A mass flow rate of periodic plane was set to be 3.534 g/s. The steady solutions for turbulent flow field were calculated using a renormalization group (RNG) k-ε model. Different grids with 400,000 to 1.3×10^6 cells were tested to verify the grid independence of solution, and the results for the grid with 800,000–900,000 cells were shown in the present study. The convergence of scaled residuals [32] for continuity, momentum, k, and ε was resolved to levels of 10^{-4}.

4 Results and Discussion

4.1 Simple Channel Cooling With Fins. For the base line data and the qualification test, a simple channel flow with the CP1 and RF1 fin configurations is examined for a fixed channel Reynolds number (Re_{D_h}) of 12,270, which corresponds to the channel flow velocity at $M=1.0$ for the array jet impingement and impingement/effusion cooling.

Figure 4 presents the contours of CP1 and RF1 for the simple channel cooling (i.e., only crossflow without either injection or
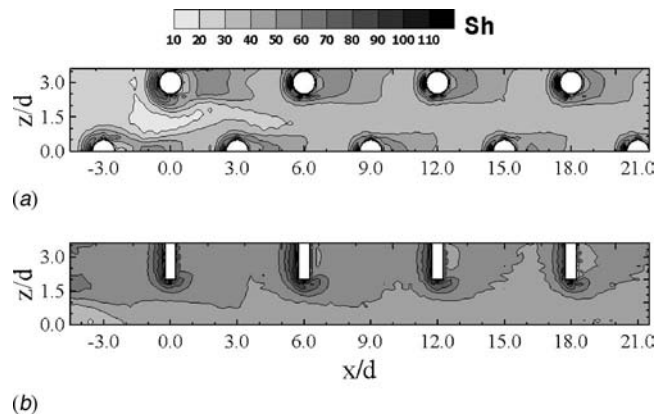

Fig. 4 Contour plots of Sh for crossflow only with various fin shapes: (a) CP fins (CP1) and (b) RFs (RF1)

effusion flows). The heat transfer characteristics influenced by the generation of a vortex and wake are observed, as reported in the previous studies [33–35]. In front of the fin, a very high heat transfer occurs due to a horseshoe vortex. In the wake, which is formed downstream of the fin, the heat transfer is enhanced due to an increase in the flow disturbance by the fin, and relatively low heat transfer distributions are observed immediately behind the fin because of flow recirculation with low local velocity.

Figure 5 shows the streamwise distributions of spanwise averaged Sh. The characteristic length of Sh is based on the channel hydraulic diameter (D_h) and the Sh values are normalized by $\mathrm{Re}_{D_h}^{0.8}$ because the heat transfer of a turbulent channel flow is proportional to this value. In the figure, the solid line represents the simple channel flow without fins (experimental data) and the dash-dot line indicates the value for a fully developed turbulent flow ($\mathrm{Sh}_0/\mathrm{Re}^{0.8}=0.023~\mathrm{Sc}^{0.4}$; the Dittus-Boelter correlation [36]).

As shown in Fig. 5, the Sh value for the cases with fins is approximately 2.4–2.8 times that for the case without fins. For CP1, the peak values occur for the region in front of the CP fins ($x/d=-0.5, 2.5$, etc.) and the high heat transfer patterns are periodically observed except in the initial region. When RFs are installed, higher heat transfer coefficients are obtained as compared to those of CP1 due to the increase in flow mixing and flow velocity.

4.2 Array Jet Cooling With Initial Crossflow. Figure 6 shows the contour plots of Sh on the target surface for array jet impingement without effusion holes at $M=1.0$. The white dotted circles represent the projected positions of the injection holes and the white rectangles indicate the fins installed in the channel. For
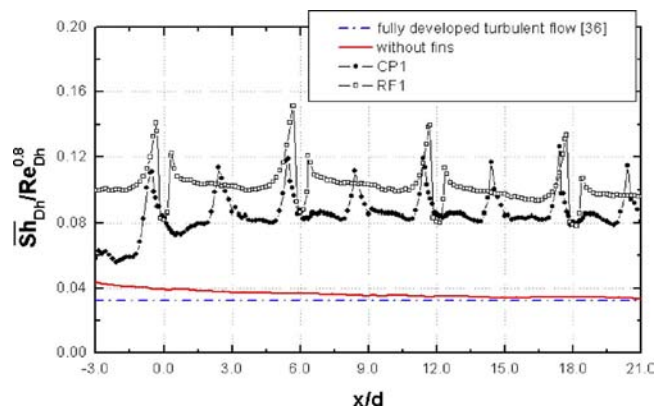

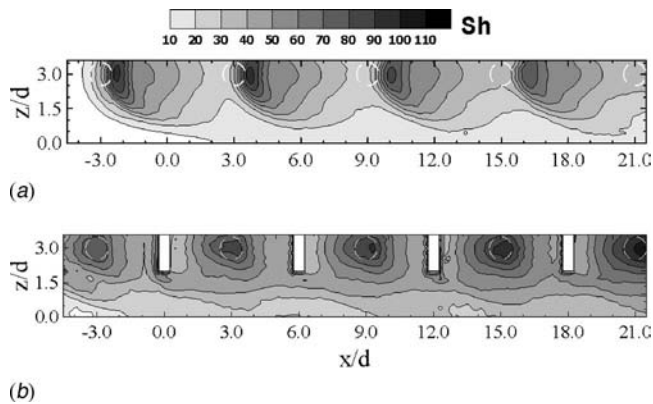Fig. 5 Spanwise averaged Sh for crossflow only with various fin shapes

Fig. 6 Contour plots of Sh for array jet cooling with initial crossflow at *M*=1.0: (*a*) without fins and (*b*) RFs (RF1)

an array jet impingement cooling without fins (Fig. 6(*a*)), since the spent air from impinging jets turns into the crossflow, the crossflow rate increases as the flow moves downstream. Thus, the stagnation points of the impinging jets shift downstream and the peak values decrease with increasing x/d. Low Sh distributions are observed in the midway region (along $z/d \cong 0.0$) due to sweeping of wall jet by the crossflow and developing of a boundary layer.

On the contrary, in the case of RFs (Fig. 6(*b*)), higher and more uniform heat transfer distributions are observed as compared to the case without fins. This is attributed to a strong blockage effect

that the installed fins obstruct the crossflow, thus significantly reducing the effects of the crossflow in the injection hole region ($z/d \cong 3.0$). In addition, at the midway region ($z/d \cong 0.0$), the decrease in the cross-sectional area of the channel induces flow acceleration and subsequently the heat/mass transfer coefficients are higher than those for the case without fins. Consequently, the RF enhances the Sh uniformity on the target plate.

4.3 Impingement/Effusion Cooling With Crossflow

4.3.1 Flow Characteristics. Figure 7 shows the velocity vector plots on the injection and effusion planes (z/d=3.0 and 0.0) for the case without fins and that with two different fin shapes (CP1 and RF1) at M=1.0.

For impingement/effusion cooling with initial crossflow, the flow pattern on the injection plane shows that the impinging jet shifts approximately 0.5d toward the downstream side, and the channel flow and spent air are entrained into the jet stream. Near the wall of the effusion plate, a small vortex is generated in the upstream region of the stagnation point, and most of the wall jet is swept downstream. On the effusion plane, the overall flow pattern is similar to the channel flow; however, the upward flow features are observed. It is mainly due to the collision between adjacent wall jet spreading toward the spanwise direction. Even though the wall jet is swept away downstream by the crossflow, some of wall jets developing toward the spanwise direction collide with the crossflow and then generate the upward flow on the center region (effusion plane) between the adjacent wall jets.

For CP1 (Fig. 7(*b*)), owing to the fin in front of the impinging jet, a wake region with recirculating flow is generated and the crossflow passing along z/d=3.0 (the injection plane) decreases.
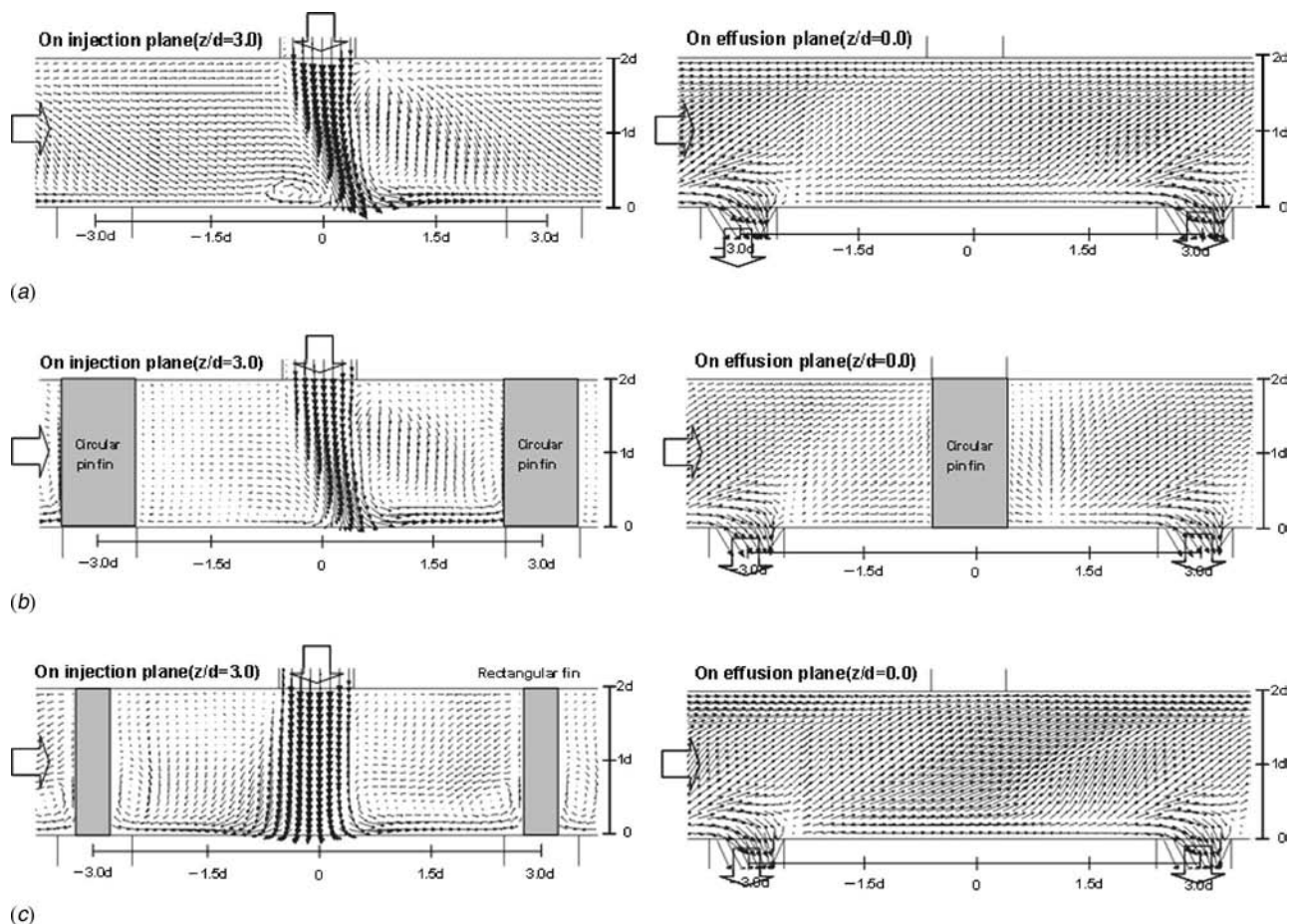

Fig. 7 Velocity vector on the injection and the effusion planes at *M*=1.0: (*a*) without fins, (*b*) CP fins (CP1), and (*c*) RFs (RF1)
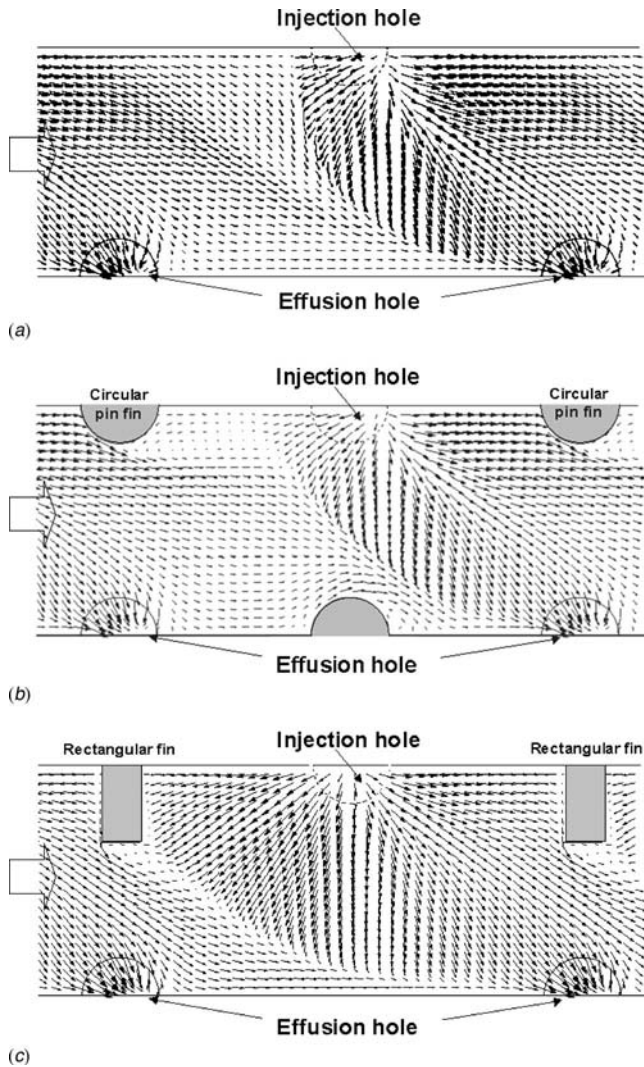
Fig. 8 Velocity vector on the bottom of the effusion planes: (a) without fins, (b) CP1, and (c)RF1

Fig. 9 Contour plots of Sh for impingement/effusion cooling with circular pin fins at $M=1.0$: (a) without fins (b) CP1, and (c)CP2

Thus, the injected flow is less affected by the crossflow as compared to the case without fins. Near the wall of the effusion plate, the wall jet spreads more widely to the upstream. In the downstream region, the wall jet reaches the CP fin and subsequently generates a vortex flow at the junction between the effusion plate and fin. On the effusion plane ($z/d=0.0$), the flow characteristics are similar to the case without fins except in the wake region behind the CP fin.

When RFs are installed in the channel, the flow pattern changes significantly on the injection plane ($z/d=3.0$). The injected jet impinges on the effusion plate without deflecting toward the downstream region. The wall jet symmetrically develops in both the upstream and downstream directions and forms recirculating flows in front and rear sides of the fins. The jet flow in the upstream free jet region slightly moves upstream because the pressure of the upstream side is relatively lower than that of the downstream side due to the wake generation behind the fin. On the effusion plane ($z/d=0.0$), the flow velocity increases due to the decrease in the cross-sectional area even though the overall flow pattern is the same as in the case without fins.

Figure 8 shows vector plots on a plane 0.5 mm above the effusion surface. The dotted and solid half circles indicate the projected position of the injection hole and the effusion holes, respectively. From these vector plots, the flow characteristics of the wall jet are clearly observed. For the case without fins (Fig. 8(a)), the
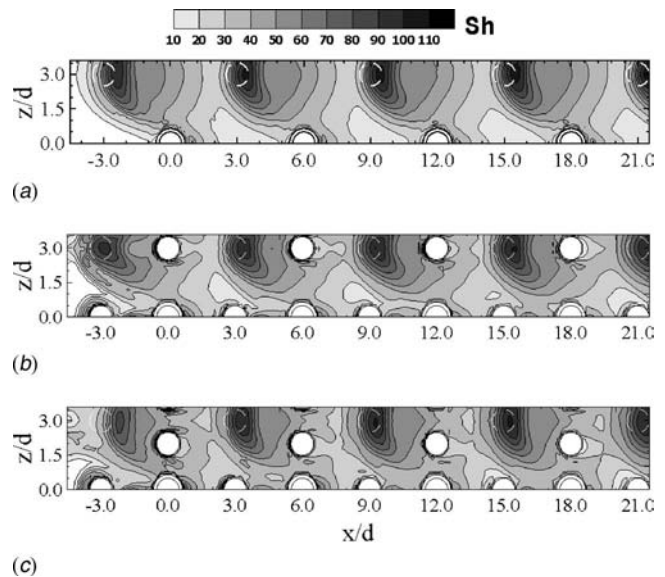
wall jet forms a hyperbolic boundary after colliding with the crossflow and is swept toward the downstream region. When the CP fin is installed in front of the impinging jet (Fig. 8(b)), the wall jet moves slightly toward the upstream side along the injection hole and a weak recirculation zone is formed behind the fin. However, the entire pattern of the near-wall flow is similar to the case without fins. On the contrary, RF1 case (Fig. 8(c)) shows that the wall jet spreads widely up to the upstream fin. Therefore, most of the effusion plate is effectively covered by the wall jet. In the effusion hole region, a considerable amount of the wall jet is rapidly discharged into the effusion hole, which is the same as the other cases.

4.3.2 Heat/Mass Transfer Characteristics

4.3.2.1 Effects of Fin Shapes and Arrangements. Local heat/mass transfer. Figure 9 presents the contour plots of Sh for the impingement/effusion cooling with CP fins cases; the figure includes the case without fins at $M=1.0$. The white dotted circles and small half circles indicate the projected positions of the injection holes and the effusion holes with an aluminum rim between two half circles, respectively. It is noted that all Sh plots are obtained by the experiment.

For the case without fins (Fig. 9(a)), the Sh distributions are nonuniform and asymmetric due to the crossflow. In particular, the upstream regions of the stagnation points are not covered by the wall jet and low heat transfer regions are formed between effusion holes as expected from the flow behaviors. These trends become more apparent with an increase in the blowing ratio, as reported by Rhee et al. [18].

The contours of Sh with CP fins are shown in Figs. 9(b) and 9(c). Since the effects of jet impingement are dominant in the entire domain, the overall Sh distributions are similar to those in the case without fins except near the regions where the fins are present. The Sh difference in the injection hole region ($z/d \cong 3.0$) is caused by the blockage effect, that is, the fin obstructs the crossflow and prevents the wall jet from being swept away. In the effusion hole region ($z/d \cong 0.0$), locally low Sh regions are reduced due to the vortex and wake induced by the CP fins.

Figure 10 presents the local distributions of Sh for the cases with and without fins. As shown in the contour plots, the heat/mass transfer distributions exhibit a periodical pattern except the inlet region. Therefore, the data in the range of $6.0 \leqslant x/d \leqslant 21.0$
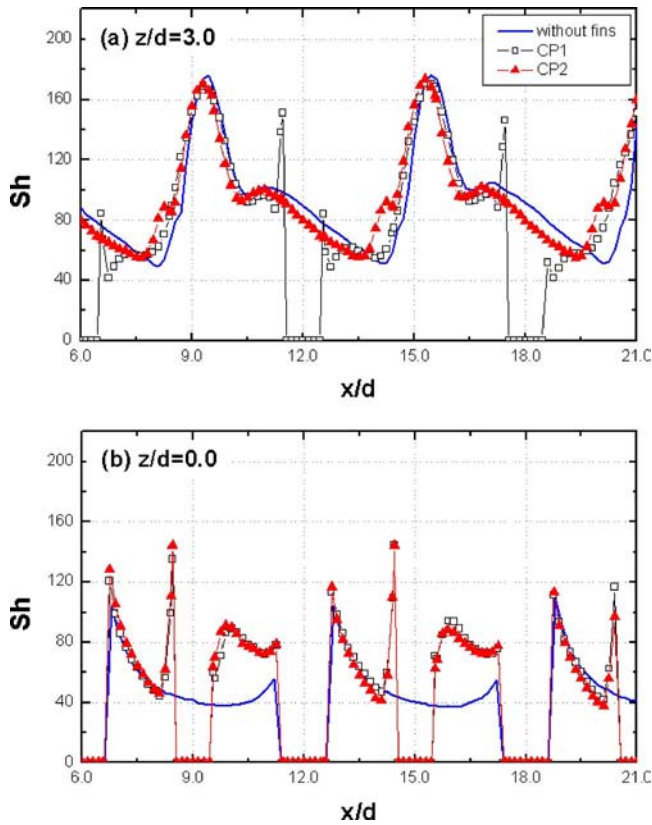
Fig. 10 Local distributions of Sh for impingement/effusion cooling with circular pin fins at $M=1.0$: (*a*) $z/d=3.0$ and (*b*) $z/d=0.0$

Fig. 11 Contour plots of Sh for impingement/effusion cooling with RFs at $M=1.0$: (*a*) RF0, (*b*) RF1, and (*c*)RF2

are presented to observe the effects of the fins on the detailed local heat transfer. In the local plots, the value of zero indicates the position of the installed fins or effusion holes.

As shown in Fig. 10(*a*), the positions of the stagnation points slightly shift upstream due to the blockage effect of the fins. For CP1, additional peaks are observed because of horseshoe vortices in front of the fins ($x/d \cong 11.5$ and 17.5). However, relatively low Sh values are obtained immediately behind the fins due to the recirculation flow in the wake region. For CP2, the Sh is slightly shifted upstream; however, it is similar to the case without fins except secondary peaks at $x/d \cong 8$, 14, and 20.

Along $z/d=0.0$ (Fig. 10(*b*)), CP1 and CP2 cases yield values that are approximately 55% higher values than those in the case without fins due to the increase in flow disturbance, and high peak values appear in front of the fins ($x/d \cong 8.5$, 14.5, and 20.5). For all the cases, the locally high values of Sh are obtained near the effusion holes ($x/d \cong 6$, 12, and 18). The reason is that the near wall flow accelerates toward the effusion holes and the duct center flow attaches on the wall behind the effusion holes, as reported by Goldstein et al. [37].

Figure 11 presents the contour plots of Sh for fins with the rectangular shape. As expected from the flow characteristics, the overall heat/mass transfer distributions are significantly different from those for the other cases. The RFs installed along the centerline of injection holes block the crossflow and divert it to the effusion hole region. Thus, in the injection hole region ($z/d \cong 3.0$), the injected flow and wall jet are not significantly affected by the crossflow. The position and level of stagnation points are all the same as in the case without the crossflow, as reported by Rhee et al. [18], and a wide high heat/mass transfer region is formed on the effusion surface without hot spots (low transfer region), as shown in Fig. 9(*a*).

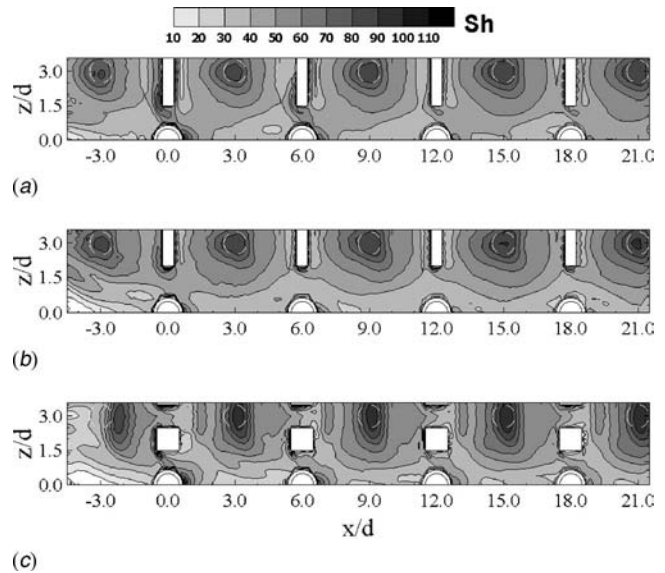RF0 (Fig. 11(*a*)) shows the Sh pattern that is different from

those of the CP fins due to a high blockage effect. At the edge region of the fin ($z/d \cong 1.5$), high Sh distributions are formed due to the strong corner vortex and the interaction between the cross-flow and the wall jet. The Sh pattern of RF1 (Fig. 11(*b*)) is almost the same as that of RF0 although the blockage area ratio is reduced from 50% to 33%. On the other hand, the Sh pattern of RF2 is different from that of the other RF cases because the injection hole region ($z/d \cong 3.0$) is open to the crossflow, as shown in Fig. 11(*c*). The heat transfer distributions of RF2 are similar to those of CP2 (Fig. 9(*c*)), except in the region surrounding the fin along the centerline of the effusion hole. However, since the blockage effect of the RF is greater than that of the CP fin against the crossflow, the high Sh region for RF2 is observed to be broader than that for CP2.

Figure 12 shows the comparison of the local distributions of Sh for various RF configurations. RF0 and RF1 show similar Sh distributions as compared to that for a simple impinging jet [5] due to the crossflow blockage by the RF. As a result, a region with higher heat transfer is formed at the upstream region of stagnation point and a relatively lower value is obtained at the downstream region, as compared to the case without fins. Relatively lower stagnation values are observed at the center of injection hole ($x/d=9$ and 15) due to little interaction between the crossflow and injected flow. In the case of RF2, the position of the stagnation point shifts downstream and its level is slightly higher than that in the other RF cases because the turbulence intensity increases by the strong interaction between crossflow and impinging jet. At $z/d=0.0$ (Fig. 12(*b*)), the Sh values are 35–55% higher as compared to the case without fins although the fins are not installed along the centerline of the effusion holes. This is attributed to the acceleration of the crossflow due to a reduced channel flow area. Therefore, RF0 with the greatest blockage area shows the highest values.

Average heat/mass transfer. Figure 13 shows the spanwise averaged Sh distributions for the various fin cases. The spanwise averaged Sh is calculated by averaging the local data in the range of $0.0 \leqslant z/d \leqslant 3.0$ and excluding the area where the fins and effusion holes are located. For CP1 and RF1, the heat/mass transfer is augmented at the upstream of stagnation point. This is due to the wide spreading of the wall jet and the increase in the flow disturbance by the fin. In particular, RF1 shows a significantly enhanced Sh uniformity and Sh value as compared to the case without the fin.

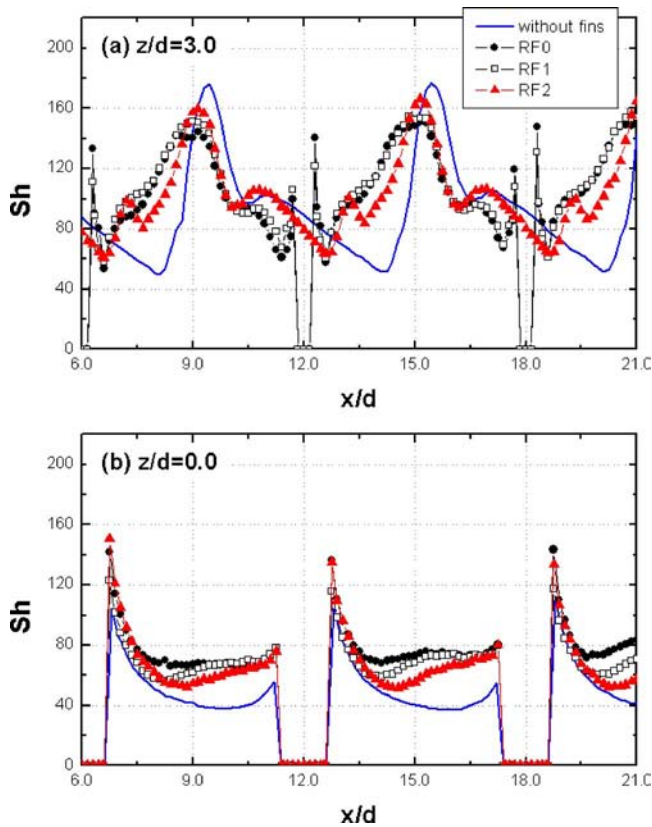The area-averaged Sh values for the various fin cases at M

Fig. 12 Local distributions of Sh for impingement/effusion cooling with RFs at $M=1.0$: (*a*) $z/d=3.0$ and (*b*) $z/d=0.0$

Fig. 13 Spanwise averaged Sh for impingement/effusion cooling with various fin cases at $M=1.0$: (*a*) CP fins and (*b*) RFs

Table 4 Overall averaged Sh for various fin cases at $M=1.0$

Without fins	CP1	CP2	RF0	RF1	RF2
71.0	75.2	78.9	87.3	86.2	86.1

Fig. 14 Contour plots of Sh for impingement/effusion cooling with RFs (RF1) at different blowing ratios: (*a*) $M=0.5$ and (*b*) $M=1.5$

$=1.0$ are listed in Table 4. The averaged values are calculated by averaging the local data in the range of $-3.0 \leqslant x/d \leqslant 21.0$ and $0 \leqslant z/d \leqslant 3.0$. It is noted that the averaged values in the inlet region ($-3.0 \leqslant x/d \leqslant 3.0$) are approximately 10% lower than those in other regions.

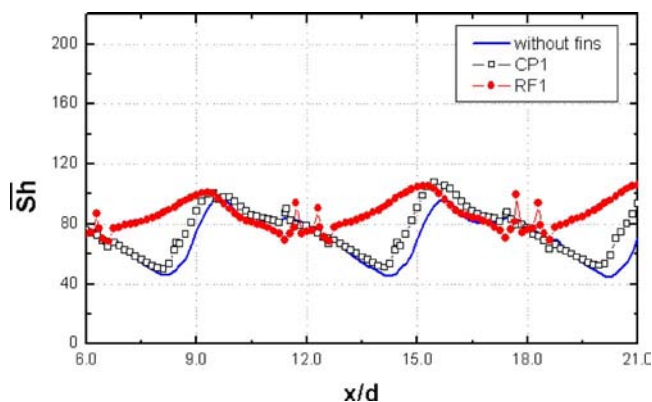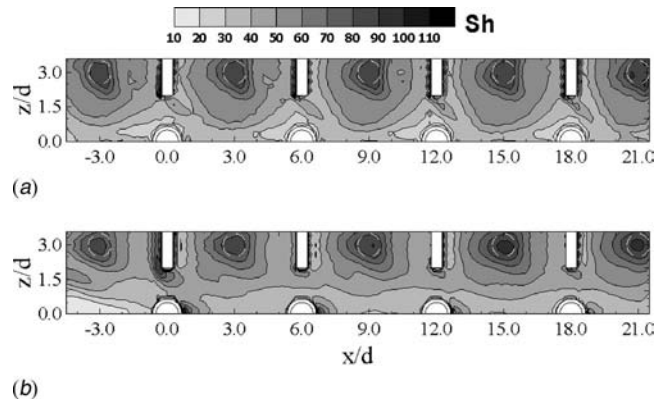As expected, the averaged Sh for cases with fins are approximately 5–20% higher than that in the case without fins. RF0 yields the highest averaged Sh value due to the strongest blockage effect against the crossflow. Further, RF1 and RF2 induce Sh values that are 10% higher as compared to CP2 with the same blockage area ratio; this indicates that the effect of the RF on the crossflow is greater than that of the CP fin.

4.3.2.2 Effects of Blowing Ratio. Experiments were conducted with various blowing ratios from 0.5 to 1.5. For the cases without fins presented by Rhee et al. [18], the values of Sh at stagnation region decrease as the blowing ratio increases. Further, the low Sh regions between the effusion holes become larger.

Figures 14(*a*), 14(*b*), and 11(*b*) present the contours of RF1 case at $M=0.5$, $M=1.5$, and $M=1.0$, respectively. At the injection hole region, a similar heat transfer pattern is obtained regardless of the blowing ratios due to strong blockage effect. At a high blowing ratio of $M=1.5$, the wall jet does not develop in the lateral direction and is swept away downstream. Therefore, the high Sh regions by the wall jet shrink as compared to the low blowing ratio of $M=0.5$ in the lateral directions (along $x/d=3.0$, 9.0, 15.0). Along $z/d=0.0$, the heat transfer features by the suction flow only appear as reported by Goldstein et al. [37]. However, high Sh are obtained due to the increase in the crossflow velocity.

As shown in Fig. 14(*b*), the peak value at $M=1.5$ slightly increases with increasing x/d due to the increase in the local injected flow rate. In this study, the flow rate based on $\mathrm{Re}_d=10{,}000$ is supplied to an injection plenum; however, the static pressure of the channel at the first injection hole area is higher than that at the last one due to the pressure loss in the channel. Thus, the local flow rate injected from the last injection hole is slightly more than that injected from the first one. This increases the peak value with increasing x/d. However, the difference between the first and the last peak values is less than 15% and the features of heat transfer are the same.

The overall averaged Sh values for various blowing ratios are presented in Fig. 15. For the cases without fins, the average value monotonously decreases as the blowing ratio increases. Further, the CP cases show that an increase in the crossflow rate decreases the averaged Sh value. However, the higher averaged value is obtained as compared to that in the case without fins due to the increased flow disturbance by the fins.

The RF cases maintain high Sh values, regardless of the blowing ratio. RF0 and RF1 show approximately 40–45% higher value as compared to the case without fins at $M=1.5$. Moreover, the averaged value of RF0 increases with the blowing ratio. This is because the Sh values increase with the high Reynolds channel flow in the effusion and midway regions, while the Sh distributions are almost the same as those for a low blowing ratio in the injection hole region due to the effective blockage of the fins. RF2
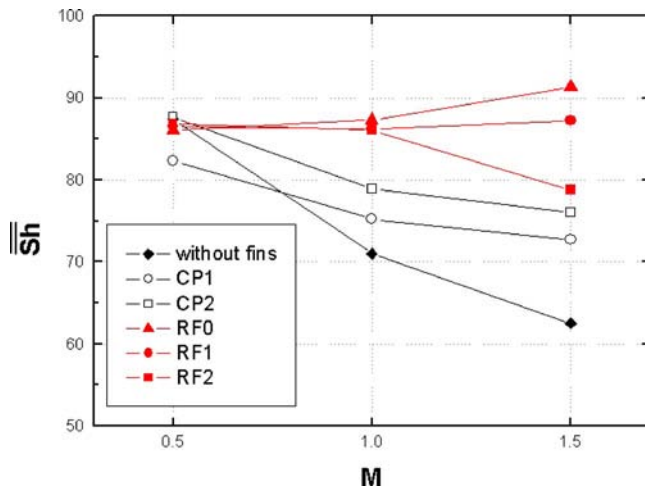
Fig. 15 Overall averaged Sh for various fins cases at different blowing ratios

Fig. 16 Pressure drop for the impingement/effusion cooling at various fins cases

has a value that is similar to other RF cases for $M \leqslant 1.0$; however, the averaged value at $M = 1.5$ is lower. This is due to the weak blockage effect as compared to RF1 and RF0 cases.

Table 5 summarizes the rate of increase of the overall Sh value based on the case without fins for the cases with the same fin blockage area ratio of 33.3% (CP2, RF1, and RF2). The overall Sh values are little affected by the attached fins at the low blowing ratio of $M = 0.5$ due to the low momentum of the crossflow. At $M = 1.0$, RF1 and RF2 yield a 20% enhancement, whereas CP2 produces only 10%. This indicates that the RF induces an increased augmentation of the overall heat transfer as compared to the CP fin. At $M = 1.5$, the increased heat transfer rate of RF1 rises up to about 40% while the value of RF2 shows only a slight increase. Therefore, the effect of fin arrangement becomes more significant than that of fin shape at the high blowing ratio. Consequently, it is concluded that the RF arrangements such as RF0 and RF1 are effective in reducing the influence of the crossflow and enhancing the heat transfer for the impingement/effusion cooling system.

4.3.3 Pressure Loss. To investigate pressure loss in the channel, the pressure drop through the channel (ΔP_{cross}) was measured. Figure 16 presents the results for all the cases at various blowing ratios. The pressure drop increases with the blowing ratio, i.e., the Reynolds number of the channel flow. The case without fins shows relatively very lower pressure drop. However, the pressure drop of the cases with fins considerably increases due to the reduction in the cross-sectional area. The pressure loss for CP2 is approximately four times than that without the fins, and the RF cases with the same blockage area ratio (RF1 and RF2) have a pressure loss value similar to that of CP2. The pressure drop for RF0, which has the highest blockage area, shows the greatest pressure loss. This suggests that the installation of a fin with an excessive blockage area causes an unfavorable effect related to the reduction in the cooling flow on the inner or outer wall of the cooling system. Therefore, to enhance the total cooling perfor-

mance by using the fin, both the cooling enhancement and pressure loss in the impingement/effusion cooling system should be considered.
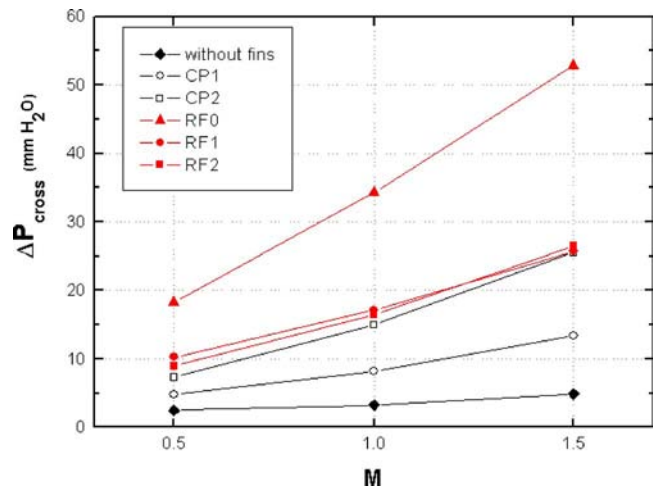
5 Conclusions

In the present study, the effects of fin on the flow and heat/mass transfer characteristics are investigated for the impingement/effusion cooling system with initial crossflow and are compared with the cases without fins. The results are summarized as follows.

The installed fin obstructs the crossflow and prevents the wall jet from being swept away downstream, and these flow characteristics become more apparent for RFs. The channel flow accelerates in the effusion hole region due to the reduced cross-sectional area in the duct.

The heat/mass transfer distributions are considerably changed by the strong blockage effect of the RF. A higher and more uniform Sh is obtained in the injection hole region and the Sh in the effusion hole region increases due to an increased velocity of the channel flow. For CP fins, the locally low Sh area reduces by the formation of a vortex and wake, and the Sh slightly increases because of the blockage effect.

When fins are installed, the overall Sh increases 5–20% times than that for the case without fins at $M = 1.0$. The averaged Sh for the RF is 10% higher as compared to that for the CP fin with the same area ratio of the fin cross section. It is caused by the increase in the actual blockage effect due to the RF shape.

With increasing blowing ratio, the cases with fins show a higher Sh value as compared to the case without fins, reaching 40–45% Sh enhancement for RF0 and RF1 at $M = 1.5$. The averaged Sh value for RF1 is higher than that for RF2, indicating that the effect of the fin arrangement becomes significant at a high blowing ratio.

The installation of the fin is effective in reducing the influence of the crossflow and enhancing the heat transfer; however, it is accompanied with a high pressure loss through the channel due to the increase of blockage area. Thus, for the enhancement of the total cooling performance by using the fin, one should consider the exact operating conditions in the impingement/effusion cooling system.

Table 5 Rate of increase of overall Sh value for cases with the same blockage area ratio

	CP2	RF1	RF2
$M = 0.5$	0.2%	−1.0%	−0.7%
$M = 1.0$	11.1%	21.3%	21.2%
$M = 1.5$	21.6%	39.5%	26.5%

Nomenclature

$A_{channel}$ = cross-sectional area in the channel
A_{fin} = windward area of fin
B = blockage area ratio, $(A_{fin}/A_{channel}) \times 100$
d = injection and effusion hole diameter
dy = local sublimation depth of naphthalene
D_h = hydraulic diameter of test duct
D_{CP} = diameter of circular pin fin
D_{naph} = mass diffusion coefficient of naphthalene vapor in air
H = gap distance between injection and effusion plates
h_m = local mass transfer coefficient, Eq. (2)
I = local momentum flux ratio of crossflow and impinging jets, $\rho_c V_c^2 / \rho_i V_i^2$
L_{RF} = length of rectangular fin
$\dot{m}$ = local naphthalene mass transfer per unit area and time
M = blowing ratio (total mass flow ratio of crossflow and impinging jets), Q_c/Q_i, Eq. (1)
MR = local mass flux ratio of crossflow and impinging jets, $\rho_c V_c / \rho_i V_i$
Nu = Nusselt number based on the hole diameter, hd/k
Pr = Prandtl number
P_{hole} = pitch of array holes
Q_c = flow rate of crossflow
Q_i = flow rate of injected jet or effused flow
Re_d = Reynolds number based on hole diameter and the average velocity in the hole
Re_{D_h} = Reynolds number based on hydraulic diameter of duct and average velocity of crossflow
S_L = longitudinal distance for fin arrangement, Fig. 2
S_T = transverse distance for fin arrangement, Fig. 2
Sc = Schmidt number
Sh = Sherwood number based on the hole diameter, Eq. (3)
Sh_0 = Sherwood number for fully developed flow in a smooth pipe, $Sh_0 = 0.023 Re_{D_h}^{0.8} Sc^{0.4}$
Sh_{D_h} = Sherwood number based on the channel hydraulic diameter and average flow velocity in the channel
$\bar{Sh}$ = spanwise averaged Sherwood number
$\bar{\bar{Sh}}$ = overall averaged Sherwood number
t = thickness of injection and effusion plates
V_c = mean velocity of crossflow
V_i = mean velocity of impinging jet
W_{RF} = width of rectangular fin
x, z = distance from the center of an effusion hole

Greek Symbols

ΔP_{cross} = differential static pressure between the inlet and the exit of the channel
ρ_c = density of crossflow
ρ_i = density of impinging jet flow
ρ_s = density of solid naphthalene
$\rho_{v,w}$ = naphthalene vapor density on the surface
$\rho_{v,\infty}$ = naphthalene vapor density of the injected jet
$d\tau$ = test duration

References

[1] Hollwarth, B. R., and Dagan, L., 1980, "Arrays of Impinging Jets With Spent Fluid Removal Through Vent Holes on the Target Surface Part 1: Average Heat Transfer," J. Eng. Power, **102**, pp. 994–999.
[2] Hollwarth, B. R., Lehmann, G., and Rosiczkowski, J., 1983, "Arrays of Impinging Jets With Spent Fluid Removal Through Vent Holes on the Target Surface Part 2: Local Heat Transfer," J. Eng. Power, **105**, pp. 393–402.
[3] Nazari, A., and Andrews, G. E., 1999, "Impingement/ Effusion Cooling: Influence of Number of the Holes and Pressure Loss on Film and Heat Transfer Coefficient," *Proceedings of Seventh IGTC*, Vol. 2, pp. 638–648.
[4] Cho, H. H., and Goldstein, R. J., 1996, "Effect of Hole Arrangements on Impingement/Effusion Cooling," *Proceeding of the Third KSME-JSME Thermal Engineering Conference*, pp. 71–76.
[5] Cho, H. H., and Rhee, D. H., 2001, "Local Heat/Mass Transfer Measurement on the Effusion Plate in Impingement/Effusion Cooling System," J. Turbomach., **123**, pp. 601–608.
[6] Rhee, D. H., Choi, J. H., and Cho, H. H., 2003, "Heat (Mass) Transfer on Effusion Plate in Impingement/Effusion Cooling Systems," J. Thermophys. Heat Transfer, **17**(1), pp. 95–102.
[7] Cho, H. H., Rhee, D. H., and Goldstein, R. J., 2004, "Effects of Hole Arrangements on Local Heat/Mass Transfer for Impingement/Effusion Cooling With Small Hole Spacing," ASME Paper No. GT2004-53685.
[8] Florschuetz, L. W., Metzger, D. E., and Su, C. C., 1984, "Heat Transfer Characteristics for Jet Array Impingement With Initial Crossflow,"J. Heat Transfer, **106**, pp. 34–41.
[9] Metzger, D. E., and Korstad, R. J., 1972, "Effects of Crossflow in Impingement Heat Transfer," ASME J. Eng. Power, **94**, pp. 35–41.
[10] Huang, Y., Ekkad, S. V., and Han, J. C., 1998, "Detailed Heat Transfer Distributions Under an Array of Orthogonal Impinging Jets," J. Thermophys. Heat Transfer, **12**(1), pp. 73–79.
[11] Haiping, C., Wanbing, C., and Taiping, H., 1999, "3-D Numerical Simulation of Impinging Jet Cooling With Initial Crossflow," ASME Paper No. 99-GT-256.
[12] Hwang, J. J., and Chang, B. Y., 2000, "Effect of Outflow Orientation on Heat Transfer and Pressure Drop in a Triangular Duct With an Array of Tangential Jets," J. Heat Transfer, **122**, pp. 669–678.
[13] Bailey, J. C., and Bunker, R. S., 2002, "Local Heat Transfer and Flow Distributions for Impinging Jet Arrays of Dense and Sparse Extent," ASME Paper No. GT-2002-30473.
[14] Rhee, D. H., Yoon, P. H., and Cho, H. H., 2003, "Local Heat/Mass Transfer and Flow Characteristics of Array Impinging Jets With Effusion Holes Ejecting Spent Air," Int. J. Heat Mass Transfer, **46**, pp. 1049–1061.
[15] Gao, L., Ekkad, S. V., and Bunker, R. S., 2003, "Impingement Heat Transfer Under Linearly Stretched Arrays of Holes," ASME Paper No. GT-2003-38178.
[16] Chambers, A. C., Gillespie, D. R. H., Ireland, P. T., and Dailey, G. M., 2005, "The Effect of Initial Crossflow on the Cooling Performance of a Narrow Impingement Channel," J. Heat Transfer, **127**, pp. 358–365.
[17] Ekkad, S. V., Huang, Y., and Han, J. C., 1999, "Impingement Heat Transfer on a Target Plate With Film Cooling Holes," J. Thermophys. Heat Transfer, **13**(4), pp. 522–528.
[18] Rhee, D. H., Choi, J. H., and Cho, H. H., 2003, "Flow and Heat (Mass) Transfer Characteristics in an Impingement/Effusion Cooling System With Crossflow," J. Turbomach., **125**, pp. 74–82.
[19] Haiping, C., Jingyu, Z., and Taiping, H., 1998, "Experimental Investigation on Impingement Heat Transfer From Rib Roughened Surface Within Arrays of Circular Jets: Effect of Geometric Parameters," ASME Paper No. 98-GT-208.
[20] Andrews, G. E., Abdul Hussain, R. A. A., and Mkpadi, M. C., 2003, "Enhanced Impingement Heat Transfer: Comparison of Co-flow and Cross-flow With Rib Turbulators," *Proceedings of IGTC2003*, Paper No. IGTC2003Tokyo TS-075.
[21] Rhee, D. H., Nam, Y. W., and Cho, H. H., 2005, "Local Heat/Mass Transfer With Various Rib Arrangements in Impingement/Effusion Cooling System With Crossflow," J. Turbomach., **126**, pp. 615–626.
[22] Andrews, G. E., Abdul Hussain, R. A. A., and Mkpadi, M. C, 2006, "Enhanced Impingement Heat Transfer: The Influence of Impingement X/D for Interrupted Rib Obstacles (Rectangular Pin Fins)," ASME J. Heat Transfer, **128**, pp. 321–331.
[23] Annerfeldt, M. O., Persson, J. L., and Torison, T., 2001, "Experimental Investigation of Impingement Cooling With Turbulators or Surface Enlarging Elements," ASME Paper No. 2001-GT-0149.
[24] Funazaki, K., Tarukawa, Y., Kudo, T., Matsuno, S., Imai, R., and Yamawki, S., 2001, "Heat Transfer Characteristics of an Integrated Cooling Configuration for Ultra-High Temperature Turbine Blades: Experimental and Numerical Investigations," ASME Paper No. 2001-GT-0148.
[25] Yamawki, S., Nakamata, C., Imai, R., Matsuno, S., Yoshida, T., Mimura, F., and Kumada, M., 2003, "Cooling Performance of an Integrated Impingement and Pin Fin Cooling Configuration," ASME Paper No. GT-2003-38215.
[26] Cho, H. H., and Goldstein, R. J., 1995, "Heat (Mass) Transfer and Film Cooling Effectiveness With Injection Through Discrete Holes. Part I: Within Holes and on the Back Surface," J. Turbomach., **117**, pp. 440–450.
[27] Ambrose, D., Lawrenson, I. J., and Sparke, C. H. S., 1975, "The Vapor Pressure of Naphthalene," J. Chem. Thermodyn., **7**, pp. 1173–1176.
[28] Goldstein, R. J., and Cho, H. H., 1995, "A Review of Mass Transfer Measurement Using Naphthalene Sublimation," Exp. Therm. Fluid Sci., **10**, pp. 416–434.
[29] Eckert, E. R. G., 1976, Analogies to Heat Transfer Processes, *in Measurements in Heat Transfer*, E. R. G. Eckert, and R. J. Goldstein, eds., Hemisphere, New York, pp. 397–423.
[30] Kline, S. J., and McClintock, F., 1953, "Describing Uncertainty in Single Sample Experiments," Mech. Eng. (Am. Soc. Mech. Eng.), **75**, pp. 3–8.
[31] Cho, H. H., 1992, "Heat/Mass Transfer Flow Through an Array of Holes and Slits," Ph. D. thesis, University of Minnesota, Twin Cities.
[32] 2001, Fluent 6.1 User's Guide, Vol. 5, Chaps. 22–16.
[33] Goldstein, R. J., Chyu, M. K., and Hain, R. C., 1985, "Measurement of Local

Mass Transfer on a Surface in the Region of the Base of a Protruding Cylinder With a Computer-Controlled Data Acquisition System," Int. J. Heat Mass Transfer, **28**, pp. 977–985.

[34] Chyu, M. K., Hsing, Y. C., Shih, T. I.-P., and Natarajan, V., 1999, "Heat Transfer Contributions of Pins and Endwall in Pin-Fin Arrays: Effects of Thermal Boundary Condition Modeling," J. Turbomach., **121**, pp. 257–263.

[35] Won, S. Y., Mahmood, G. I., and Ligrani, P. M., 2004, "Spatially-Resolved Heat Transfer and Flow Structure in a Rectangular Channel With Pin Fins," Int. J. Heat Mass Transfer, **47**, pp. 1731–1743.

[36] Dittus, P. W., and Boelter, L. M. K., 1930, Univ. Calif. Publ. Eng., **2**(13), pp. 443–461; 1985, Int. Commun. Heat Mass Transfer, **12**, pp. 3–22.

[37] Goldstein, R. J., Cho, H. H., and Jabbari, M. Y., 1997, "Effect of Plenum Crossflow on Heat (Mass) Transfer Near and Within the Entrance of Film Cooling Holes," J. Turbomach., **119**, pp. 761–769.

S. Shateyi
Department of Mathematics,
Bindura University of Science Education,
Private Bag 1020,
Bindura, Zimbabwe
e-mail: sshateyi@yahoo.com

P. Sibanda
School of Mathematical Sciences,
University of KwaZulu-Natal,
Private Bag X01,
Scottsville 3209,
Pietermaritzburg, South Africa
e-mail: sibandap@ukzn.ac.za

S. S. Motsa
Department of Mathematics,
University of Swaziland,
Private Bag 4,
Kwaluseni, Swaziland
e-mail: sandile@science.uniswa.ac.sz

Magnetohydrodynamic Flow Past a Vertical Plate With Radiative Heat Transfer

The problem of steady, laminar, magnetohydrodynamic flow past a semi-infinite vertical plate is studied. The primary purpose of this study was to characterize the effects of thermal radiative heat transfer, magnetic field strength, and Hall currents on the flow properties. The governing nonlinear coupled differential equations comprising the laws of mass, linear momentum, and energy modified to include magnetic and radiative effects were solved numerically. The effects of the Hall current, the Hartmann number, and the radiative parameter on the velocity and temperature profiles are presented graphically. Large Hall currents and radiation effects cause the fluid to heat up and the velocity to increase in the lateral direction but decrease in the tangential direction. This study showed inter alia that reducing Hall currents and increasing the strength of the magnetic field lead to a reduction in the temperature and, consequently, in the thermal boundary layer, and so confirming that heat transfer mitigation through magnetic control is possible. [DOI: 10.1115/1.2767750]

Keywords: MHD flow, free convection, Hall effect, Hartmann number, radiative heat transfer

1 Introduction

The past three decades have seen a tremendous interest in studies involving magnetohydrodynamic (MHD) flow and heat transfer in porous and nonporous media. This is primarily due to an increase in industrial and technological applications of flows involving electrically conducting fluids. Most of the theoretical studies involve flow oversimple geometries such as a semi-infinite vertical plate, and among the recent theoretical studies of interest are those of Sparrow and Cess [1], Watanabe and Pop [2], Pop and Watanabe [3], Aldoss et al. [4], Chamkha [5], Chiam [6], Chandran et al. [7], and Vajravelu and Hadjinicolaou [8]. Many other studies and reviews that look at various aspects of heat and mass transfer characteristics of boundary-layer flows have been published in the literature.

In their study of the skin-friction coefficient and the shear stresses in a flow with an applied magnetic field, Kumari and Nath [9] established that surface shear stresses increase with increases in the magnetic field strength. A related study by Chamkha and Khaled [10] considered similarity solutions for hydromagnetic mixed convection heat and mass transfer for Hiemenz flow through porous media. This study established that the local Nusselt number increases in tandem with increases in the Prandtl number, the mixed convection parameter, and the buoyancy ratio. The skin-friction parameter was found to increase when both the buoyancy ratio and the dimensionless wall heat transfer increased.

The effects of thermal radiation on MHD flow have been studied by, among others, Hossain et al. [11] and Chamkha [12]. In Ref. [12], it was found that the wall heat transfer rate decreased owing to the presence of thermal radiation but increased due to the presence of the thermal buoyancy. Hossain et al. [11] found that both the skin-friction coefficient and the rate of heat transfer decrease as the radiation increases. They also noted that increases in the radiation lead to a decrease in both the momentum and thermal boundary-layer thickness. The study by Chamkha and Khaled [13] considered the problem of steady, laminar, simulta-

neous heat and mass transfer by mixed convection boundary-layer flow of an electrically conducting and heat absorbing fluid over a permeable vertical plate embedded in a uniform porous medium with thermal dispersion. It was found that while the local Nusselt number decreased as a result of the presence of either the magnetic field, negative freestream temperature stratification, or positive wall mass transfer, it increased due to imposition of both negative wall mass transfer and freestream temperature stratification.

MHD flows have many commercial and industrial applications. These types of flows have been studied extensively by many authors. For example, in the case of subsonic and supersonic flow of gases, MHD has been proposed as a means of controlling boundary-layer transition, see, for instance, Poggie and Gaitonde [14] and Nishihara et al. [15]. However, Hall effects have been shown to counterbalance the beneficial aspects of the magnetic field, thus rendering it less effective.

In this study, we consider Hall and radiative heat transfer effects on MHD free convection flow past a semi-infinite vertical plate. This study aims to characterize radiative heat transfer and Hall effects on the flow of a conducting fluid past a semi-infinite vertical plate.

2 Problem Formulation

We consider natural convection and radiative heat transfer from a semi-infinite vertical plate adjacent to a boundary flow. The viscous incompressible fluid is steady, laminar, three dimensional, and electrically conducting. A uniform magnetic field is applied normal to the surface causing a resistive force in the x direction. The plate is maintained at a constant temperature and with significant thermal radiation and Hall effects. The magnetic Reynolds number is assumed to be small so that the induced magnetic field can be neglected. Under the electromagnetic and Boussinesq approximations, the governing equations are given by

$$\frac{\partial u}{\partial x} + \frac{\partial v}{\partial y} = 0 \qquad (1a)$$

$$u\frac{\partial u}{\partial x} + v\frac{\partial u}{\partial y} = \nu\frac{\partial^2 u}{\partial y^2} + g\beta(T - T_\infty) - \frac{\sigma B_0^2}{\rho(1+m^2)}(mu + w) \quad (1b)$$

$$u\frac{\partial w}{\partial x} + v\frac{\partial w}{\partial y} = \nu\frac{\partial^2 w}{\partial y^2} - \frac{\sigma B_0^2}{\rho(1+m^2)}(mw - u) \quad (1c)$$

$$u\frac{\partial T}{\partial x} + v\frac{\partial T}{\partial y} = \alpha\frac{\partial^2 T}{\partial y^2} - \frac{1}{\rho c_p}\frac{\partial q_r}{\partial y} \quad (1d)$$

where x and y are displacements parallel and normal to the plate, respectively, with the z axis coincident with the leading edge; u, v, and w are the fluid velocity components in the x, y, and z directions, respectively; T and T_∞ are the fluid and ambient temperatures, respectively; β and g are the coefficient of volumetric thermal expansion and acceleration due to gravity, respectively; $\nu(=\mu/\rho)$ is the momentum diffusivity; ρ is the fluid density; μ is the dynamic viscosity; σ, B_0, and m are the fluid electrical conductivity, magnetic induction, and Hall parameter, respectively; c_p is the specific heat at constant pressure; and $\alpha(=\lambda_c/\rho c_p)$ is the thermal diffusivity, where λ_c is the fluid thermal conductivity.

The fluid and temperature fields are subject to the following boundary conditions:

$$u(0,y) = w(0,y) = 0$$

$$u(x,0) = v(x,0) = w(x,0) = 0$$

$$u(x,\infty) = w(x,\infty) = 0$$

$$T(x,0) = T_w \quad T(x,\infty) = T_\infty \quad (2)$$

The radiative heat flux q_r in the energy equation is described by the Rosseland approximation,

$$q_r = -\frac{4\sigma^*}{3K}\frac{\partial T^4}{\partial y} \quad (3)$$

where σ^* and K are the Stefan–Boltzmann constant and the mean absorption coefficient, respectively. Following Abel et al. [16] and Chamkha [5], we assume that the temperature differences within the flow are sufficiently small so that T^4 can be expressed as a linear function of temperature. This approach requires that T^4 be expanded in a Taylor series about the ambient temperature T_∞ and neglecting higher order terms to get the following approximation:

$$T^4 \approx 4T_\infty^3 T - 3T_\infty^4 \quad (4)$$

Using Eqs. (2) and (3) in Eq. (1d), we obtain

$$\frac{\partial q_r}{\partial y} = -\frac{16\sigma^* T_\infty^3}{3K}\frac{\partial^2 T}{\partial y^2}$$

We nondimensionalize Eqs. (1a)–(1d) using the following transformations:

$$x = L\xi \quad y = LGr^{-1/4}\eta \quad u = \frac{\nu}{L}Gr^{1/2}F \quad v = \frac{\nu}{L}Gr^{1/4}G$$

$$w = \frac{\nu}{L}Gr^{1/2}H \quad \theta = \frac{T - T_\infty}{T_w - T_\infty} \quad Gr = \frac{g\beta(T_w - T_\infty)L^3}{\nu^2}$$

where L is a characteristic length, T_w is the temperature of the heated surface, and Gr is the local Grashof number that characterizes the natural convection data. Using these transformations, the governing equations become

$$\frac{\partial F}{\partial \xi} + \frac{\partial G}{\partial \eta} = 0 \quad (5a)$$

$$F\frac{\partial F}{\partial \xi} + G\frac{\partial F}{\partial \eta} = \theta + \frac{\partial^2 F}{\partial \eta^2} - \frac{M^2}{1+m^2}(mF + H) \quad (5b)$$

Table 1 Comparison of the temperature values for the analytic and numerical methods when $M=1$, $m=1$, Pr=3, $N=1$, and $G=1$

	θ	
$\eta(\xi=1)$	Analytical method	Numerical method
0.0	1.0000	1.0000
0.2	0.7408	0.7414
0.4	0.5458	0.5420
0.6	0.4066	0.4056
0.8	0.3012	0.3056
1.0	0.2231	0.2212
1.2	0.1653	0.1658
1.4	0.1225	0.1210
1.6	0.0907	0.0939
1.8	0.0672	0.0674
2.0	0.0498	0.0491

$$F\frac{\partial H}{\partial \xi} + G\frac{\partial H}{\partial \eta} = \frac{\partial^2 H}{\partial \eta^2} - \frac{M^2}{1+m^2}(mH - F) \quad (5c)$$

$$F\frac{\partial \theta}{\partial \xi} + G\frac{\partial \theta}{\partial \eta} = \frac{1}{\text{Pr}}(1+N)\frac{\partial^2 \theta}{\partial \eta^2} \quad (5d)$$

where F, G, and H are the nondimensional fluid velocity components and θ is the temperature. The central parameters are the Hall current m, the Prandtl number Pr, which is a ratio of the momentum diffusivity to the heat diffusivity, the Hartmann number M, and the dimensionless thermal radiation coefficient N. These parameters are defined, respectively, by

$$\text{Pr} = \frac{\nu}{\alpha} \quad M^2 = \frac{\sigma B_0^2 L^2}{\rho\nu Gr^{1/2}} \quad \text{and } N = \frac{16\sigma^* T_\infty^3}{3K\lambda_c}$$

Physically, the square of the Hartmann number is a measure of the relative importance of the electromagnetic to the viscous forces in the fluid. In this notation, the intensity of radiation, a fundamental concept in the characterization of radiant heat transfer, is given by increasing values of N. Physically, N characterizes the quantity of radiation that travels from the plate surface in all directions.

The boundary conditions become

$$F(0,\eta) = H(0,\eta) = 0$$

$$F(\xi,0) = G(\xi,0) = H(\xi,0) = 0 \quad \theta(\xi,0) = 1$$

$$F(\xi,\infty) = H(\xi,\infty) = 0 \quad \theta(\xi,\infty) = 0 \quad (6)$$

The flow behavior in terms of the convective heat transfer may be characterized by analyzing the nondimensionless local shear stress τ_w and the Nusselt number Nu. This has been done, for example, by Abel et al. [16]. However, in this study, our primary focus is on the effects of radiative heat transfer and the Hall parameter rather than on convective heat transfer.

3 Results and Discussion

Equations (5) are coupled nonlinear partial differential equations that possess no similarity or closed-form solutions. Therefore, a numerical solution of the problem under consideration is needed. However, for large values of ξ, an analytical solution is possible for the energy equation [Eq. (5d)], and, in particular,

$$\theta = \exp(-\omega\eta) \quad \text{where } \omega = \frac{\text{Pr } G}{1+N} \quad (7)$$

Table 1 presents a comparison between temperature values obtained by the numerical method to those obtained analytically. The analytic and numerical results are in excellent agreement, lending confidence in the numerical results to be reported subsequently.

The momentum equations and the energy equation were solved using the classical implicit finite-difference method of Blottner
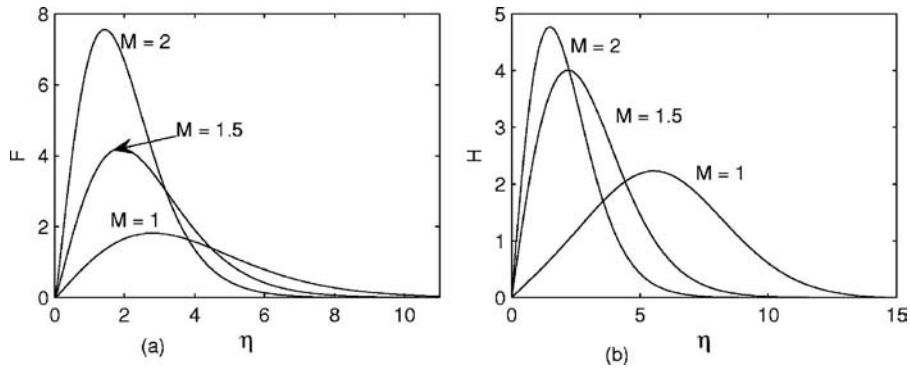
Fig. 1 The distribution of (*a*) tangential and (*b*) lateral velocities in the vicinity of a vertical plate as a function of increasing magnetic field strength for $m=1$, $Pr=0.71$, and $N=1$

[17], which, apart from its simplicity, has also been shown to be accurate giving reliable results. Owing to the nonlinear nature of the equations, we employed an iterative procedure with 10^{-6} as the maximum absolute error between two successive iterations.

A parametric study was carried out, and Figs. 1–8 show the behavioral characteristics of the boundary-layer velocity and temperature distributions for different parameter values. Physically, the primary purpose of these figures is to illustrate the relative influences of the Hall current, the magnetic field strength through the Hartmann number, and the loss of heat through radiation as characterized by the radiative parameter on the fluid properties. In practice, heat loss would be through the combined influences of convection and radiation rather than as an isolated phenomenon.

Figures 1–3 show typical distributions in the boundary layer of the tangential velocity F, the lateral velocity H, and the tempera-

ture θ for different values of the magnetic field strength as characterized by the Hartmann number M. It is now a well established fact that the application of a uniform magnetic field normal to the flow direction causes a reduction in the velocity of the flow (see Chamkha [12]). This, however, seems not to be the case for the present problem where we have Hall effects and radiative effects.

Figure 1(*a*) shows that the tangential velocity rises steeply near the vertical plate surface as the Hartmann number increases. Moving away from the surface, a cross flow in the tangential velocity is induced and the resistive Lorentz force now slows down the motion of the fluid and the velocity reduces rapidly to zero. These results are similar to those obtained by Chamkha [18], where they assumed the magnetic field to vary with the distance along the plate. Figure 1(*b*) shows that the magnetic field strength has a similar effect on the lateral velocity. Along the leading edge of the
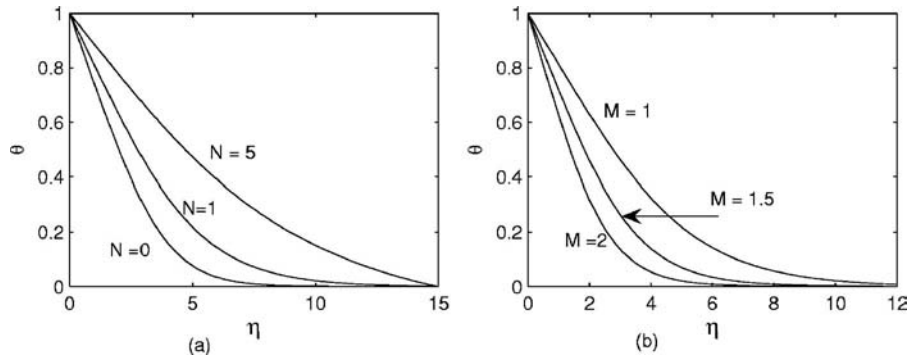

Fig. 2 The variation of temperature with (*a*) increasing radiation and (*b*) increasing magnetic field strength for $m=1$ and $Pr=0.71$
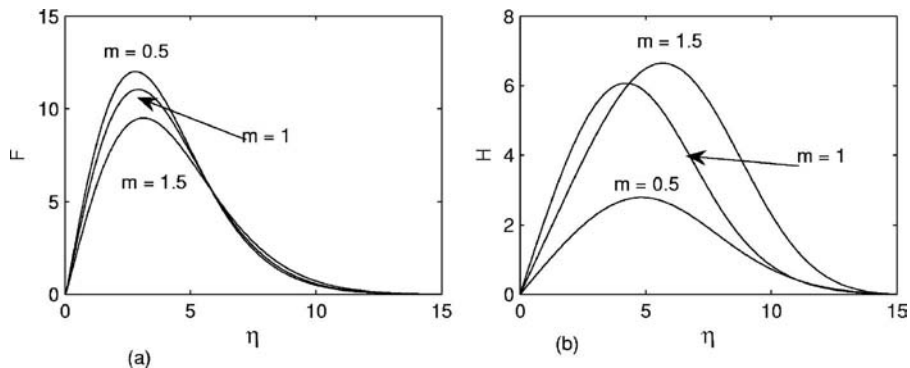

Fig. 3 The variation of (*a*) tangential and (*b*) lateral velocity distributions with increasing Hall parameter values for $M=1$, $Pr=0.71$, and $N=1$
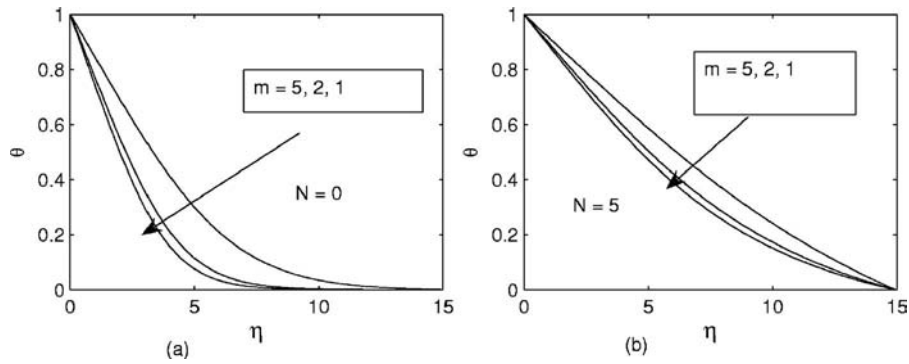
Fig. 4 The temperature distribution (a) without radiation effects and (b) with radiation for M=1 and Pr=0.71

plate, which coincides with the z direction, the lateral velocity gradient becomes very steep as the strength of the magnetic field increases. The conclusion to be drawn from Fig. 1 is that increasing the magnetic field strength reduces the momentum boundary-layer thickness.

Figure 2 shows that the thermal boundary layer (a) increases with thermal radiation and (b) decreases with increasing magnetic field strength. As the Hartmann number increases, the thermal buoyancy of the fluid decreases resulting in a rapid drop in the fluid temperature and thus supporting the notion that a magnetic field could be used as a temperature control mechanism, Poggie and Gaitonde [14]. This is, however, contrary to findings in some earlier studies, for example, Sobha and Ramakrishna [19], who, in the case of a porous plate, found that the application of a uniform magnetic field normal to the flow direction causes increments in the fluid temperature. We can only surmise that the different con-

clusions reached by these investigators could be as a result of the porosity effect in their study and/or the result of Hall and radiative effects that are present in this study but were not taken into consideration in the earlier work. The main conclusion that can be drawn from this result is that the heat transfer rate is clearly governed by both the intensity of radiation and the magnetic field strength [20].

Figure 3 shows the effect of the Hall current on the boundary-layer velocity distribution. The tangential velocity decreases with increases in the Hall parameter, while the lateral velocity increases with m. The increase in the lateral velocity is attributed to the fact that the lateral velocity coincides with the direction of Lorentz force, which is generated by the application of the magnetic field normal to the flow so increasing the flow velocity in that direction.

Figure 4 shows the interaction of the radiative heat effect with the Hall current. As expected, it is noted that both radiation and
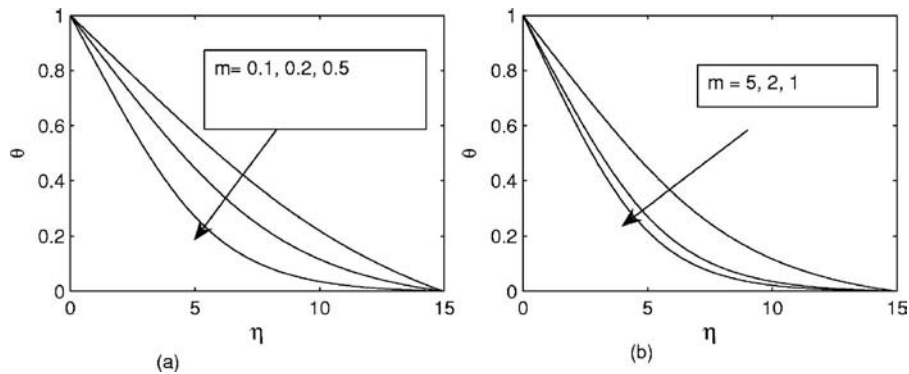

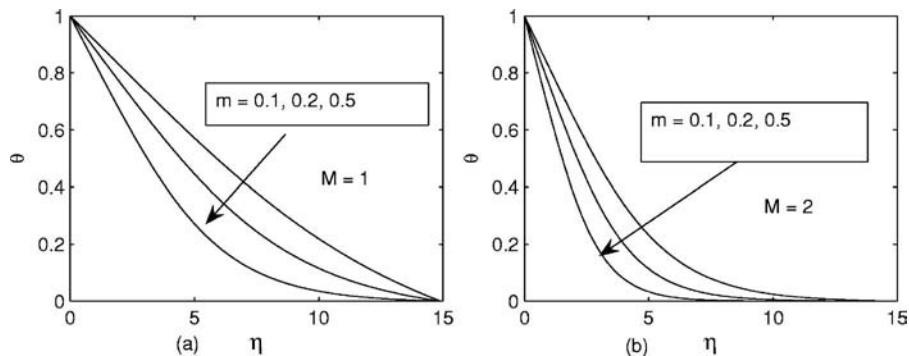**Fig. 5 The temperature distribution for (a) $m<1$ and (b) $m\geq1$ for M=1, Pr=0.71, and N=1**

Fig. 6 The variation of the temperature distribution with increasing Prandtl numbers (a) without radiation and (b) with radiation

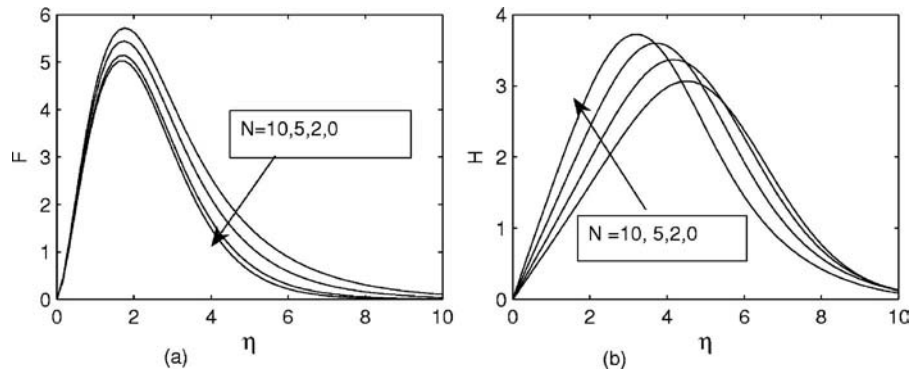**Fig. 7 The variation of temperature with Hall parameter (*a*) *M*=1 and (*b*) *M*=2, for Pr =0.71 and *N*=1**

large Hall effects ($m \geq 1$) act to increase the thermal boundary layer. The radiative heat transfer is, however, the more dominant of the two parameters. In Fig. 5, a comparison is given between the temperature distribution when (*a*) $m < 1$ and (*b*) when $m \geq 1$. Of particular interest is that when $m < 1$ (Fig. 5(*a*)), the Hall current, in fact, acts to reduce the boundary-layer temperature distribution.

A comparison of the interaction of the Hall current and the magnetic field strength in Figs. 6(*a*) and 6(*b*) shows that a combination of a small *m* and large Hartmann numbers is most effective in reducing the boundary-layer temperature distribution. However, in practice, this ideal combination of low Hall currents and enhanced magnetic field strength would be very difficult to realize since, for instance, in the case of an ionized gas, a stronger magnetic field leads to stronger Hall currents.

Figure 7 shows typical tangential velocity and lateral velocity distributions when loss of heat through radiation is increasing. In Fig. 7(*a*), increasing radiation causes an increase in the tangential velocity near the plate surface. In Fig. 7(*b*), the effect of thermal radiation is to reduce the lateral velocity close to the plate surface while increasing the lateral boundary-layer thickness. This is in line with the findings of Abel et al. [16], who, in the case of a continuously moving stretching surface, showed that the effect of thermal radiation is to enhance the velocity in the boundary layer, except that, in this study, the increase in velocity is confined to the tangential direction only.

The combined effects of the Prandtl number and the thermal radiation on the temperature distribution in the boundary layer are illustrated in Fig. 8. Without radiation (Fig. 8(*a*)), the thermal boundary layer is thinner as compared with Fig. 8(*b*) when radiation is present. Two conclusions can be drawn from the results depicted in Fig. 8: (a) that increasing the Prandtl number leads to

a decrease in the fluid temperature and (b) that radiation produces significant increases in the thermal boundary layer. These results confirm the earlier findings by Chamkha [12], who considered the case of thermal radiation and buoyancy effects on hydromagnetic flow over an accelerating permeable surface with a heat source or sink. The results are, however, different from those of Hossain et al. [11] study. The latter study did not, however, consider MHD flow.

4 Conclusions

In this paper, we have sought to determine how the presence of radiation and Hall effects alter the characteristics of MHD flow past a semi-infinite vertical plate. The governing continuum equations were solved numerically using an implicit-finite-difference method. The specific conclusions derived from this study are summarized as follows.

- Increasing the strength of the magnetic field as characterized by the Hartmann number accelerates the motion of the fluid in the boundary layer in both the tangential and lateral directions. The initial increase in the fluid velocity within the boundary layer is contrary to the now widely held notion that the Lorentz force should increase the drag so slowing the flow near the surface of the body. This can be attributed to the negative impact of the Hall effect. Away from the immediate proximity of the surface, a cross flow is induced, and at this stage, the Lorentz force becomes significant so that increases in the Hartmann number causes reduction in the flow velocity.
- Increasing the radiation parameter causes an increase in the tangential velocity component but a decrease in the lateral velocity component.
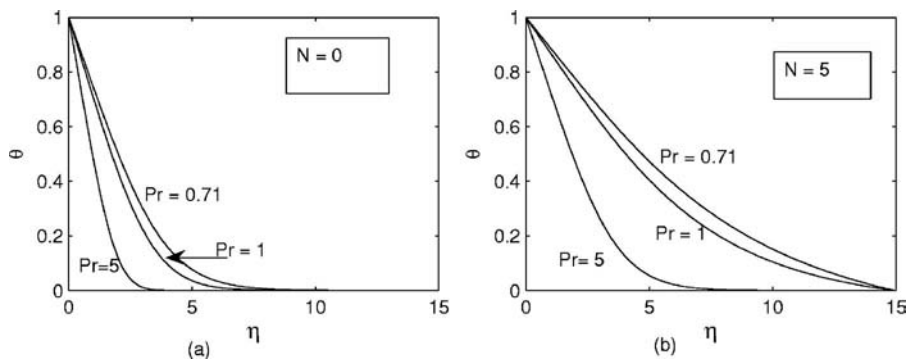

Fig. 8 The variation of (*a*) tangential velocity and (*b*) lateral velocity distributions with increasing radiation. The tangential velocity decreases with radiation, while the tangential velocity initially increases before reducing sharply to zero.

- Increasing the Hartmann numbers leads to a reduction in the temperature and, consequently, in the thermal boundary layer. Hence, in line with Poggie and Gaitonde [14], we find that heat transfer mitigation through magnetic control is possible.
- Large Hall currents ($m \geqslant 1$) cause an increase in the fluid temperature distribution, while small Hall currents ($m < 1$) act to reduce the extent of the thermal boundary layer and thus act to reinforce the beneficial temperature reducing properties of a large magnetic field.

Acknowledgment

Nomenclature

B_0 = magnetic field induction
c_p = specific heat
F = nondimensional streamwise velocity
G = nondimensional normal velocity
g = acceleration due to gravity
Gr = Grashof number
H = nondimensional spanwise velocity
K = mean absorption coefficient
L = typical length scale
M = Hartmann number
m = Hall current
N = thermal radiation coefficient
Nu = Nusselt number
Pr = Prandtl number
q_r = radiative heat flux
T = fluid temperature
u = streamwise velocity
v = normal velocity
w = spanwise velocity component
x = streamwise coordinate axis
y = normal coordinate axis

Greek Symbols

α = thermal diffusivity
β = coefficient of volumetric expansion
η = scaled normal displacement
θ = nondimensional temperature
λ_c = fluid thermal conductivity
μ = coefficient of dynamic viscosity
ν = momentum diffusivity
ξ = scaled streamwise displacement
σ = fluid electrical conductivity
σ^* = Stefan–Boltzmann constant
τ = shear stress

Subscripts

∞ = far away from the wall surface
w = at the wall surface

References

[1] Sparrow, E. M., and Cess, R. D., 1961, "Free Convection With Blowing and Suction," Int. J. Heat Mass Transfer, **83**, pp. 243–248.
[2] Watanabe, T., and Pop, I., 1993, "Magnetohydrodynamic Free Convection Flow Over a Wedge in the Presence of a Transverse Magnetic Field," Int. Commun. Heat Mass Transfer, **20**, pp. 871–881.
[3] Pop, I., and Watanabe, T., 1994, "Hall Effects on Magnetohydrodynamic Free Convection About a Semi-Infinite Vertical Plate," Int. J. Eng. Sci., **32**(12), pp. 1903–1911.
[4] Aldoss, T. K., Al-Nimr, M. A., Jarrah, M. A., and Al-Sha'er, B., 1995, "Magnetohydrodynamic Mixed Convection From a Vertical Plate Embedded in a Porous Medium," Numer. Heat Transfer, Part A, **28**, pp. 635–645.
[5] Chamkha, A. J., 1997, "Hydromagnetic Natural Convection From an Isothermal Inclined Surface Adjacent to a Thermally Stratified Porous Medium," Int. J. Eng. Sci., **37**(10/11), pp. 975–986.
[6] Chiam, T. C., 1995, "Hydromagnetic Flow Over a Surface Stretching With a Power-Law Velocity," Int. J. Eng. Sci., **33**, pp. 429–435.
[7] Chandran, P., Sacheti, N. C., and Singh, A. K., 1996, "Hydromagnetic Flow and Heat Transfer Past a Continuously Moving Porous Boundary," Int. Commun. Heat Mass Transfer, **23**, pp. 889–98.
[8] Vajravelu, K., and Hadjinicolaou, A., 1997, "Convective Heat Transfer in an Electrically Conducting Fluid at a Stretching Surface With Uniform Free Stream," Int. J. Eng. Sci., **35**, pp. 1237–1244.
[9] Kumari, M., and Nath, G., 1999, "Development of Two Dimensional Boundary Layer With an Applied Magnetic Field Due to Impulsive Motion," Indian J. Pure Appl. Math., **30**(7), pp. 695–703.
[10] Chamkha, A. J., and Khaled, A. R. A., 2000, "Similarity Solutions for Hydromagnetic Mixed Convection Heat and Mass Transfer for Hiemenz Flow Through a Porous Medium," Int. J. Numer. Methods Heat Fluid Flow, **10**, pp. 94–115.
[11] Hossain, M. A., Lim, M. A., and Rees, D. A. S., 1999, "The Effect of Radiation on Free Convection from a Porous Vertical Plate," Int. J. Heat Mass Transfer, **42**, pp. 181–191.
[12] Chamkha, A. J., 2000, "Thermal Radiation and Buoyancy Effects on Hydromagnetic Flow Over and Accelerating Surface With Heat Source Or Sink," Int. J. Eng. Sci., **38**, pp. 1699–1712.
[13] Chamkha, A. J., and Khaled, A. R. A., 2000, "Hydromagnetic Simultaneous Heat and Mass Transfer by Mixed Convection From a Vertical Plate Embedded in a Stratified Porous Medium With Thermal Dispersion Effects," Heat Mass Transfer, **36**, pp. 63–70.
[14] Poggie, J., and Gaitonde, D. V., 2002, "Magnetic Control of Flow Past a Blunt Body: Numerical Validation and Exploration," Phys. Fluids, **14**(5), pp. 1720–1731.
[15] Nishihara, M., Jiang, N., Rich, W. J., Lempert, W. R., and Adamovich, I. V., 2005, "Low-Temperature Supersonic Boundary Layer Control Using Repetitively Pulsed Magnetohydrodynamic Forcing," Phys. Fluids, **17**, p. 106102.
[16] Abel, S., Prasad, K. V., and Mahaboob, A., 2005, "Buoyancy Force and Thermal Radiation Effects in MHD Boundary Layer Visco-Elastic Flow Over Continuously Moving Stretching Surface," Int. J. Therm. Sci., **44**, pp. 465–476.
[17] Blottner, F. G., 1970, "Finite Difference Methods of Solution of the Boundary Layer Equations," AIAA J., **8**, pp. 193–205.
[18] Chamkha, A. J., 1997, "MHD-Free Convection From a Vertical Plate Embedded in a Thermally Stratified Porous Medium With Hall Effects," Appl. Math. Model., **21**, pp. 603–609.
[19] Sobha, V. V., and Ramakrishna, K., 2003, "Convective Heat Transfer Past a Vertical Plate Embedded in a Porous Medium With an Applied Magnetic Field," IE(I) Journal-MC, **84**, pp. 130–134.
[20] Chamkha, A. J., 1998, "Hydromagnetic Mixed Convection Stagnation Flow With Suction and Blowing," Int. Commun. Heat Mass Transfer, **25**(3), pp. 417–426.

The Onset of Convection in a Porous Medium Occupying an Enclosure of Variable Width or Height

D. A. Nield

Department of Engineering Science,
University of Auckland,
Private Bag 92019,
Auckland, New Zealand

A. V. Kuznetsov

Department of Mechanical and Aerospace Engineering,
North Carolina State University,
Campus Box 7910,
Raleigh, NC 27695-7910

An analytical study is made of the onset of convection in a saturated porous medium occupying a two-dimensional enclosure of uniform height, but whose width is slowly varying in an arbitrary manner, or one of uniform width, but whose height is slowly varying in an arbitrary manner. It is found that the variation of width generally has a stabilizing effect, whereas variation of height generally has a destabilizing effect. [DOI: 10.1115/1.2768097]

1 Introduction

The classical Horton–Rogers–Lapwood (HRL) problem, for the onset of convection in a horizontal layer of a saturated porous medium uniformly heated from below, has been extensively studied. Studies of various aspects of this problem are surveyed in Nield and Bejan [1]. The case of an enclosure of variable depth was analyzed by Lowell [2] and Hartline and Lister [3]. However, it appears that the case of an enclosure of variable width has not previously been studied.

The problem studied here is an extension of the analysis for the HRL problem for the case of impervious thermally conducting bottom and top boundaries. A two-dimensional enclosure with impervious thermally insulated sidewalls is examined. The enclosure is assumed to be almost rectangular. Attention is focused on the case where the aspect ratio $A \geq 1$, where A is defined as the ratio of the height to mean width of the enclosure. This geometry is selected so that the convection occurs in the form of a single cell.

The analysis involves a perturbation of the solution for an exactly rectangular box. A Galerkin approximation [4] is employed to determine the critical Rayleigh number for the onset of convection. In Sec. 4, the analysis is modified to treat the case of variable height rather than variable width.

2 Analysis

Single-phase flow in a saturated porous medium is considered. Asterisks are used to denote dimensional variables. We consider an almost rectangular box, $0 \leq x^* \leq L + \delta^*(y^*)$, $0 \leq y^* \leq H$, where the y^*-axis is in the upward vertical direction and $|\delta^*(y^*)/L| \ll 1$, and it is assumed that $\delta^*(y^*)$ has zero mean. The sidewalls are taken as insulated, and uniform temperatures T_0 and T_1 are imposed at the upper and lower boundaries, respectively.

Within this box, the permeability is K and the overall (effective) thermal conductivity is k. The Darcy velocity is denoted by $\mathbf{u}^* = (u^*, v^*)$. The Oberbeck–Boussinesq approximation is invoked, and local thermal equilibrium is assumed. The equations representing the conservation of mass, thermal energy, and Darcy's law take the form

$$\frac{\partial u^*}{\partial x^*} + \frac{\partial v^*}{\partial y^*} = 0 \tag{1}$$

$$(\rho c)_m \frac{\partial T^*}{\partial t^*} + (\rho c)_f \left[u^* \frac{\partial T^*}{\partial x^*} + v^* \frac{\partial T^*}{\partial y^*} \right] = k \left[\frac{\partial^2 T^*}{\partial x^{*2}} + \frac{\partial^2 T^*}{\partial y^{*2}} \right] \tag{2}$$

$$u^* = -\frac{K}{\mu} \frac{\partial P^*}{\partial x^*} \tag{3a}$$

$$v^* = \frac{K}{\mu} \left[-\frac{\partial P^*}{\partial y^*} - \rho_0 \beta g (T^* - T_0) \right] \tag{3b}$$

where $(\rho c)_m$ and $(\rho c)_f$ are the heat capacities of the overall porous medium and the fluid, respectively, μ is the fluid viscosity, ρ_0 is the fluid density at temperature T_0, and β is the volumetric expansion coefficient.

We introduce dimensionless variables by defining

$$x = \frac{x^*}{L}, \quad y = \frac{y^*}{H} \tag{4a}$$

$$(u,v) = \frac{(\rho c)_m H}{k} (u^*, v^*) \tag{4b}$$

$$t = \frac{k}{(\rho c)_m H^2} t^* \tag{4c}$$

$$\theta = \frac{T^* - T_0}{T_1 - T_0} \tag{4d}$$

$$P = \frac{(\rho c)_f K}{\mu k} P^* \qquad (4e)$$

We also define a Rayleigh number Ra by

$$\mathrm{Ra} = \frac{(\rho c)_f \rho_0 g \beta K H (T_1 - T_0)}{\mu k} \qquad (5)$$

and the heat capacity ratio

$$\sigma = \frac{(\rho c)_m}{(\rho c)_f} \qquad (6)$$

The governing equations then take the form

$$A \frac{\partial u}{\partial x} + \frac{\partial v}{\partial y} = 0 \qquad (7)$$

$$\frac{\partial \theta}{\partial \tau} + \frac{1}{\sigma} \left[A u \frac{\partial \theta}{\partial x} + v \frac{\partial \theta}{\partial y} \right] = A^2 \frac{\partial^2 \theta}{\partial x^2} + \frac{\partial^2 \theta}{\partial y^2} \qquad (8)$$

$$u = -A \frac{\partial P}{\partial x}, \quad v = -\frac{\partial P}{\partial y} + \sigma \, \mathrm{Ra} \, \theta \qquad (9)$$

We introduce a streamfunction ψ so that

$$u = \sigma \, \mathrm{Ra} \, \frac{\partial \psi}{\partial y} \qquad (10a)$$

$$v = -\sigma \, \mathrm{Ra} \, A \frac{\partial \psi}{\partial x} \qquad (10b)$$

We also eliminate P. The result is

$$A^2 \frac{\partial^2 \psi}{\partial x^2} + \frac{\partial^2 \psi}{\partial y^2} = -\frac{\partial \theta}{\partial x} \qquad (11)$$

$$\frac{\partial \theta}{\partial \tau} + \mathrm{Ra} \, A \left[\frac{\partial \psi}{\partial y} \frac{\partial \theta}{\partial x} - \frac{\partial \psi}{\partial x} \frac{\partial \theta}{\partial y} \right] = A^2 \frac{\partial^2 \theta}{\partial x^2} + \frac{\partial^2 \theta}{\partial y^2} \qquad (12)$$

The conduction solution is given by

$$\psi = 0 \qquad (13a)$$

$$\theta = 1 - y \qquad (13b)$$

The perturbed solution is given by

$$\psi = \varepsilon \psi' \qquad (14a)$$

$$\theta = 1 - y + \varepsilon \theta' \qquad (14b)$$

To first order in the small constant ε, we get

$$A^2 \frac{\partial^2 \psi'}{\partial x^2} + \frac{\partial^2 \psi'}{\partial y^2} + A \frac{\partial \theta'}{\partial x} = 0 \qquad (15)$$

$$\frac{\partial \theta'}{\partial \tau} + \mathrm{Ra} \, A \frac{\partial \psi'}{\partial x} - \left[A^2 \frac{\partial^2 \theta'}{\partial x^2} + \frac{\partial^2 \theta'}{\partial y^2} \right] = 0 \qquad (16)$$

For the onset of convection, we can invoke the "principal of exchange of stabilities" and hence take the time derivative in Eq. (16) to be zero.

We now introduce a transformation of coordinates,

$$\xi = \frac{x}{g(y)}, \quad \eta = y \qquad (17)$$

where

$$g(y) = 1 + \frac{\delta^*(y^*)}{L} \qquad (18)$$

Thus, the mean value of $g(y)$ is 1.

It is now assumed that

$$\frac{d\delta^*}{dy^*} \ll \frac{L}{H} \qquad (19)$$

so that

$$\left| \frac{1}{g(\eta)} \frac{dg(\eta)}{d\eta} \right| \ll 1 \qquad (20)$$

Then, Eqs. (15) and (16) take the form

$$A^2 \frac{\partial^2 \psi'}{\partial \xi^2} + [g(\eta)]^2 \frac{\partial^2 \psi'}{\partial \eta^2} + A g(\eta) \frac{\partial \theta'}{\partial \xi} = 0 \qquad (21)$$

$$\mathrm{Ra} \, A g(\eta) \frac{\partial \psi'}{\partial \xi} - \left[A^2 \frac{\partial^2 \theta'}{\partial \xi^2} + [g(\eta)]^2 \frac{\partial^2 \theta'}{\partial \eta^2} \right] = 0 \qquad (22)$$

The boundary conditions are taken to be

$$\psi' = 0 \quad \text{and} \quad \theta' = 0 \quad \text{on} \quad \eta = 0 \qquad (23)$$

$$\psi' = 0 \quad \text{and} \quad \theta' = 0 \quad \text{on} \quad \eta = 1 \qquad (24)$$

$$\psi' = 0 \quad \text{and} \quad \frac{\partial \theta'}{\partial \xi} = 0 \quad \text{on} \quad \xi = 0 \qquad (25)$$

$$\psi' = 0 \quad \text{and} \quad \frac{\partial \theta'}{\partial \xi} = 0 \quad \text{on} \quad \xi = 1 \qquad (26)$$

We have used the assumption in Eq. (20) to approximate the normal derivative on the boundary by the horizontal derivative.

This set of boundary conditions is satisfied by

$$\psi'_m = \sin \pi \xi \sin m \pi \eta, \quad m = 1, 2, 3, \ldots \qquad (27)$$

$$\theta'_n = \cos \pi \xi \sin n \pi \eta, \quad n = 1, 2, 3, \ldots \qquad (28)$$

We can take this set of functions (which are exact eigenfunctions for the strictly rectangular case) as trial functions for an approximate solution of the general case. For example, working at second order, we can try

$$\psi' = A_1 \psi'_1 + A_2 \psi'_2 \qquad (29)$$

$$\theta' = B_1 \theta'_1 + B_2 \theta'_2 \qquad (30)$$

In the Galerkin method, the expression (29) is substituted into the left-hand side of Eq. (21) and the resulting residual is made orthogonal to the separate trial functions ψ'_1, ψ'_2, in turn. Likewise the residual on the substitution of the expression (30) into Eq. (22) is made orthogonal to θ'_1, θ'_2, in turn. We use the notation

$$\langle f(\eta) \rangle = \int_0^1 f(\eta) d\eta \qquad (31)$$

and define

$$I_{mn} = 2 \langle g(\eta) \sin m \pi \eta \sin n \pi \eta \rangle \qquad (32)$$

$$J_{mn} = 2 \langle [g(\eta)]^2 \sin m \pi \eta \sin n \pi \eta \rangle \qquad (33)$$

The output of the Galerkin procedure is a set of four homogeneous linear equations in the four unknown constants A_1, A_2, B_1, B_2. Eliminating these constants, we get

$$\det \mathbf{M} = 0 \qquad (34)$$

where the matrix $\mathbf{M}$ takes the form

$$\mathbf{M} = \begin{bmatrix} \pi^2(A^2 + J_{11}) & 4\pi^2 J_{12} & \pi I_{11} & \pi I_{12} \\ \pi^2 J_{12} & \pi^2(A^2 + 4J_{22}) & \pi I_{12} & \pi I_{22} \\ \mathrm{Ra}\ \pi I_{11} & \mathrm{Ra}\ \pi I_{12} & \pi^2(A^2 + J_{11}) & 4\pi^2 J_{12} \\ \mathrm{Ra}\ \pi I_{12} & \mathrm{Ra}\ \pi I_{22} & \pi^2 J_{12} & \pi^2(A^2 + 4J_{22}) \end{bmatrix}$$

$$(35)$$

In the general case, the integrals in Eq. (35) can be obtained by quadrature. The eigenvalue equation (Eq. (30)) can then be solved to give the critical Rayleigh number.

3 Results and Discussion

3.1 First-Order Results. For example, the order-one Galerkin method (using a single trial function for each of ψ and θ) yields the eigenvalue equation

$$\det \begin{bmatrix} \pi^2(A^2 + J_{11}) & \pi A I_{11} \\ \pi \mathrm{Ra}\ A I_{11} & \pi^2(A^2 + J_{11}) \end{bmatrix} = 0 \qquad (36)$$

which gives

$$\mathrm{Ra} = \frac{\pi^2(A^2 + J_{11})^2}{A^2 I_{11}^2} \qquad (37)$$

For the rectangular case $I_{11}=1$ and $J_{11}=1$, and thus, $\mathrm{Ra}=\mathrm{Ra}_0$, where

$$\mathrm{Ra}_0 = \frac{\pi^2(A^2 + 1)^2}{A^2} \qquad (38)$$

For a square box $A=1$, and then $\mathrm{Ra}_0=4\pi^2$, the well-known value for the standard Horton–Rogers–Lapwood problem.

Returning to the case of general A and defining S by

$$\mathrm{Ra} = \mathrm{Ra}_0(1 + S) \qquad (39)$$

one finds that to first order in small quantities

$$S = 2\left[\frac{J_{11} - 1}{A^2 + 1} - (I_{11} - 1)\right] \qquad (40)$$

We now consider some special cases.

Case 1. For a linear variation in the enclosure width, necessarily antisymmetric about the horizontal midline, modeled by $g=g_1$, where

$$g_1(\eta) = 1 + \alpha(2\eta - 1) \qquad (41)$$

one finds that

$$I_{11} = 1 \qquad (42a)$$

and

$$J_{11} = 1 + \alpha^2\left(\frac{1}{3} - \frac{2}{\pi^2}\right) \approx 1 + 0.131\alpha^2 \qquad (42b)$$

$$S = \frac{\alpha^2}{A^2 + 1}\left(\frac{2}{3} - \frac{4}{\pi^2}\right) \approx 0.261\frac{\alpha^2}{A^2 + 1} \qquad (43)$$

This implies that $\mathrm{Ra} > \mathrm{Ra}_0$ when α is nonzero, for all values of A, i.e., a small departure from the exact rectangular shape is stabilizing.

Case 2. For a quadratic variation of enclosure width, symmetric about the horizontal midline, modeled by $g=g_2$, where

$$g_2(\eta) = 1 + \beta(6\eta^2 - 6\eta + 1) \qquad (44)$$

one finds that

$$I_{11} = 1 - \frac{3\beta}{\pi^2} \approx 1 - 0.304\beta \qquad (42a')$$

$$J_{11} = 1 - \frac{6\beta}{\pi^2} + \beta^2\left(\frac{1}{5} - \frac{6}{\pi^2} + \frac{54}{\pi^4}\right) \approx 1 - 0.608\beta + 0.146\beta^2$$

$$(42b')$$

$$S = \frac{1}{A^2 + 1}\left[-\frac{12\beta}{\pi^2} + \beta^2\left(\frac{2}{5} - \frac{12}{\pi^2} + \frac{108}{\pi^4}\right)\right] + \frac{6\beta}{\pi^2}$$

$$\approx \frac{-1.216\beta + 0.293\beta^2}{A^2 + 1} + 0.608\beta \qquad (43')$$

One finds that the departure from a rectangular shape is stabilizing for all values of β under the assumption that $A \geq 1$.

Case 3. For a sinusoidal variation of enclosure width, symmetric about the horizontal midline, modeled by $g=g_3$, where

$$g_3(\eta) = 1 + \sigma \sin \pi\eta \qquad (44')$$

one finds that

$$I_{11} = 1 + \frac{2\sigma}{3\pi} \approx 1 + 0.212\sigma \qquad (45a)$$

$$J_{11} = 1 + \frac{4\sigma}{3\pi} + \sigma^2\left(\frac{3}{4} - \frac{20}{3\pi^2}\right) \approx 1 + 0.424\sigma + 0.074\sigma^2$$

$$(45b)$$

$$S = \frac{1}{A^2 + 1}\left[\frac{8\sigma}{3\pi} + \sigma^2\left(\frac{3}{2} - \frac{10}{3\pi^2}\right)\right] - \frac{4\beta}{3\pi}$$

$$\approx \frac{0.849\sigma + 0.149\sigma^2}{A^2 + 1} - 0.424\sigma \qquad (46)$$

Thus, the departure from a rectangular shape is stabilizing for all values of σ when $A \geq 1$.

In cases 2 and 3, the profiles have a similar shape, so the similarity in the results is as expected.

Case 4. For a sinusoidal variation of enclosure width, antisymmetric about the horizontal midline, modeled by $g=g_4$, where

$$g_4(\eta) = 1 + \tau \sin 2\pi\eta, \qquad (47)$$

one finds that

$$I_{11} = 1 \qquad (48a)$$

$$J_{11} = 1 + \frac{\tau^2}{2} \qquad (48b)$$

$$S = \frac{\tau^2}{A^2 + 1} \qquad (49)$$

Thus, for this case the departure from a rectangular shape is stabilizing for all values of τ and for all values of A. This case is similar to case 1.

We also have a general result. For a square enclosure $A=1$, and then $\mathrm{Ra} \geq \mathrm{Ra}_0$ for any function $g(\eta)$ with unit mean. This follows quickly from the identity

$$1 + J_{11} \pm 2I_{11} = 2\int_0^1 (g \pm 1)^2 \sin^2 \pi\eta\, d\eta \geq 0 \qquad (50)$$

which implies that

$$\mathrm{Ra} - \mathrm{Ra}_0 = \frac{\pi^2}{I_{11}^2}[(1 + J_{11})^2 - 4I_{11}^2] \geq 0 \qquad (51)$$

3.2 Second-Order Results. Using the second-order Galerkin approximation, the following results were obtained. For a general value of A, the expressions are complicated; thus, results just for the case $A=1$ are reported, as follows:

Case 1

$$S = 0.1307\alpha^2 + 0.0043\alpha^4 + O(\alpha^6) \qquad (52)$$

Case 2

$$S = 0.1464\beta^2 + 0.0445\beta^3 + 0.0189\beta^4 + O(\beta^5) \qquad (53)$$

Case 3

$$S = 0.0745\sigma^2 - 0.0158\sigma^3 + 0.0047\sigma^4 + O(\sigma^5) \qquad (54)$$

Case 4

$$S = 0.5\tau^2 + 0.0625\tau^4 + O(\tau^6) \qquad (55)$$

These results confirm the first-order results and give an indication of the accuracy of those results.

$$\mathbf{M} = \begin{bmatrix} \pi^2(A^2 J_{11}+1) & 4\pi^2 J_{12} & \pi J_{11} & \pi J_{12} \\ \pi^2 J_{12} & \pi^2(4A^2 J_{22}+1) & \pi J_{12} & \pi J_{22} \\ \mathrm{Ra}\,\pi J_{11} & \mathrm{Ra}\,\pi J_{12} & \pi^2(A^2 J_{11}+1) & 4\pi^2 J_{12} \\ \mathrm{Ra}\,\pi J_{12} & \mathrm{Ra}\,\pi J_{22} & \pi^2 J_{12} & \pi^2(4A^2 J_{22}+1) \end{bmatrix} \qquad (59)$$

where instead of Eq. (33), one now defines

$$J_{mn} = 2\langle [f(\xi)]^2 \sin m\pi\xi \sin n\pi\xi \rangle \qquad (60)$$

The first-order Galerkin approximation yields, instead of Eq. (37),

$$\mathrm{Ra} = \frac{\pi^2(A^2 J_{11}+1)^2}{A^2 J_{11}^2} \qquad (61)$$

Instead of Eq. (40), one has

$$S = \frac{2(1 - J_{11})}{A^2 + 1} \qquad (62)$$

This gives the following results. (Since ξ in Eq. (60) is a dummy variable in a definite integral, the formula in Eq. (60) is essentially the same as that in Eq. (33) when the functions $f(\xi)$ and $g(\eta)$ are made identical, and thus, one can make use of previous expressions for integrals.)

Case 1

$$f_1(\xi) = 1 + \alpha(2\xi - 1) \qquad (63)$$

$$S = \frac{\alpha^2}{A^2+1}\left(\frac{4}{\pi^2} - \frac{2}{3}\right) \approx -0.261\frac{\alpha^2}{A^2+1} \qquad (64)$$

This implies that $\mathrm{Ra} < \mathrm{Ra}_0$ when α is nonzero, for all values of A, i.e., a small departure from the exact rectangular shape is destabilizing,

Case 2

$$f_2(\xi) = 1 + \beta(6\xi^2 - 6\xi + 1) \qquad (65)$$

$$S = \frac{1}{A^2+1}\left[\frac{12\beta}{\pi^2} - \beta^2\left(\frac{2}{5} - \frac{12}{\pi^2} + \frac{108}{\pi^4}\right)\right] \approx \frac{1.216\beta - 0.293\beta^2}{A^2+1} \qquad (66)$$

One finds that the departure from a rectangular shape is stabilizing for small positive values β and destabilizing for negative values of β,

Case 3

$$\xi_3(\xi) = 1 + \sigma \sin \pi\xi \qquad (67)$$

4 Enclosure of Variable Height

The above analysis can be modified to model an enclosure of variable height rather than variable width. When one introduces the transformation

$$\xi = x, \quad \eta = \frac{y}{f(x)} \qquad (56)$$

in place of Eq. (17), one finds that the variable height analog of Eqs. (21) and (22) are

$$A^2[f(\xi)]^2\frac{\partial^2 \psi'}{\partial \xi^2} + \frac{\partial^2 \psi'}{\partial \eta^2} + A[f(\xi)]^2\frac{\partial \theta'}{\partial \xi} = 0 \qquad (57)$$

$$\mathrm{Ra}\,A[f(\xi)]^2\frac{\partial \psi'}{\partial \xi} - \left[A^2[f(\xi)]^2\frac{\partial^2 \theta'}{\partial \xi^2} + \frac{\partial^2 \theta'}{\partial \eta^2}\right] = 0 \qquad (58)$$

In place of Eq. (35), one has

$$J_{11} = 1 + \frac{4\sigma}{3\pi} + \sigma^2\left(\frac{3}{4} - \frac{20}{3\pi^2}\right) \approx 1 + 0.424\sigma + 0.074\sigma^2 \quad (68)$$

$$S = \frac{-1}{A^2+1}\left[\frac{8\sigma}{3\pi} + \sigma^2\left(\frac{3}{2} - \frac{40}{3\pi^2}\right)\right] \approx \frac{-(0.849\sigma + 0.149\sigma^2)}{A^2+1} \qquad (69)$$

Thus, the departure from a rectangular shape is stabilizing for small negative values of σ (relatively shallow in the middle of the enclosure) and destabilizing for positive values of σ.

Case 4

$$f_4(\xi) = 1 + \tau \sin 2\pi\xi, \qquad (70)$$

$$S = \frac{-\tau^2}{A^2+1} \qquad (71)$$

Thus, for this case, the departure from a rectangular shape is destabilizing for all values of τ and for all values of A. This case is similar to case 1.

The fact that variability of width is generally stabilizing while variability of height is generally destabilizing is not surprising. Variability of width leads to a reduction of coherence for the agency causing instability. With variability of height, there is a net gain in coherence.

5 Conclusions

We have examined the situation where the width of the enclosure varies weakly with respect to the vertical coordinate. We have found that in all the cases studied the departure from uniform width leads to an increase in the value of the critical Rayleigh number, that is to an increase in stability. In the case of a square enclosure, the increase in stability occurs for any weak variation of width.

The situation where there is a weak variation of height has also been examined. In this case, there is generally a decrease in stability.

Nomenclature

A = aspect ratio (height to width)
c = specific heat
k = overall (effective) thermal conductivity
K = permeability
H = height of the enclosure
L = mean width of the enclosure
P = dimensionless pressure, $[(\rho c)_f K / \mu k] P^*$
P^* = pressure
Ra = Rayleigh number, $(\rho c)_f \rho_0 g \beta K H (T_1 - T_0)/\mu k$
S = variable defined in terms of Ra by Eq. (39)
t^* = time
t = dimensionless time, $[k/(\rho c)_m H^2] t^*$
T^* = temperature
T_0 = temperature at the upper boundary
T_1 = temperature at the lower boundary
u = dimensionless horizontal velocity, $[(\rho c)_m H/k] u^*$
$\mathbf{u}^*$ = vector of Darcy velocity, (u^*, v^*)
v = dimensionless vertical velocity, $[(\rho c)_m H/k] v^*$
x = dimensionless horizontal coordinate, x^*/L
x^* = horizontal coordinate
y = dimensionless upward vertical coordinate, y^*/H
y^* = upward vertical coordinate

Greek Symbols

β = fluid volumetric expansion coefficient
θ = dimensionless temperature, $(T^* - T_0)/(T_1 - T_0)$
μ = fluid viscosity
ρ = density
ρ_0 = fluid density at temperature T_0
σ = heat capacity ratio, $(\rho c)_m/(\rho c)_f$
ψ = stream function defined by Eqs. (10a) and (10b)

Subscript

f = fluid
m = overall porous medium

Superscript

$*$ = dimensional variable

References

[1] Nield, D. A., and Bejan, A., 2006, *Convection in Porous Media*, 3rd ed., Springer, New York.
[2] Lowell, R. P., 1980, "Topographically Driven Subcritical Hydrothermal Convection in the Oceanic Crust," Earth Planet. Sci. Lett., **49**, pp. 21–28.
[3] Hartline, B. K., and Lister, C. R. B., 1981, "Topographic Forcing of Supercritical Convection in a Porous Medium Such as the Ocean Crust," Earth Planet. Sci. Lett., **55**, pp. 75–86.
[4] Finlayson, B. A., 1972, *The Method of Weighted Residuals and Variational Principles*, Academic Press, New York.

Assessment of a Second-Moment Closure Model for Strongly Heated Internal Gas Flows

Robert E. Spall
Department of Mechanical and Aerospace Engineering,
Utah State University,
Logan, UT 84322-4130
e-mail: spall@engineering.usu.edu

Eugen Nisipeanu
Fluent, Inc.,
1007 Church St.,
Evanston, IL 60201
e-mail: en@evanston.fluent.com

Adam Richards
Advanced Engineering & Sciences,
5009 Centennial Boulevard,
Colorado Springs, CO 80919
e-mail: Adamh_richards@hotmail.com

Both low- and high-Reynolds-number versions of the stress-ω model of Wilcox (Turbulence Modeling for CFD, 2nd ed., DCW Industries, Inc.) were used to predict velocity and heat transfer data in a high-heat-flux cylindrical tube for which fluid properties varied strongly with temperature. The results indicate that for accurate heat transfer calculations under the conditions considered in this study, inclusion of low-Reynolds-number viscous corrections to the model are essential. The failure of the high-Reynolds-number model to accurately predict the wall temperature was attributed to an overprediction of the near-wall velocity. [DOI: 10.1115/1.2768098]

Keywords: computational fluid dynamics, forced convection, turbulence models

Introduction

A stress-ω second-moment closure model [1] is assessed for a low-Mach-number vertical flow of air within a tube under conditions of high wall heat flux. Our motivation for this problem stems from considerations that gases may be effectively used as a coolant for advanced power reactors. For these systems to achieve high thermal efficiencies requires high gas exit temperatures. To achieve these high temperatures, gas velocities may be low enough so that relevant Reynolds numbers are <10,000. For instance, the high-temperature engineering test reactor (HTTR) in Japan has an exit Reynolds number of ~3500 [2]. This type of flow presents a challenge to turbulence models, in part, due to the strong dependence of the fluid properties on temperature, which means that fully developed mean flows do not develop.

In terms of experimental data, Perkins [3] presents mean temperature distributions for forced convection through a vertically oriented circular cylinder with the application of strong wall heat flux at inlet Reynolds numbers of ~4200 and ~6000. Shehata [4], using essentially the same experimental apparatus and under the same conditions, measured mean velocity profiles. In particular,

Perkins [3] and Shehata [4] obtained data at an inlet Reynolds number of 6000 with two different (in relative terms, lower and moderate) wall heat fluxes. They also obtained data for a higher heat flux at an inlet Reynolds number of 4200. Their results provide the opportunity to assess the performance of turbulence models under conditions of significant wall heat flux with associated large variations in fluid properties. The results of Perkins [3] and Shehata [4] were subsequently reported in detail by Shehata and McEligot [5,6]. Experimental uncertainties were reported to be on the order of 8–10% for the velocities and 1–2% for the absolute temperature [5]. These data are used to assess the performance of a second-moment closure in this work and will herein be referred to as the Shehata/McEligot data.

The performance of a number of turbulence models in predicting the Shehata/McEligot data have been presented in the literature. Mikielewicz et al. [7] presented results for eleven turbulence models, including mixing length, one-equation, and low-Reynolds-number two-equation k-ε and k-τ models. Their general conclusions were that the low-Reynolds-number formulation of Launder and Sharma [8] performed best in predicting the Shehata/McEligot experimental data. In general, most of the models considerably overpredicted convective heat transfer coefficients, resulting in wall temperatures well below those determined experimentally.

Spall et al. [9] investigated the performance of $k-\varepsilon-v^2-f$ and $k-\omega$ models. The advantage of these formulations is that they may be integrated to the wall without the addition of near-wall damping functions. Their results showed that the $k-\omega$ model performed similar to most of the models reported in [7]; that is, the convective heat transfer coefficients were considerably overpredicted. However, the performance of the $k-\varepsilon-v^2-f$ model was quite good. This improvement in performance may be attributed to the ability of the $k-\varepsilon-v^2-f$ model to take into account the anisotropy of near-wall turbulence.

In the work presented herein, we have performed a series of calculations for the Shehata/McEligot data using the second-moment closure formulation of Wilcox [1] as implemented in the general purpose CFD code FLUENT [10]. Second-moment closure models still offer the most comprehensive predictive capabilities for complex, industrially significant flows using present-generation computers. Consequently, they may represent an optimal choice for calculations involving advanced power systems. The work presented herein represents an essential step in the validation process for complex flows inherent in advanced power generation systems; that is, assessment under conditions of high wall heat flux and strongly varying fluid properties.

Governing Equations

The governing equations were solved using the pressure-based finite-volume code FLUENT [10]. For purposes of brevity, the complete set of governing equations is not shown; rather, appropriate references are provided. In particular, the stress-ω turbulence model employed is equivalent to that described in Wilcox [1]. In essence, the model is based on the work of Launder et al. [11], except that an equation for specific dissipation rate ω is used rather than an equation for the dissipation rate ε. Both high- and low-Reynolds-number versions of the model have been employed in this work [1]. The low-Reynolds-number version includes viscous corrections similar to those used in low-Reynolds-number $k-\omega$ formulations. In addition, the body force term was included in the momentum equation (acting in the negative x direction), but the effect of buoyancy on turbulence in the Reynolds stress transport equation was not modeled. The energy equation was solved using a turbulent Prandtl number approach. In particular, Pr_t was set to a constant value of 0.85 [12].

In the solution procedure, interpolation to cell faces for all transport equations was performed using a second-order upwind scheme. Pressure-velocity coupling utilized the SIMPLEC method.

During the iterative solution procedure, normalized residuals for all equations were reduced to 10^{-6} or less.

Fluid Properties

Density and viscosity were defined by the incompressible ideal gas law and Sutherland's law, respectively. Polynomial fits were used to define the thermal conductivity and specific heat. In particular,

$$\rho = \frac{p_{\text{ref}}}{RT} \tag{1}$$

$$\mu = \mu_0 \left(\frac{T}{T_0}\right)^{1.5} \left(\frac{T_0 + S}{T + S}\right) \tag{2}$$

$$\lambda = 6.64465 \times 10^{-3} + 7.1845 \times 10^{-5}T - 1.3276 \times 10^{-8}T^2 \tag{3}$$

$$c_p = 1.0526 \times 10^{-3} - 2.8029 \times 10^{-1}T + 4.2562 \times 10^{-4}T^2 \tag{4}$$

where $\mu_0 = 1.716 \times 10^{-5}$ N S/m^2, $T_0 = 273.11$, $S = 110.56$, and $p_{\text{ref}} = 92{,}640$ Pa.

Inlet and Wall Thermal Boundary Conditions

The test section described by Shehata and McEligot [5,6] was constructed of resistively heated, seamless, extruded Inconel 600 tube with an inside diameter $D = 0.0274$ m. Their experimental apparatus was set up to provide axisymmetric, steady, fully developed turbulent flow at the start of the heating section located at $x/D = 0$. However, axial conduction along the test section walls resulted in elevated wall temperatures that extended approximately 15 tube diameters upstream from the beginning of the heated section. Consequently, the inlet of the computational domain was specified at $x/D = -15.615$. The outlet of the computational domain was fixed at $x/D = 29$.

Fully developed profiles were specified as the inlet boundary conditions. In particular, values of the axial and radial velocities, Reynolds stresses, and specific dissipation rate were initially computed for isothermal flow over the domain using periodic inlet/outlet boundary conditions, at the appropriate Reynolds number. The resulting radial profiles were then specified as the inlet boundary conditions for each turbulence model/run combination
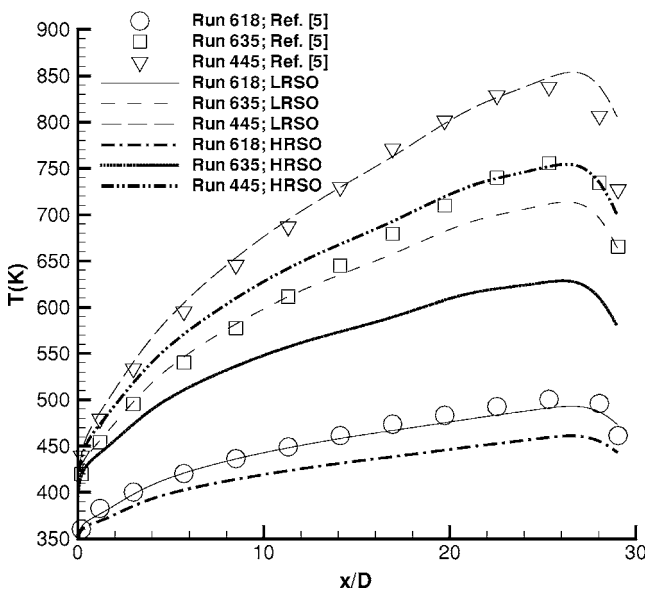

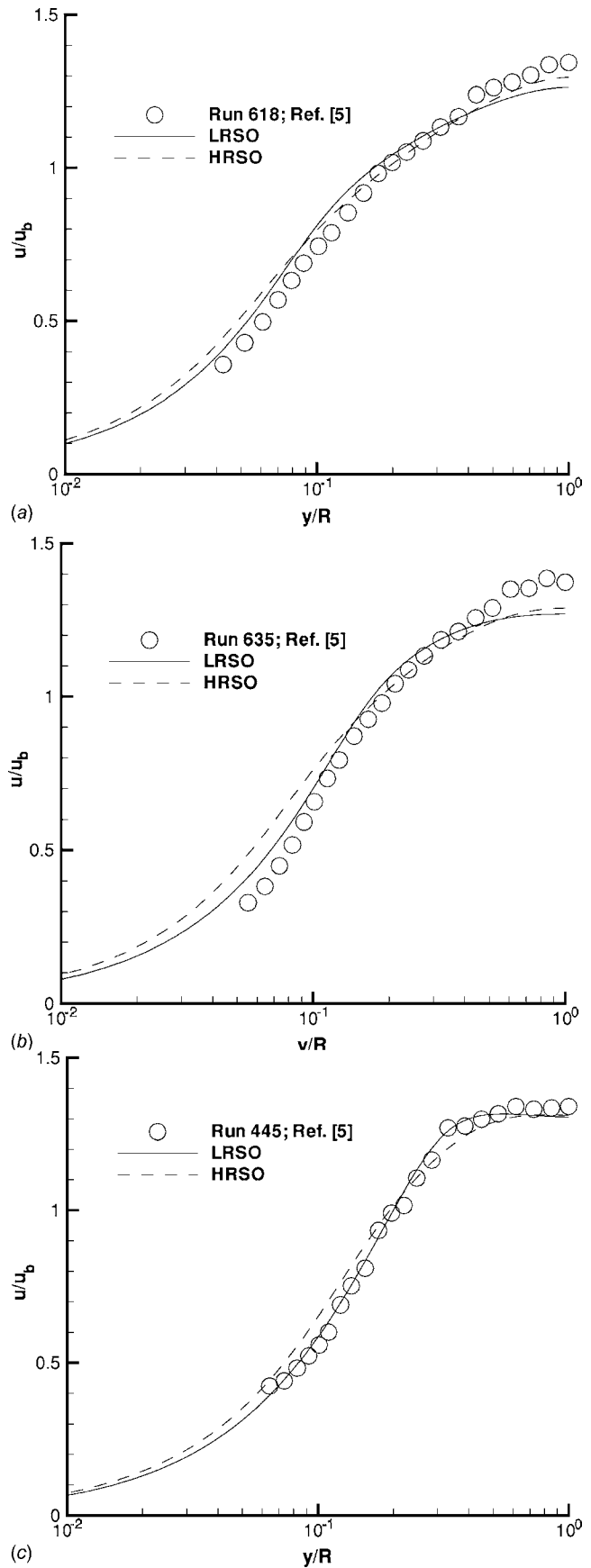Fig. 1 Comparison between predicted wall temperatures and experimental data [5]

Fig. 2 Comparison between predicted and experimental mean velocity profiles [5] at $x/D = 24.5$: (a) Run 618, (b) Run 635, and (c) Run 445

considered. Temperatures at the inlet to the computational domain were set to uniform values, depending on the experimentally measured data for each specific case.

Over the heated section of the wall, the heat flux thermal boundary conditions were obtained from data presented in Shehata and McEligot [5]. Following their notation, we consider three distinct cases as Run 618, Run 635, and Run 445, where the relevant dimensionless heating rate was defined in Ref. [5] as $q^+ = q_w/(Gc_pT_i)$. In particular, Run 618 represents a relatively low heating rate turbulent case with $q^+ \approx 0.0018$ and an inlet Reynolds number (based on tube diameter, D) of ~ 6000. Run 635 represents a "subturbulent," intermediate heating rate case with $q^+ \approx 0.0035$ and an inlet Reynolds number of ~ 6000. Run 445 represents a "laminarizing," high heating rate case with $q^+ = 0.0045$ and an inlet Reynolds number of ~ 4200. For implementation as numerical boundary conditions, curve fits to the wall heat flux data presented in Ref. [5] were employed over the region $0 \leq x/D \leq 29$. We note that due to end-wall conduction effects in the experiments, a drop in the heat flux near the end of the domain is observed. Over the region $-15.615 \leq x/D < 0$, wall temperatures were fixed using a curve fit to the experimental temperature values presented in Ref [5].

Results

We present results in terms of wall temperatures, and radial profiles of velocity and temperature computed using both low- and high-Reynolds-number formulations of the stress-ω model. These numerical results are compared to the experimental data of Shehata and McEligot [5]. We then discuss the sensitivity of the results with respect to grid refinement.

We first present in Fig. 1 predicted wall temperatures as a function of x/D for the three wall heat flux rates defined above by Runs 618, 635, and 445. These results are compared to experimental data from Ref. [5]. The results show that the low-Reynolds-number version of the stress-ω model (herein denoted as LRSO) does an excellent job in predicting the experimentally observed wall temperatures. The results are particularly good for Runs 618 and 445. For Run 635, one observes that the values are underpredicted by $\sim 6\%$ (in terms of absolute temperatures) near the point of maximum wall temperature ($x/D \approx 25$). Given that uncertainty levels in the experimental data were reported to be 1–2% of the local absolute temperatures [5], predictions using the LRSO model are within experimental error for all but the downstream region of Run 635. The high-Reynolds-number version of the model (herein denoted as HRSO) did not perform as well. In particular, at the axial location $x/D \approx 25$ the HRSO model underpredicts wall temperatures by approximately 8%, 17%, and 10% for Runs 618, 635, and 445, respectively. The above results can be compared to those previously reported [9] for a low-Reynolds-number $k-\omega$ model in which wall temperatures were underpredicted by approximately 11%, 22%, and 23% for Runs 618, 635, and 445, respectively. Associated with these increases in wall temperature are strong increases in the molecular viscosity and thermal conductivity of the air. In particular, from the inlet to $x/D = 24.5$, the near wall values for μ and λ approximately double for Runs 635 and 445, and increase by over 40% for Run 618.

A comparison between computed and experimental [5] velocity profiles (normalized by the bulk velocity) for Runs 618, 635, and 445 are shown in Figs. 2(a)–2(c), respectively. The data are presented at an axial location of $x/D = 24.5$ and plotted in terms of y/R, the normalized distance from the wall. The results show a strong correlation between predicted near-wall velocities that are larger than the experimental data and an underprediction of the wall temperature. For instance, considering the LRSO, the velocity profiles are well predicted in the near-wall region (at $x/D = 24.5$) for all but Run 635. Here, the near-wall velocities are somewhat overpredicted, and the corresponding wall temperature is, as shown in Fig. 1, underpredicted. This same trend holds for
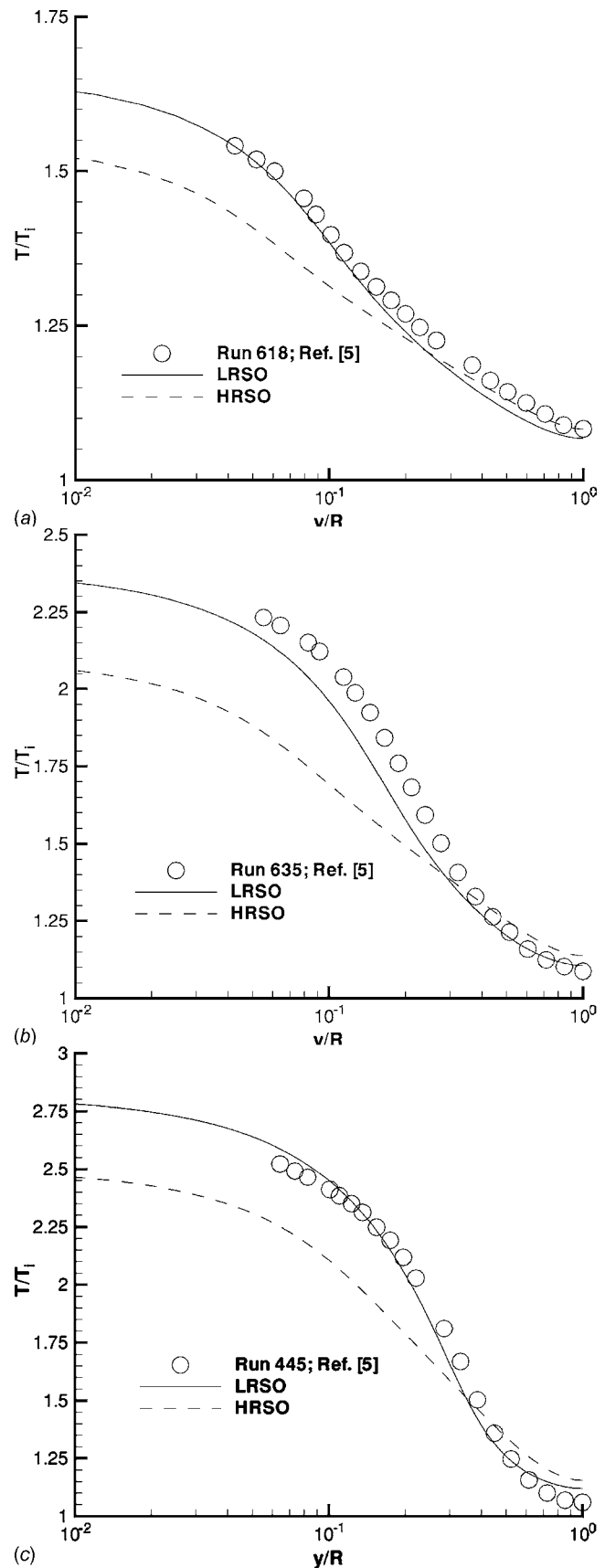

Fig. 3 Comparison between predicted and experimental [5] mean temperature profiles at $x/D=24.5$: (a) Run 618, (b) 635, and (c) Run 445

Run 618, although to a much lesser extent. In terms of the HRSO model, the near-wall velocities are overpredicted for all three cases and, in particular, Run 635. This leads to an overprediction of convective heat transfer coefficients and a concomitant underprediction of the wall temperatures. Wilcox [1] provides comparisons for the skin friction coefficient between high- and low-Reynolds-number stress-ω models for the isothermal flow within a pipe. Those results indicate that for $Re > 10,000$ the values of c_f predicted by the two models are nearly indistinguishable. However, for $Re < 10,000$ the high-Reynolds-number model predicts slightly higher values of c_f than does the low-Reynolds-number model. This is consistent with our observations, which involve Reynolds numbers significantly below 10,000.

Shown in Figs. 3(a)–3(c) are temperature profiles, normalized by the inlet temperature, and plotted as a function of y/R at the axial location $x/D = 24.5$. The results reveal that for all three cases, the LRSO model does good job of predicting the experimental data of Shehata and McEligot [5]. The only location where the LRSO results depart somewhat from the experimental data is in the near-wall region for Run 635. For the HRSO model, the results indicate that the underprediction of the temperatures is essentially limited to the region near the wall, that is, approximately $0 \leq y/R \leq 0.25$.

The results were computed using two different levels of grid resolution. (The finer grid results were presented in Figs. 1–3.) The base-level grid consisted of 288 cells in the streamwise direction and 50 cells in the radial direction. Cells were clustered radially toward the wall and axially toward $x/D = 0$. The base-level grid was halved in each direction and the solutions recomputed. The base-level grid resulted in average values of y^+ on the order of 0.5, depending on the specific case. The finer grid values of y^+ were approximately half that level. The values of the mean wall temperature for each of the six different sets of results presented varied by $< 0.75\%$ between base-level and refined grids. Computed velocity profiles were essentially indistinguishable.

Conclusions

Both low- and high-Reynolds-number versions of the stress-ω model of Wilcox [1] were used to predict velocity and heat transfer data in a high-heat-flux cylindrical tube for which fluid properties varied strongly with temperature. The results indicated that inclusion of the low-Reynolds-number corrections were essential in accurate predictions of both velocity and temperature data. The failure of the HRSO model to accurately predict the wall temperature was due to its overprediction of the near-wall velocity. In summary, the results presented herein indicate that for accurate heat transfer calculations under the conditions considered in this study, inclusion of low-Reynolds-number viscous corrections to the stress-ω model are essential.

Acknowledgment

Nomenclature

c_f	=	skin friction coefficient
c_p	=	specific heat
D	=	tube inside diameter
G	=	mass flux per unit area per unit time
Nu	=	Nusselt number
p_{ref}	=	reference pressure
Pr_t	=	turbulent Prandtl number
q^+	=	dimensionless heating rate
q_w	=	wall heat flux
R	=	tube inside radius
Re	=	Reynolds number
T	=	temperature
T_i	=	inlet temperature
u	=	mean axial velocity
u_b	=	bulk axial velocity
x	=	axial coordinate
y	=	wall normal distance
ε	=	dissipation rate
λ	=	thermal conductivity
μ	=	dynamic viscosity
ω	=	specific dissipation rate
ρ	=	density

References

[1] Wilcox, D. W., 1998, *Turbulence Modeling for CFD*, 2nd ed., DCW Industries, Inc., La Cañada, CA.

[2] Takase, K., Hino, R., and Miyamoto, Y., 1990, "Thermal and Hydraulic Tests of Standard Fuel Rod of HTTR With HENDEL," J. At. Energy Soc. Jpn., **32**(11), pp. 1107–1110.

[3] Perkins, K. R., 1975, "Turbulence Structure in Gas Flows Laminarizing by Heating," Ph.D. dissertation, University of Arizona.

[4] Shehata, A. M., 1984, "Mean Turbulence Structure in Strongly Heated Air Flows," Ph.D. dissertation, University of Arizona.

[5] Shehata, A. M., and McEligot, D. M., 1995, "Turbulence Structure in the Viscous Layer of Strongly Heated Gas Flows," Tech. Report No. INEL-95/0223, Idaho National Engineering Laboratory.

[6] Shehata, A. M., and McEligot, D. M., 1998, "Mean Turbulence Structure in the Viscous Layer of Strongly-Heated Internal Gas Flows: Measurements," Int. J. Heat Mass Transfer, **41**, pp. 4297–4313.

[7] Mikielewicz, D. P., Shehata, A. M., Jackson, J. D., and McEligot, D. M., 2002, "Temperature, Velocity and Mean Turbulence Structure in Strongly Heated Gas Flows, Comparison of Numerical Predictions With Data," Int. J. Heat Mass Transfer, **45**, 4333–4352.

[8] Launder, B., and Sharma, B., 1974, "Application of Energy-Dissipation Model of Turbulence to the Calculation of Flow Near a Spinning Disk," Lett. Heat Mass Transfer, **1**, pp. 131–138.

[9] Spall, R. E., Richards, A., and McEligot, D. M., 2004, "An Assessment of $k - \omega$ and $v^2 - f$ Turbulence Models for Strongly Heated Internal Gas Flows," Numer. Heat Transfer, Part A, **46**, pp. 831–849.

[10] Fluent, Inc., Lebanon, NH.

[11] Launder, B. E., Reece, G. J., and Rodi, W., 1975, "Progress in the Development of a Reynolds-Stress Turbulence Closure," J. Fluid Mech., **68**, pp. 537–566.

[12] Kader, B. A., and Yaglom, A. M., 1972, "Heat and Mass Transfer Laws for Fully Turbulent Wall Flows," Int. J. Heat Mass Transfer, **12**, pp. 2239–2351.

Effect of the Temperature Difference Aspect Ratio on Natural Convection in a Square Cavity for Nonuniform Thermal Boundary Conditions

M. Sathiyamoorthy
Department of Applied Mathematics,
Birla Institute of Technology,
Mesra, Ranchi-835215, India
e-mail: m.sathiya@yahoo.com

Tanmay Basak
Department of Chemical Engineering,
Indian Institute of Technology Madras,
Chennai-600036, India
e-mail: tanmay@iitm.ac.in

S. Roy[1]
Department of Mathematics,
Indian Institute of Technology Madras,
Chennai-600036, India
e-mail: sjroy@iitm.ac.in

N. C. Mahanti
Department of Applied Mathematics,
Birla Institute of Technology,
Mesra, Ranchi-835215, India

The present numerical investigation deals with steady natural convection flow in a closed square cavity when the bottom wall is sinusoidal heated and vertical walls are linearly heated, whereas the top wall is well insulated. In the nonuniformly heated bottom wall maximum temperature T_H attains at the center of the bottom wall. The sidewalls are linearly heated, maintained at minimum temperature T_c at top edges of the sidewalls and at temperature T_h at the bottom edges of the sidewalls, i.e., $T_c \leq T_h \leq T_H$. Nonlinear coupled PDEs governing the flow have been solved by the penalty finite element method with biquadratic rectangular elements. Numerical results are obtained for various values of Prandtl number (Pr) $(0.01 \leq Pr \leq 10)$ and temperature difference aspect ratio A $=[(T_h - T_c)/(T_H - T_c)]$ $(0 \leq A \leq 1)$ for higher Raleigh number Ra $= 10^5$. Results are presented in the form of streamlines, isotherm contours, local Nusselt number, and the average Nusselt number as a function of temperature difference aspect ratio A. The overall heat transfer process is shown to be tuned efficiently with suitable selection of A. [DOI: 10.1115/1.2768099]

Keywords: natural convection, square cavity, nonuniform heating, temperature difference aspect ratio

1 Introduction

The studies of natural convection in cavities primarily focus on cases of uniformly heating from bottom walls or sidewalls [1–3]. The literature survey on natural convection in enclosures shows

that earlier studies [4–9] have made attempts to acquire a basic understanding of natural convection flows and transfer characteristics in an enclosure where one vertical wall is cooled and another one heated while the remaining top and bottom walls are well insulated. Recently, Sarris et al. [10], Calcagni et al. [11], and Ridouane and Hasnaoui [12] have analyzed natural convection in a square cavity with a partially heated bottom wall. However, in most of the studies, one vertical wall of the enclosure is cooled and another one is heated, or the bottom wall is heated while the remaining wall(s) are well insulated. In the case of a nonuniform heated bottom wall and sidewall(s), a limited number of case studies has been reported. Sarris et al. [13] have reported the effect of sinusoidal top-wall temperature variations in a natural convection within a square enclosure where the other walls are insulated. Roy and Basak [14] and Basak et al. [15] have recently studied natural convection flows in a square cavity with a nonuniform heated bottom wall and/or sidewall. Bilgen and Ben Yedder [16] have studied natural convection in an enclosure with heating and cooling by sinusoidal temperature profile on one side. Furthermore, Sathiyamoorthy et al. [17] have investigated steady natural convection flows in square cavity with a uniformly heated bottom wall and linearly heated sidewalls, and it was observed that a pair of stronger secondary circulations was formed at the lower portion of the cavity for higher Rayleigh number Ra=10^5 and lower Prandtl number (Pr$<$1).

The present work is to numerically study natural convection in a square cavity when the bottom wall is sinusoidally heated and vertical walls are linearly heated, whereas the top wall is well insulated for various temperature difference aspect ratio at Ra $=10^5$. The effect of the temperature difference aspect ratio will be further investigated to examine the efficiency and/or enhanced heating rates in the enclosure. The Galerkin finite element method with penalty parameter has been used to solve the nonlinear coupled partial differential equations for flow and temperature field. The objective is to determine the influence of the temperature difference aspect ratio on the flow, temperature distributions within the cavity, and heat transfer rate at the heated walls in terms of local and average Nusselt numbers as a function of temperature difference aspect ratio for various Prandtl numbers.

2 Formulation and Numerical Method

Thermophysical properties of the fluid in the flow model were assumed to be constant, except the density variations causing a body force term in the momentum equation. The Boussinesq approximation is invoked for the fluid properties to relate density changes to temperature changes and to couple, in this way, the temperature field to the flow field. The governing equations for the steady natural convection flow using conservation of mass, momentum, and energy can be written in a nondimensional form as follows:

$$\frac{\partial U}{\partial X} + \frac{\partial V}{\partial Y} = 0 \tag{1}$$

$$U\frac{\partial U}{\partial X} + V\frac{\partial U}{\partial Y} = -\frac{\partial P}{\partial X} + \Pr\left(\frac{\partial^2 U}{\partial X^2} + \frac{\partial^2 U}{\partial Y^2}\right) \tag{2}$$

$$U\frac{\partial V}{\partial X} + V\frac{\partial V}{\partial Y} = -\frac{\partial P}{\partial Y} + \Pr\left(\frac{\partial^2 V}{\partial X^2} + \frac{\partial^2 V}{\partial Y^2}\right) + \text{RaPr}\,\theta \tag{3}$$

$$U\frac{\partial \theta}{\partial X} + V\frac{\partial \theta}{\partial Y} = \left(\frac{\partial^2 \theta}{\partial X^2} + \frac{\partial^2 \theta}{\partial Y^2}\right) \tag{4}$$
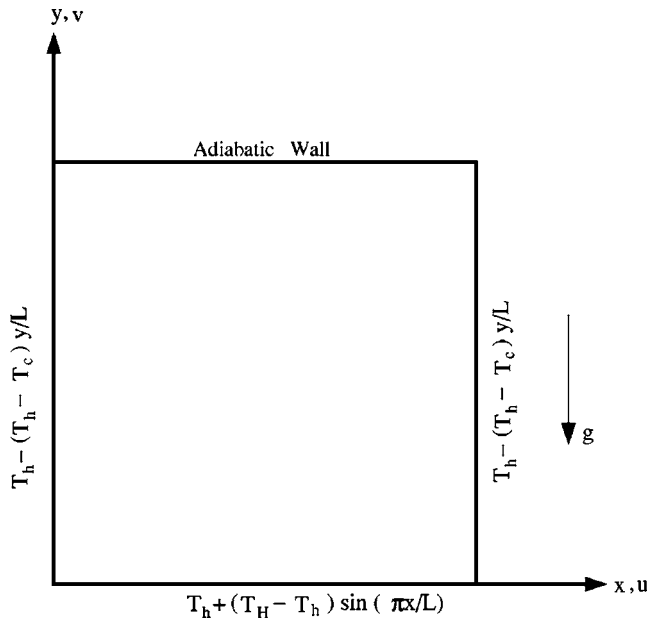
Fig. 1 Schematic diagram of the physical system

with the boundary conditions

$$U(X,0) = U(X,1) = U(0,Y) = U(1,Y) = 0$$

$$V(X,0) = V(X,1) = V(0,Y) = V(1,Y) = 0$$

$$\theta(X,0) = A + (1-A)\sin(\pi X), \quad \frac{\partial \theta}{\partial Y}(X,1) = 0$$

$$\theta(0,Y) = A(1-Y), \quad \theta(1,Y) = A(1-Y) \tag{5}$$

by using the following change of variables (Fig. 1):

$$X = \frac{x}{L}, \quad Y = \frac{y}{L}, \quad U = \frac{uL}{\alpha}, \quad V = \frac{vL}{\alpha}, \quad \theta = \frac{T - T_c}{T_H - T_c}, \quad A$$

$$= \frac{T_h - T_c}{T_H - T_c}$$

$$P = \frac{pL^2}{\rho\alpha^2}, \quad \mathrm{Pr} = \frac{\nu}{\alpha}, \quad \mathrm{Ra} = \frac{g\beta(T_H - T_c)L^3\mathrm{Pr}}{\nu^2} \tag{6}$$

The momentum and energy balance equations (2)–(4) along with the boundary conditions (5) are solved using the Galerkin finite element method. Since the solution procedure is explained in Refs. [14,15], the detailed description is not included in this paper. The numerical solutions are obtained in terms of velocity components (U, V), and the stream function (ψ) is evaluated using the relationship between the stream function (ψ) and velocity components [18]. It may be noted that the positive sign of ψ denotes anti-clockwise circulation, and the clockwise circulation is represented by the negative sign of ψ. The no-slip condition is valid at all boundaries because there is no cross-flow; hence, $\psi=0$ is used for the boundaries.

The heat transfer coefficient in terms of the local Nusselt number is defined by

$$\mathrm{Nu} = -\frac{\partial \theta}{\partial n} \tag{7}$$

where n denotes the normal direction on a plane. The local Nusselt numbers at bottom wall (Nu_b) and at the sidewall (Nu_s) are evaluated for various wall boundary conditions using the above

definition. The average Nusselt numbers at the bottom walls and sidewalls are computed as follows:

$$\overline{\mathrm{Nu}_b} = \int_0^1 \mathrm{Nu}_b dX \quad \text{and} \quad \overline{\mathrm{Nu}_s} = \int_0^1 \mathrm{Nu}_s dY \tag{8}$$

The computational domain consists of 20×20 biquadratic elements, which correspond to 41×41 grid points. In order to assess the accuracy of the numerical procedure, the present algorithm based on the grid size (41×41) for a square enclosure have been tested with the work of Mallinson and Vahl Davis [19] for Ra $=10^3-10^5$, and the results are in good agreement. In addition, we have also carried out the validation of the thermal equilibrium via computing the average Nusselt number for the bottom wall, which is two times of that for the vertical wall, as discussed later. A parametric study was carried out to determine the influence of temperature aspect ratio A on the flow of high Rayleigh number Ra$=10^5$ for low Prandtl numbers Pr$=0.01-0.7$ and Prandtl numbers Pr$=10-1000$.

3 Results and Discussion

3.1 Effects of Temperature Difference Aspect Ratio. Figures 2–7 illustrate the stream function and isotherm contours for various values of temperature difference aspect ratio $A=0.1-0.9$ and low Prandtl number Pr$=0.01-10$ for Ra$=10^5$. As expected due to the symmetric boundary condition at sinusoidal heated bottom wall together with the linearly heated side walls and insulated top wall, both the flow and temperature profiles are symmetric about the midplane of the cavity. It may be noted that, the temperature of bottom wall varies between A and 1 and temperature of side walls varies between 0 and A. It is also found that due to convection at high Rayleigh number (Ra$=10^5$), the circulations are stronger.

Figure 2 shows the streamlines and the isotherm contours for Pr$=0.01$ at $A=0.1$ with Ra$=10^5$. It may be noted that the variation of temperature at the bottom wall is greater and the sidewalls being almost uniformly cooled. A pair of identical counterrotating cells is formed in the upper portion of the cavity, and many weaker secondary circulations are formed at lower portion of the cavity, as the fluid corresponds to small viscous effect for Pr $=0.01$. As A increases to 0.7, the variation of the temperature at the sidewalls is greater, and the secondary circulations break into more circulations due to convection created by the hot lower part of the cavity (Fig. 3). At $A=0.9$, the bottom wall is almost hot and the temperature at the sidewalls varies linearly. As a consequence, the secondary circulations become more prominent due to enhanced convection from the hot lower portion of the vertical walls (see Fig. 4).

Figures 5 and 6 illustrate the stream function and temperature contours for Pr$=0.7$. At $A=0.1$, the circulations are strong and the secondary circulations are suppressed at lower part of the cavity for Pr$=0.7$. For $A=0.9$, the temperature of the lower part is hot, which generates enhanced convection, i.e., hot fluid moves toward the center of the cavity and the secondary circulations are developed due to the primary circulation becoming weaker (see Fig. 6). Figure 7 illustrates the stream function and isotherm contour for $A=0.9$ with high Prandtl number (Pr$=10$). The circulations are stronger than those with the lower Prandtl numbers, and a pair of small secondary circulations is observed at corners of the bottom wall, which remain up to a very large Prandtl number (figures not shown). The general trend is that as Prandtl number Pr increases for $A\geq0.7$, and the secondary circulations that appear at bottom of the sidewalls move toward the bottom wall and gradually
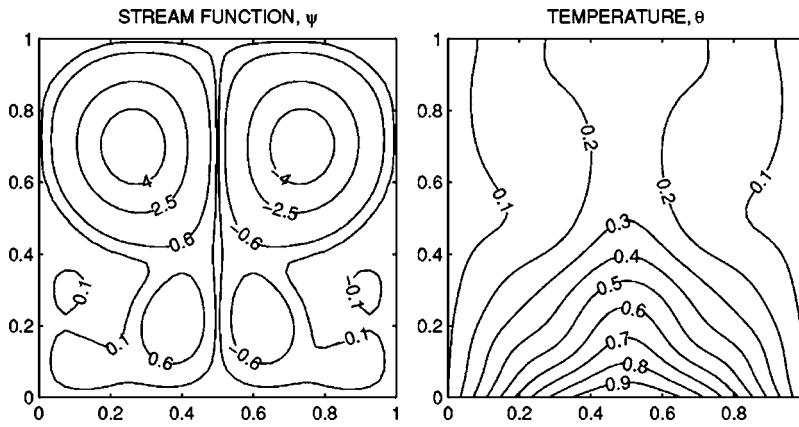
Fig. 2 Contour plots of Ra=10^5 for Pr=0.01 and A=0.1. Clockwise and anti-clockwise flows are shown via negative and positive signs of stream functions, respectively.

become weaker. The physical reason is that higher Prandtl number fluid implies more viscous fluid or less thermal diffusivity, which makes the secondary circulations weaker.

3.2 Heat Transfer Rates: Local and Average Nusselt Numbers. Figures 8 and 9 display the effects of A on the local Nusselt numbers at the sinusoidally heated bottom wall and lin-

early heated sidewalls (Nu_b, Nu_s). Since the temperature profile at the bottom wall is the sinusoidal type (which is symmetrical) together with the linearly heated sidewalls, the local heat transfer rate Nu_b is symmetrical with respect to the midplane (X=0.5). The heat transfer rate Nu_b is A at edges of bottom wall due to the prescribed temperature profile at sidewalls is $A(1-Y)$. In general,
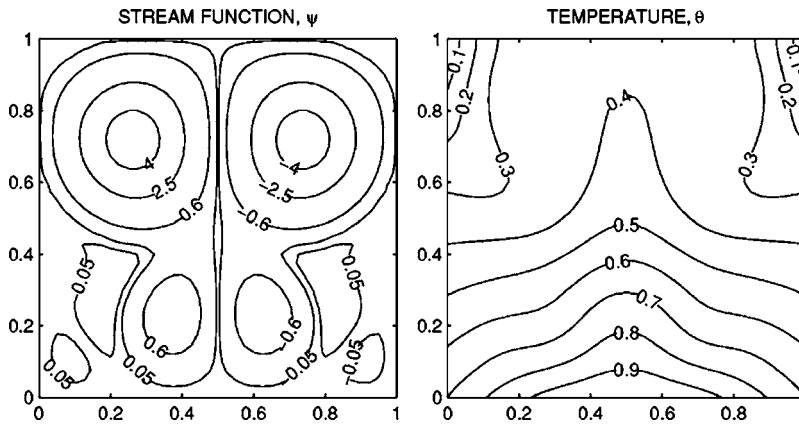

Fig. 3 Contour plots of Ra=10^5 for Pr=0.01 and A=0.7. Clockwise and anti-clockwise flows are shown via negative and positive signs of stream functions, respectively.
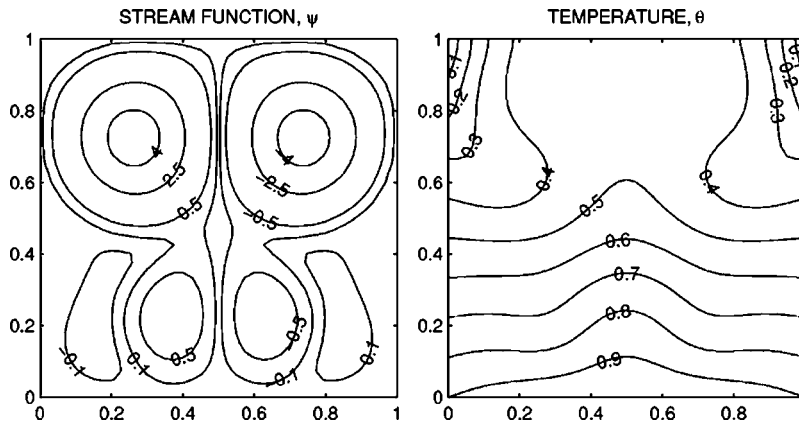

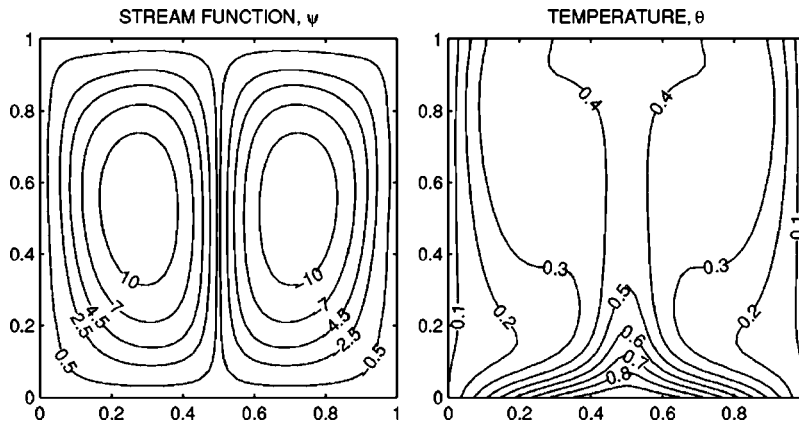**Fig. 4 Contour plots of Ra=10^5 for Pr=0.01 and A=0.9. Clockwise and anti-clockwise flows are shown via negative and positive signs of stream functions, respectively.**

Fig. 5 Contour plots of Ra=10⁵ for Pr=0.7 and A=0.1. Clockwise and anticlockwise flows are shown via negative and positive signs of stream functions, respectively.

the sinusoidal type of local heat transfer rate (Nu_b) occurs at bottom wall, with its minimum value at the middle of the bottom wall as well as at edges of bottom wall and maximum value at X =0.25 and 0.75. Furthermore, the magnitude of variations in the local heat transfer rate at the bottom wall decreases with the increase of aspect ratio A.

Figure 9 shows that local heat transfer rate (Nu_s) at bottom edge of the sidewalls is $\pi(1-A)$ for all A due to the prescribed
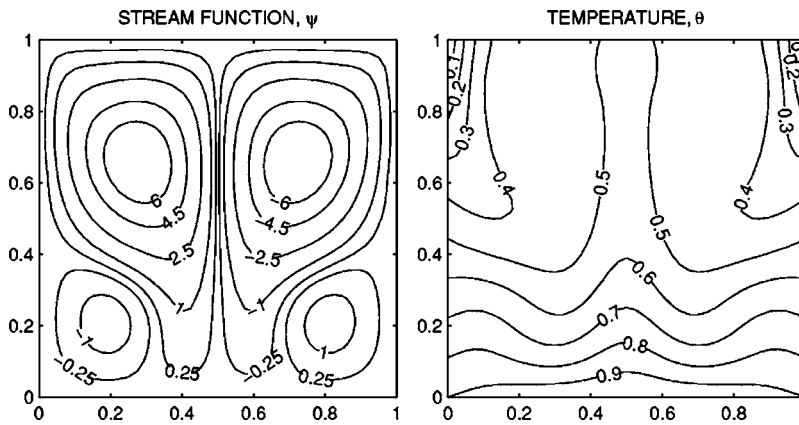

Fig. 6 Contour plots of Ra=10⁵ for Pr=0.7 and A=0.9. Clockwise and anticlockwise flows are shown via negative and positive signs of stream functions, respectively.

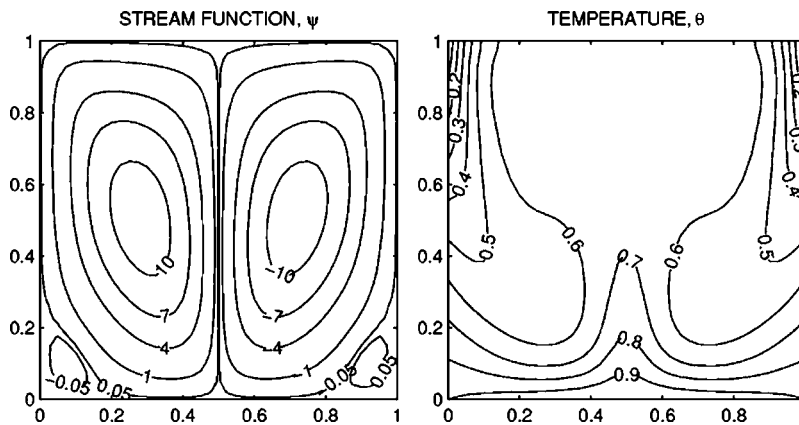**Fig. 7 Contour plots of Ra=10⁵ for Pr=10 and A=0.9. Clockwise and anticlockwise flows are shown via negative and positive signs of stream functions, respectively.**

Bottom Wall

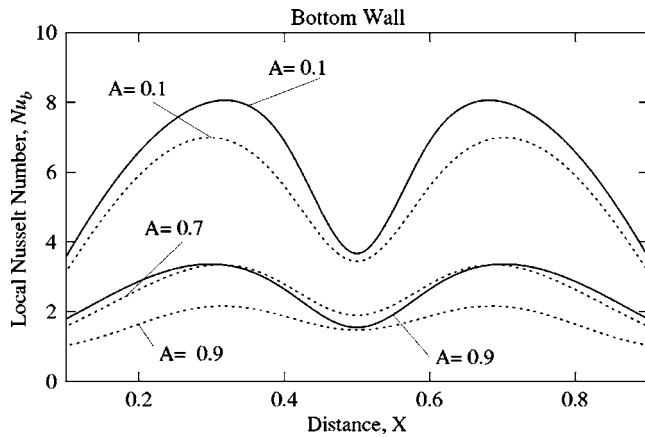**Fig. 8 Variation of local Nusselt number with distance at the bottom wall for Pr=0.7, (dashed line) and Pr=10, (solid line) at Ra=10^5**

temperature profile at bottom wall being $A+(1-A)\sin(\pi X)$, and the heat transfer rate is maximum at top edge of the sidewalls due to the insulated top wall. In general, the local heat transfer rate (Nu_s) smoothly decreases at the lower half of cavity and increases
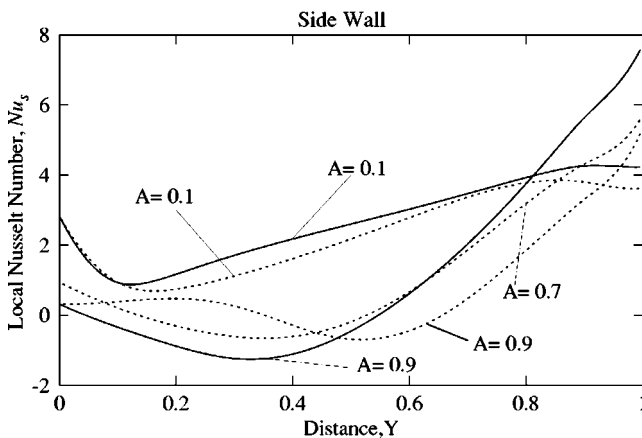
Side Wall

Fig. 9 Variation of local Nusselt number with distance at the sidewalls for Pr=0.7 (dashed line) and Pr=10 (solid line) at Ra=10^5

at the upper half of the cavity. At $A=0.9$ for Pr=0.7, the heat transfer rate is oscillatory in the lower part due to the presence of a pair of symmetric secondary circulations with clockwise and anti-clockwise rotations at the lower part of the cavity. But for higher Prandtl number, Pr=10 at $A=0.9$, the secondary circulations are weaker and the heat transfer rate observed is nonoscillatory.

The overall effects on the heat transfer rates are displayed in Fig. 10, where the distributions of the average Nusselt number at bottom wall and sidewalls are plotted versus aspect ratio A for Ra=10^5 at Pr=0.7 and 10. It is observed from Fig. 8 that, for Pr=0.7 and 10, the local Nusselt number Nu_b decreases locally for all values of X ($0 \le X \le 1$) as the temperature aspect ratio increases. This implies that average Nusselt number at the bottom wall linearly decreases as the temperature difference aspect ratio increases for Pr=0.7 and 10 (see Fig. 10(a)). As the boundary conditions at the sidewalls are identical and the top wall is well insulated, the average heat transfer rates follow the relationship $\overline{Nu}_s=(1/2)\overline{Nu}_b$, where $\overline{Nu}_s$ and $\overline{Nu}_b$ are average Nusselt numbers at the sidewall and bottom walls, respectively. Thus, the average Nusselt number at the sidewall also linearly decreases as the temperature aspect ratio increases (Fig. 10(b)).

4 Conclusions

The conclusions of the present numerical investigation for natural convection flow in a square cavity with sinusoidally heated bottom wall and linearly heated vertical walls with insulated top wall may be drawn as follows:

1. For small value of Pr, many secondary circulations are formed at the lower part of cavity for all values of A. But at Pr$\ge$0.7 only one pair of secondary circulations are formed at lower part of the cavity for $A \ge 0.7$
2. The sinusoidal type of local heat transfer rate occurs at the bottom wall with maximum at $X=0.25$ and 0.75, and the heat transfer rate at lower part of sidewalls is oscillatory due to the presence of a pair of symmetric secondary circulations.

Finally, as the temperature difference aspect ratio increases, the average Nusselt number decreases linearly. Therefore, the sinusoidal bottom heating with almost uniform heating on the sidewall gives higher heat transfer for a square enclosure. In addition, the heat transfer effects can be controlled by suitably tuning the temperature difference aspect ratio.
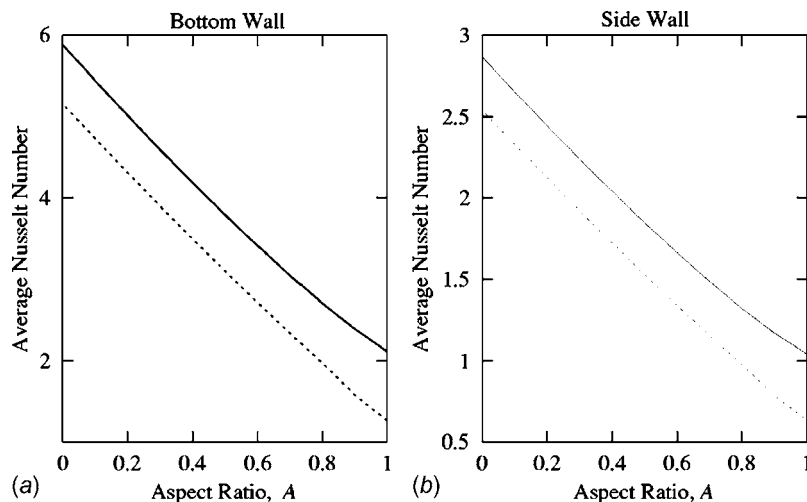

Fig. 10 Variation of average Nusselt number with temperature difference aspect ratio for Pr=0.7 (dashed line) and Pr=10 (solid line) at Ra=10^5

Acknowledgment

Nomenclature

g = acceleration due to gravity, m s^{-2}
k = thermal conductivity, W m^{-1} K^{-1}
L = side of the square cavity, m
n = normal direction on a cavity wall
Nu = local Nusselt number
Nu$_b$ = local Nusselt number at the bottom wall
Nu$_s$ = local Nusselt number at the sidewall
$\overline{\text{Nu}}_b$ = average Nusselt number at the bottom wall
$\overline{\text{Nu}}_s$ = average Nusselt number at the sidewall
p = pressure, Pa
P = dimensionless fluid pressure
Pr = Prandtl number
Ra = Rayleigh number
T = fluid temperature, K
T_c = temperature of cold top edges of the sidewalls, K
T_h = temperature of hot bottom edges of the sidewall, K
T_H = maximum temperature of middle of the bottom wall, K
A = aspect ratio of temperature difference, $=(T_h - T_c)/(T_H - T_c)$
u = x component of velocity
U = x component of dimensionless velocity
v = y component of velocity
V = y component of dimensionless velocity
X = dimensionless distance along x coordinate
Y = dimensionless distance along y coordinate

Greek Symbols

α = thermal diffusivity, m^2 s^{-1}
β = volume expansion coefficient, K^{-1}
γ = penalty parameter
θ = dimensionless temperature
ν = kinematic viscosity, m^2 s^{-1}
ρ = density, kg m^{-3}
ψ = stream function

Subscripts

b = bottom wall
c = cooled top edges
h = hot bottom edges
H = maximum hot middle of bottom wall
s = sidewall

References

[1] Ostrach, S., 1972, "Natural Convection in Enclosures," *Advances in Heat Transfer*, Vol. VII, Academic Press, New York, pp. 161–227.
[2] Ostrach, S., 1982, "Low-Gravity Fluid Flows," Annu. Rev. Fluid Mech., **14**, pp. 313–345.
[3] Ostrach, S., 1988, "Natural Convection in Enclosures," ASME J. Heat Transfer, **110**, pp. 1175–1190.
[4] Fusegi, T., Hyun, J. M., and Kuwahara, K., 1992, "Natural Convection in a Differentially Heated Square Cavity With Internal Heat Generation," Numer. Heat Transfer, Part A, **21**, pp. 215–229.
[5] Lage, J. L., and Bejan, A., 1991, "The Ra-Pr Domain of Laminar Natural Convection in a Enclosure Heated From the Side," Numer. Heat Transfer, Part A, **19**, pp. 21–41.
[6] Lage, J. L., and Bejan, A., 1993, "The Resonance of Natural Convection in an Enclosure Heated Periodically From the Side," Int. J. Heat Mass Transfer, **36**, pp. 2027–2038.
[7] Xia, C. M., and Murthy, J. Y., 2002, "Buoyancy-Driven Flow Transitions in Deep Cavities Heated From Below," ASME J. Heat Transfer, **124**, pp. 650–659.
[8] Bennacer, R., Mohamad, A. A., and Akrour, D., 2001, "Transient Natural Convection in an Enclosure With Horizontal Temperature and Vertical Solutal Gradients," Int. J. Therm. Sci., **40**, pp. 899–910.
[9] Zhu, Z. J., and Yang, H. X., 2003, "Numerical Investigation of Transient Laminar Natural Convection of Air in a Tall Cavity," Heat Mass Transfer, **39**, pp. 579–587.
[10] Sarris, I. E., Lekakis, I., and Vlachos, N. S., 2004, "Natural Convection in Rectangular Tanks Heated Locally From Below," Int. J. Heat Mass Transfer, **47**, pp. 3549–3563.
[11] Calcagni, B., Marsili, F., and Paroncini, M., 2005, "Natural Convective Heat Transfer in Square Enclosures Heated From Below," Appl. Therm. Eng., **25**, pp. 2522–2531.
[12] Ridouane, E. H., and Hasnaoui, M., 2006, "Effect of Surface Radiation on Multiple Natural Convection Solutions in a Square Cavity Partially Heated From Below," ASME J. Heat Transfer, **128**, pp. 1012–1021.
[13] Sarris, I. E., Lekakis, I., and Vlachos, N. S., 2002, "Natural Convection in a 2D Enclosure With Sinusoidal Upper Wall Temperature," Numer. Heat Transfer, Part A, **42**, pp. 513–530.
[14] Roy, S., and Basak, T., 2005, "Finite Element Analysis of Natural Convection Flows in a Square Cavity With Non Uniformly Heated Wall(s)," Int. J. Eng. Sci., **43**, pp. 668–680.
[15] Basak, T., Roy, S., and Balakrishnan, A. R., 2006, "Effects of Thermal Boundary Conditions on Natural Convection Flows Within a Square Cavity," Int. J. Heat Mass Transfer, **49**, pp. 4525–4535.
[16] Bilgen, E., and Ben Yedder, R., 2007, "Natural Convection in Enclosure With Heating and Cooling by Sinusoidal Temperature Profile on One Side," Int. J. Heat Mass Transfer, **50**, pp. 139–150.
[17] Sathiyamoorthy, M., Basak, T., Roy, S., and Pop, I., 2007, "Steady Natural Convection Flows in a Square Cavity With Linearly Heated Side Wall(s)," Int. J. Heat Mass Transfer, **50**, pp. 766–775.
[18] Batchelor, G. K., 1993, *An Introduction to Fluid Dynamics*, Cambridge University Press, Cambridge, UK.
[19] Mallinson, G. D., and Vahl Davis, G. D., 1977, 'Three-Dimensional Natural Convection in a Box: A Numerical Study," J. Fluid Mech., **83**, pp. 1–31.

A Methodology for Blast Furnace Hearth Inner Profile Analysis

Yu Zhang

Rohit Deshpande

Department of Mechanical Engineering,
Purdue University Calumet,
Hammond, IN 46321

D. Huang

Pinakin Chaubal

USA R&D Center,
Mittal Steel Company,
East Chicago, IN 46312

Chenn Q. Zhou

Department of Mechanical Engineering,
Purdue University Calumet,
Hammond, IN 46321
e-mail: qzhou@calumet.purdue.edu

The wear of a blast furnace hearth and the hearth inner profile are highly dependent on the liquid iron flow pattern, refractory temperatures, and temperature distributions at the hot face. In this paper, the detailed methodology is presented along with the examples of hearth inner profile predictions. A new methodology along with new algorithms is proposed to calculate the hearth erosion and its inner profile. The methodology is to estimate the hearth primary inner profile based on 1D heat transfer and to compute the hot-face temperature using the 3D CFD hearth model according to the 1D preestimated and reestimated profiles. After the hot-face temperatures are converged, the hot-face positions are refined by a new algorithm, which is based on the difference between the calculated and measured results, for the 3D computational fluid dynamics (CFD) hearth model further computations, until the calculated temperatures well agree with those measured by the thermocouples. [DOI: 10.1115/1.2768100]

Keywords: CFD, blast furnace hearth, erosion, skull

Introduction

Blast furnaces will remain the predominant iron-producing equipment in the foreseeable future. Building a blast furnace is a capital cost intensive process. Thus, it becomes more imperative to prolong the campaign life, to reduce the iron-making cost. A longer campaign life can significantly lower costs and increase productivity because less blast furnace downtime and financial cost would be needed for repairs and refractory relining. The most crucial part of the blast furnace is the lower part, known as the hearth, where the erosion mostly happens due to the direct contact of the hot metal with the refractory wall.

The inner state of the hearth must be accurately estimated to avoid severe erosion in less time. The interface between hot metal and solid inside the hearth is defined as the hot face, and the outline of the hot face is defined as the inner profile. The inner profile of a hearth is the key to predicting hearth erosion, maintenance of the hearth, and casting operations. Currently, monitoring and understanding phenomena in the hearth are not feasible by intrusive techniques. At most, a well-instrumented hearth refers to one that has numerous thermocouples strategically located at the cold face of the sidewall refractory and at various depths up to the center in the bottom layers on different levels.

At present time, most of the existing hearth erosion models are based on the heat transfer through refractory lining only [1–4], and some of them considered the effect of hot metal flow [5]. The traditional approach to define the hot face position is based on the inverse heat transfer calculation. It is assumed that, the hot-face temperatures are always 1150°C, which is the solidification point of the molten iron saturated with carbon. The idea of using 1150°C isothermal line as the inner profile is that, under this temperature, the hot metal either has been solidified or has been saturated with carbon and is no longer able to absorb any more carbon from the carbon brick. The 1150°C isothermal line might be a good divider to separate the good lining and bad lining; however, it would not be the inner profile because the building up of the skull and erosion could not happen at the same time and at the same location. The refractory is exposed to hot metal flows and erosion only when there is no skull. Thus, the temperature contour cannot accurately represent the whole inner profile.

In order to provide a more accurate and efficient method for predicting the inner profiles, a new methodology has been developed in this research that uses a 1D inverse heat transfer model and thermocouple data that are obtained from an online experiment in real operation to estimate the hearth erosion and inner profiles, and then uses the 3D CFD model to refine it. An iteration procedure has been developed to efficiently and accurately perform the calculations. In this procedure, the inner profiles are adjusted based on heat transfer theory and CFD calculations until there is a good match between the measured and calculated temperatures. This methodology has been used to estimate the erosion and inner profile for the hearth of IH7 Blast Furnace of Mittal Steel for different time periods. The details of the methodology along with an example to demonstrate the methodology are described in the following sections.

New Methodology

The CFD method has been applied to simulate the temperatures and velocities inside the hearth, but the hearth inner profile must be given before CFD calculation [6]. In reality, the hot-face temperatures vary at different locations due to skull and erosion. It is almost impossible to make measurements of these temperatures. However, the 3D CFD model, which predicts the distributions of hot metal velocity and temperature inside the hearth, the skull, and the refractory, can provide detailed hot-face temperatures at every location. From the CFD results, the heat transfer in the refractory was confirmed one dimensional [6]. Based on the 1D heat transfer model, the thermocouple data, and the 3D CFD model, the hearth erosion and inner profiles can be estimated in the following iterative procedure. Basically, this whole methodology contains inverse heat transfer calculation and CFD simulation, which is illustrated as follows:

1. Using the 3D CFD model, simulate a base case which has the original hearth geometry without skull
2. Using the thermocouple data and the 1D heat transfer model, estimate the inner profile with the hot-face temperatures from the base case in step 1
3. Using the 3D CFD model, compute the hot metal flow field and all the temperature distributions based on the estimated inner profile
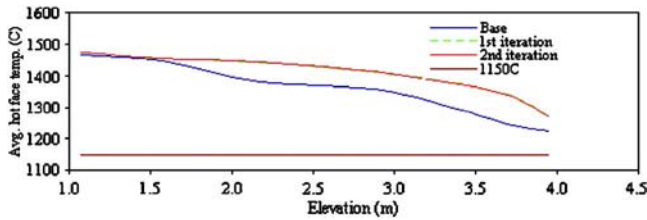
Fig. 1 Average hot face temperatures

4. Obtain the hot-face temperatures from step 2 and reestimate the inner profile from the thermocouple data and the 1D heat transfer model
5. Repeat steps 2 and 3 until the hot-face temperature is converged
6. Using the 1D fine tuning model, adjust the inner profile until all the calculated temperatures match with those measured with a required accuracy

When the CFD errors are less than criteria, the iterations are stopped. At that time, the hot-face temperatures are converged and the inner profile is finalized. It should be pointed out that the experimental temperature data are essential requirements for the whole methodology being applicable because the methodology involves inverse heat transfer calculation, and temperatures are the input for this methodology. In reality, all the blast furnaces have the thermocouples placed inner the refractory for monitoring the hearth situation.

3D CFD Model and 1D Heat Transfer Model

The 3D CFD software numerically solves the governing equations of the flow properties on a computational grid with specified boundary and initial conditions. The hearth is considered to be at steady state. The equations of mass, momentum, enthalpy, and
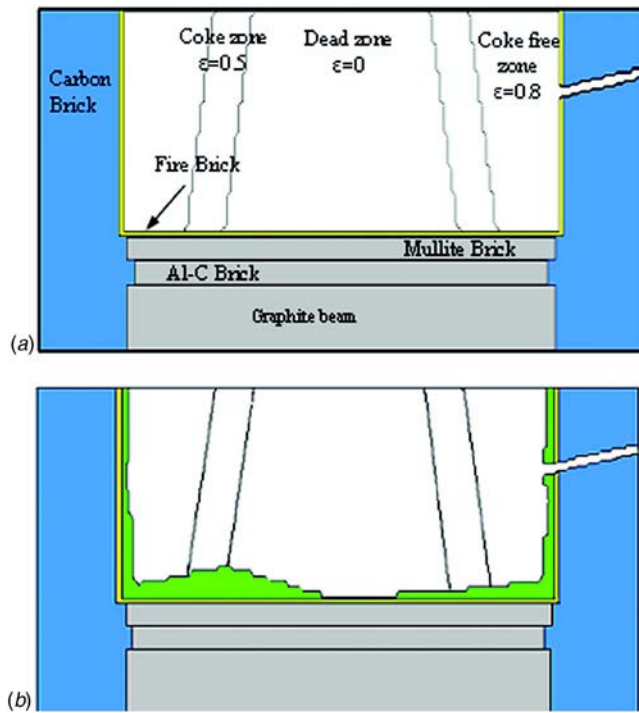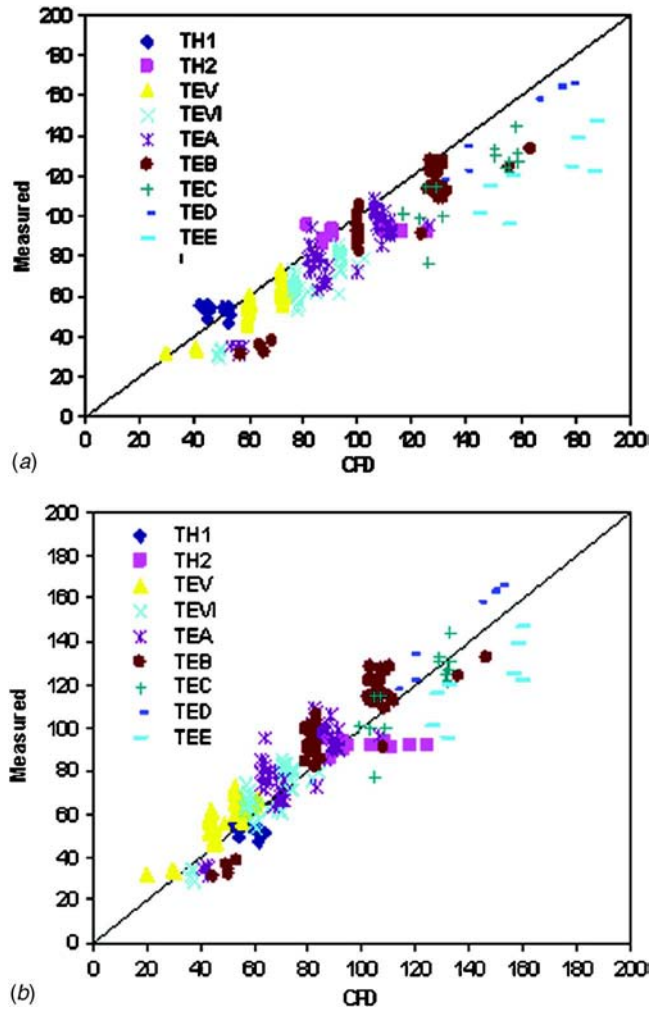

Fig. 3 Comparison of measured and calculated temperatures in the refractory of hearth: (a) base case without erosion and skull buildup and (b) final case with finalized inner profile

species are all elliptic-type partial differential equations. For convenience in numerical formulation, these equations are arranged in a common form,

$$\sum_{i=1}^{3} \frac{\partial}{\partial x_i}\left(\rho u_i \xi - \Gamma_\xi \frac{\partial \xi}{\partial x_i}\right) = S_\xi \tag{1}$$

More details on the governing equations used in the CFD model can be found in [6]. The general equations for the 1D transfer model and the 1D fine tuning model are listed below, the details of which can be found in [7].

Results and Discussion

The new methodology has been used to simulate an actual-scale blast furnace at Mittal Steel. The hearth is divided into three zones: the dead zone, coke zone, and coke-free zone having the porosities of 0.0, 0.5, and 0.8, respectively. Case 1 is the base case without skull and erosion inside the hearth. Case 2 represents the case with estimated skull and erosion after fine tunings.

Figure 1 illustrates the average hot-face temperature as a function of height. After each iteration, the results show that the average hot-face temperature decreases as the height increases, which is defined as the distance from the top to the bottom of the hearth. This is because when the hot metal flows to the bottom, more energy is being lost through the sidewalls, which leads to the

Fig. 2 Inner profiles in a side view along the taphole: (a) case 1—base geometry and (b) case 2—inner profile after fine tunings

temperature decrease. The results indicate that it is important to consider the nonuniform distributions of the hot-face temperatures. Furthermore, because the skull has good thermal resistance and it is difficult to melt, the temperatures on the hot face are much higher than 1150°C in most of the region.

The inner profiles of different cases are shown in Figs. 2(*a*) and 2(*b*), respectively, in which there is skull formation on both the sidewalls and bottom walls of the hearth after fine tunings. The results detailed in this paper are only for the first month of operation of the blast furnace. The focus here was to show the application of the methodology for a given set of data, which can be extended to other sets of data. In the first month of blast furnace campaign, there is only skull buildup, and no erosion happens.

Figure 3 gives the comparisons of prediction temperatures and measured temperatures by thermocouples. The *X* value of the point represents the CFD predicted results, and the *Y* value represents the measurement temperature. It can be seen that the predicted temperatures of the final case are more accurate. For the base case, the skull is not taken into account; thus, the prediction temperatures are higher than the reality.

Summary

1. A new methodology and algorithm have been developed in this research, which integrates the 1D heat transfer model with the 3D CFD model to predict the hearth erosion and inner profiles. This methodology is being used to estimate the erosion and inner profile for the hearth of IH7 Blast Furnace of Mittal Steel for different time periods.
2. 3D CFD computed results show that the hot-face temperature is not uniform. The temperature of the hot face, i.e., the inner surface of hearth, is position dependent. The 1150°C isothermal line is not the temperature at the inner surface of a hearth.
3. The predicted results are in good agreement with the measurement within the refractory, except near the corner and taphole region, because heat transfer in these areas is not one-dimensional.

Acknowledgment

References

[1] Shibata, K., Kimura, Y., Shimizu, M., and Inaba, S., 1990, "Dynamics of Dead-Man Coke and Hot Metal Flow in a Blast Furnace Hearth," ISIJ Int., **30**(3), pp. 208–215.
[2] Torrkulla, J., and Saxen, H., 1999, "Model for Estimation of Blast Furnace Hearth Conditions," *Ironmaking Conference Proceedings*, Vol. 58, pp. 649–655.
[3] Torrkulla, J., and Saxen, H., 2000, "Model of the State of the Blast Furnace Hearth," ISIJ Int., **40**(5), pp. 438–447.
[4] Torrkulla, J., Brannbacks, J., and Saxen, H., 2002, "Indicators of the Internal State of the Blast Furnace Hearth," ISIJ Int., **42**(5), pp. 504–511.
[5] Takatani, K., Inada, T., and Takata, K., 2001, "Mathematical Model for Transient Erosion Process of Blast Furnace Hearth," ISIJ Int., **41**(10), pp. 1139–1145.
[6] Yan, F., Zhou, C. Q., Huang, D., Chaubal, P., and Zhao, A., 2005, "3-D Computational Modeling of a Blast Furnace Hearth," Iron and Steel Technology, **2**(1), pp. 48–58.
[7] Zhang, Y., Deshpande, R., Huang, D., Chaubal, P., and Zhou, C. Q., 2006, "A Methodology for Blast Furnace Hearth Wear Analysis," ASME Paper No. IMECE2006-15144.

Flow and Heat Transfer Characteristics in Rectangular Channels With Staggered Transverse Ribs on Two Opposite Walls

Rong Fung Huang[1]
Department of Mechanical Engineering,
National Taiwan University of Science and Technology,
43 Keelung Road,
Section 4,
106 Taipei, Taiwan, ROC
e-mail: rfhuang@mail.ntust.edu.tw

Shyy Woei Chang
Department of Marine Engineering,
National Kaohsiung Marine University,
142 Hai-Chuan Road,
Nan-Tzu District,
811 Kaohsiung, Taiwan, ROC

Kun-Hung Chen
Department of Mechanical Engineering,
National Taiwan University of Science and Technology,
43 Keelung Road,
Section 4,
106 Taipei, Taiwan, ROC

The flow characteristics and the heat transfer properties of the rectangular channels with staggered transverse ribs on two opposite walls are experimentally studied. The rib height to channel height ratio ranges from 0.15 to 0.61 (rib height to channel hydraulic diameter ratio from 0.09 to 0.38). The pitch to rib height ratio covers from 2.5 to 26. The aspect ratio of the rectangular channel is 4. The flow characteristics are studied in a water channel, while the heat transfer experiments are performed in a wind tunnel. Particle image velocimetry (PIV) is employed to obtain the quantitative flow field characteristics. Fine-wire thermocouples imbedded near the inner surface of the bottom channel wall are used to measure the temperature distributions of the wall and to calculate the local and average Nusselt numbers. Using the PIV measured streamline patterns, various characteristic flow modes, thru flow, oscillating flow, and cell flow, are identified in different regimes of the domain of the rib height to channel height ratio and pitch to rib height ratio. The vorticity, turbulence intensity, and wall shear stress of the cell flow are found to be particularly larger than those of other characteristic flow modes. The measured local and average Nusselt numbers of the cell flow are also particularly higher than those of other characteristic flow modes. The distinctive flow properties are responsible for the drastic increase of the heat transfer due to the enhancement of the momentum, heat, and mass exchanges within the flow field induced by the large values of the vorticity and turbulence intensity. Although the thru flow mode is conventionally used in the ribbed channel for industrial application, the cell flow could become the choice if the heat transfer rate, instead of the pressure loss, is the primary concern. [DOI: 10.1115/1.2768101]

1 Introduction

In many engineering applications requiring augmentation of heat transfer capability, the repeated ribs were usually installed on the heat transfer surfaces to promote turbulence and to enhance convective heat transfer. Investigations on the heat transfer and friction characteristics in rib-roughened channels with rib height to hydraulic diameter ratio from 0.06 to 0.15, rib pitch to height ratio from 8 to 40, and channel aspect ratio from 0.25 to 4 were widely studied [1–7]. The rib height to channel height ratio lower than 0.1 was recommended [8] for consideration of less pumping power consumption.

In practical use, e.g., cooling of small turbine blade, the rib height to channel hydraulic diameter ratios may cover the range up to 0.25 or even larger [2,3]. The flow and its associated heat transfer characteristics at h/D_{hyd} were less studied, previously. This paper conducted experimental studies for wide h/D_{hyd} from 0.09 to 0.38 (h/B from 0.15 to 0.61). Flow velocity measurement was performed in a water channel. A heat transfer experiment was conducted in a wind tunnel with a heated test section. The reason why the flow experiment was not conducted in the heated wind tunnel was because seeing through the thermal insulators was technically difficult. The molecular diffusions of the individual experimental results obtained from the water channel and the wind tunnel tests could not be analogous to each other because the Prandtl number of water at standard situation is ~6.6, which is much larger than that (~0.7) of air at temperature between 20°C and 100°C. However, according to similarity theory [9], by setting the Reynolds numbers for the flow and heat transfer experiments at the same values in the turbulent range, cross reference of the flow patterns in both cases could become possible.

2 Experimental Apparatus and Procedures

2.1 Heat Transfer Experiments. The heat transfer experiments were conducted in an open-circuit, suction-type wind tunnel, including the flow conditioner, nozzle, test section, and diffuser. The test section, as shown in Fig. 1, was made of aluminum alloy 6061 T6 (thermal conductivity=154 W/m °C). The upper and lower plates with the transverse ribs were fabricated from an aluminum alloy block by using a milling machine so that no contact thermal resistance existed between the ribs and the plates. The geometric parameters used in the experiments were listed in Table 1. The range of Reynolds numbers based on the hydraulic diameter Re_{hyd} was varied from 4000 to 20,000. The coordinate system (x,y,z) was originated at upstream root of the first rib on the bottom channel wall.

Thirty-seven type-T thermocouples (wire diameter=125 μm) were inserted into the small holes that were drilled along the symmetry line of the bottom aluminum alloy plate of the test section to measure the wall temperature distributions. The measurement points were 0.7 mm from the inner surface of the test section. The small holes with the thermocouple imbedded were filled with grease of high thermal conductivity (10 W/m °C). Two electrically heated plate heaters were tightly clamped to the outer surfaces of the upper and bottom plates of the test section. The heat fluxes $\dot{q}''$ used in this study were 700, 1100, and 1560 W/m^2. The heaters and side plates of the test section were enclosed by thick thermal insulators with thermal conductivity of <0.2 W/m °C. Temperature data were scanned by using a Keithley data logger with a sampling rate of 5 Hz. For each channel, 500 steady-state data were employed to calculate the average values. The bulk mean temperatures of the airflow was calculated by using the air temperatures measured at the inlet and outlet of the test section. The temperature of environment was controlled at 20±1°C. In
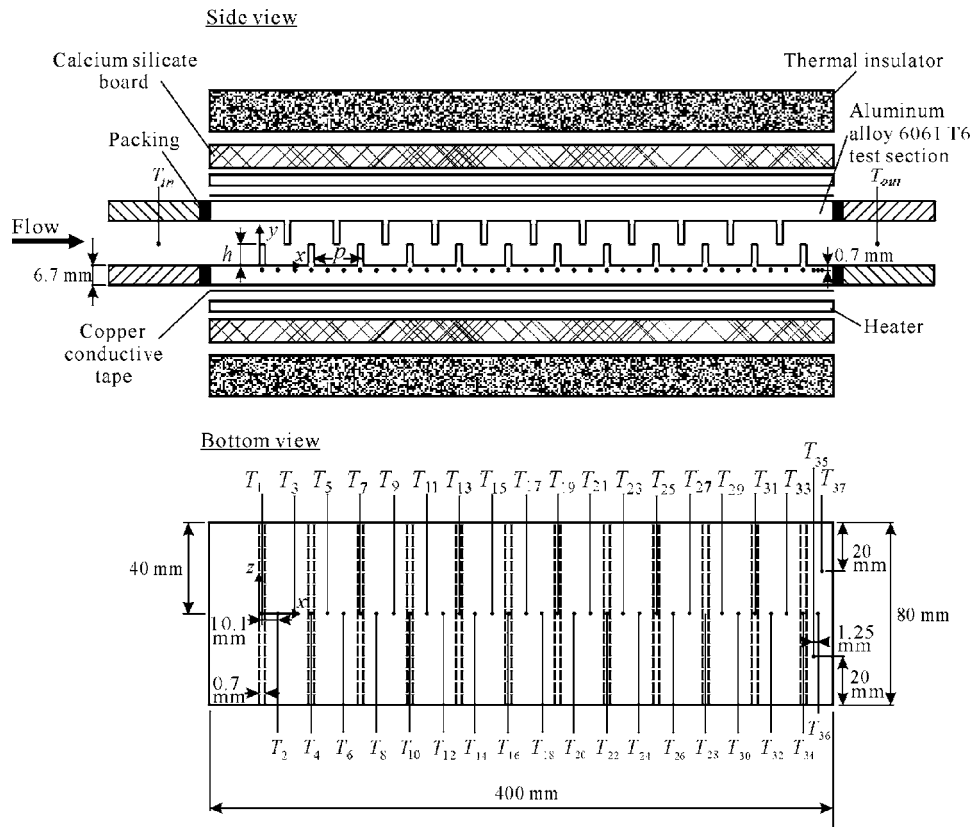
Fig. 1 Test section configuration of wind tunnel for thermal measurements. Side view shows test section, heaters, and insulators. Bottom view of test section shows attachment locations of type-T thermal couples.

order to calculate the friction factor, the pressure drops between inlet and outlet of the test section were measured by a calibrated electronic pressure transducer.

2.2 Particle Image Velocimetry (PIV) Velocity Field Measurements. The flow field measurements were performed in a closed-loop water channel with a test section made of plates of transparent Plexiglas®. The water temperature was maintained at $25 \pm 1\,^{\circ}\text{C}$. The geometric parameters in the flow experiments were

listed in Table 1. The values of dimensionless parameters, w/B, h/B, h/D_{hyd}, and p/h, and the Reynolds numbers were all the same as those used in the heat transfer experiments. The measurements were performed in the symmetry plane, i.e., the plane of $z=0$. A PIV system, which consisted of a 10 W solid-state laser (wave length=795 nm), a high-speed complementary metal-oxide semiconductor (CMOS) camera, an electronic synchronizer, and a cross-correlation software, was used to measure the velocity prop-

Table 1 Geometric parameters used in experiments of wind tunnel and water channel

Geometric parameter	Heat transfer experiment in wind tunnel	Flow experiment in water channel
B (mm) Height of test channel	20	33
w (mm) Width of test channel	80	132
w/B Aspect ratio	4	4
D_{hyd} (mm) Hydraulic diameter	32	52.8
h (mm) Rib height	3.0, 4.2, 6.1, 12.1	5, 7, 10, 20
p (mm) Rib pitch	30.3	50, 80, 100, 130
h/B Rib height to channel height ratio	0.15, 0.21, 0.30, 0.61	0.15, 0.21, 0.30, 0.61
h/D_{hyd} Rib height to hydraulic diameter ratio	0.09, 0.13, 0.19, 0.38	0.09, 0.13, 0.19, 0.38
p/h Rib pitch to rib height ratio	2.5, 5.0, 7.1, 10.0	2.5–26

erties. The light-sensing array of 512×512 pixels was zoomed and mapped to a physical region of $100-200$ mm so that the spatial resolution was about $195-390$ μm/pixel. The time separation used between two consecutive images was varied from 333 μs to 3333 μs. Two consecutive image frames were analyzed by using the cross-correlation software. Plastic particles made of polyamide (PA) with diameter of 50 ± 20 μm and specific weight of 1.03 were seeded into the water tank to scatter the laser light.

2.3 Uncertainty Estimate. The uncertainty estimates for each variable in the graphs were based on the method of Abernethy et al. [10]. The uncertainty of temperature measurement was within $\pm 0.5\,^{\circ}$C. The uncertainties of the velocity and velocity fluctuation measurements were estimated to be about $\pm 2.15\%$ and $\pm 3.21\%$ of local values, respectively. The uncertainties in the evaluation of the Nusselt number enhancement ratio and of the friction factor were respectively estimated to be about $\pm 5\%$ and $\pm 4\%$.

3 Results and Discussion

3.1 Flow Patterns and Characteristic Flow Modes. In this paper, all averaged or turbulence data are processed over 8000 sets of instantaneous measurements. The period for average may last for $2.7-26.7$ s, which depends on the Reynolds number. Figure 2 shows four typical velocity vector maps and streamline patterns at $\mathrm{Re}_{\mathrm{hyd}} = 14,000$. In Fig. 2(a), separation bubble is formed behind each rib. The axial lengths of the recirculation bubbles never exceed $0.5p$. The mainstream seems to go through the center core of the channel without significant deflection. This type of flow is therefore denoted as *thru flow I*. In Fig. 2(b), behind the second and the following downstream ribs, the recirculation bubble occupies the whole groove between the consecutive ribs and, therefore, no reattach point exists on the channel walls. The mainstream behaves similar to that of thru flow I so that it is denoted as *thru flow II*. Most of the previous studies found in the literature [1–8] were focused on the range of $h/B < 0.4$ (i.e., $h/D_{\mathrm{hyd}} < 0.25$), which corresponds to the thru-flow mode.

In Fig. 2(c), the recirculation bubbles with reattach points on the channel walls are observed between two consecutive ribs. Since the values of h/B are large, the mainstream in the core region of the channel is deflected drastically up and down when it passes the ribs. This type of flow is therefore denoted as *deflected flow*. In Figs. 2(c) and 2(d), recirculation bubbles are formed downstream of the ribs and occupy almost the entire cavity between the bottom-wall rib and the neighboring upper-wall rib. It is denoted as *cell flow* because the neighboring upper and lower ribs seem to form a "cell" to constrain the recirculation bubble.

The above-discussed characteristic flow modes can be found in different regimes of Fig. 3. The characteristic regimes and border bands of short slashed lines shown in Fig. 3 do not change appreciably with the Reynolds number in the range of this study.

3.2 Turbulence Intensity, Circulation, and Vorticity. In Figs. 4(a) and 4(b), the turbulence intensities I_u and I_v along the separation lines downstream of the second rib of the bottom channel wall of the cell flow can attain much higher values than those of the thru flow and deflected flow. In Figs. 4(c) and 4(d), the turbulence intensities near the wall along $y/B = 0.04$ of the cell flow are also particularly larger than the other flow modes. Actually, although not shown here, the turbulence intensities in the whole flow field of the cell flow present much higher fluctuations than the other flow modes. The circulations and vorticities about the contours surrounding the recirculation bubbles behind the second ribs of Figs. 2(a)–2(d) can be evaluated according to [11]. The results are listed in Table 2. Both the circulations and vorticities associated with the recirculation bubbles appearing in the cell flow are several times higher than those of other characteristic flow modes.

3.3 Heat Transfer Properties. Figures 5(a) and 5(b) show the distributions of normalized local Nusselt number along the
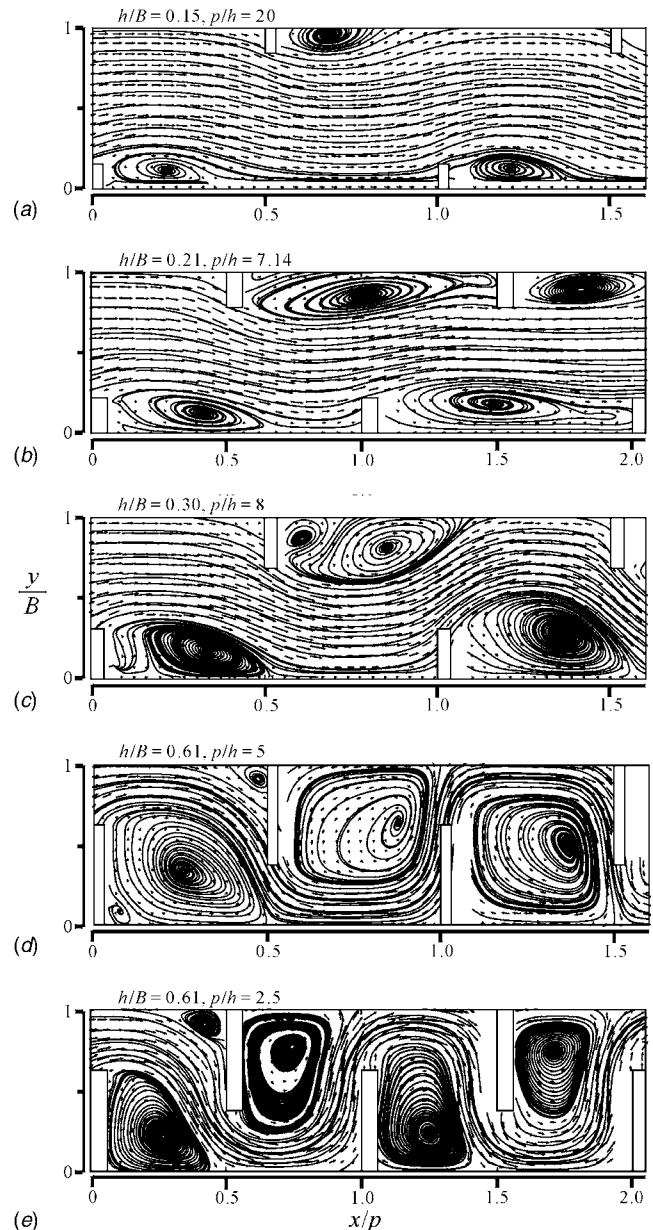

Fig. 2 Typical velocity vectors and streamline patterns measured by PIV in symmetry plane at $\mathrm{Re}_{\mathrm{hyd}} = 14,000$: (a) thru flow I, (b) thru flow II, (c) deflected flow, (d) and (e) cell flow

bottom wall at $\mathrm{Re}_{\mathrm{hyd}} = 4000$ and 8000, respectively. The data for the local Nusselt numbers Nu_o were measured with a nonribbed, smooth channel. The results show a difference by, at most, 12% from those calculated by using the Dittus–Boelter equation obtained in a smooth circular tube [2]. The three-dimensional effect induced by the low aspect ratio of the present rectangular channel may cause this difference. The local Nusselt number of the cell flow is apparently larger than those of other characteristic flow modes, particularly in the fore half of the test channel. Figure 5(c) shows the normalized channel-length-averaged Nusselt numbers at different flow modes. Present results of $\mathrm{Nu}/\mathrm{Nu}_o$ in the thru-flow regime have comparable values to the previous results [3,12,13], which are also in the regime of thru flow. $\mathrm{Nu}/\mathrm{Nu}_o$ of cell flow, however, is augmented by at least 2.5–3.5 times when compared to those of thru flow. Although no data for the cell flow at the Reynolds number larger than 8000 is shown in Fig. 5(c)
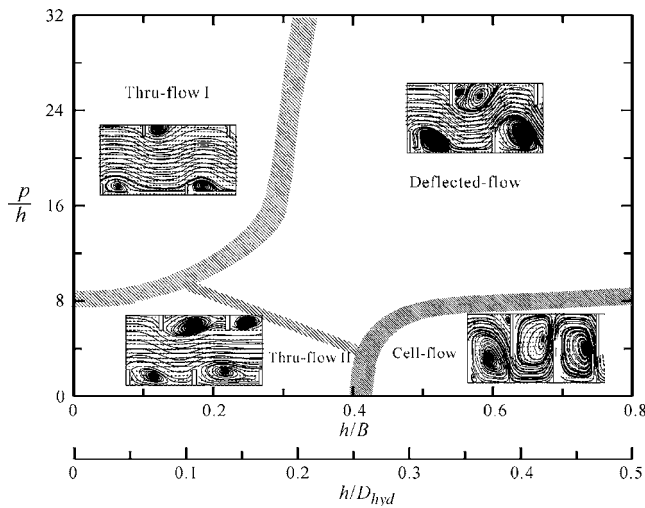
Fig. 3 Characteristic flow regimes on the domain of h/B and p/h

because the blower used for this study cannot overcome the pressure drop in this range, it is reasonably expected that $\overline{Nu}/\overline{Nu}_o$ of cell flow would attain a value of at least 11 at high Reynolds numbers.

The dramatically large values of the Nusselt number obtained in the regime of cell flow, as shown in Figs. 5(a)–5(c), are corre-
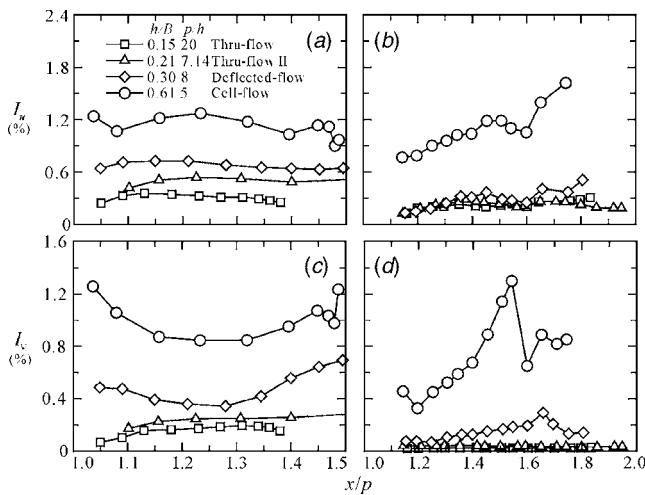

Fig. 4 Turbulence intensities measured by PIV in symmetry plane at $Re_{hyd}=14{,}000$: (a) and (b) distribution along separation line evolving from tip of second rib on bottom wall of channel, and (c) and (d) axial distributions near bottom wall at $y/B =0.04$

Table 2 Circulation and vorticity of recirculation bubble behind second rib, $Re_{hyd}=14{,}000$

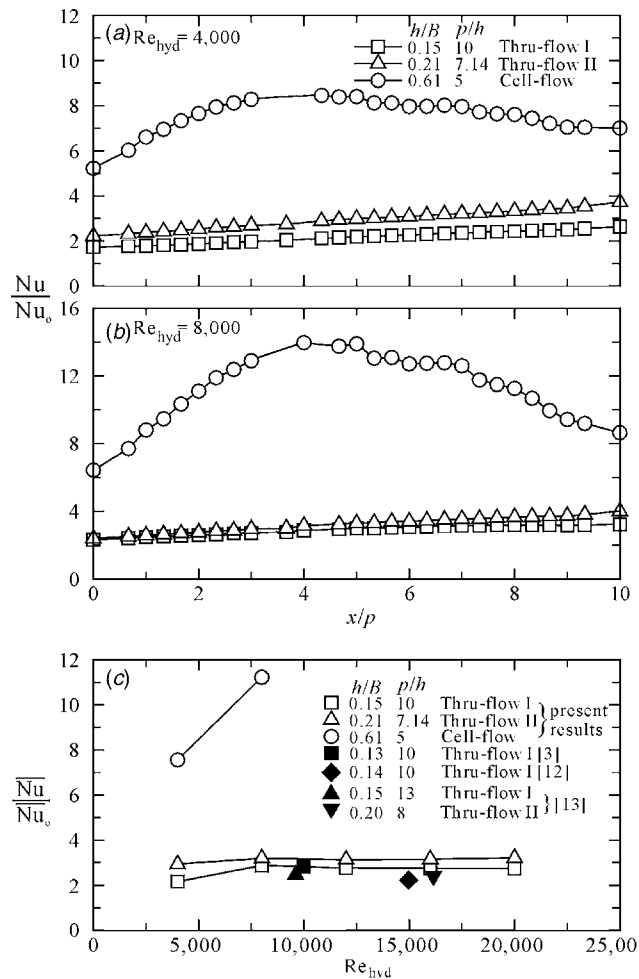|	Circulation (m²/s)	Vorticity (1/s)
Thru flow I Fig. 2(a)	0.004	35
Thru flow II Fig. 2(b)	0.010	40
Deflected flow Fig. 2(c)	0.015	33
Cell flow Fig. 2(d)	0.070	72

Fig. 5 Heat transfer characteristics: (a) and (b) axial distributions of normalized Nusselt numbers, heat flux 1100 W/m², (c) variations of normalized area-averaged Nusselt numbers with Reynolds number, and (d) correlation of area-averaged Nusselt number

sponding to the prominent increases of the turbulence intensity, circulation, and vorticity shown in Figs. 3 and 4. From the point of view of the diffusion theory of the turbulent boundary layer [14], the induced high turbulence near the wall of the cell flow would be of great assistance to the transport of physical quantities from the wall to the boundary layer. Physically, the vorticity is a quantitative estimate of the rotation rate, while the circulation can be interpreted as an index for the capability of diffusion of physical quantities [15]. Higher circulation and vorticity imply a shorter residence time and larger diffusivity for the physical quantities in the recirculation bubble. Large turbulent fluctuations existing in the recirculation bubble, shear layer, and core flow of the cell flow would further be beneficial to the transport of physical quantities from the boundary layer through the recirculation bubble to the mainstream. It is therefore argued that the flow properties induced by the featured flow pattern of the cell flow must have significant contributions to the drastic enhancement of heat transfer.

3.4 Friction Factor and Thermal Performance. In Fig. 6(a), the normalized Darcy friction factors f/f_o [4] of the thru flow are much smaller than those of the cell flow. The pumping loss of the cell flow would hence be much larger than that of the thru flow. The *thermal performance* η [4] is usually used to evaluate the heat transfer performance based on the same pumping power. Figure 6(b) shows the calculated results according to the
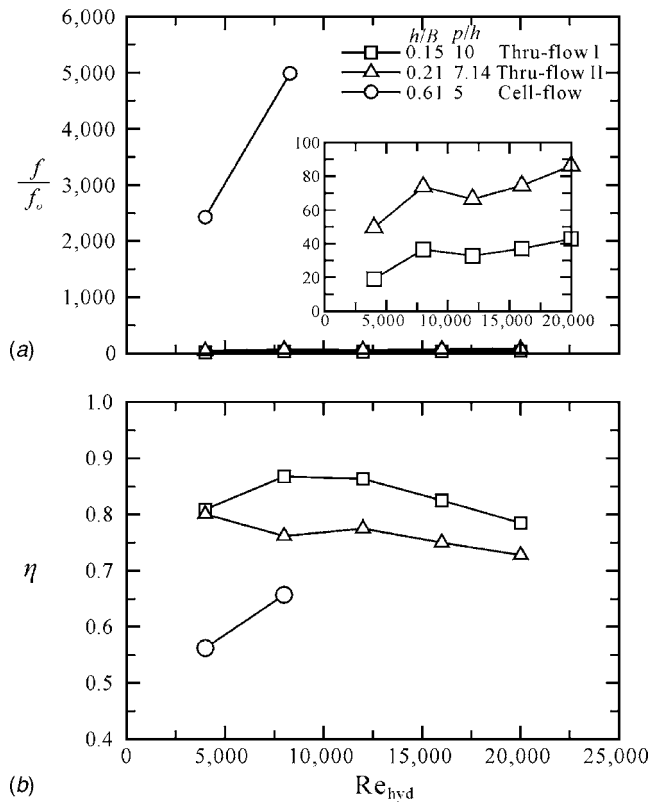
Fig. 6 (*a*) **friction factor and** (*b*) **thermal performance**

definition listed in the Nomenclature. The *thermal performances* of the cell flow are lower than those of the thru flow. Therefore, in the applications when the cell flow is chosen for consideration of its drastic augmentation in heat transfer rate, the lower values of *thermal performance* must be noted for the accompanied large pressure loss.

4 Conclusions

Flow characteristics and heat transfer properties of the ribbed rectangular channel are experimentally studied for extensive rib height to channel height ratios. Typical flow patterns—thru flow, deflected flow, and cell flow—are identified. At large rib height to channel height ratios ($h/B > 0.4$ or $h/D_{hyd} > 0.25$) and small rib pitch to rib height ratios ($p/h < 8$) (which is in the regime of cell flow), the turbulence intensity, circulation, vorticity, and friction factor all present drastically larger values than those in the regime of thru flow. The Nusselt number is also dramatically augmented by several times due to the increase of turbulent transport of physical quantities. However, because the expense of pumping loss overwhelms the increase of heat transfer performance, the thermal performance of the cell flow presents lower values than those of the thru flow by a large factor. It is recommended that the cell flow be applied only in the case when augmentation of the heat transfer rate is a primary consideration and the pumping expense is not a concern.

Nomenclature

B = height of rectangular channel, mm
D_{hyd} = hydraulic diameter of channel, $2wB/(w+B)$, mm
f = Darcy friction factor of ribbed channel, $\Delta P(D_{hyd}/L)/(0.5\rho U_o^2)$
f_o = Darcy friction factor of nonribbed channel
h = rib height, mm
I_u = axial turbulence intensity, u'/U_o
I_v = transverse turbulence intensity, v'/U_o
k = thermal conductivity of air, W m^{-1} °C^{-1}
L = channel length, 400 mm
Nu = local Nusselt number, $\dot{q}''D_{hyd}/k(T_w-T_b)$
$\underline{Nu_o}$ = local Nusselt number of unribbed channel
$\overline{Nu}$ = average Nusselt number over channel length
$\overline{Nu_o}$ = average Nusselt number over channel length of unribbed channel
p = rib pitch, mm
$\dot{q}''$ = heat flux, W/m^2
Re_{hyd} = Reynolds number, $U_o D_{hyd}/\nu$
T_b = linearly interpolated local bulk air temperature between T_{in} and T_{out} in the axial direction, °C
T_{in} = inlet air temperature, °C
T_{out} = outlet air temperature, °C
T_w = wall temperature, °C
U_o = average flow velocity at inlet of channel, m s^{-1}
u' = root mean square of fluctuating velocity in the x direction, m s^{-1}
v' = root mean square of fluctuating velocity in the y direction, m s^{-1}
w = channel width, mm
x = axial coordinate
y = transverse coordinate
z = lateral coordinate
η = thermal performance, $(\overline{Nu}/\overline{Nu_o})/(f/f_o)^{1/3}$
ρ = air density, kg$_m$ m^{-3}
ν = kinematic viscosity of working fluid, m^2 s^{-1}
ΔP = pressure difference between inlet and outlet of test channel, kg$_m$ m^{-1} s^{-2}

References

[1] Han, J. C., 1984, "Heat Transfer and Friction in Channels With Two Opposite Rib-Roughened Walls," ASME J. Heat Transfer, **106**, pp. 774–781.
[2] Han, J. C., and Park, J. S., 1988, "Developing Heat Transfer in Rectangular Channels With Rib Turbulators," Int. J. Heat Mass Transfer, **31**, pp. 183–195.
[3] Park, J. S., Han, J. C., Huang, Y., and Ou, S., 1992, "Heat Transfer Performance Comparisons of Five Different Rectangular Channels With Parallel Angled Ribs," Int. J. Heat Mass Transfer, **35**, pp. 2891–2903.
[4] Han, J. C., Park, J. S., and Lei, C. K., 1985, "Heat Transfer Enhancement in Channels With Turbulence Promoters," ASME J. Eng. Gas Turbines Power, **107**, pp. 628–635.
[5] Taslim, M. E., and Wadsworth, C. M., 1997, "An Experimental Investigation of the Rib Surface-Averaged Heat Transfer Coefficient in a Rib-Roughened Square Passage," ASME J. Turbomach., **119**, pp. 381–389.
[6] Yuan, Z. X., 2000, "Numerical Study of Periodically Turbulent Flow and Heat Transfer in a Channel With Transverse Fin Arrays," Int. J. Numer. Methods Heat Fluid Flow, **10**, pp. 842–861.
[7] Valencia, A., and Sen, M., 2003, "Unsteady Flow and Heat Transfer in Plane Channels With Spatially Periodic Vortex Generators," Int. J. Heat Mass Transfer, **46**, pp. 3189–3199.
[8] Webb, R., 1994, *Principles of Enhanced Heat Transfer*, Wiley, New York.
[9] Shames, I. H., 1992, *Mechanics of Fluids*, 3rd ed., McGraw-Hill, New York.
[10] Abernethy, R. B., Benedict, R. P., and Doedell, R. B., 1985, "ASME Measurement Uncertainty," ASME J. Fluids Eng., **107**, pp. 161–164.
[11] Yuan, S. W., 1967, *Foundations of Fluid Mechanics*, Prentice-Hall, Englewood Cliffs, NJ.
[12] Taslim, M. E., Li, T., and Kercher, D. M., 1996, "Experimental Heat Transfer and Friction in Channels Roughened With Angled, V-Shaped, and Discrete Ribs on Two Opposite Walls," ASME J. Turbomach., **118**, pp. 20–28.
[13] Tanda, G., 2004, "Heat Transfer in Rectangular Channels With Transverse and V-Shaped Broken Ribs," Int. J. Heat Mass Transfer, **47**, pp. 229–243.
[14] Tennekes, H., and Lumley, J. L., 1972, *A First Course in Turbulence*, MIT Press, Cambridge, MA.
[15] Tritton, D. J., 1988, *Physical Fluid Dynamics*, Oxford University Press, London.

A Coupled Map Lattice Model of Flow Boiling in a Horizontal Tube

P. S. Ghoshdastidar[1]
Mem. ASME
e-mail: psg@iitk.ac.in

Indrajit Chakraborty
e-mail: indrac@iitk.ac.in

Department of Mechanical Engineering,
Indian Institute of Technology Kanpur,
Kanpur, U.P. 208016, India

In this work laminar, stratified flow boiling of water is simulated qualitatively by the coupled map lattice (CML) method. The liquid is entering a constant wall temperature horizontal tube ($T_w > T_{\text{sat}}$ at p_{entrance}) in a subcooled condition. A CML is a dynamical system with discrete-time, discrete-space, and continuous states. The procedure basically consists of the following steps: (i) Choose a set of macroscopic variables on a lattice; (ii) decompose the problem into independent components, such as convection, diffusion, phase change, and so on; (iii) replace each component by a simple parallel dynamics on a lattice; and (iv) carry out each unit dynamics successively in each time step until some termination criterion is satisfied. In the present problem, the termination criterion is the laminar-turbulent transition, and hence, the results do not correspond to the steady state. The present modeling by CML is based on the assumption that the flow boiling is governed by (i) nucleation from cavities on the heated surface and migration of vapor into the core, (ii) forced convection, and (iii) phase change in the fluid bulk and mixing. The stirring action of the bubbles is modeled by increasing the fluid momentum and thermal diffusivities by an enhancement factor. The results show that the CML has been able to model flow boiling in a realistic manner. [DOI: 10.1115/1.2768102]

Keywords: flow boiling, coupled map lattice, CML, horizontal tube, stratified flow

1 Introduction

1.1 What is CML? A CML [1] is a dynamical system with discrete-time, discrete-space, and continuous states. It usually consists of dynamical elements on a lattice which interact (are "coupled") with suitably chosen sets of other elements. The strategy of modeling dynamical phenomena in spatially extended systems by a CML model is based on the following steps:

Step 1. Choose a (set of) macroscopic variable(s) on a lattice. A lattice is like a grid or a control volume.

Step 2. Decompose the processes underlying the phenomena into independent component (or "elements," not to be confused with finite elements), such as convection, diffusion, phase change, and so on. Each element is considered as a map.

Step 3. Replace each component (or element) by a simple parallel dynamics on a lattice. The "dynamics" in this case implies that the problem is to be solved as a transient phenomenon to start

with. Thus, each map that is coupled with each other by an algebraic equation changes with time.

Step 4. Carry out each unit dynamics (or procedure) successively in each time step until steady state is reached, that is, when the macroscopic variable does not change with time in the computational domain. In the present problem, however, the results are shown only at time just before laminar-turbulent transition since only laminar flow boiling is simulated.

It may be noted that CFD (computational fluid dynamics) techniques can be used to solve a particular phenomenon, such as convection or diffusion in CML. Thus, CML is not entirely void of CFD. However, even in a two-phase flow, CFD is used to solve the problem of convection as if the flow is single phase, by incorporating void fraction weighted fluid property values ($P_{eq} = fP_v + (1-f)P_l$), where P is a particular property, such as k, ρ, c_p, v, α. The effect of phase change shows up in the phase-change map. The basic advantage of CML is that individual bubbles are not tracked, and yet the effects of bubbles in the flow are reflected qualitatively in the final solution.

1.2 Literature Review. Coupled map lattice (CML) has been recognized as a powerful tool of analysis to grasp the qualitative and fundamental nature of complex boiling phenomena and has been applied to many physical systems [2]. The CML method is based on a dynamic system with continuous field variables but discrete space and time, in which local dynamics propagates in space by diffusion or flow and time is advanced by repeated mapping. From the study of nonlinear chaos dynamics, it is known that a complex physical system, such as boiling, is not always governed by a complex system of equations. The relevant papers in nonlinear chaos dynamics in this regard are by [3–7]. However, applications to CML are not restricted to the problems in spatiotemporal chaos but include pattern formations, some solid-state problems, biological information processing, and engineering problems [1]. Using the CML method, Yanagita [8] simulated the pool boiling phenomenon and succeeded in explaining the mode of transition from nucleate to film boiling. Shoji [5] corrected the deficiencies of the model of Yanagita [8] by including nucleation sites on the heater surface and the Taylor instability. The model was applied to saturated and transient pool boiling of water on a small heated surface at 1 atm pressure. Ghoshdastidar et al. [9] modified the basic theoretical model proposed by Shoji [5] in terms of nucleation superheat distribution and mixing. The stirring action of the bubbles was modeled by increasing the fluid thermal diffusivity by an enhancement factor. Gupta and Ghoshdastidar [10] significantly improved the prediction of CHF for the atmospheric saturated pool boiling of water with respect to the 2D CML model of Ghoshdastidar et al. [9] by developing a 3D CML model in which the 3D thermal diffusion equation was solved and a 2D distribution of nucleating cavity sizes was assumed.

Thus far, no studies showing CML simulation of flow boiling have been found in the open literature. The present work is a first attempt in this direction. In this work, stratified flow boiling of water in a horizontal tube whose wall is maintained at constant temperature that is greater than the saturation temperature of the liquid at the entrance pressure is simulated by CML. The liquid is entering the tube in a subcooled condition.

1.3 Objectives. The objectives of this study are to obtain mean heat transfer coefficient, mean wall heat flux, mean fluid temperature, and void fraction as a function of axial coordinate at the time just before of the laminar-turbulent transition for water, and also to carry out a parametric study based on variation of wall temperature, level of entry subcooling, and axial pressure gradient.

2 Problem Formulation

2.1 Modeling. In the present study, the liquid is entering a constant wall temperature tube ($T_W > T_{\text{sat}}$) in a subcooled condi-
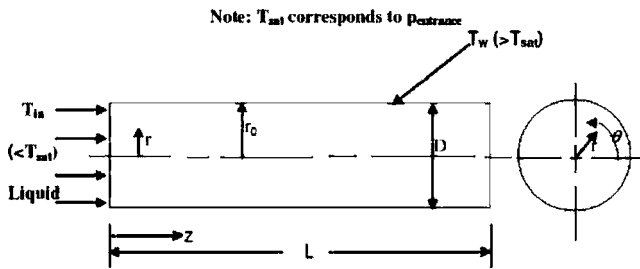
Fig. 1 Flow geometry and the computational domain

tion (Fig. 1). The modeling by CML is based on the assumption that the flow boiling is governed by (i) nucleation from cavities on the heated surface and migration of vapor into the core, (ii) forced convection, and (iii) phase change in the fluid bulk and mixing. The macroscopic variable chosen is temperature. In this work, flow boiling is investigated in horizontal tube of 0.02 m diam and 9 m in length. The temperature distribution in the tube wall is ignored because it has a very high thermal conductivity and small thickness. The three-dimensional boiling field is approximated, and modeling is based on CML. No prior assumption regarding the chaotic nature of the boiling phenomena needs to be made.

2.2 Computational Domain and Lattices. The computational domain in the $r-\theta$ plane is divided into 20×20 lattices as shown in Fig. 2. A grid-independence test has been conducted to arrive at the choice of the number of lattices. Each lattice can contain either liquid or vapor but not a liquid-vapor mixture. There are 20 grid points in the radial direction, 20 grid points in the angular direction, and 10 grid points in the axial direction. The dots in Fig. 2 represent grid points, and the broken lines indicate the faces of lattices. Each lattice contains one grid point at its center. A typical lattice is shown by the shaded region in Fig. 2. Grid points at the boundary are surrounded by half lattices, as shown in Fig. 2. Another representative "half lattice" is depicted also adjacent to the "central lattice" in the computational domain.

2.3 Field Variable. For simplicity, temperature is employed as the only one field variable. In addition, a flag function $F_{i,j,k}$ is used for the convenience of calculations to show the phase of each lattice. $F_{i,j,k}=0$ and 1 represent the lattice (i,j,k) in liquid and vapor phases, respectively.
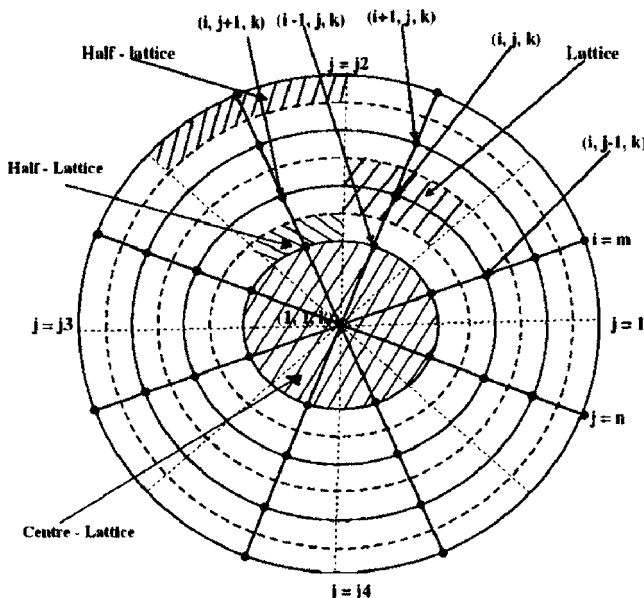

Fig. 2 Computational domain and lattices in (r, θ) planes

2.4 Formulation of Dynamic Processes. In the CML method, dynamic processes are usually formulated in mappings. In the present model, it is assumed that boiling is governed by the following physics and dynamics.

2.4.1 Modeling of Nucleation on the Heated Surface. According to Wang and Dhir [11], nucleation cavities are distributed at random on the heated surface. Many cavities are distributed on each surface lattice, but if it is assumed that every cavity has a conical shape, a larger cavity yields lower nucleation superheat. Therefore, only the cavity of maximum size (in this case, D_c as calculated from Eq. (2)) is employed, since the active cavity of each surface lattice, which determines the local nucleation superheat, ΔT_{act} (Eq. (1)), is required for bubble nucleation. The term βR is added to D_m to create randomness among the size of the large cavities. The nucleation superheat is given by

$$\Delta T_{act} = T_{act} - T_{sat} = \frac{4\sigma T_{sat}}{\rho_v h_{fg} D_c} \tag{1}$$

where D_c is the diameter of the largest nucleation cavity on a surface lattice. To calculate D_c, the following formula is used:

$$D_c(m,j,k) = D_m + \beta R \tag{2}$$

where $D_c (m,j,k)$ represents the diameter of the largest nucleating cavity on the lattice (m,j,k), D_m is the minimum diameter of nucleating cavities on a heater surface lattice β, which is assigned a value of 0.99, indicates the maximum deviation from D_m and has same unit as D_c and D_m, i.e., micrometer, and R is a random number between 0 and 1 assigned at the jth surface lattice. Although the number of grid points in the circumferential direction is taken as 20 in the present study, it may be varied. A total of 1020 random numbers is generated using a NAG (numerical algorithm group) library random number generator subroutine. Every fiftieth random number of the set is employed at each surface lattice starting from the first.

The minimum cavity diameter is arbitrarily taken as 1 μm. It is assumed that sites smaller than 1 μm do not exist on this particular heater surface. Thus, the maximum diameter of the nucleating cavities on a heater surface lattice becomes 1.99 μm as calculated from Eq. (2) when the random number takes on a value of 1. Thus, using Eqs. (1) and (2), the nucleation superheat distribution on the heated surface is calculated.

2.4.2 Modeling of Migration of Vapor. Two cases are considered, namely, when nucleation is not suppressed (case I) and when nucleation is suppressed (case II). Case I refers to subcooled and near-saturated nucleate boiling. Case II refers to convective boiling. In Case I ($T_{sat}-T_{mean}>0°C$), there are two subregimes: (i) when $T_{sat}-T_{mean}>15°C$ (subcooled nucleate boiling) and (ii) when $T_{sat}-T_{mean}<15°C$ (near-saturated nucleate boiling). In subregime (i), the vapor generated due to nucleation stays near the wall and the large portion of the core is still subcooled, and hence, i is set at 18 (i at the wall being 20), whereas in subregime (ii), the mean temperature is nearing saturation and more vapor has formed and smaller portion of the core is still subcooled, and hence, i is set at 10. Note that $i=1$ at the center. The choice of the value of 15 is arbitrary in this case. Basically, this value should not be high as when $T_{sat}-T_{mean}$ is less than this quantity, it indicates a near-saturation condition of the fluid. In case II, that is, some distance down the tube, mean temperature exceeds the saturation temperature and "boiling" is replaced by evaporation. The convective heat transfer coefficient increases with increasing void fraction, and bubble nucleation at the wall is suppressed. Since the flow is taking place in a horizontal tube, stratified flow boiling occurs since the axial velocity is not too great. Thus, under the influence of gravity, the liquid predominantly collects at the bottom of the tube, while the top of the tube is barely or not wet. In the present case, Froude number (Fr) is <0.04 [12] and hence, modeling based on stratified flow boiling is justified. This situa-

tion is shown in case II. $j3$ is grid point index at $\theta = 180$ deg (see Fig. 2). Basically, the modeling of case II shows that vapor formed at the bottom half of the tube wall does not migrate to the core while the upper half of the tube is nearly full of vapor, and hence, i is set at 2.

Case I: (Nucleation not Suppressed). If at a particular axial location (k)

$$T_{\text{sat}(k)} - T_{\text{mean}(k)} > 0 \quad \text{and if} \quad T_{\text{sat}} - T_{\text{mean}} > 15\,^\circ\text{C}$$

$$\text{and if} \quad T_{(m,j,k)} > T_{\text{act}(m,j,k)}, \quad \text{where} \quad j = 1-n$$

$$\text{and} \quad F_{(i,j,k)} = 0, \quad \text{where} \quad i = 1-m, \quad j = 1-n$$

$$\text{then} \quad F_{(i,j,k)} = 1, \quad \text{where} \quad i = 18, \quad j = 1-n \qquad (3)$$

If $T_{\text{sat}} - T_{\text{mean}} < 15\,^\circ\text{C}$, then $i = 10$ in Eq. (3).

Case II: (Suppression of Nucleation). If at a particular axial location (k)

$$T_{\text{sat}(k)} - T_{\text{mean}(k)} < 0, \quad \text{and if} \quad T_{(m,j,k)} > T_{\text{act}(m,j,k)} \quad \text{and if} \quad F_{(i,j,k)}$$

$$= 0, \quad \text{where} \quad i = 1-m, \quad j = 1-n$$

$$\text{then} \quad F_{(m,j,k)} = 1, \quad \text{where} \quad j = j3 + 1-n \qquad (4)$$

$$\text{and} \quad F(i,j,k) = 1, \quad \text{where} \quad j = 1-j3, \quad i = 2 \qquad (5)$$

2.4.3 Governing Equations. Assuming the flow to be laminar ($\text{Re} < 2000$) and locally fully developed ($v_r = 0$, $(\partial v_z / \partial z) = 0$ in each axial segment) and having no swirl ($v_\theta = 0$), the z-momentum equation takes the form

$$\rho \frac{\partial v_z}{\partial t} = -\frac{\partial p}{\partial z} + \mu \frac{1}{r}\frac{\partial}{\partial r}\left(r\frac{\partial v_z}{\partial r}\right) + \mu \frac{1}{r^2}\frac{\partial^2 v_z}{\partial \theta^2} \qquad (6)$$

Each axial segment of the tube is 1 m, and thus, the assumption of the locally fully developed nature of the flow is justified. Void fraction is assumed to be constant in each axial segment.

Actually, the mass conservation is already used in obtaining Eq. (6). In the present model, the flow is assumed to be incompressible based on the fact that it is a low-speed flow (Mach number is <0.3). Furthermore, although the actual flow is two phase, governing equations for single phase have been used by incorporating void fraction-weighted property values. However, the effect of change of density of the mixture due to generation of vapor is included in the momentum and energy equations applicable to each axial segment of the tube.

In Eq. (6), $\partial p / \partial z$ is assumed to be a known quantity with p decreasing linearly with z.

$$\text{At} \quad t = 0, \quad v_z = 0 \qquad (7)$$

$$\text{At} \quad r = 0, \quad v_z = \text{finite} \qquad (8)$$

$$\text{At} \quad r = r_0, \quad v_z = 0 \text{ (no slip)} \qquad (9)$$

In addition, the following periodic boundary conditions are valid.

$$\mu \frac{1}{r}\frac{\partial v_z}{\partial \theta}\bigg|_{r,\theta} = \mu \frac{1}{r}\frac{\partial v_z}{\partial \theta}\bigg|_{r,\theta+2\pi} \qquad (10)$$

$$(v_z)|_{r,\theta} = (v_z)|_{r,\theta+2\pi} \qquad (11)$$

The energy equation is

$$\rho c_p \frac{\partial T}{\partial t} + \rho c_p v_z \frac{\partial T}{\partial z} = k_f\left[\frac{1}{r}\frac{\partial}{\partial r}\left(r\frac{\partial T}{\partial r}\right)\right] + \frac{k_f}{r^2}\frac{\partial^2 T}{\partial \theta^2} \qquad (12)$$

$$\text{At} \quad t = 0, \quad T = T_{\text{sat}} - \Delta T_{\text{sub}} \qquad (13)$$

$$\text{At} \quad z = 0, \quad T = T_{\text{sat}} - \Delta T_{\text{sub}} \qquad (14)$$

$$\text{At} \quad r = 0, \quad T = \text{finite} \qquad (15)$$

$$\text{At} \quad r = r_0, \quad T = T_w \ (T_w > T_{\text{sat}}) \qquad (16)$$

Also, the following periodic boundary conditions apply:

$$-\frac{k_f}{r}\frac{\partial T}{\partial \theta}\bigg|_{r,\theta} = -\frac{k_f}{r}\frac{\partial T}{\partial \theta}\bigg|_{r,\theta+2\pi} \qquad (17)$$

$$T|_{r,\theta} = T|_{r,\theta+2\pi} \qquad (18)$$

The momentum and energy equations are solved by the explicit finite difference method. $\Delta z = 1$ m, $\Delta r = 5.26 \times 10^{-4}$ m, and $\Delta \theta = 18$ deg $= 0.35415$ rad. $\Delta t = 10^{-5}$ s is used to ensure stability.

2.4.4 Validation of Results. Since no experimental results are available for the transient laminar, stratified flow boiling in a horizontal tube, the present numerical solution has been validated with the analytical solutions for two limiting cases, such as (i) transient, laminar hydrodynamically fully developed flow and (ii) transient, laminar hydrodynamically fully developed but thermally developing flow of water through a circular tube [14].

2.4.5 Phase Change and Effects of Bubble Motion. Equations (19) and (20) are based on the principle that if a liquid lattice evaporates, then it will receive the latent heat of vaporization from the neighboring lattices and, hence, the surrounding lattice temperatures will decrease by a small quantity η. On the other hand, if a vapor lattice condenses, then it will release the latent heat of condensation and, hence, the temperature of the neighboring lattices will increase by the same amount, η. This phase change process is formulated as follows [5]:

$$\text{If} \quad F_{i,j,k} = 0 \quad \text{and} \quad T^p_{i,j,k} > T_{c(i,j,k)}, \quad \text{then} \quad T^p_{\eta(i,j,k)} = T^p_{\eta(i,j,k)} - \eta \qquad (19)$$

$$\text{If} \quad F_{i,j,k} = 1.0 \quad \text{and} \quad T^p_{i,j,k} < T_{c(i,j,k)}, \quad \text{then} \quad T^p_{\eta(i,j,k)} = T^p_{\eta(i,j,k)} + \eta \qquad (20)$$

The subscript $\eta(i,j,k)$ represents the nearest-neighboring four lattices and $T_{c(i,j)}$ is the phase-change temperature, which is determined according to the phase-change criteria given below. In Eqs. (19) and (20), η is a parameter related to the enthalpy of vaporization and is in degrees Celsius. The aforesaid equations also represent the mixing effect of bulk liquid due to bubble motion.

2.4.5.1 Phase change criteria. The value of $T_{c(i,j,k)}$ for the liquid lattice adjacent to the wall is nucleation superheat. The value for liquid lattices in the bulk is assumed to be the homogeneous nucleation temperature of the liquid, but for liquid lattice, neighboring the vapor lattice is the saturation temperature of the liquid.

3 Method of Solution

3.1 Solution Methodology. In this section, the method of solution by CML and the overall solution algorithm are presented.

3.1.1 Time Advancement. Time is advanced by repeating a set of mapping the dynamic processes (Secs. 2.4.2–2.4.4) in such a manner that

$$T^p \rightarrow T' \rightarrow T^{p+1} \qquad (21)$$

The superscripts p and $p+1$ indicate the present and future time values of the temperature, respectively.

3.1.2 Parameter Values. In the CML method, the parameter values are determined so as to reproduce the phenomena satisfactorily. In the present computations, the parameter is η, whose value is taken as 0.01. It has been found that stability of the solution is affected by η. Higher values of η result in an unstable solution.

3.1.3 Calculation of Void Fraction. The void fraction is calculated at any given time and at a given axial location by locating the lattices having a flag function value of 1 (that is, vapor). It may be noted that a lattice can contain either vapor or liquid but not a liquid-vapor mixture. Thus, by summing the area of each lattice containing vapor, the total area in the circular cross section having vapor can be obtained. This area divided by the area of the circle gives the void fraction at a *z* location.

3.1.4 Overall Solution Algorithm. The basic solution methodology is briefly as follows. To start with, a random distribution of nucleating cavity sizes are specified on each axial wall segment. Thus, on each wall segment an activation superheat distribution is obtained. The iteration loop begins with the transient single-phase forced convection problem, which is solved by CFD techniques. Thus, at the end of the time step Δt, the new axial velocity and temperature are obtained. Then, the temperature at each wall-segment grid point is checked to see whether it is more than the nucleation temperature. If it is, then bubble formation takes place in that surface lattice and vapor bubbles migrate to the core of the liquid. Each fluid lattice is then checked to see which one contains vapor and which has liquid. The phase-change temperature for liquid lattices in the bulk is assumed to be homogeneous nucleation temperature of the liquid, but for a liquid lattice neighboring a vapor lattice, it is the saturation temperature of the liquid. At this stage, the temperature of each fluid lattice is updated based on the fact that a vaporizing lattice will result in decrease of its neighboring lattice temperatures while the condensing lattice will result in the increase of its neighboring lattice temperature by a small amount, say η. The phase state of each fluid lattice is checked again. Then the void fraction at each axial location is calculated. Now it is checked whether Reynolds number ($=\rho_{eq} v_m D / \mu_{eq}$) has exceeded 2000. If not, then momentum and thermal diffusivities are increased by an enhancement factor of 1.2 to take into account mixing due to bubble stirring action, equivalent property values of the two-phase mixture based on current void fraction are calculated, and the procedure is repeated till Reynolds number reaches the critical value of 2000. At this time mean fluid temperature (T_{mean}), which is the integrated average of the temperature in the $r-\theta$ plane, heat transfer coefficient (h_{mean}), and wall heat flux (q''_{mean}) are computed at each axial location.

4 Results and Discussion

4.1 Introductory Remarks. The results are presented for flow boiling of water. It may be noted that pressure changes along the axial direction and, as a result, the saturation temperature (T_{sat}) and thermophysical properties of the liquid and vapor also vary. T_{sat} and property variations with respect to pressure have been represented in the form of best-fit equations for convenience in computer implementation. The source of data for water is EES [13]. The Reynolds number of the flow is <2000 to ensure laminar flow. The time step is taken as 10^{-5} s. The explicit finite difference method is used to solve the transient forced convection problem. The CPU time required for executing this CML simulation on SUN enterprise 10,000 computer system of IIT Kanpur is ~3 h for a typical run (Fig. 3). The results are presented at $t=7.3$ s for the input data of Fig. 3, because it is seen that after this time the flow turns into a turbulent state. Thus, truly speaking, a steady-state solution would be obtained after the flow reached the turbulent state.

4.2 Results. The results are presented for the entrance pressure of 25 bar, level of entry subcooling of 30°C, axial pressure gradient of -1.5 N/m^3 and wall temperature of 230°C. It is observed that the mean heat transfer coefficient undergoes an initial steep drop from a large value followed by a slow decrease, until at $z=5$ m, it encounters a sharp fall again and then slowly decreases until the exit of the tube. The sharp drop at $z=5$ m can be explained by the sudden rise of the void fraction at that location, and
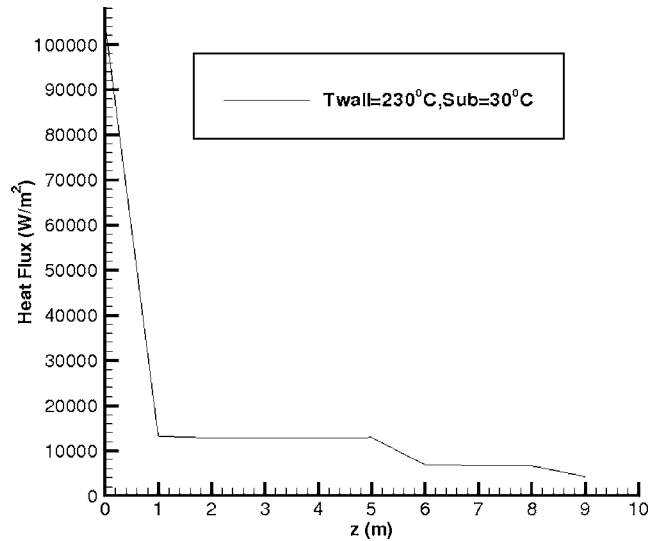

Fig. 3 Heat flux versus axial coordinate plot for water

hence, the thermal conductivity of the liquid-vapor mixture decreases because of higher vapor content. The mean wall heat flux at $z=5$ m is ~13 kW/m^2 (Fig. 3).

4.2.1 Parametric Study. The parameters varied are wall temperature, level of entry subcooling, and axial pressure gradient (in other words, the mass flow rate, whose value is not explicitly given because the results presented are not for the steady state). The main observations from the parametric study are as follows: (i) Changing the wall temperature does not affect the mean heat transfer coefficient in the inlet section (up to $z=1$ m), but in the subsequent portion of the tube, the mean heat transfer coefficient slightly increases with increase of the wall temperature (Fig. 4). The void fraction, however, remains invariant with the change of wall temperature throughout the tube length. This may be explained as follows. As long as the wall temperature is greater than the nucleation activation temperature distribution specified on each axial wall segment, the vapor nucleation will have the same pattern (see Sec. 2.4.1). Since the vapor migration pattern is determined by whether $T_{\text{sat}} - T_{\text{mean}} \gtrless 0$ and $T_{\text{sat}} - T_{\text{mean}} \gtrless 15°C$, even
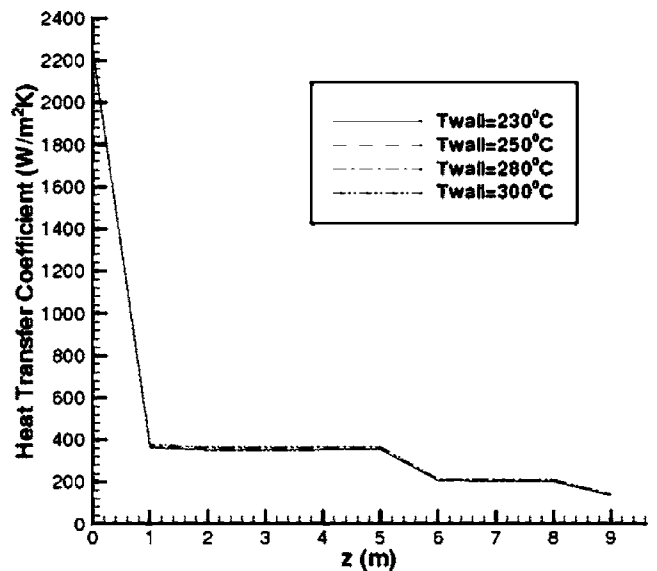

Fig. 4 Comparison of h_{mean} versus z plots for different wall temperatures
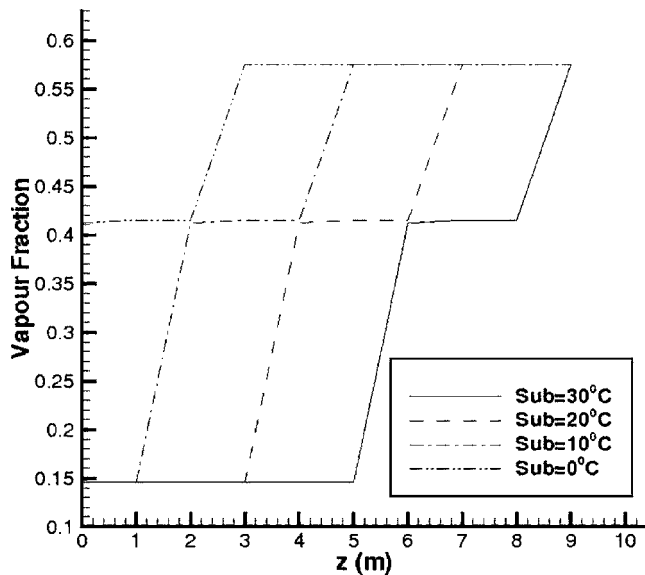
Fig. 5 Comparison of f versus z plots for different ΔT_{sub}

Fig. 6 Comparison of h_{mean} versus z plots for different axial pressure gradients

though T_{mean} is changing due to change of wall temperature, the phase state of the lattices will be unaffected as long as the phase-change pattern in the fluid bulk remains same (Sec. 2.4.1.1). It appears that this is the case in the present problem. Hence, the axial void fraction distribution remains unchanged with the wall temperature variation from 230°C to 300°C and, since heat transfer coefficient is a strong function of void fraction, the former also does not change significantly. (ii) The decrease in the level of entry subcooling lowers the mean heat transfer coefficient near the tube entrance and also influences the mean heat transfer coefficient in the latter part of the tube. Furthermore, void fraction is high near the tube entrance for low ΔT_{sub}, whereas the maximum void fraction is same for all ΔT_{sub} (Fig. 5). The maximum void fraction has not reached the value of 1 at the tube exit because the present computations correspond to the time at which laminar-turbulent flow transition has occurred and steady state has not yet been reached. (iii) The mean heat transfer coefficient is virtually independent of mass flow rate (arising out of higher axial pressure gradient) in the initial section of the tube, where the nucleate boiling effect is dominant. On the other hand, in the latter part of the tube, where convective vaporization is significant, the mean heat transfer coefficient increases with an increase in mass flow rate for some distance due to higher vapor velocity, but decreases in the latter part of the tube as more vapor forms and lower conductivity of the mixture nullifies the effect of high vapor velocity. The relevant plot is shown in Fig. 6.

5 Conclusions

In conclusion, it may be said that a complex phenomenon, such as flow boiling, has been qualitatively simulated by a simple CML model. The results show computations for stratified flow boiling until laminar-turbulent transition. The main observations from the results are the following: (i) The wall temperature does not affect the mean heat transfer coefficient in the inlet section of the tube. However, in the subsequent portion of the tube a slight increase of heat transfer coefficient with wall temperature is observed. The axial void fraction distribution remains unaffected with the change of wall temperature. (ii) The decrease in entry subcooling lowers the mean heat transfer coefficient near the tube entrance and also influences the heat transfer coefficient in the latter part of the tube. Furthermore, void fraction is high near the tube entrance for low entry subcooling, whereas exit void fraction is the same for all levels of entry subcooling. (iii) The mean heat transfer coefficient
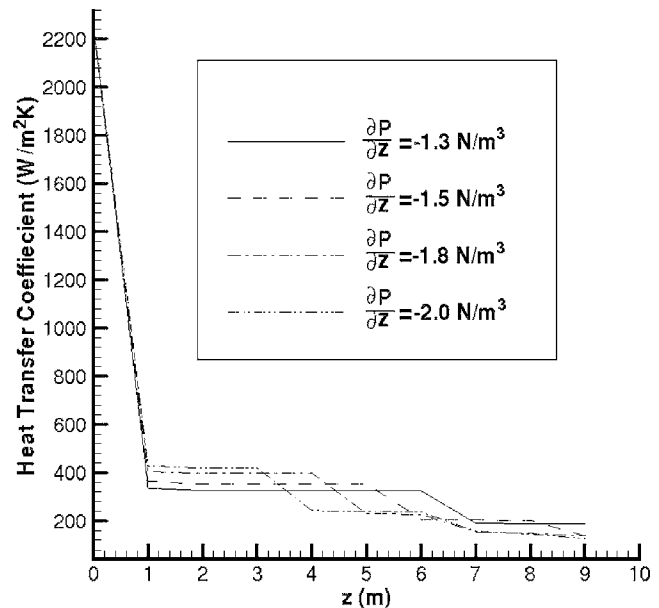
is virtually independent of mass flow rate in the initial section of the tube where the nucleate boiling effect is dominant. On the other hand, in the latter part of the tube where the convective vaporization is significant, the mean heat transfer coefficient increases with an increase in mass flow rate for some distance and then falls in the latter part of the tube.

The present analysis can be extended to model turbulent flow boiling in which case steady-state mean fluid temperature, mean heat transfer coefficient, mean wall heat flux, and void fraction can be predicted.

References

[1] Kaneko, K., 1993, *Theory and Application of Coupled Map Lattices*, Wiley, New York.
[2] Yanagita, T., and Kaneko, K., 1993, "Coupled Map Lattice Model for Convection," Phys. Lett. A, **175**, pp. 415–420.
[3] Sadasivan, P., Unal, C., and Nelson, R. A., 1995, "Nonlinear Aspects of High Heat Flux Nucleate Boiling Heat Transfer," Report No. LA-UR-95-609.
[4] Shoji, M., and Tajima, K., 1997, "Mathematical Simulation Model of Boiling: Modes and Chaos," Convective Flow and Pool Boiling Conference, May 18–23, Kloster Irsee, Germany, May 18–23.
[5] Shoji, M., 1998, "Boiling Simulator—A Simple Theoretical Model of Boiling," 3rd International Conference on Multiphase Flow, Lyon, France, June 8–12.
[6] Ellepola, J., and Kenning, D., 1996, "Nucleation Site Interactions in Pool Boiling," *Proc. of 2nd European Thermal sciences and 14th UK National Heat Transfer Conference*, Rome, Italy.
[7] Nelson, R., Kenning, D., and Shoji, M., 1997, "Nonlinear Effects and Behavior in Nucleate Boiling," 4th Experimental Chaos Conference, Boca Raton, Aug. 6–8.
[8] Yanagita, T., 1992, "Phenomenology for Boiling: A Coupled Map Lattice Model," Chaos, **2**, pp. 343–350.
[9] Ghoshdastidar, P. S., Kabelac, S., and Mohanty, A., 2004, "Numerical Modelling of Atmospheric Pool Boiling by the Coupled Map Lattice Method," J. Mech. Eng. Sci., **218**, pp. 195–205.
[10] Gupta, A., and Ghoshdastidar, P. S., 2006, "A Three-Dimensional Numerical Modeling of Atmospheric Pool Boiling by the Coupled Map Lattice Method," ASME J. Heat Transfer, **128**(11), pp. 1149–1158.
[11] Wang, C. H., and Dhir, V. K., 1993, "Effect of Surface Wettability on Active Nucleation Site Density," ASME J. Heat Transfer, **115**, pp. 659–669.
[12] Lienhard, IV, J. H., and Lienhard, V, J. H., 2006, *A Heat Transfer Textbook*, 3rd ed., Philogiston Press, Cambridge, MA, http://web.mit.edu/lienhard/www/ahtt.html
[13] F-Chart Software, 1992–2000, Engineering Equation Solver (EES), Thermodynamic Property Data, Software, Academic Version 6.036, Madison, WI.
[14] Kays, W. M., and Crawford, M. E., 1993, *Convective Heat and Mass Transfer*, 3rd ed., McGraw-Hill, New York.

Fully Developed Couette Flow of Three Fluids With Variable Thermophysical Properties Flowing Through a Porous Medium Channel Heated Asymmetrically With Large Temperature Differences

Asterios Pantokratoras

School of Engineering,
Democritus University of Thrace,
67100 Xanthi, Greece
e-mail: apantokr@civil.duth.gr

In this paper, we study the steady laminar flow in a fluid-saturated porous medium channel bounded by two parallel plates with constant but unequal temperatures. One plate is moving with constant velocity while the other is stationary. For the porous medium, the Brinkman–Darcy–Forchheimer model is used. The investigation concerns engine oil, water, and air, taking into account the variation of their physical properties with temperature. The results are obtained with the direct numerical solution of the governing equations and cover large temperature differences. It is found that dynamic viscosity plays an important role on the results, which depart significantly from those of a fluid with constant properties when the temperature difference between the plates is large. Except that there are cases where the flow is restricted near the moving plate while at the lower part of the channel, the fluid is motionless. [DOI: 10.1115/1.2768103]

Keywords: porous medium, forced convection, variable properties, Couette flow

1 Introduction

The study of convection through a porous medium channel was initiated by Kaviany [1], who presented an analytical solution based on the Brinkman–Darcy flow model. A complete review of the works done until 1996 is given by Nield et al. [2] and includes the papers by Poulikakos and Renken [3], Renken and Poulikakos [4], Cheng et al. [5], Nakayama et al. [6], and Vafai and Kim [7]. Nield et al. [2] studied the fully developed forced convection in a porous medium channel bounded by parallel plates with uniform heat flux or with constant and equal temperatures. They used the Brinkman–Darcy–Forchheimer model and obtained for the first time an "exact solution" for this problem. In a series of papers, Lage and his co-workers (Nield et al. [8], Narasimhan and Lage [9,10], Narasimhan et al. [11,12], and Narasimhan and Lage [13]) studied the effect of temperature-dependent viscosity on the flow through a porous medium channel using the Darcy–Forchheimer model. Haji-Sheikh [14] studied the heat transfer between parallel plates using the Brinkman–Darcy model and constant fluid properties. Nield et al. [15] investigated the fully developed forced convection in a channel using the Brinkman–Darcy model, taking into account the viscous dissipation and flow work and considering constant fluid properties. In all the above works, the fluid motion was caused by a pressure gradient (Poiseuille flow).

The first work of convection through a porous medium channel due to a moving plate (Couette flow) is that of Nakayama [16],

who presented analytical solutions for Newtonian and power-law non-Newtonian fluids through an inelastic porous medium without taking into account the heat transfer problem. Kuznetsov [17] investigated the fluid flow and heat transfer in Couette flow through a Brinkman–Darcy–Forchheimer porous medium. The heat transfer situations considered was (i) isoflux fixed wall and insulated moving wall and (ii) insulated fixed wall and isoflux moving wall. In both cases, the fluid thermophysical properties have been considered constant and independent of temperature.

The objective of the present paper is to investigate the fully developed Couette flow of three fluids with variable thermophysical properties flowing through a Brinkman–Darcy–Forchheimer porous medium channel with constant but unequal temperatures. The working fluids are engine oil, water, and air. The temperature range covered is 273–430 K for engine oil, 273–373 K for water, and 150–3000 K for air. The author believes that this is the first work on forced convection in a Couette flow through a porous medium channel that treats real fluids with their real physical properties.

2 Mathematical Model

The momentum and energy equation for Couette fully developed flow (both hydrodynamically and thermally) through a porous medium channel with variable properties are [2,17]

$$\text{Momentum equation:} \quad \frac{\partial}{\partial y}\left(\mu_{\text{eff}}\frac{\partial u}{\partial y}\right) - \frac{\mu}{K}u - c_F\rho K^{-1/2}u^2 = 0 \tag{1}$$

$$\text{Energy equation:} \quad \frac{\partial}{\partial y}\left(k_{\text{eff}}\frac{\partial T}{\partial y}\right) = 0 \tag{2}$$

where x is the horizontal coordinate, y is the vertical coordinate, u is the fluid velocity along the plates, K is permeability, c_F is the inertial coefficient of the Forchheimer term, ρ is the fluid density, μ is the fluid dynamic viscosity, μ_{eff} is the effective viscosity of the Brinkman term, c_p is the fluid specific heat, k_{eff} is the effective thermal conductivity of the porous medium, and T is the fluid temperature. For low-speed flows, such as those treated in the present paper, the Brinkman number is very small, even for oil, and for that reason the viscous dissipation term in the energy equation has been ignored.

The boundary conditions at the two plates are

$$y = 0, \quad u = 0, \quad T = T_1, \quad y = H, \quad u = u_2, \quad T = T_2 \tag{3}$$

where T_1 is the temperature of the lower plate, T_2 is the temperature of the upper plate, H is the distance between the plates and u_2 is the velocity of the upper plate.

The effective thermal conductivity k_{eff} is provided by the weighted geometric mean of k_{fl} and k_s [18]

$$k_{\text{eff}} = k_{fl}^{\varphi}k_s^{(1-\varphi)} \tag{4}$$

where φ is the porosity of the porous medium, and k_{fl} and k_s are thermal conductivity of the fluid and solid, respectively. This provides a good estimate as long as k_{fl} and k_s are not too different from each other. More complicated correlation formulas for the conductivity of packed beds have been proposed. The problem of the overall thermal conductivity of a porous medium is a difficult task and becomes more complex if k_{fl} and k_s are functions of temperature. Engine oil and water thermal conductivity does not change significantly with temperature in the temperature ranges covered in the present work. For engine oil, the change is 10% between 273 K and 430 K, and for water, the change is 17% between 273 K and 373 K. For that reason, we assumed that porous medium thermal conductivity is constant for engine oil and water. For air, things are different because the temperature range covered is broad (150–3000 K) and air thermal conductivity changes significantly in this range (100%). For that reason, for air,
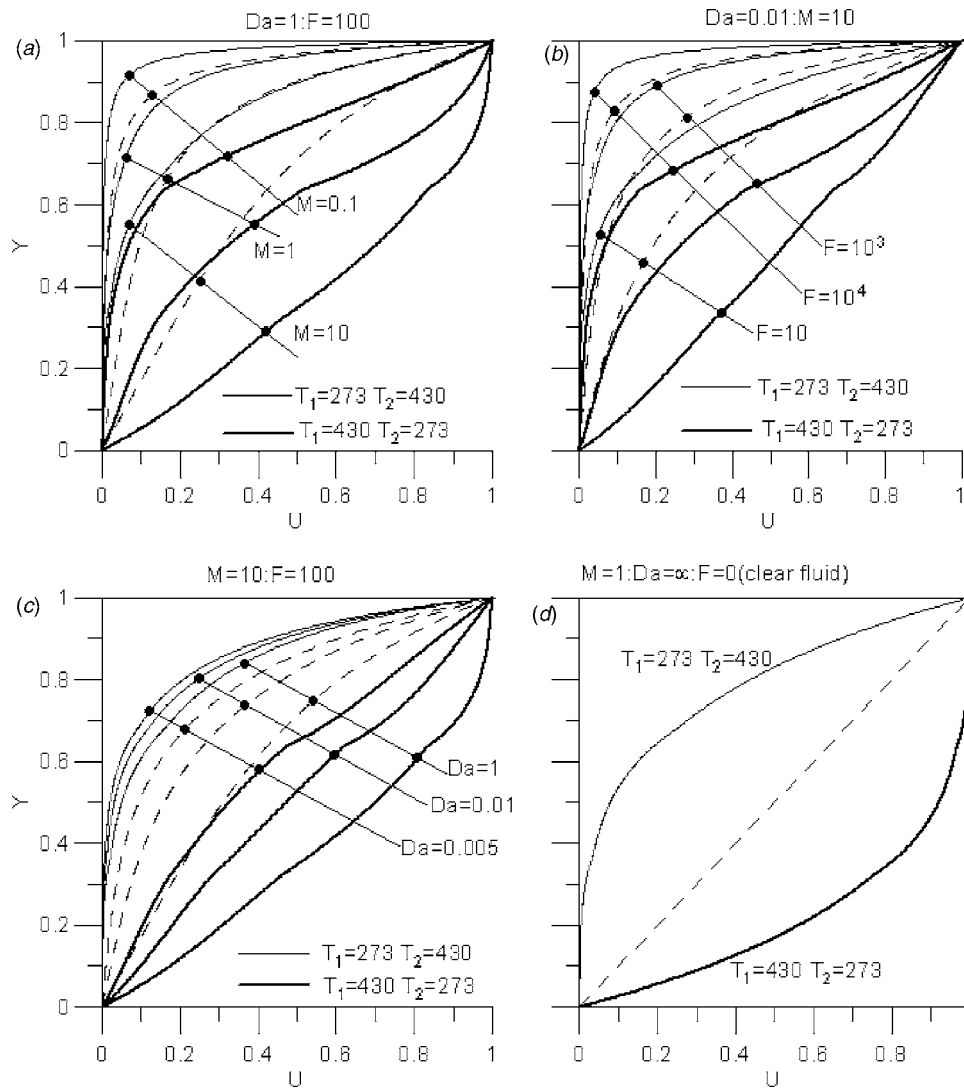
Fig. 1 Velocity distribution for oil: solid and bold lines correspond to variable ρ and μ while dashed lines correspond to constant properties

we present results both for constant and variable effective thermal conductivity.

In some cases of the present work, large temperature differences exist between the plates and the question arises whether buoyancy should be taken into account. The flow between two very long and wide, nonmoving horizontal plates (without porous medium) with constant but unequal temperatures with $T_1 > T_2$ is known in the literature as the Rayleigh–Benard problem. The corresponding problem in a channel filled with a porous medium is known as the Horton–Rogers–Lapwood problem ([18], p. 175). As happens in a clear fluid flow, there is a critical Rayleigh number for the onset of convection in the Horton–Rogers–Lapwood problem and its value is 39.48 ([18], p. 179). The Rayleigh number is defined as

$$\text{Ra} = \frac{g\beta_r(T_1 - T_2)KH}{a_r \nu_r} \tag{5}$$

where β is the fluid coefficient of thermal expansion, α is the overall thermal diffusivity and ν is the fluid kinematic viscosity, all calculated at reference temperature $(T_1 + T_2)/2$. Our results are valid only for Rayleigh numbers lower than 39.48, where buoyancy is negligible. For the cases with $T_1 < T_2$, we have stable

density stratification and our results are valid without the above limit.

For fluids with constant properties, Eqs. (1) and (2) accept "analytical" solutions. In the present work, these equations are partially coupled; that is, the energy equation is independent from the momentum equation, but the momentum equation is dependent on the energy equation because viscosity and density are functions of temperature. For that reason, we solved them directly, without any transformation, using the finite difference method of Patankar [19]. The solution procedure starts with a known distribution of velocity and temperature at the channel entrance ($x = 0$) and marches along the plates. These profiles were used only to start the computations, and their shape had no influence on the results, which were taken far downstream. At the channel entrance, the temperature and velocity were taken uniform with a very small value. At each downstream position, the discretized equations are solved using the tridiagonal matrix algorithm (TDMA). As x increases, the successive velocity profiles become more and more similar and the same happens with temperature profiles. The solution procedure stops at the point where the successive velocity and successive temperature profiles become identical. The forward step size Δx was 0.01 mm and the lateral grid
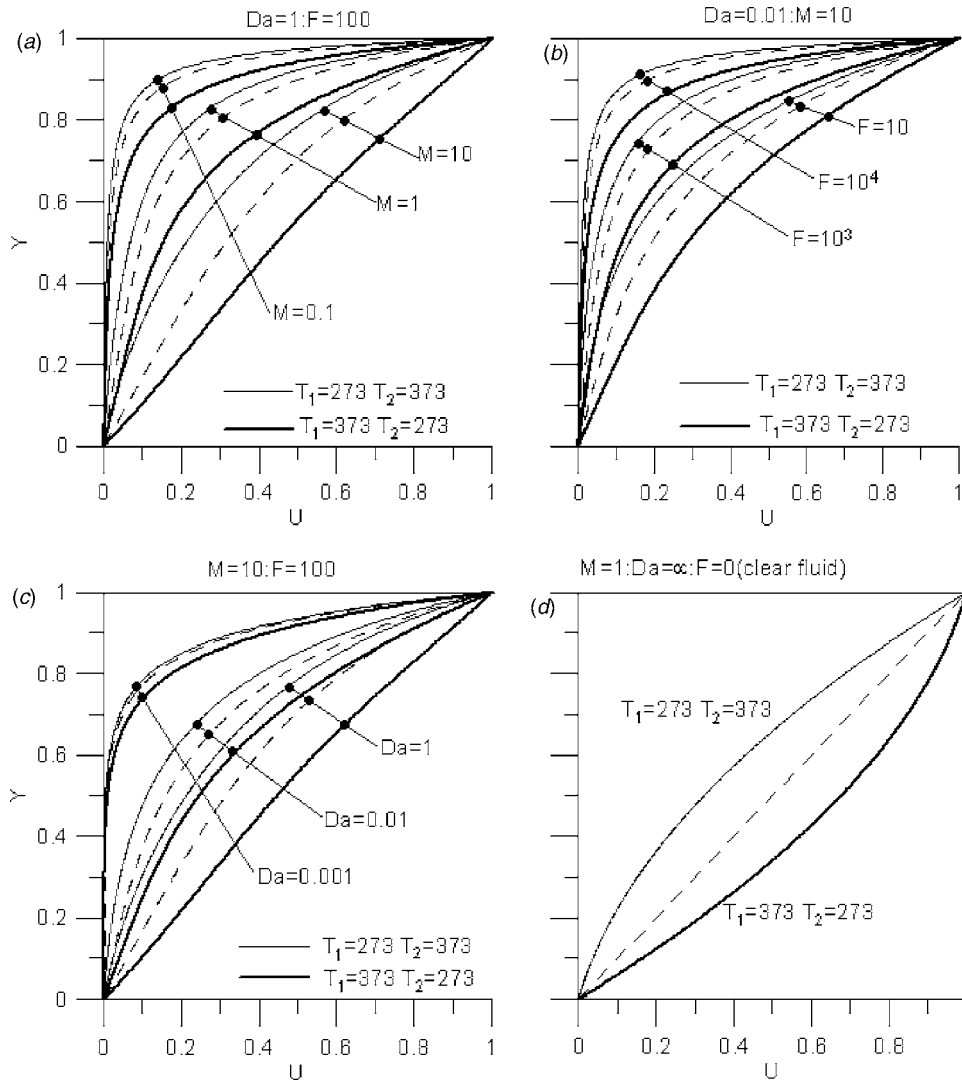
Fig. 2 Velocity distribution for water: solid and bold lines correspond to variable ρ and μ while dashed lines correspond to constant properties

cells, 500. The accuracy depends on the number of lateral grid points. We found, by trial and error, that 500 lateral grid points are needed to obtain grid-independent results. In the solution procedure, μ, ρ, and k have been considered as functions of temperature.

3 Results and Discussion

The governing parameters for the Poiseuille problem treated by Nield et al. [2] is the viscosity ratio M, the Darcy number Da, and the Forchheimer number defined as

$$M = \frac{\mu_{\text{eff}}}{\mu} \tag{6}$$

$$\text{Da} = \frac{K}{H^2} \tag{7}$$

$$F = \frac{c_F \rho_r G H^4}{K^{1/2} \mu_r^2} \tag{8}$$

where ρ_r is the reference fluid density and μ_r is the reference fluid viscosity both calculated at reference temperature $(T_1 + T_2)/2$, while $G = -dp/dx$ is the pressure gradient. In the present work, the parameters M and Da remain the same while the quantity G is

substituted by the quantity $\mu_r u_2/H^2$, which is the equivalent of the pressure gradient (both have dimensions Newtons per meter to the -3). Therefore, the Forchheimer number for Couette flow is

$$F = \frac{c_F \rho_r u_2 H^2}{K^{1/2} \mu_r} \tag{9}$$

The dimensionless temperature θ, the dimensionless distance Y and the dimensionless velocity U are given by the following for Poiseuille problem [2]:

$$\vartheta = \frac{T - T_1}{T_2 - T_1} \tag{10}$$

$$Y = \frac{y}{H} \tag{11}$$

$$U = \frac{\mu_r u}{GH^2} \tag{12}$$

In the present work, the quantities θ and Y remain the same. Substituting the quantity G in Eq. (12) by $\mu_r u_2/H^2$, the dimensionless velocity takes the form
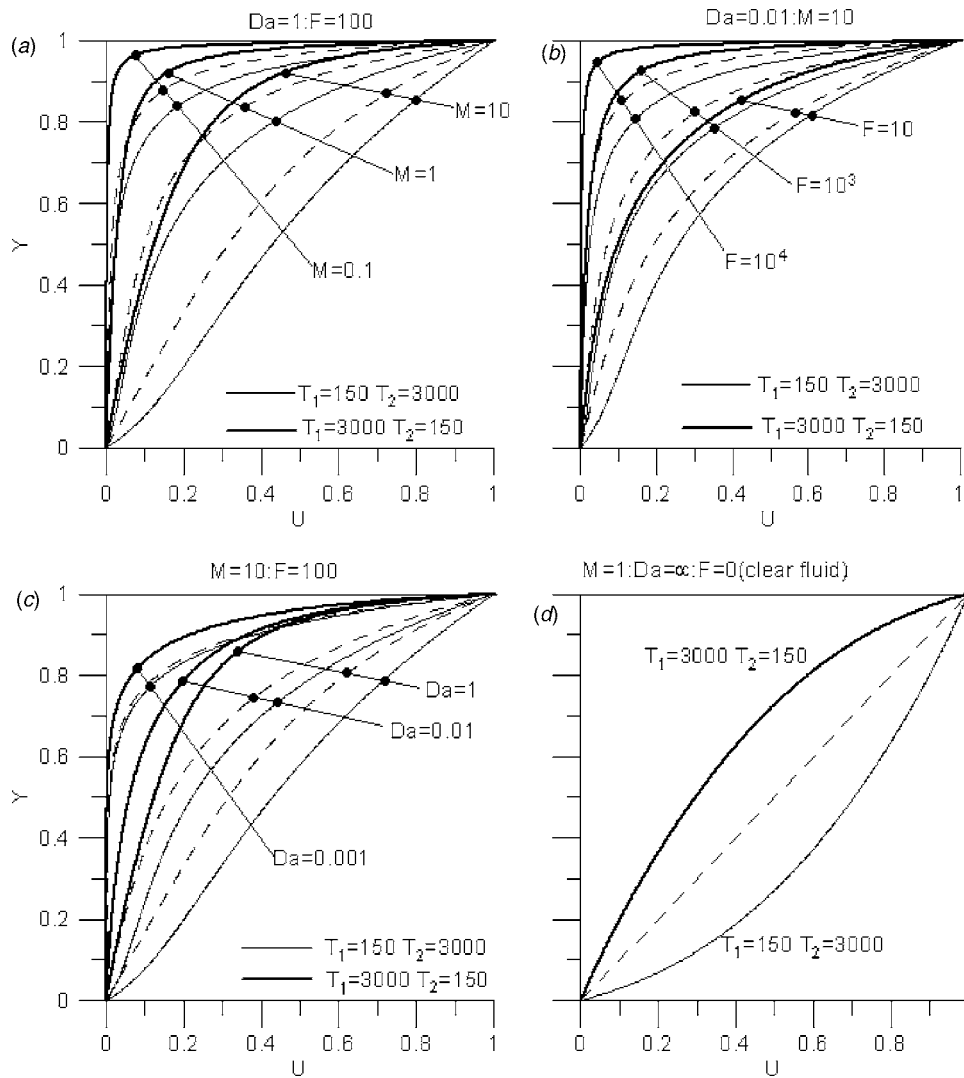
Fig. 3 Velocity distribution for air: solid and bold lines correspond to variable ρ and μ while dashed lines correspond to constant properties

$$U = \frac{u}{u_2} \tag{13}$$

3.1 Results for Engine Oil. For engine oil, the density, dynamic viscosity, and thermal conductivity in the temperature range 273 K $\leq T \leq$ 430 K are given by Zografos et al. [20]. In Fig. 1, velocity profiles are shown for different values of M, Da, and F for $T_1 = 273$ to $T_2 = 430$ and $T_1 = 430$ to $T_2 = 273$. We chose the largest temperature difference between the plates in order to clearly show the influence of variable properties on the results. At the same temperatures, the results that correspond to a fluid with constant properties (dashed lines) have been included for comparison. From Fig. 1, it is seen that the variation of viscosity with temperature has a strong influence on velocity. Oil viscosity is large near the cold plate and small near the hot plate. The high viscosity hinders velocity while low viscosity enhances velocity, and for that reason, oil velocity is low near the lower plate and higher near the upper plate for $T_1 = 273$ to $T_2 = 430$ and vice versa for $T_1 = 430$ to $T_2 = 273$. The variable property profiles approach those of constant properties profiles (dashed lines) as ΔT decreases and coincide completely when $T_1 = T_2$. We do not present velocity profiles for other ΔT to avoid confusion by many curves. Except of viscosity both M, F, and Da play an important role on

the results. Because the porous medium creates resistance to the fluid flow, the fluid velocity decreases with distance from the moving plate and there are cases where the flow is restricted near the moving plate while at the lower part of the channel the fluid is motionless. This phenomenon becomes more evident with increasing F and Da and with decreasing M. The same phenomenon is observed in a clear fluid (Fig. 1(d)), but in this case, the low velocity near the lower plate is caused only by high viscosity at the cold plate.

3.2 Results for Water. For water, the density, dynamic viscosity, and thermal conductivity in the temperature range 273 K $\leq T \leq$ 600 K are given by Zografos et al. [20]. The results are presented in Fig. 2 for different values of M, Da, and F. Viscosity of water decreases with increasing temperature and increases as temperature decreases. This behavior is similar to that of oil and for that reason the characteristics of Fig. 2 are, in general, similar to those in Fig. 1. However, water viscosity is less dependent on temperature than in engine oil, and for that reason, the departure from constant properties profiles is smaller. The stagnation phenomenon at the lower plate is observed again.

3.3 Results for Air. For air, the density, dynamic viscosity, and thermal conductivity in the temperature range 150 K $\leq T$
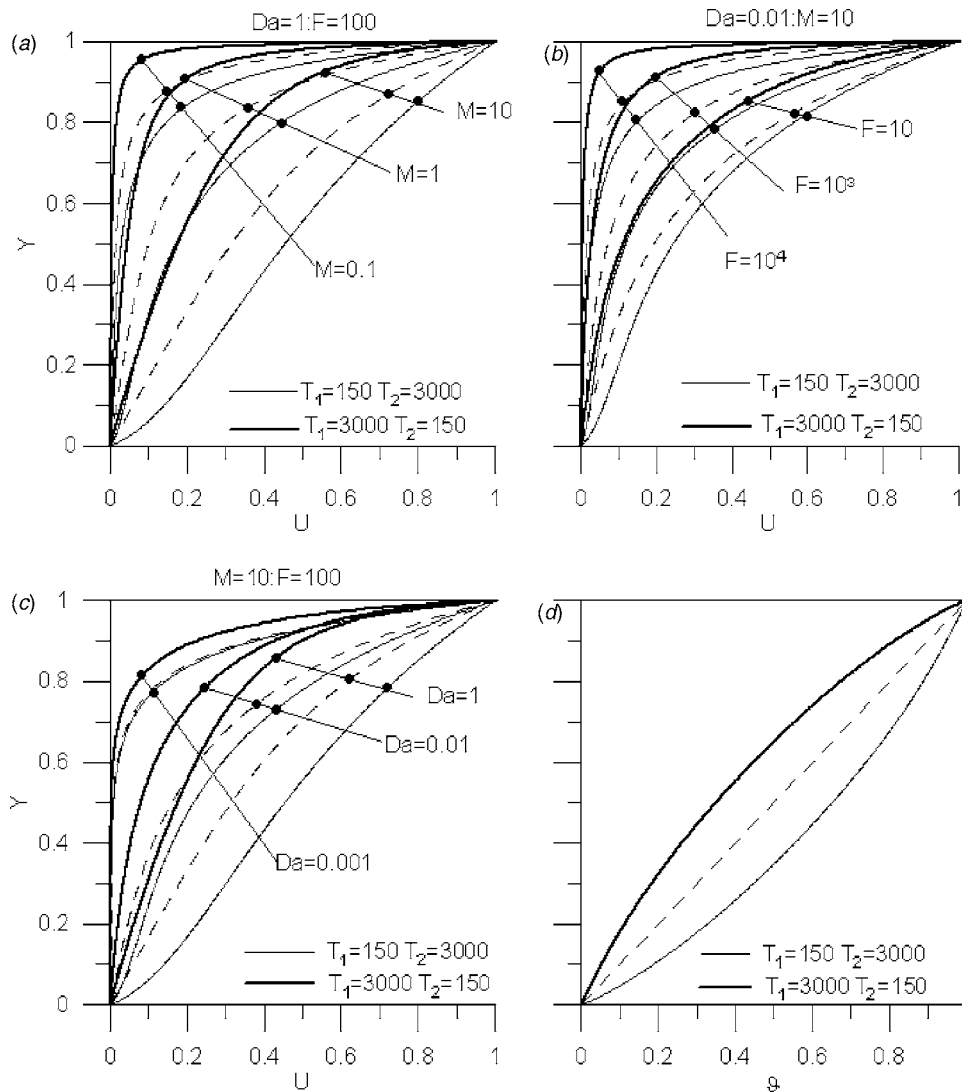
Fig. 4 Velocity and temperature distribution for air: solid and bold lines correspond to variable ρ, μ, k, and $\varphi=0.5$ while dashed lines correspond to constant properties

≤ 3000 K are given by Zografos et al. [20]. Figure 3 includes velocity profiles. Viscosity of air, in contrast to engine oil and water, increases with increasing temperature and decreases as temperature decreases. This means that viscosity is low near the cold plate and high near the hot plate, and for that reason, the position of bold and solid lines in Fig. 3 are in the opposite situation in comparison to what happens in the Figs. 1 and 2. In some cases, we see again that air remains motionless at lower plate. It should be also noted that inflection points appear in some velocity profiles (Fig. 3(a), $T_1=150$ to $T_2=3000$, $M=10$; Fig. 3(b), $T_1=150$ to $T_2=3000$, $F=10$; and Fig. 3(c), $T_1=150$ to $T_2=3000$, Da=1). Probably, inflection points exist also in Fig. 1 but cannot be observed clearly due to discontinuities in the velocity profiles produced by viscosity functions.

All the above results have been produced with constant effective thermal conductivity, and this means that the temperature distribution between the plates is a straight line. As was mentioned before, the variation of air thermal conductivity in the 150–3000 K range is significant, and for that reason, we present some results with variable effective thermal conductivity. We used Eq. (4), assuming that the solid thermal conductivity is constant. For this case, the effective thermal conductivity is

$$k_{\text{eff}} = k_{fl}^{\varphi} \qquad (14)$$

where k_{fl} is a function of temperature. In Fig. 4(d), the temperature profiles are presented for porosity $\varphi=0.5$. We see that when effective thermal conductivity is a function of temperature the temperature distribution departs from the straight line. In Figs. 4(a)–4(c), velocity profiles are shown for the same values of M, Da, and F of Fig. 3 and variable k_{eff} with $\varphi=0.5$. In general, the velocity profiles are similar to those of Fig. 3, although there are quantitative differences. These quantitative differences increase as φ increases and tend to disappear as φ decreases, and the k_{eff} tends to be constant.

Another general conclusion drawn from Figs. 1–4 is that when M decreases significantly or Da decreases significantly or F increases significantly and the flow is restricted to a very small region near the moving plate, the influence of temperature dependent fluid properties tends to diminish (characteristic cases are Fig. 2(c), Da=0.001 and Fig. 4(c), Da=0.001).

4 Conclusions

In this paper, the problem of Couette flow between parallel plates filled with a porous medium has been investigated with the

finite difference solution of the governing equations, taking into account the variation of fluid properties with temperature. Results have been produced for engine oil, water, and air. The major findings from the present study can be summarized as follows:

1. Viscosity plays an important role on velocity, especially when the temperature difference between the plates is large.
2. Velocity decreases as the Darcy number and the Forchheimer number increases and the viscosity ratio decreases, whereas velocity increases as the Darcy number and the Forchheimer number decreases and the viscosity ratio increases.
3. The velocity behavior is similar in oil and water and reverse in air due to temperature-dependent viscosity.
4. In some cases, the flow is restricted in a region near the moving plate while at the lower part of the channel the fluid is motionless, and in these cases, the influence of temperature-dependent fluid properties tends to diminish. This phenomenon becomes more evident with increasing F and Da and with decreasing M.

References

[1] Kaviany, M., 1985, "Laminar Flow Through a Porous Channel Bounded by Isothermal Parallel Plates," Int. J. Heat Mass Transfer, **28**, pp. 851–858.
[2] Nield, D. A., Junqueira, S. L. M., and Lage, J. L., 1996, "Forced Convection in a Fluid-Saturated Porous-Medium Channel With Isothermal or Isoflux Boundaries," J. Fluid Mech., **322**, pp. 201–214.
[3] Poulikakos, D., and Renken, K., 1987, "Forced Convection in a Channel Filled With Porous Medium, Including the Effects of Flow Inertia, Variable Porosity, and Brinkman Friction," ASME J. Heat Transfer, **109**, pp. 880–888.
[4] Renken, K., and Poulikakos, D., 1988, "Experiment and Analysis of Forced Convective Heat Transport in a Packed Bed of Spheres," Int. J. Heat Mass Transfer, **31**, pp. 1399–1408.
[5] Cheng, P., Hsu, C. T., and Chowdhury, A., 1988, "Forced Convection in the Entrance Region of a Packed Channel With Asymmetrical Heating," ASME J. Heat Transfer, **110**, pp. 946–954.
[6] Nakayama, A., Koyama, H., and Kuwahara, F., 1988, "An Analysis on Forced Convection in a Channel Filled With a Brinkman-Darcy Porous Medium: Exact and Approximate Solutions," Waerme- Stoffuebertrag., **23**, pp. 291–295.
[7] Vafai, K., and Kim, S. J., 1989, "Forced Convection in a Channel Filled With a Porous Medium: An Exact Solution," ASME J. Heat Transfer, **111**, pp. 1103–1106.
[8] Nield, D. A., Porneala, D. C., and Lage, J. L., 1999, "A Theoretical Study, With Experimental Verification, of the Temperature-Dependent Viscosity Effect on the Forced Convection Through a Porous Medium Channel," ASME J. Heat Transfer, **121**, pp. 500–503.
[9] Narasimhan, A., and Lage, J. L., 2001, "Forced Convection of a Fluid With Temperature-Dependent Viscosity Flowing Through a Porous Medium Channel," Numer. Heat Transfer, Part A, **40**, pp. 801–820.
[10] Narasimhan, A., and Lage, J. L., 2001, "Modified Hazen-Dupuit-Darcy Model for Forced Convection of a Fluid With Temperature-Dependent Viscosity," ASME J. Heat Transfer, **123**, pp. 31–38.
[11] Narasimhan, A., Lage, J. L., and Nield, D. A., 2001, "New Theory for Forced Convection Through Porous Media by Fluids With Temperature-Dependent Viscosity," ASME J. Heat Transfer, **123**, pp. 1045–1051.
[12] Narasimhan, A., Lage, J. L., Nield, D. A., and Porneala, D. C., 2001, "Experimental Verification of Two New Theories Predicting Temperature-Dependent Viscosity Effects on the Forced Convection in a Porous Channel," ASME J. Fluids Eng., **123**, pp. 948–951.
[13] Narasimhan, A., and Lage, J. L., 2003, "Temperature-Dependent Viscosity Effects on the Thermohydraulics of Heated Porous-Medium Channel Flows," J. Porous Media, **6**, pp. 149–158.
[14] Haji-Sheikh, A., 2004, "Estimation of Average and Local Heat Transfer in Parallel Plates and Circular Ducts Filled With Porous Material," ASME J. Heat Transfer, **126**, pp. 400–409.
[15] Nield, D. A., Kuznetsov, A. V., and Xiong, M., 2004, "Effects of Viscous Dissipation and Flow Work on Forced Convection in a Channel Filled by a Saturated Porous Medium," Transp. Porous Media, **56**, pp. 351–367.
[16] Nakayama, A., 1992, "Non-Darcy Couette Flow in a Porous Medium Filled With an Inelastic Non-Newtonian Fluid," ASME J. Fluids Eng., **114**, pp. 642–647.
[17] Kuznetsov, A. V., 1998, "Analytical Investigation of Heat Transfer in Couette Flow Through a Porous Medium Utilizing the Brinkman-Forchheimer-Extended Darcy Model," Acta Mech., **129**, pp. 13–24.
[18] Nield, D. A., and Bejan, A., 1999, *Convection in Porous Media*, 2nd ed., Springer-Verlag, Berlin.
[19] Patankar, S. V., 1980, *Numerical Heat Transfer and Fluid Flow*, McGraw-Hill, New York.
[20] Zografos, A. I., Martin, W. A., and Sunderland, J. E., 1987, "Equations of Properties as a Function of Temperature for Seven Fluids," Comput. Methods Appl. Mech. Eng., **61**, pp. 177–187.